Second Order QED Processes in an Intense Electromagnetic Field

Anthony Francis Hartin

A dissertation submitted in partial fulfillment

of the requirements for the degree of

Doctor of Philosophy

of the

University of London.

Department of Physics

Queen Mary
University of London

2006

Abstract

Some non linear, second order QED processes in the presence of intense plane electromagnetic waves are investigated. Analytic expressions with general kinematics are derived for Compton scattering and e^+e^- pair production in a circularly polarised external electromagnetic field. Special kinematics, including collinear photons and vanishing external field intensity, are employed to show that the general expressions reduce to expressions obtained in previous work. The differential cross sections were investigated numerically for photon energies up to 50 MeV, external field intensity parameter ν^2 to value 2, and all scattering angles. The variation of full cross sections with respect to external field intensity was also established.

The presence of the external field led to resonances in the Compton scattering and pair production differential cross sections. These resonances were investigated by calculating the electron self energy in the presence of the external field. Numerical analysis of the external field electron self energy showed agreement with previous work in appropriate limits. However the more general expressions were utilised to calculate resonance widths. At resonance the differential cross sections were enhanced by several orders of magnitude. The resonances occurred for values of external field intensity parameter $\nu^2 < 1$, lowering the limit of $\nu^2 \sim 1$ at which point non linear effects in first order external field QED processes become important. Generally, full cross sections increased with increasing external field intensity, though peaking sharply for Compton scattering and levelling off for pair production.

An application was made to non linear background studies at e^+e^- linear colliders. The pair production process and electron self energy were studied for the case of a constant crossed electromagnetic field. It was found that previous analytic expressions required the external field to be azimuthally symmetric. New analytic expressions for the more general non azimuthally symmetric case were developed and a numerical parameter range equivalent to that proposed for the International Linear Collider was considered. The resonant pair production cross section exceeded the non resonant one by 5 to 6 orders of magnitude. Extra background pair particles are expected at ILC bunch collisions, raising previous estimations.

Acknowledgements

The Physics Department at Monash University provided me with many years of employment and the inspiration to pursue a career in physics. Drs Harry S Perlman and Gordon Troup provided much encouragement to pursue work in the field of QED and were coauthors on more than one occasion. Harry's cigar smoke always provided notice of his presence in the department. Thanks also to Dr. Peter Derlet who was a group member worthy of emulation and whose latex outlines I made use of.

My thanks to John Dawkins, former Australian Minister for Higher Education in the Australian Labour government. His attacks on the Higher Education sector in 1987 and 1988 introduced me to political activism and my development as a human being. Tony Blair would have been proud of him. John convinced me that the pursuit of knowledge is always more important than the pursuit of profit.

The Physics Department at Queen Mary provided employment and the opportunity to revisit my thesis. Particular thanks must go to my supervisor Prof Phil Burrows and the FONT research group. Phil always took me seriously and provided years of financial, moral and physics support. The ILC was the practical application to which some modest theoretical work in this thesis could be directed.

Above all, thanks must go to my family and my partner. My parents, brother and sisters never stop believing in me and encouraging me to complete my work. My partner, with constant love and support, endured the writing up period with never a word of complaint.

Contents

1 Introduction **8**

1.1 QED and the external field . . . 9
1.2 First order external field QED processes . . . 12
1.3 Second order external field QED processes . . . 16
1.4 Experimental Work . . . 21
1.5 The Present Work . . . 24

2 General Theory **26**

2.1 Introduction . . . 26
2.2 Units, normalisation constants, notation and metric . . . 27
2.3 The Bound Interaction Picture . . . 27
2.4 S-matrix Theory . . . 29
2.5 Wicks theorem and Feynman diagrams . . . 30
2.6 Crossing symmetry . . . 32
2.7 Summation over spin and polarisation states . . . 32
2.8 The transition probability and the scattering cross section . . . 34
2.9 The external field . . . 35
2.10 The Volkov solution and the Bound Electron Propagator . . . 36
2.11 Radiative corrections to the bound electron propagator . . . 38
2.12 The external field electron energy shift . . . 39
2.13 Non external field regularisation and renormalisation . . . 40
2.14 The optical theorem . . . 41

3 Cross section Calculations **43**

3.1 Introduction . . . 43
3.2 The stimulated Compton scattering (SCS) matrix element . . . 44
3.3 The SCS phase space integral . . . 48
3.4 Symbolic evaluation of the SCS cross section . . . 49

3.5 Numerical evaluation of the SCS cross section 51
3.6 The SCS cross section in various limiting cases 52
3.7 Stimulated Two Photon e^+e^- pair production (STPPP) in an External Field 54

4 SCS in a circularly polarised electromagnetic field - Results and Analysis 58

4.1 Introduction 58
4.2 SCS Plots 59
4.2.1 Differential Cross section l Contributions 59
4.2.2 Differential Cross sections summed over all l 70
4.3 SCS Analysis 82
4.3.1 Differential Cross Section l Contributions 82
4.3.2 Differential Cross Sections Summed Over All l 89

5 STPPP in a circularly polarised electromagnetic field - Results and Analysis 93

5.1 Introduction 93
5.2 STPPP Plots 94
5.2.1 Differential cross section l contributions 94
5.2.2 Differential Cross sections summed over all l 106
5.3 STPPP Analysis 116
5.3.1 Differential Cross Section l Contributions 116
5.3.2 Differential Cross Sections Summed Over All l 121

6 External Field Electron Propagator Radiative Corrections 126

6.1 Introduction 126
6.2 The external field electron energy shift in a circularly polarised external field 128
6.3 EFEES Plots 134
6.4 EFEES Analysis 141

7 SCS and STPPP Resonance Cross sections 143

7.1 Introduction 143
7.2 Renormalisation in the external field 144
7.3 Resonance Conditions 147
7.4 Resonance Figures 151
7.4.1 SCS Resonances 151
7.4.2 STPPP Resonances 159
7.5 Analysis of Resonance Plots 167
7.6 Experimental Considerations 171

8 STPPP in the Beam Field of an e^+e^- Collider **176**

8.1 Introduction . . . 176

8.2 Electromagnetic Field of a Relativistic Charged Beam . . . 177

8.3 Volkov functions in a constant crossed electromagnetic field . . . 179

8.4 Numerical comparison of Fourier transforms $F_{n,r}$ and $F^{(\varphi)}_{n,r}$ . . . 182

8.5 Electron self energy in a constant crossed electromagnetic field . . . 184

8.6 STPPP in a constant crossed electromagnetic field . . . 189

8.7 Conclusion . . . 195

9 Conclusion **197**

Appendices **205**

A The Jacobian of the Transformation $d^4p \to d^4q$ **206**

B The Full Expressions and Trace results for Tr Q_1 and Tr Q_2 **207**

B.1 The results for Tr Q_1 . . . 207

B.2 The results for Tr Q_2 . . . 209

C The explicit form of certain functions of M_j and M_k **212**

D Solution to $\sum\limits_{n=-\infty}^{\infty} \frac{1}{n+a}\left(\frac{z_1}{z_2}\right)^n J_n(z_1)J_{n-l}(z_2)$ **214**

E Dispersion Relation Method used in self energy Calculations **216**

Bibliography **218**

List of Tables

2.1 **Crossing symmetry correspondences.** 32

4.1 **The parameter range for which the SCS differential cross section l and r contributions are investigated.** 59

4.2 **The parameter range for which the SCS differential cross section summed over all l is investigated.** 70

4.3 **Peak maximums for the $\theta_i = 30°$ plots of figures 4.21 - 4.23, and the $\theta_i = 90°$ plots of figures 4.24 - 4.26.** 89

5.1 **The parameter range for which the STPPP differential cross section l and r contributions are investigated.** 94

5.2 **The parameter range for which the STPPP differential cross section summed over all l is investigated.** 106

5.3 **The ratio of peak heights and particle energies for figures 5.13 - 5.16.** 119

5.4 **A comparison of the number of final states and the differential cross section values for various ratios of l contributions for the STPPP process represented in figures 5.13 - 5.16.** 120

6.1 **The parameter range for which the regularised imaginary part of the EFEES is investigated.** 134

7.1 **The parameter range for which the SCS cross section resonances are investigated.** 151

7.2 **The parameter range for which the STPPP cross section resonances are investigated.** 159

7.3 **Variation of the number of SCS and STPPP resonances with $\frac{\omega_i}{\omega}$, $\frac{\omega_1}{\omega}$.** 170

C.1 **General algebraic functions involving M_i and N_j** 212

Chapter 1

Introduction

Quantum electrodynamics (QED) is one of the most successful physics theories of the last century. A measure of that success is in terms of the range of phenomena described and the accordance of its numerical calculations with experimental results. The presence of an external field has the effect of introducing a new range of QED phenomena. Analytic study of these external field phenomena is of interest to provide further QED predictions that can be tested experimentally. This then is the motivation for this thesis which attempts a detailed theoretical evaluation of some second order QED processes in the presence of an intense electromagnetic field.

To achieve this aim, in the first instance, Chapter 1 is devoted to a review of the literature which deals with the subject of interest. Section 1.1 provides a broad sweep of QED since its inception, dealing in some detail with the development of the theory in regards to the external field, and in particular the external electromagnetic field. Sections 1.2 and 1.3 deal, respectively and in greater detail, with the first and second order QED processes in the presence of an external electromagnetic field. The space devoted to the first order processes is larger than may otherwise have been expected for two reasons. The techniques developed for the first order external field processes serve as the basis for the more complicated second order external field processes. Secondly, limiting cases of second order processes bear a direct relationship to first order processes and provide an important test for the correctness of the second order calculations which are more complex and therefore more open to error.

Section 1.4 provides a review of the experimental attempts at measurement of Intense Field Quantum Electrodynamics (IFQED) phenomena. So far these experimental efforts have been confined to the first order processes. A brief review of laser systems is also provided, which are a source of intense, polarised electromagnetic fields, and which have been used in IFQED experimental studies. Finally in section 1.5 we determine the particular problems to be studied in this thesis and the means by which numerical predictions of experimentally observable parameters will be arrived at over the course of the remaining chapters.

1.1 QED and the external field

QED is the theory of interactions involving electrons, positrons and photons. Containing at its heart a wave particle duality, QED had twin origins in the electromagnetic field equations of [Max92] and the discovery, due to [Pla01] and [Ein05], that the electromagnetic field is quantised. The development of the theory was spurred on by electron beam experiments which revealed the wave nature of the electron [DG27, Tho27] in apparent contradiction to its initial discovery as a particle [Tho97].

The differing strands were first drawn together into a relativistic quantum field theory by [Dir28a, Dir28b, HP29, HP30, Fer32]. However the proposed, quantised interacting field equations proved extremely difficult to exactly solve. A way forward was provided for the case of QED by the weak coupling of the electron and photon fields and the expansion of the field equations in powers of the coupling constant[1] which allowed perturbation theory to be employed.

With the theory of QED in place, theoretical calculations of the basic QED interactions were performed. The theoretical description of the scattering of an electron and photon, which was experimentally discovered by [Com23], were first written down by [KN28]. [BW34] developed the equations connected with the production of an electron-positron pair from the interaction of two photons. [Mol32] and [Bha35] described, respectively, electron-electron scattering and electron-positron scattering. For a general historical review of the developments of this early period see [Pai86].

Perturbation theory however was limited by the fact that only the first term in the perturbation series gave results that were in agreement with experiment. All further terms led to meaningless divergences. Various methods of removing the divergences were developed. The main methods included renormalisation of the electron mass and charge to take into account the effect of the Dirac-Maxwell field interaction on the fundamental parameters of the theory, the introduction of cut-off parameters which presume the incorrectness of the theory at very high energies, and various regularisation procedures such as that due to [PV49]. A thorough review of issues involved with divergences is contained in chapters 9 and 10 of [JR76].

The experimental discovery of the electron anomalous moment [KF47, KF48] and the Lamb shift [LR47] spurred on further theoretical developments of QED in the late 1940's. Two main developmental strands emerged. A reformulation of the fundamental field equations which aided the program of renormalisation was developed [Tom46, Tea47, Tom48, Sch48a, Sch48b]. In this view wave functions develop from one space-like surface to another resulting in equations which are covariant at each stage of calculation. This is known as the proper time method.

The second reformulation of QED, based on earlier work by [Stu43], was due to Feynman. This reformulation pictured portions of a mapped out space-time in which QED interactions take

[1] The coupling constant for QED is the fine structure constant α which is $\sim \frac{1}{137}$.

place. Expressions containing the Feynman matrix element solutions could be written down directly with the aid of diagrams [Fey48a, Fey48b, Fey49a, Fey49b]. The equivalence of the Schwinger and Feynman reformulations was proved [Dys49]. It is Feynman's reformulation of QED that will serve as the basis for the theoretical work in this thesis.

The problem of the interaction of an external field with an electron was first attempted by [Tho33] who calculated the solution for the orbit of a non relativistic electron moving in the field of a monochromatic plane electromagnetic wave. However the advent of the quantised relativistic theory presented difficulties for a rigorous treatment of the external field. The interactions with each particle of a quantised external field lead to impossibly complex calculations. A semi classical approximation which, for example, treated the external field as classical and neglected the photon-external field interaction, proved necessary. Such calculations proceeded with the solution of the Dirac equation for an electron embedded in the external classical field. These solutions were found for a constant crossed electric and magnetic field [Sch51] and for a plane wave electromagnetic field [Vol35]. For external fields in which the Dirac equation could not be solved exactly, the Born approximation was required. The Born approximation consists of a further expansion of the QED matrix elements in powers of the coupling to the external field. For a review of the basic theory associated with QED and the external field see chapters 14 and 15 of [JR76].

One of the first consequences of the external field in QED was the possible polarisation of the vacuum into electron and positron pairs. [Ueh35] investigated Dirac positron theory for the case of an external electrostatic field. The existence of a formula for the charge induced by a charge distribution implied polarisation of the vacuum. Deviations from Coulomb's law were investigated for the scattering of heavy particles and shifts in energy levels for atomic electrons. [Sch48b] applied their proper time method to the problem of vacuum polarisation by a prescribed electromagnetic field, and [Val51] reinvestigated the method Dirac and Heisenberg introduced to deal with the appearance of divergent integrals connected with vacuum polarisation.

[KR63] showed that the Feynman-Dyson formulation of QED leads to vacuum polarisation terms that violate gauge invariance. They found the inconsistency to lie in the unjustified interchange of integrations and limiting processes. With a more careful integration procedure, divergent integrals were avoided along with the need for cut-off procedures or appeals to invariance for undefined integrals. [Fer73] extended the work of [KR63] by showing that calculations of the vacuum polarisation tensor which allow for gauge invariance at each step, result in the divergent counter-term which was introduced in the original calculation to keep the photon mass zero.

One of the other fundamental external field problems considered was that of electron motion in an external electromagnetic field. Various authors considered the original Volkov solution as an infinite sum of contributions related to the number of external field photons that interact with the electron. [Zel67] interpreted this as the electron obtaining a quasi-level structure in the external field.

Other authors extended the work of Volkov, with [SG67] solving the Dirac equation for an electron in an external field consisting of two polarised plane electromagnetic waves, [Bea74, Bea75] discussing the exact solution of a relativistic electron interacting with a quantised and a classical plane wave travelling in the same direction, and [Fed75] proposing a method of constructing a complete orthonormal system for the electron wave function for an electron embedded in a quantised monochromatic electromagnetic wave.

The electron propagator in an external electromagnetic field was the subject of study by [Sch51] and [Val51], who both obtained a proper-time representation. Schwinger considered the case of a constant crossed electromagnetic field whereas [RE66] found an expression for the exact Greens function of the electron in the presence of an intense, circularly polarised electromagnetic plane wave. [RE66]'s result, written as a single integration over the electron 4-momentum and as an infinite sum of products of Bessel functions, revealed that the electron under the influence of the external field gained a mass increment above the field free mass (see also [BK64]). [Rit72] obtained another representation for the electron propagator in the presence of a plane wave electromagnetic field in terms of Volkov functions, the properties of which were investigated by [Mit75]. The Ritus representation will be used in this thesis. Other work on the external field electron propagator included [Fed75] who obtained the electron Green's function for an electron in a quantised monochromatic electromagnetic wave.

Consideration of IFQED in a reference frame moving almost at the speed of light was found useful for avoiding gauge problems. This method, which was developed independently by [KS70], and [NR71], involved the construction of a new time variable which forms light-like surfaces rather than the usual space-like surfaces. [BS71b] formed a new physical picture which considered the electron as composed of bare constituents which interact with each other and the external field to form a final state. They applied this formulation to elastic electron and photon scattering, bremsstrahlung and pair production.

An alternative to the semi classical method of incorporating the external field into QED, is the method of coherent states. The semi classical method implied that a discrete number of external field photons contribute to the scattering process and a quantum treatment of external field photons was suggested. Such a quantised treatment was rendered less formidable by coherent states which allowed the replacement of quantum field operators by their classical counterparts [Gla63]. Work on fundamental external field QED processes using coherent states was performed by [DT95], and a general review of coherent states is presented by [ZG90].

An approximation to the semi classical method is possible for external field QED processes in which electron energies are ultra relativistic. For these electron energies the solutions to the Dirac equation in the presence of the external field could be replaced by their classical counterparts. With this approximation the first order external field QED processes were evaluated for the cases of an external magnetic field [BS68], an external Coulomb field [BS69] and an external electromagnetic field [BS72]. The method was also applied to the some of the second order processes, in particular vacuum polarisation [BS75a] and electron and photon elastic scattering [BS75b, BS76].

1.2 First order external field QED processes

The development of the laser in the early 1960's stimulated further research into interactions involving electrons, photons and an external electromagnetic field. Studies of the first order IFQED processes are examined in this section. First order processes are represented by Feynman diagrams with one vertex and an odd number of fermion and boson lines in initial and final states. A 1969 review of the work done on finite order IFQED processes was provided by [Ebe69].

Several papers in the first half of the 1960's considered the first order external field process in which an electron embedded in a plane wave laser field scatters a single photon. This process is dependent on the intensity of the external field and is referred to as High Intensity Compton scattering (HICS).

The first attempts at obtaining IFQED cross sections dealt with the interaction of external field and electron as given by terms in a perturbation series expansion. The nth term in such a perturbation series corresponds to the external field contributing n photons to the process. [Fri61] considered non linear processes in which two or three external field photons interact with the electron in the initial state. Comparison of the matrix elements of these processes yield the expansion parameter of the perturbation series, which approaches unity for high intensity of the external field [Ste63]. [Vac62, Vac63] obtained similar results by considering the scattering process using classical theory. Much later, the HICS process in which $n + N$ photons contribute in the initial state and n in the final state, was also considered in the context of perturbation theory [Kor84]. Perturbation terms in the transition amplitudes were found to diverge for vanishing external field intensity. This difficulty was avoided by use of special kinematics or appropriate approximations. For instance, [Fri63] considered the HICS process using approximate solutions to the Dirac Hamiltonian obtained by [BN37] in which negative energy states are neglected.

A common semi classical approximation used exact solutions, of the Dirac equation for fermions embedded in a classical plane electromagnetic wave [Vol35]. With use of Volkov solutions, the transition amplitude of the HICS process decomposed into an infinite sum of incoherent amplitudes corresponding to the number of laser field photons that contribute to the process. Each contribution to the transition amplitude produces a final state which can be thought of as an harmonic of the external field photons. The nth harmonic contribution is proportional to the nth power of the external field intensity parameter ν^2. For laser intensities that were foreseeable in the 1960s, the intensity parameter was much less than one, and only the first few harmonic contributions to the transition amplitude were considered. In the limit of vanishing intensity of the external field, the first harmonic contribution to the cross section reduces to the Klein-Nishina formula for single external field photon scattering from the asymptotically free electron [BK64, NR64a, Gol64].

The transition amplitude of the HICS process is dependent on the state of polarisation of the external field. [NR64a] considered the case of a linearly polarised external electromagnetic field. The transition probability contained an infinite summation of complicated functions which were evaluated in limiting cases only. In contrast a circularly polarised external field produces Bessel functions, the properties of which are well known [NR65a, BK64]. A circular polarised external field introduces an azimuthal symmetry into the HICS process which results in analytically less complicated HICS cross sections [Mit75]. The HICS process for the case of an elliptically polarised external electromagnetic field was considered by [Lyu75].

One important debate that took place concerned the dependency of a frequency shift in the scattered photon on the intensity of the external laser field. In the semi classical approximation, various authors found an expression for the energy-momentum of the scattered photon dependent both on the number of laser photons that contributed to the process, and the intensity of the laser field [BK64, Gol64].

This semi classical expression for a frequency shift was dismissed on the grounds that external field boundary conditions were omitted. The HICS cross section was reevaluated making use of the adiabatic switching hypothesis in which the external field was represented as a linear combination of monochromatic occupation number states with boundary conditions consisting of asymptotically free electrons and photons (at $t = \pm\infty$). A distinct analytic expression for an intensity dependent frequency shift was obtained [FE64].

In turn, the [FE64] result was brought into question by appealing to the correspondence principle in that the semi classical and fully quantum mechanical treatments of the HICS process should yield the same result in the classical limit. Neglecting radiative corrections, it was indeed found that a quantum mechanical treatment of the external field as coherent states gave the same intensity dependent frequency shift as obtained in the semi classical treatment [Fra65]. To complete the rebuttal, the results of [FE64] were explained as arising from the physically problematic, adiabatic switching of spatially infinite external field states. Correct boundary conditions for the switching on and off of the external field were obtained by considering finite wave trains. In such a case the intensity dependent frequency shift re-emerged [Kib65]. An intensity dependent frequency shift could be interpreted in terms of a Doppler shift produced by the electron in the external field acquiring an average velocity in the direction of propagation of the external field photons. In such an interpretation the way the laser is switched on or off is irrelevant.

The existence of the frequency shift mechanism allows the HICS process to be used as a generator of high energy photons [Mil63, Bea65, Sea83]. The polarisation properties of these high energy photons are of fundamental importance in nuclear physics applications [GR83]. [Gri82, Gea83b] considered polarisation effects of the interaction of an electron with an external laser field in the lowest order of perturbation theory. With the polarisation states of the electron expressed in Stokes parameters, and those of the photon in helicity states, the differential cross section of the process was obtained for general kinematics [Gea83b] and in the rest frame of the initial electron [McM61]. Later papers expressed the polarisation state of the scattered HICS particle as a function of polarisation states of the initial particles for a circularly polarised external field [GR83, Tsa93].

One point of interest concerning the HICS process was the impact that a second external field would have on the scattering. The problem of photon emission by an electron in a bi-chromatic electromagnetic field was considered in the lowest order of perturbation theory. There was a significant enhancement of the cross section of the scattering process, proportional to the ratio of frequencies of the two external fields [PV68]. In later work, the second external field was considered exactly by writing the external field four-potential in the Volkov solution as a sum of two co-directional plane wave fields with different frequencies. In the limit of weak intensity of one external field, calculations indicated a ten percent enhancement of the scattering cross section for a range of intensities of the second external field [GGG75]. The same process was re-examined non relativistically with allowance for initial electron momentum in light of contemporary experimental work [Ehl87].

Since intense external fields are usually supplied experimentally by intense laser beams, photon depletion of the laser beam by a single HICS multi-photon process can be neglected [Mit79]. However most experimental work also use electron beams (see for example [ER83]) and photon depletion may become significant. If such is the case the external field cannot be treated as a classical field with constant photon number density and the semi classical method breaks down. An approach in which the external laser field is considered quantised from the outset, becomes necessary [BV81a, Bec88, Bec89].

Using the method of coherent states developed by [Gla63], the HICS process was considered using an electron wave function solution of the Dirac equation for an external field consisting of one quantised, circularly polarised electromagnetic mode. Expressions obtained for the frequency of the scattered photon and the transition probability for the HICS process reduced to those obtained in the semi classical approximation when the expectation value of the external field photon number was very large [BV81b]. The transition probability of the HICS process depends strongly on the state of polarisation of the external quantised field. For linearly polarised modes, the external field photons form squeezed states and for circular polarisation they form coherent states [GS89].

In other work the HICS process for a non relativistic electron retarded by a Coulomb field was considered [Leb70]. Phonon scattering of conduction band electrons in the presence of an intense electromagnetic field was studied by [BO67]. [Bec81] examined the radiation emitted by a relativistic electron moving in a dispersive non absorptive medium under the influence of an electromagnetic wave. [VE84] considered the HICS in an external field consisting of a strong homogeneous magnetic field and an intense microwave field.

The other first order IFQED process to be reviewed is the production of an electron and positron from an initial state consisting of one photon and an external field. This process is referred to as One Photon pair production (OPPP).

[Rei62] was the first to consider the OPPP process in the semi classical approximation with a plane wave electromagnetic field. [Rei62] calculated transition probabilities by considering perturbations to the solution of the Dirac equation in the experimental field. In contemporary work several authors considered the same process using Volkov solutions in the Feynman-Dyson formulation of QED. Expressions obtained for the OPPP process contained many of the same features present in the HICS process. The transition amplitudes obtained were an infinite sum of incoherent amplitudes corresponding to the number of external field photons that combine with the initial photon to produce the pair. Indeed, the transition probability of the OPPP process was obtained directly from the transition probability of the HICS process by an exchange of particle momenta via the substitution rule [NR64a]. In the limit of vanishing external field intensity parameter ν^2, the transition probability of the OPPP process reduces to that of the Breit-Wheeler process for two photon pair production. For vanishing frequency of the external field the Toll-Wheeler result for the absorption of a photon by a constant electromagnetic field was obtained [Rei62, NR64a]. [NR67] investigated the OPPP process in the limit of vanishing ratio of external field frequency parameter $\frac{\omega}{m} \equiv \frac{\hbar\omega}{mc^2}$ to intensity parameter ν^2.

The state of polarisation of the external electromagnetic field has a significant effect on the OPPP process, as it does for the HICS process. Transition probabilities for an initial photon polarised parallel and perpendicular to a linearly polarised external electromagnetic field were obtained by [Rei62] and [NR64a]. A circularly polarised electromagnetic field was considered by [NR65a], and the more general case of elliptical polarisation by [Lyu75]. Spin effects were dealt with by [TK68]. [BS76] also considered the OPPP process for an elliptically polarised external electromagnetic field. They obtained a new representation for the transition probability in terms of Hankel functions, by considering the imaginary part of the polarisation operator in the external field.

The transition probability of the OPPP process passes through a series of maxima and minima as the intensity of the external field increases [NR65a]. The increase in external field intensity has a limiting effect on the process, increasing the likelihood that more external field photons will contribute to the pair production, but increasing the lepton mass and thus the energy required to produce the pair [Bec91].

The dependence of the OPPP process on the spectral composition of the external electromagnetic field was of interest to several authors. An external electromagnetic field consisting of two co-directional linearly polarised waves of different frequencies and orthogonal planes of polarisation, yielded a transition probability of similar structure to that obtained for a monochromatic electromagnetic field [Lyu75]. [BZ77] considered an external field of similar form with two circularly polarised wave components. [BZ77] obtained transition probabilities which, in the limit of vanishing frequency of one electromagnetic wave component, reduced to those for an external field consisting of a circularly polarised field and a constant crossed field [ZH72].

The advent of new high powered laser beams in the 1990s led to a renewed flurry of analytic work. The HICS process was considered numerically for laser intensities up to 10^{21} Wcm^{-2} and for elliptical polarisation of the external field [PE02, PE03]. A series of papers considered the first order IFQED processes for one or two external fields of elliptical polarisation [RA00]. Complete polarisation effects of all contributing particles were studied for a circularly polarised external field and arbitrary polarisation of all other particles [IS03].

The OPPP process was also considered in external fields other than electromagnetic waves. For example, OPPP in a magnetic field was considered by [Sch54, DH83, Bes84] and an external field consisting of one electromagnetic wave and one magnetic wave was considered by [Ole72].

1.3 Second order external field QED processes

The second order IFQED processes provide an abundance of phenomena for study. These are represented by Feynman diagrams with two vertices and include Compton scattering, Two Photon pair production, Two Photon Pair Annihilation, Möller scattering and electron self energy. The second order IFQED processes require the external field photon propagator [Sch51, Ole67] or the external field electron propagator which is available either in a proper time representation [Ole68] or a Volkov representation [NR64a, NR64b, Mit75]. A 1975 review of work done on second order IFQED processes was provided by [Mit75].

External field Compton scattering or stimulated Compton scattering (SCS) was first considered with an external field consisting of a linearly polarised electromagnetic wave. The cross section was calculated in the non relativistic limit of small photon energy and external field intensity for a reference frame in which the initial electron is at rest. Resonant singularities in the cross section due to the poles of the electron propagator in the external field being reached for physical values of the energies involved. This contrasted with Compton scattering in the absence of the external field which does not contain these singularities. The singularities were interpreted in terms of a quasi-level energy structure [Zel67] for the electron in the external field. Resonance takes place when the energy of the incident or scattered photon is approximately the difference between two of the electron quasi-levels. The cross section resonances were avoided by inserting the external field electron self energy into the electron propagator. The resonant cross section exceeded the non resonant cross section by several orders of magnitude [Ole67].

[AM85] considered the SCS cross section in a linearly polarised external electromagnetic field and wrote down the SCS matrix element for a circularly polarised external field. This calculation was performed for the special case where the momentum of the incoming photon is parallel to the photon momentum associated with the external field. [AM85] avoided the resonant infinities found by [Ole67] by considering a range of photon energies for which resonance did not occur.

The two photon, electron-positron pair production process in the presence of an external electromagnetic field or stimulated two photon pair production (STPPP) has remained uncalculated. However [KM87] dealt with the process in a strong magnetic field for the case in which the energy of each of the photons is alone insufficient to produce the pair. The cross section obtained also contains resonances.

The calculation of the SCS cross section revived discussion on the existence of an intensity dependent frequency shift in the scattered photon. Drawing on the earlier debate, the intensity dependent frequency shift was tied to the choice of boundary conditions for the electron wave function. An intensity dependent frequency shift emerged analytically as long as the electron and the external field always remained coupled [VR66].

[OS75] used a modified form of the Volkov solution which allows for the adiabatic switching on and off of the external field at times in the remote past and remote future. This procedure turned out to be equivalent to equating the quasi electron momentum with the free field electron momentum and introducing an electron mass shift. Allowance for adiabatic switching lead to a modified energy-momentum conservation law for the first order HICS process. As a result the scattered photon frequency differed by several orders of magnitude to previous calculations [BK64, NR64a]. This result was significant since previously it was thought that the intensity dependent frequency shift would be a small effect [VR66].

[Bel77] applied the adiabatically modified Volkov solution to the second order SCS process and obtained an expression for the frequency shift of the scattered photon. The resultant, adiabatically modified, SCS cross section expressions contained frequency shifted resonances. [Bel84] considered the SCS process with adiabatic boundary conditions in two inertial reference frames to show that the scattered photon frequency shift is a relativistic effect.

Several papers have dealt with the second order Möller process (the scattering of two electrons) in the presence of a strong electromagnetic field. [Ole67] considered the process in an external field consisting of a linearly polarised electromagnetic wave. As in other IFQED processes, the external field modifies the energy-momentum conservation of the scattering process and contributes external field quanta. [Ole67] found it necessary to calculate the transition probability in a centre of mass-like reference frame in which the external field quanta are absorbed in the initial electron momenta. Under certain conditions the Möller scattering transition probability acquired terms corresponding to electron attraction, giving rise to the possibility of electron pairing in an electromagnetic field [Ole67].

[Bea79a] performed a calculation of the Möller scattering cross section in a circularly polarised electromagnetic plane wave with a greater emphasis on numerical results. These calculations were performed in a non relativistic energy regime with a reference frame in which incoming electrons have opposite and equal quasi-momentum. Numerical investigations calculated the SCS differential cross section with variation of the intensity of the external field, the geometry of the scattering process, and the number of external field quanta that participate in the process. The SCS differential cross section differed considerably from basic Compton scattering in experimentally accessible regions [Bea79a, Bea79b].

Further investigations in the 1980's considered the external field Möller process in a relativistic regime and with a low intensity, elliptically polarised, external electromagnetic field. Mathematically simpler differential cross section expressions were obtained. The analytic cross sections indicated an intensity dependent electron mass shift as expected, however the contribution of external field quanta was neglected in the low intensity limit [Ros84]. In contrast with Möller scattering in a Coulomb field, the Möller scattering in an electromagnetic field contained terms which suppressed the cross channel of the scattering cross section [FR84].

The possibility that IFQED differential cross sections could contain resonant infinities was recognised soon after the initial first order calculations were performed. Increasing intensities of available lasers led to the consideration of cross section terms involving contributions from two or more external field quanta. It was recognised that employment of perturbation theory for these contributions would lead to infinite electron propagation functions. The solution proposed was the inclusion of the electron self energy [NR65b].

[Ole67] was the first to encounter these resonant infinities in a calculation of the external field Möller scattering differential cross section. The obtained propagator poles coincided with transitions between the electron energy quasi-levels of the electron embedded in the electromagnetic wave, in direct analogy to the resonance scattering of light by atoms [Mit75]. The infinities were removed by recalculating the differential cross section using a photon propagator corrected for the photon self energy. The differential cross section infinities were rendered finite and the resultant resonant peaks exceeded the non resonant differential cross section by several orders of magnitude. The calculation of resonant cross sections was extended to the SCS process by inclusion of the electron self energy into the electron propagator [Ole68].

[Fed75] considered, as an approximation to the second order SCS process, the resonant scattering of an electron in the field of two external electromagnetic waves. The induced resonance width was calculated by summing an infinite series of resonance terms and was greater than that obtained by [Ole68]. Resonant scattering in two external fields allowed for multiple transitions between two distinct sets of electron energy states. Whereas [Ole68] made an analogy with spontaneous resonant emission, [Fed75] made an analogy with stimulated resonant emission.

[Bea79a] provided a more extensive evaluation of the resonant Möller scattering in an external field by calculating the width, spacing and heights of the differential cross section resonance peaks. The resonant differential cross section exceeded the non resonant differential cross section by several orders of magnitude as stated by [Ole67], but only under certain conditions. Numerical calculations showed that, at the time, conditions that produced resonant cross sections would be difficult to reach experimentally. More recently, the resonant Möller process was revisited analytically and numerically for high radiation powers in a external field of elliptical polarisation [PE04, Ros96].

The calculation of the resonant cross sections of second order IFQED processes required the calculation of the electron and photon self energies in the presence of an external field. These external field self-energies are also second order IFQED processes.

[Rit70] was one of the first to consider the electron and photon self energy processes in an external electromagnetic field. Both the electron and photon mass shifts in a constant crossed electromagnetic wave were calculated.[2] These calculated mass shifts became appreciable as the external field intensity reached that of Schwinger's characteristic field [Sch54]. The method used to calculate the Mass Operator began by calculating the total probability for radiation in the external field. The imaginary part of the mass operator was then obtained via the optical theorem and was proportional to the intensity of the external field. The electron mass operator was also dependent on spin and an anomalous magnetic moment was calculated.

The expression obtained for the electron mass operator in a constant crossed electromagnetic field was confirmed by calculating the mass operator directly using Schwinger's equation. This approach allowed a better assessment of the analytic properties of the external field mass operator and vacuum polarisation operator. The analytic properties revealed that these operators, in contrast to the non external field case, are transcendental functions of the momenta squared and depend non trivially on the dynamic variable. The Green's functions obtained from these operators contained an infinite number of poles which depend on external field variables [Rit72]. In a later paper, the mass correction to the elastic scattering amplitude of the electron in a constant crossed electromagnetic field was calculated and the probability for two photon emission by the electron in the external field, the mass correction to the probability for one photon emission, and the mass correction to the anomalous magnetic moment of the electron were all found [MR75].

Other work on the mass operator for an electron embedded in a constant crossed electromagnetic wave was performed by [Nar79]. Asymptotic expressions were obtained to calculate the corrected electron propagator to third order in the fine structure constant which yielded an estimation of the lower bound for an IFQED expansion parameter.

The electron mass operator in a circularly polarised electromagnetic field was calculated and

[2] A constant crossed electromagnetic wave is one in which the electric and magnetic field vectors are constant, equal in magnitude and orthogonal.

used to obtain a corrected external field electron propagator [BM76]. This corrected propagator was written explicitly to first order in the fine structure constant in both numerator and denominator. The symmetry of the circularly polarised external field led to a matrix structure for the mass operator and electron propagator that was almost diagonal. [BM76] obtained numerical results for the real and imaginary parts of the electron mass shift with the aid of approximation formulae.

An external field consisting of a constant crossed electromagnetic field and an elliptically polarised electromagnetic plane wave was considered in a calculation of the mass operator for both an unpolarised [Kea90a] and a polarised [Kea90b] electron. The analytic form of this mass operator reduced to that of previous work by allowing each of the electromagnetic waves making up the external field to go to zero in turn.

The presence of an external electromagnetic field alters the photon self energy, the photon propagator and the probability of polarisation of the vacuum. A plane wave electromagnetic field alone does not polarise the vacuum, but the presence of another agent such as a second field or a photon leads to real effects [Tol52].

Most of the early work on external field vacuum polarisation was performed with a constant crossed electromagnetic field. [San67, San95] considered photon elastic scattering. The effect on the photon was a change of polarisation with the direction of propagation remaining unchanged. [Nar69] calculated the vacuum polarisation operator in a constant crossed field and made radiative corrections to the photon propagator. A more general treatment was provided by [BS71a] who used relativistic, gauge and charge invariance to write an eigenvector representation for the vacuum polarisation operator. [BBB70] used a slightly varying external electromagnetic field of otherwise arbitrary form.

The presence of an intense electromagnetic field system renders the vacuum a birefringent medium. This view emerges from the non linear properties of Maxwell's equations when allowance is made for virtual electron-positron pair creation [KN64]. [Nar69] showed that two waves with different dispersion laws can propagate in an external field and that the two refractive indices can be determined. The direction of propagation of the two waves coincide and their polarisation is orthogonal. [BBB70] calculated the group and phase velocities of both propagation modes.

A mass correction to the elastic scattering amplitude of a photon in a constant crossed electromagnetic field was calculated to order α^2. The mass correction was used to obtain the probability of pair production [MN77]. Renormalisation group methods were used to study external field vacuum polarisation for asymptotic forms of a static electromagnetic wave [CW73, Kry80].

[BM75] obtained an expression for the vacuum polarisation tensor with a circularly polarised electromagnetic field. The calculation was performed with light-like coordinates which are used in null-plane formulations of quantum electrodynamics [NR71]. [BM75] used a proper time representation for the external field electron Green's function. This lead to expressions for the vacuum polarisation tensor which have proved cumbersome to use [AK87]. This form for the vacuum polarisation tensor contained integrations with infinitely bounded integrations of Hankel functions. These integrations were performed by using asymptotic expressions for the Hankel functions and imposing limits on the intensity of the external field. The effects of vacuum polarisation on a photon in a circularly polarised external field were approximately described by a vacuum with two complex indices of refraction. Numerical calculations showed that vacuum birefringence was a small effect unless the photon which probes the vacuum has very high energy.

Vacuum polarisation studies were performed in other types of external fields. The scattering of circularly polarised waves in a Coulomb field was considered for low intensity and frequency of the electromagnetic wave [Yak67]. Analytical properties of the photon polarisation tensor in an external magnetic field using the Furry picture were investigated [Sha75]. The vacuum polarisation tensors in a constant electromagnetic field was calculated using a technique borrowed from string theory [Sch01].

1.4 Experimental Work

There have been few attempts at experimental detection of IFQED processes until comparatively recently. This was mainly due to the availability of ultra intense electromagnetic fields which are required to produce detectable phenomena particular to IFQED. The main laboratory source of intense electromagnetic fields are lasers. Indeed it has been the ongoing development of the laser that has provided the impetus for the theoretical calculations reviewed in this chapter. It is therefore worth devoting some space to discussing ultra intense lasers and their relevant experimental parameters

The most common laser in use for present day experiments is the so called T^3 or Table Top Terawatt laser system [Bec91, Bea99]. These laser systems produce ultra intense, ultra short pulses via the technique of Chirped Pulse Amplification (CPA). CPA begins with an ultra short low energy pulse from a standard mode-locked optical laser such as a Nd:YAG or a dye laser. The normal operation for an optical laser involves many lasing modes, the number of which is determined by the gain bandwidth $\triangle\nu_g$ which in turn is determined by the uncertainty relations ([ME88] pg.355). The modes of oscillation are locked together via suitable electronic circuitry to produce single peaks of higher amplitude and shorter duration. The mode-locked oscillations are passed through a non linear refractive medium (such as an optical fibre) to introduce a small time dependence to the carrier frequency of the mode locked oscillations. This ”chirping” allows the laser pulse to be temporally stretched. The pulse is then amplified to modest energies and passed through a dispersive medium which compresses and produces an ultra intense pulse. The resultant laser intensities can exceed $10^{18}\,\mathrm{Wcm}^{-2}$ [ES92]. CPA has the advantage of avoiding undesirable high field effects like self-focusing which can result in a beam of much smaller intensity or a smaller spot size.

Using the CPA technique a 20 TW peak power, 1.2 ps pulse was generated from a mode-locked Nd:YAG oscillator. Initially, 120 ps pulses at a 76 MHz were coupled into a single mode optical fibre which provided the dispersive medium of which stretch and linearly chirped the pulses. The chirped pulse was amplified by passes through a Nd:silicate medium resulting in pulse energies of as much as 70 J [Sea91].

An experimental proposal at the Stanford Linear Accelerator Center (SLAC) included a CPA high intensity laser beam. A seed pulse from a Nd:YLF laser could be amplified to in excess of 1 J and intensities in excess of 10^{19} Wcm^{-2}. Since frequency tripling of nanosecond pulses could be achieved with $\sim 80\%$ efficiency, an ultra intense UV beam ($\gamma = 350\,nm$) with peak energy flux $\sim 4 \times 10^{17}$ Wcm^{-2} would also be available [McD91].

An alternative to the CPA technique is the production of ultra intense laser beams via direct amplification of a series of lasing media. For instance, a 248 nm seed pulse was generated via a Nd:YAG-pumped, mode-locked dye laser, pre-amplified to a gain of 10^6 and frequency doubled via passage through a KDP crystal. The seed pulse passed through an electron beam-pumped KrF medium to produce a 248 nm, 4 TW (390 fs, 1.5 J) peak power laser pulse with intensity 10^{19} Wcm^{-2} [Wat89]. A similar system producing 248 nm pulses with intensity $\sim 2 \times 10^{19}$ Wcm^{-2} could be focused to a spot size of diameter $1.7\,\mu$m obtaining intensities in excess of 10^{20} Wcm^{-2} [Lea89].

The arrival of ultra intense lasers for which IFQED phenomena could feasibly be detected led to a number of experimental studies. A Neodym-glass laser, focused to an intensity of 1.7×10^{14} Wcm^{-2} was brought into collision with a low energy (500-1600 eV) electron beam to generate various harmonics. The greatest yield was obtained for second harmonic photons at 0.032 ± 0.003 photons per laser pulse for an electron energy of 1600 eV. These results provided only an order of magnitude confirmation of approximate theoretical cross sections [ER83]. A modification to this experimental configuration was proposed in order to take advantage of a distinct forward-backward asymmetry in observed cross sections [PL89].

[Fea80] produced 5-78 MeV γ-rays with intensity 10^4-10^5 photons s^{-1} and an energy resolution of 1-10% from the interaction of an argon ion laser and electrons produced from the ADONE storage ring at Frascati. [Gea83b] proposed the production of a similar high energy, high luminosity γ-beam using parameters appropriate for the VLEPP and SLAC linear colliders.

Back scattered radiation produced from collisions of intense laser beams with electron beams was studied using a cold fluid model. The radiation occurred in odd harmonics of the incident laser frequency and the strength of the harmonics was strongly dependent on the incident laser frequency [ES91].

Interaction of an incident laser source of wavelength 1μm, pulse length 2 ps and energy 20 J per pulse, with an electron beam from an RF linear accelerator, produced hard x-rays (photon energy = 50-1200 keV) with 1 ps pulse length and $6{\times}10^9$ photons per pulse. Electron beams from a betatron resulted in hard x-rays with a more moderate photon flux and spectral brightness [Sea92].

Other studies concentrated on the photon-plasma interactions generated by collisions of laser beams with solid targets. Intense laser pulses of power density 10^{16} Wcm^{-2} were directed onto a silicon target to produce 12 nm, 2 ps x-ray pulses with a conversion efficiency of approximately 0.3%. It was estimated that 1.5 nm,10 fs pulses could be produced at a conversion efficiency in excess of 10% [Mea91]. More recently the Rutherford-Appleton Laboratory's VULCAN laser system was focused to 10^{19} Wcm$^{-}2$ onto a lead target. Up to 4 harmonics were observed in the emission spectrum [Wea02].

[ES92] discussed the possibility of experimentally investigating new IFQED phenomena such as the optical guiding of laser pulses, wake fields, laser frequency amplification and relativistic harmonic generation. [Hor88] proposed a new type of accelerator driven by the frequency and phase modulation of the two interacting ultra intense lasers. A 100 TW laser pulse power could produce a particle acceleration of 600 GeV cm^{-1}. Beamsstrahlung radiation produced by the proximity of intense electron and positron beams and the resultant intense electromagnetic fields was modelled in order to determine transverse beam sizes from observed beamsstrahlung fluxes at SLAC [Zei91].

Experimental study of IFQED processes in intense Coulomb fields can be achieved via heavy-ion collisions. [GR85] provides a review of IFQED studies involving heavy ion collisions. For instance, one experimental study scattered electrons from Argon in the presence of a CO^2 laser pulse. The kinetic energy of scattered electrons indicated the absorption of up to 11 photons were observed at theoretically predicted rates [KW73, Wea83].

[Mik82] discussed the possibility of observing the scattering of light by light at SLAC using a 19.5 GeV γ-beam and 4.66 eV laser light. Using the form of the electric and magnetic field produced by an ideal lens and a given focal length, it was calculated that a single e^+e^- pair could be produced from a focused ruby laser pulse of duration 10^{-11} sec and total power 10^{19} W [BW65, BT70]. Order of magnitude cross section estimates of external field pair prod near a Coulomb centre and by a single photon indicated that experimental observation of these processes would be practicable [Bec91].

The experimental program proposed by [McD91] was completed and reported on by the end of the 1990's. A Nd:glass laser with peak intensities of $\sim 0.5 \times 10^{18}$ Wcm$^{-}2$ and a 46 GeV electron beam were used to observe the first order non linear OPPP and HICS processes. Up to four external field photons were found to contribute to the process in excellent agreement with theoretical predictions. It was hoped that the mass spectrum of e^+e^- pairs produced from the OPPP process may shed some light on cross section peaks observed in previous heavy ion collision experiments [Bea99].

Another program of experimental work used a 1.053 μm laser focused to a 5 μm spot size to generate a peak laser intensity of $\sim 10^{18}$ Wcm$^{-}2$. A longitudinal shift in scattered electron momenta due to multi-photon contributions from the laser field was observed. Also observed was the predicted electron mass shift due to the presence of the external field [Mea95, Mea96].

1.5 The Present Work

The second order IFQED processes have generally received less attention than the first order IFQED processes. Without taking resonances into account, the cross sections of the second order IFQED processes are diminished by a factor of the fine structure constant compared to the cross sections of the first order processes and, at first glance appear experimentally less viable. However, the potential resonances in the second order IFQED cross sections provide much motivation for study. These resonances are interesting phenomena in their own right and may be experimentally more viable than the first order IFQED processes. The subject matter of the this thesis involves consideration of some of the second order IFQED processes and their resonances.

Some of the standard theory of QED required as a basis for further calculations is presented in Chapter 2. The Feynman formulation of S-matrix theory was used to perform the cross section calculations. A derivation of the Volkov wave function for fermions in an external, plane wave electromagnetic field is provided, and the Volkov solutions are used in the Ritus representation of the external field electron propagator. The electron self energy, optical theorem and regularisation procedures will all be used to calculate radiative corrections.

As part of the original work presented in this thesis, stimulated Compton scattering (SCS) with a circularly polarised external electromagnetic field, arbitrary kinematics and without recourse to a non relativistic regime, is considered. A circularly polarised external electromagnetic field results in well known Bessel functions appearing in the cross section. Circularly polarised electromagnetic field are easily achieved experimentally using intense laser beams. The stimulated two photon pair production (STPPP) process in the same circularly polarised external field is also considered with the aid of expressions obtained for the SCS calculations and by use of crossing symmetry which links the two processes. The analytic expressions for both SCS and STPPP processes are contained in Chapter 3.

Numerical results and analysis of the SCS and STPPP differential cross sections are presented in Chapters 4 and 5 respectively. Analysis is presented in terms of the discrete contribution of external field quanta to the process. A subset of the complete parameter space in which the differential cross sections vary, is examined. Since experimental validation is important, parameter sets which maximise the STPPP and SCS differential cross sections are a priority.

One crucial feature that emerged from the literature is the possibility of resonances in the second order IFQED processes. The calculation of resonant SCS and STPPP cross sections require the electron self energy in the presence of the external field. Though this self energy exists in the literature for the case of a circularly polarised electromagnetic field, the given proper time representation proves technically difficult to include in the calculations in this thesis. In chapter 6 an alternative calculation of the external field electron self energy using dispersion relations is provided, and a representation in terms of infinite summations of Bessel functions is obtained. The correctness of the result will be established with use of the optical theorem and the well known HICS differential cross section.

The results of Chapter 6 enable an analytic and numerical calculation of the SCS and STPPP resonant cross sections to be performed in Chapter 7. Attention is given to the requirements of any future attempt at experimental measurement. Radiative corrections to first order in the fine structure constant are included in the external field electron propagator and an external field regularisation and renormalisation procedure is outlined.

Research and development of e^+e^- colliders involve background studies of pair production processes. These processes occur in the midst of focused electron and positron bunches which produce intense bunch fields. These fields are almost plane wave and contain constant electric and magnetic components that are mutually orthogonal to the direction of propagation of the bunches. It is of interest therefore to perform the STPPP calculation in the presence of a constant crossed electromagnetic field. The differential cross section is calculated using real beam parameters proposed for the International Linear Collider (ILC) with the aim of estimating whether there will be a significant increase in expected background pairs. This is the subject of Chapter 8 which draws on the preceeding chapters.

In chapter 9 the work of all preceeding chapters is drawn together in conclusion.

Chapter 2

General Theory

2.1 Introduction

Presented in this chapter is some of the basic QED theory required to perform the cross section calculations of the IFQED processes to be considered in this thesis.

Basic matters such as the metric to be used, the units employed and certain normalisations are stated in section 2.2. Section 2.3 presents the Lagrangian of the interacting Maxwell and Dirac fields. IFQED calculations are most conveniently performed in the Bound Interaction Picture. The standard S-matrix theory describing the time evolution of the State vector is outlined in section 2.4. Section 2.5 discusses the Feynman diagrams for which the task of extracting the desired transition of states from the iteration solution of the S-matrix is considerably simplified. The crossing symmetry of the S-matrix will be used to simplify the calculation of related IFQED processes. This is described in section 2.6. Section 2.8 outlines how the differential cross section is obtained from squaring the matrix element and introducing the phase integral. The differential cross section requires summation over all fermion spins and photon polarisations which introduces a trace calculation of products of Dirac γ matrices. This is explained in section 2.7.

Section 2.9 defines the 4-potential of the external fields required for the IFQED calculations. Those described are a circularly polarised and a constant crossed plane electromagnetic wave. The derivation of the Volkov solution of the Dirac equation in an external plane wave field of general form is outlined in section 2.10. The resulting Volkov E_p functions are used to construct the Ritus form of the external field (bound) electron propagator.

Section 2.11 discusses the radiative corrections to the external field electron propagator. These corrections are necessary since the presence of the external field leads to propagator poles. The radiative corrections produce a shift in intermediate electron energy to complex values. An expression for the electron energy shift in an external field is obtained in section 2.12. The radiative corrections require regularisation and renormalisation in order to remove divergences. The usual, non external field version of these is presented in section 2.13. The optical theorem described in section 2.14

relates elastic scattering amplitude to transition probability will be useful for validation of the self energy calculations in Chapter 6.

The content of this chapter draws on several texts including [Sch62, AB65, JR76, Nac90, IZ80, MS84, GR03, BP82, Mui65].

2.2 Units, normalisation constants, notation and metric

In this thesis Planck (natural) units are used in which the speed of light in a vacuum c, reduced Planck constant $\hbar$ and Coulomb force constant $\dfrac{1}{4\pi\epsilon_0}$ are all equal to 1. The metric to be used, $g_{\mu\nu}$, has signature (1,-1,-1,-1) so that for any contravariant 4-vector $x^\nu = (x^0, \underset{\sim}{x})$, a covariant 4-vector is formed via $x_\mu = g_{\mu\nu}x^\nu = (x_0, -\underset{\sim}{x})$.

Dirac bispinors are $u(p)$ for electrons and $v(p)$ for positrons. Projection Operators $\Lambda^{\pm}(p)$ pick out electron or positron bispinors from linear combinations. The symbol $e(k)$ represent photon polarisation 4-vectors.

Normalisation constants $\sqrt{\frac{m}{V\epsilon_p}}$ for Dirac bispinors, and $\sqrt{\frac{1}{2V\omega}}$ for polarisation 4-vectors are chosen so that the probability of finding either a fermion of mass m and energy ε_p, or a photon of energy ω in a box of Volume V, is unity (see for example [Mui65]).

A particular representation for Dirac γ matrices is unimportant since only their anti-commutation and hermicity properties are required. The "slash" notation will be used to denote products of 4-vectors and Dirac γ matrices so that $\not{a} = \gamma^\mu a_\mu$.

The script letters $\Im$ and $\Re$ will be used to refer to the imaginary and real parts of some quantity. The convention of implied summation is assumed so that

$$x^\mu x_\mu \equiv \sum_0^3 x^\mu x_\mu \tag{2.1}$$

2.3 The Bound Interaction Picture

The theory of quantum electrodynamics describes the interactions between the quantised Maxwell and Dirac fields. The description requires the free Maxwell and free Dirac Lagrangian densities L_M and L_D.

$$\begin{aligned} L_M &= -\tfrac{1}{4} F^{\mu\nu}F_{\mu\nu} \qquad \text{where} \quad F_{\mu\nu} = \partial_\mu A_\nu - \partial_\nu A_\mu \\ L_D &= \overline{\psi}(i\not{\partial} - m)\psi \qquad \text{where} \quad \not{\partial} = \gamma^\mu \frac{\partial}{\partial x_\mu} \end{aligned} \tag{2.2}$$

The Lagrangian densities entail the free Maxwell and free Dirac field equations specifying the space-time evolution of the Maxwell field operator $A_\mu(x)$ and the Dirac field operator $\psi(x)$.

$$\begin{aligned} \partial_\mu^2 A_\mu(x) &= 0 \\ (i\partial\!\!\!/ - m)\psi(x) &= 0 \end{aligned} \tag{2.3}$$

The solutions to equations 2.3 are written in terms of operators that create (denoted by the superscript $+$) or destroy (denoted by the superscript $-$) an electron, positron or photon at space-time point x_μ. The electron and positron field operators are written in terms of Dirac bispinors $u_s(p)$ and $v_s(p)$, and the photon field operators are written in terms of polarisation 4-vectors $e_r^\mu(k)$.

$$\begin{aligned} \psi_p^{\mu+}(x,p) &= \sqrt{\frac{m}{V\epsilon_p}}\, u_s^\mu(p)\, e^{-ipx} & \psi_p^{\mu-}(x,p) &= \sqrt{\frac{m}{V\epsilon_p}}\, v_s^\mu(p)\, e^{ipx} \\ \overline{\psi}_p^{\mu+}(x,p) &= \sqrt{\frac{m}{V\epsilon_p}}\, \overline{u}_s^\mu(p)\, e^{ipx} & \overline{\psi}_p^{\mu-}(x,p) &= \sqrt{\frac{m}{V\epsilon_p}}\, \overline{v}_s^\mu(p)\, e^{-ipx} \\ A_k^{\mu+}(x) &= \sqrt{\frac{1}{2V\omega}}\, e_r^\mu(k)\, e^{-ikx} & A_k^{\mu-}(x) &= \sqrt{\frac{1}{2V\omega}}\, e_r^\mu(k)\, e^{ikx} \end{aligned} \tag{2.4}$$

Interaction between the Maxwell and Dirac fields in the presence of an external electromagnetic field specified[1] by the 4-potential A_μ^e, is usually viewed in the bound interaction picture [Fur51]. The bound interaction picture provides a way of describing the interacting system of free Maxwell field, free Dirac field and the external field such that the solutions of the combined field equations are as simple as possible.

In the bound interaction picture the total Lagrangian density for the interacting Maxwell and Dirac fields is a sum of the free Maxwell Lagrangian density L_M, the bound Dirac Lagrangian density L_{BD} and the interaction Lagrangian density L_I

$$\begin{aligned} L &= L_M + L_{BD} + L_I \\ \text{where} \qquad L_{BD} &= \overline{\psi}(x)[(i\partial\!\!\!/ - eA\!\!\!/^e) - m]\psi(x) \\ L_I &= -e\overline{\psi}(x)A\!\!\!/\psi(x) \end{aligned} \tag{2.5}$$

In the bound interaction picture the interaction between the Dirac field and external field is implicit in a bound Dirac Lagrangian L_{BD}. Then the interaction Lagrangian L_I describes interaction between bound Dirac and Maxwell fields. A solution for the bound Dirac field operator is required and the Maxwell field operator is left unchanged.

[1] the explicit form of A_μ^e will be considered in section 2.9.

2.4 S-matrix Theory

The system of interacting fields viewed in the Bound Interaction Picture can be specified by a state vector $|\Phi(t)\rangle_F$. The time evolution of such a state vector from a time t_0 in the past, can be written with the aid of a unitary operator $U(t, t_0)$ which itself evolves in time

$$\begin{aligned} |\Phi(t)\rangle_F &= U(t,t_0)\ |\Phi(t_0)\rangle_F \\ \text{where} \qquad i\frac{d}{dt}U(t,t_0) &= H_I(t)\,U(t,t_0) \\ H_I(t) &= -\textstyle\int L_I(x_\mu)\ d^3x \end{aligned} \tag{2.6}$$

There is no exact solution for these equations. However an approximation can be made by an expansion in powers of the interaction Hamiltonian H_I. The approximation is valid because the coupling between the Maxwell and Dirac fields is proportional to the fine structure constant, and is therefore weak. The result is written with the aid of the Dyson chronological product P

$$\begin{aligned} U(t,t_0) = & \sum_{n=0}^{\infty}\frac{(-i)^n}{n!}\int_{t_0}^{t}dt_1\int_{t_0}^{t}dt_2\ldots\int_{t_0}^{t}dt_n\ P[H_I(t_1)H_I(t_2)\ldots H_I(t_n)] \\ \text{where} \qquad & P[H_I(t_1)H_I(t_2)\ldots H_I(t_n)] = H_I(t_{i_1})H_I(t_{i_2})\ldots H_I(t_{i_n}) \\ & \quad t_{i_n} \le t_{i_{n-1}} \le \ldots \le t_{i_1} \end{aligned} \tag{2.7}$$

The S-operator and S-matrix are defined respectively in equation 2.8. These describe the time evolution of the interacting system from an initial state $|i(t_0)\rangle$ in the remote past to a final state $|f(t)\rangle$ in the remote future.

$$\begin{aligned} S &= \lim_{t\to\infty}\ \lim_{t_0\to-\infty} U(t,t_0) \\ S_{fi} &= \langle f(\infty)|\, S\, |i(-\infty)\rangle \end{aligned} \tag{2.8}$$

Substituting in the expressions for the U-operator in equation 2.7 and extracting integrations over spatial variables for the Dyson chronological product, the iteration solution for the S-operator can be written in terms of the interaction Lagrangian

$$\begin{aligned} S &= \sum_{n=0}^{\infty} S^{(n)} \qquad \text{where} \qquad S^{(0)} = 1 \\ S^{(n)} &= \frac{(-i)^n}{n!}\int_{-\infty}^{\infty}d^4x_1\int_{-\infty}^{\infty}d^4x_2\ldots\int_{-\infty}^{\infty}d^4x_n P[L_I(x_1)L_I(x_2)\ldots L_I(x_n)] \end{aligned} \tag{2.9}$$

Since pairs of Dirac operators in the Dyson chronological product above occur at identical space-time points, $S^{(n)}$ can be written in terms of the time ordering product T

$$S^{(n)} = \frac{(-i)^n}{n!}\int_{-\infty}^{\infty} d^4x_1 \int_{-\infty}^{\infty} d^4x_2 \ldots \int_{-\infty}^{\infty} d^4x_n \, T[L_I(x_1)L_I(x_2)\ldots L_I(x_n)]$$

where

$$T[M(t_1)N(t_2)] = \left\{ \begin{array}{cc} M(t_1)\,N(t_2) & \text{if} \quad t_1 > t_2 \\ -N(t_1)\,M(t_2) & \text{if} \quad t_2 > t_1 \end{array} \right\} \quad \text{fermions} \tag{2.10}$$

$$T[M(t_1)N(t_2)] = P[M(t_1)N(t_2)] \qquad \text{bosons}$$

The second order terms of the S-operator iteration solution constitute the second order processes. A subset of these represent the specific interactions that will be studied in this thesis.

2.5 Wicks theorem and Feynman diagrams

The expression for the S-operator obtained in section 2.4 provides a perturbative expansion in which terms of the desired order can be extracted. The second order terms are written

$$S^{(2)} = -\frac{1}{2}\int_{-\infty}^{\infty} d^4x_1 \int_{-\infty}^{\infty} d^4x_2 \, T[L_I(x_1)L_I(x_2)] \tag{2.11}$$

Each field operator present in equation 2.11 consists of a sum of creation and destruction operators. For a specific transition $|i\rangle \rightarrow |f\rangle$ all that is required are the correct number of destruction operators for states $|i\rangle$ to vanish and the correct number of creation operators for states $|f\rangle$ to exist. Selection of the desired set of operators is simplified by use of the normal product N which places creation operators to the left of destruction operators. The normal product can be introduced into equation 2.11 by Wick's Theorem which allows the time ordering product T to be written as a sum of the normal products N and vacuum expectation values. For instance the time ordering of two field operators A,B is

$$T[A(x_1), B(x_2)] = N[A(x), B(x)] + \langle 0|\, T[A(x_1)B(x_2)]\, |0\rangle \tag{2.12}$$

The complete $S^{(2)}$ expansion which involves the time ordering of six field operators yields eight normal product terms, some of which are identical under permutation operations ([MS84] p.109-110). There are two identical normal product terms for both Compton scattering and pair production so the S-matrix for these processes gains a factor of two. Additionally, either of the two Maxwell field operators can absorb initial photons leading to two terms in, for instance, the Compton Scattering S-matrix

$$\begin{aligned} S_{fi} \quad = \quad & -e^2 \int_{-\infty}^{\infty} d^4x_1 \; d^4x_2 \; \Big\{ \overline{\psi}_f(x_2) A_f^{\mu +}(x_2) \underbrace{\psi(x_2)\overline{\psi}(x_1)} A_i^{\nu -}(x_1) \psi_i(x_1) \\ & + \overline{\psi}_f(x_2) A_i^{\nu -}(x_2) \underbrace{\psi(x_2)\overline{\psi}(x_1)} A_f^{\mu +}(x_1) \psi_i(x_1) \Big\} \end{aligned} \tag{2.13}$$

The fermion contraction $\underbrace{\psi(x_2)\overline{\psi}(x_1)}$ is a vacuum expectation value $\langle 0|\, T[\psi(x_2)\overline{\psi}(x_1)]\, |0\rangle$ from which the fermion propagator is derived.

Equation 2.13 can be written down directly with the aid of Feynman diagrams which graphically represent the transition of states desired. Straight lines represent fermion operators, wavy lines represent photon operators and straight lines running between two vertices represent fermion propagators. The Dirac equation can also be solved for fermions in the presence of an external field (see section 2.10) and these solutions are represented within Feynman diagrams by double straight lines. The complete rules pertaining to Feynman diagrams can be found in the standard texts (see for example [Mui65] pg.326 or [MS84] section 7.3)

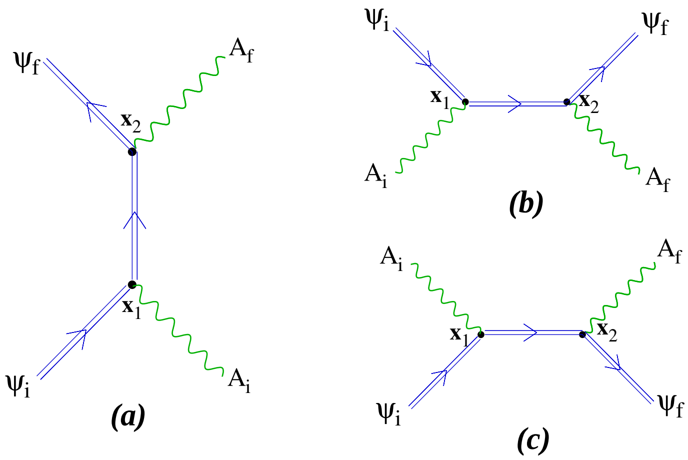

Figure 2.1: **Feynman diagrams for (a) Compton scattering (b) e^+e^- pair production, and (c) e^+e^- Pair Annihilation.**

2.6 Crossing symmetry

The structure of the iteration solution in equation 2.10 is such that the S-matrix is invariant under certain symmetry operations. Particular sets of these symmetry operations permit a detailed evaluation of the S-matrix for one scattering process to be used, after suitable substitutions of 4-momenta, to obtain results for other related scattering processes. This crossing symmetry entails a set of rules that govern this exchange of 4-momenta.

A crossing symmetry rests on the premise that the annihilation of a particle is equivalent to the creation of its anti-particle and is most clearly expressed using the Feynman diagrams. Consider two Feynman diagrams M, M' which involve electrons with momenta p, p', positrons with momenta q, q' and photons with momenta k, k'. If M, M' differ in only one external line such that an outgoing particle in M' is an ingoing particle in M (or vice versa) then a set of correspondences can be found (table 2.1).

diagram M'	diagram M	correspondence
k' out	k in	$k' \leftrightarrow -k \quad e' \leftrightarrow e$
p' out	q in	$p' \leftrightarrow -q \quad u(p') \leftrightarrow v(p) \quad \Lambda_-(p') \leftrightarrow \Lambda_+(q)$
q' out	p in	$q' \leftrightarrow -p \quad v(q') \leftrightarrow u(p) \quad \Lambda_+(q') \leftrightarrow \Lambda_-(p)$

Table 2.1: **Crossing symmetry correspondences.**

The symbols $u(p), v(p), e(k), \Lambda_-(p), \Lambda_+(p)$ were introduced in section 2.2 and respectively are the electron and positron bispinors, the photon 4-polarisation and the projection operators [JR76].

The Feynman diagrams depicted in figure 2.1 represent Compton scattering, pair production and pair annihilation. These three processes are all related by crossing symmetries.

2.7 Summation over spin and polarisation states

A calculation of the cross section of a transition from states $|i\rangle$ to states $|f\rangle$ requires a summation over fermion spin states and photon polarisation states. Initial states have to be averaged.

The fermion spin states are expressed by Dirac bispinors and for Compton scattering and pair production appear in the S-matrix in the form

$$\begin{aligned} S_{fi} &= \overline{u}_r^\alpha(p_f)\, Q_{\alpha\beta}\, u_s^\beta(p_i) \qquad \text{Compton scattering} \\ S_{fi} &= \overline{u}_r^\alpha(p_-)\, P_{\alpha\beta}\, v_s^\beta(p_+) \qquad \text{pair production} \end{aligned} \tag{2.14}$$

$Q_{\alpha\beta}$ and $P_{\alpha\beta}$ are functions of Dirac γ-matrices, and $u_s(p)$ and $v_s(p)$ are Dirac bispinors of the electron and positron respectively. Leaving aside averaging for now, the sum over initial and final spin states in the square of the matrix element is written

$$\begin{array}{rll} \sum\limits_{r,s} \overline{u}_r^{\alpha}(p_f)\, Q_{\alpha\beta}\, u_s^{\beta}(p_i)\, \overline{u}_s^{\gamma}(p_i)\, \overline{Q}_{\gamma\delta}\, u_r^{\delta}(p_f) & & \text{Compton scattering} \\ \sum\limits_{r,s} \overline{u}_r^{\alpha}(p_-)\, P_{\alpha\beta}\, v_s^{\beta}(p_+)\, \overline{v}_s^{\gamma}(p_+)\, \overline{P}_{\gamma\delta}\, u_r^{\delta}(p_-) & & \text{pair production} \end{array} \tag{2.15}$$

Equation 2.15 can be rearranged and written in terms of products of Dirac bispinors which yield the projection operators $\Lambda^{+}_{\alpha\beta}(p)$ and $\Lambda^{-}_{\alpha\beta}(p)$.

$$\begin{array}{rcccl} \sum\limits_{r} u_r^{\alpha}(p)\,\overline{u}_r^{\beta}(p) & = & \dfrac{1}{2m}(\not{p}+m)_{\alpha\beta} & \equiv & \Lambda^{+}_{\alpha\beta}(p) \\ \sum\limits_{r} v_r^{\alpha}(p)\,\overline{v}_r^{\beta}(p) & = & \dfrac{1}{2m}(\not{p}-m)_{\alpha\beta} & \equiv & \Lambda^{-}_{\alpha\beta}(p) \end{array} \tag{2.16}$$

The combination of projection operators and γ-matrix functions, $\Lambda_{\alpha\beta}Q_{\alpha\beta}$ will result in a summation over diagonal terms (a trace) which in turn yields a function of scalar products of the 4-vectors taking part in the process.

Photon polarisation 4-vectors $e_r^{\alpha}(k)$ appear in the S-matrix as slash vectors. Both the Compton and pair production processes involve two photons and the trace contains four polarisation vectors whose polarisation states can be denoted by subscripts i and j.

$$\sum_{i}\sum_{j} \mathrm{Tr}\left[\ldots \not{e}_i(k_1)\ldots \not{e}_j(k_2)\ldots \overline{\not{e}}_j(k_2)\ldots \overline{\not{e}}_i(k_1)\ldots\right] \tag{2.17}$$

Polarisation 4-vectors are extracted from the trace leaving behind Dirac γ-matrices.

$$\sum_{i} e_i^{\alpha}(k_1)\overline{e}_i^{\beta}(k_1) \sum_{j} e_j^{\mu}(k_2)\overline{e}_j^{\nu}(k_2)\ \mathrm{Tr}\left[\ldots\gamma_a\ldots\gamma_{\mu}\ldots\gamma_{\nu}\ldots\gamma_{\beta}\ldots\right] \tag{2.18}$$

Polarisation 4-vectors can be viewed in a reference frame such that longitudinal, transverse and scalar components can be separated. For free photons the summation over polarisation states reduces to a summation over transverse components. With $g^{\alpha\beta}$ representing the metric tensor and n a time like unit vector

$$\sum_{i=1}^{2} e_i^{\alpha}(k_1)\overline{e}_i^{\beta}(k_1) = -g^{\alpha\beta} - \frac{1}{(kn)^2}\left[k^{\alpha}k^{\beta} - (kn)(k^{\alpha}n^{\beta} + k^{\beta}n^{\alpha})\right] \tag{2.19}$$

For a real photon ($k^2 = 0$) gauge invariance requires that $-g^{\alpha\beta}$ be the only non vanishing term on the right hand side of equation 2.19 and the summation over polarisation states (equation 2.18) reduces to

$$\mathrm{Tr}\left[\ldots\gamma_\mu\ldots\gamma_\nu\ldots\gamma_\nu\ldots\gamma_\mu\ldots\right] \tag{2.20}$$

Both the fermion spins and photon polarisations consist of two states. Since both Compton scattering and pair production contain two each of these particles in their initial states, then initial state averaging results in an additional factor of $\frac{1}{4}$.

The final result after all summing and averaging is

$$\begin{array}{ll} \frac{1}{16m^2}\mathrm{Tr}\left[(\not{p}_f+m)Q(\not{p}_i+m)\overline{Q}\right] & \text{Compton scattering} \\ -\frac{1}{16m^2}\mathrm{Tr}\left[(\not{p}_-+m)P(\not{p}_+-m)\overline{P}\right] & \text{pair production} \end{array} \tag{2.21}$$

2.8 The transition probability and the scattering cross section

Numerical values quantifying the particular interaction of interest are obtained via the transition probability W or the scattering cross section σ. The transition probability and scattering cross section are both derived from the T-matrix specifying a transition from an initial state i of total 4-momentum P_i to a final state f of total 4-momentum P_f. The T-matrix is related to the S-matrix by

$$S_{fi} = \delta_{fi} + i(2\pi)^4\,\delta(P_i - P_f)\,T_{fi} \tag{2.22}$$

In any scattering process a specific initial state can result in any number N_f of final states. If the scattering process takes place in a spatial volume V and consists of asymptotically free initial particles, an interaction region and asymptotically free final states, the small number of final states of 3-momentum lying between p and $p+dp$ available to a single particle is given by

$$dN_f = \frac{V}{(2\pi)^3}\,dp \tag{2.23}$$

The cross section of the scattering is defined by a product of the transition probability per unit of space-time W, the flux density of initial particles J_i and the number of final states

$$\begin{array}{rrl} & d\sigma_{fi} & = \frac{W}{J_i}\,dN_f \\ \text{where} & W & = (2\pi)^4\,\delta(P_i - P_f)\sum_i\sum_f |T_{fi}|^2 \end{array} \tag{2.24}$$

For scattering processes involving two initial particles with relative velocity v, the flux density is $J_i = \dfrac{v}{V^2}$. The two IFQED processes to be studied in Chapter 3 both have two particles in the initial state. The SCS process has a photon (ω_i, k_i) and electron (ϵ_i, q_i) in the initial state and a photon (ω_f, k_f) and electron (ϵ_f, q_f) in the final state. The STPPP process has two photons (ω_1, k_1), (ω_2, k_2) in the initial state and an electron (ϵ_-, q_-) and positron (ϵ_+, q_+) in the final state. After extracting the normalisation constants of field operators from the T-matrix the differential cross sections for the SCS and STPPP process can be written

$$\begin{aligned} d\sigma_{fi} &= \frac{1}{v(2\pi)^2}\frac{m^2}{4\epsilon_i\omega_i}\,\delta(P_i - P_f)\overline{\sum_i}\sum_f |T_{fi}|^2\,\frac{dp_f\,dk_f}{\epsilon_f\,\omega_f} \qquad \text{SCS process} \\ d\sigma_{fi} &= \frac{1}{v(2\pi)^2}\frac{m^2}{4\omega_1\omega_2}\,\delta(P_i - P_f)\overline{\sum_i}\sum_f |T_{fi}|^2\,\frac{dp_-\,dp_+}{\epsilon_-\,\epsilon_+} \qquad \text{STPPP process} \end{aligned} \tag{2.25}$$

2.9 The external field

There will be two external fields considered in this thesis; a circularly polarised electromagnetic field and a constant crossed electromagnetic field. The experimental source of circularly polarised fields are intense laser beams. The idealisation of the laser beam as a plane wave of constant energy and intensity is reasonable given the monochromaticity and coherence properties of the laser and since photon depletion of the beam can be neglected.

The circularly polarised external field can be described by a 4-potential $A^e_\mu(x)$ which is a sum of sinusoidal components containing the 4-potential components $a_{1\mu}, a_{2\mu}$ and the 4-momentum of the external field k_μ

$$A^e_\mu(x) = a_{1\mu}\cos(kx) + a_{2\mu}\sin(kx) \tag{2.26}$$

The 4-potential $A^e_\mu(x)$ can be viewed with a gauge in which the time (zeroth) component vanishes. The Lorentz gauge condition $(kA^e) = 0$ then requires the 3-vectors $\underset{\sim}{a}_1$, $\underset{\sim}{a}_2$ and $\underset{\sim}{k}$ to be mutually orthogonal. With a^2 being the square of the magnitude of the 3-vectors $a_{1\mu}$ and $a_{2\mu}$, and with a minus sign resulting from the choice of metric (see section 2.2), scalar products of 4-vectors $a_{1\mu}$, $a_{2\mu}$ and k_μ satisfy

$$\begin{aligned} (a_1 a_1) = (a_2, a_2) &= -a^2 \\ (a_1 k) = (a_2 k) = (kk) &= 0 \end{aligned} \tag{2.27}$$

A subsequent identity which any 4-vectors Q_μ and P_μ satisfy can be found

$$\begin{aligned} &\text{If} && (kQ), (kP) = 0 \\ &\text{then} && (a_1 Q)\,(a_1 P) \;+\; (a_2 Q)\,(a_2 P) = a^2 (QP) \end{aligned} \tag{2.28}$$

The source of the constant crossed electromagnetic fields considered in this thesis are dense, ultra relativistic fermion bunches. A plane wave representation for these bunches is valid as long as the bunch profile is not significantly disrupted. The constant crossed electromagnetic field 4-potential contains only one component and satisfies

$$\begin{aligned} A^e_\mu(x) &= a_{1\mu}(kx) \\ (a_1 a_1) &= -a^2 \\ (a_1 k) &= 0 \end{aligned} \tag{2.29}$$

2.10 The Volkov solution and the Bound Electron Propagator

In the bound interaction picture the external field is taken into account by the electron - external field interaction. A solution of the Dirac equation modified by the inclusion of the external field operator $A^e_\mu(x)$ is required. The necessary modification is achieved by the replacement of the momentum operator ∂_μ with $\partial_\mu + ieA^e_\mu$. The quadratic Dirac equation with an external field is obtained by applying the operator $i\not\partial - e\not A^e + m$ to the linear Dirac equation with external field (equation 2.3). It is written in terms of the antisymmetric spin tensor $\sigma^{\mu\nu}$ and the field tensor of the external field $F^e_{\mu\nu}$

$$\begin{aligned} &\left[(p - eA^e)^2 - m^2 - \tfrac{ie}{2} F^e_{\mu\nu}\sigma^{\mu\nu}\right] \psi_V(x,p) = 0 \\ \text{and} \qquad & F^e_{\mu\nu} = k_\mu \frac{\partial A_\nu}{\partial\phi} - k_\nu \frac{\partial A_\mu}{\partial \phi} \\ & \text{where} \qquad \phi = k^\mu x_\mu \end{aligned} \tag{2.30}$$

Equation 2.30 can be solved exactly when the external field is a classical electromagnetic wave [Vol35]. The general solution is a product of the bispinor solution $u_s(p)$ to the free Dirac equation $(p - m)u_s(p) = 0$ and a function $F(\phi)$ whose form is to be determined

$$\psi_V(x,p) = u_s(p)\, F(\phi) \tag{2.31}$$

Expansion of operator products in equation 2.30 and substitution of the general solution $\psi_V(x,p)$ yields a first order differential equation in $F(\phi)$. With use of the Lorentz gauge condition, the solution is

$$F(\phi) = \exp\left[\frac{e}{2(kp)}\not{k}\not{A}^e\right] \exp\left(-ipx - i\int_0^{kx}\left[\frac{(A^e p)}{(kp)} - \frac{e^2 A^{e2}}{2(kp)}\right] d\phi\right) \tag{2.32}$$

By expanding $\exp[e/2(kp)]$ in a power series and using $(kA^e) = 0$, the Volkov solution for electrons is written in equation 2.33. The positron solution is obtained by substituting the anti-particle bispinor $v(p)$ and setting the momentum negative $p \rightarrow -p$.

$$\begin{aligned} \psi_V(x,p) &= E_p(x)\; u_s(p) \\ E_p(x) &= \left[1 + \frac{e}{2(kp)}\not{k}\not{A}^e\right] \exp\left(-ipx - i\int_0^{kx}\left[\frac{e(A^e p)}{(kp)} - \frac{e^2 A^{e2}}{2(kp)}\right] d\phi\right) \end{aligned} \tag{2.33}$$

The final element required in a calculation of second order process in the presence of the external field are the particle propagators which link the destruction of initial states at space-time point x_μ with the creation of final states at x'_μ. In this work only the bound electron propagator $G^e(x, x')$, which can be constructed from products of the Volkov electron propagator in direct analogy to the non external field case[2], is required. $G^e(x, x')$ can be written as the Green's function solution of the equation

$$(\not{p} - e\not{A}^e - m)G^e(x, x') = \delta(x - x') \tag{2.34}$$

An integral representation for $G^e(x, x')$ has been obtained for a linearly polarised external electromagnetic field using a proper time method [Sch51]. However for this thesis a representation obtained by [Rit72], which consists of the non external field fermion propagator sandwiched between Volkov E_p functions [Mit75], was chosen.

$$G^e(x, x') = \frac{1}{(2\pi)^4}\int d^4p\, E_p(x)\frac{\not{p} + m}{p^2 - m^2}\overline{E}_p(x') \tag{2.35}$$

In the absence of the external field, the Volkov E_p functions reduce to simple exponential functions, and the free fermion propagator is recovered. That equation 2.35 is a solution of equation 2.34 is due to the orthogonality properties of the E_p functions [Mit75]

$$\begin{aligned} \frac{1}{(2\pi)^4}\int E_p(x)\,\overline{E}_p(x')\,d^4p &= \delta^4(x - x') \\ \frac{1}{(2\pi)^4}\int E_p(x)\,\overline{E}_{p'}(x)\,d^4x &= \delta^4(p - p') \end{aligned} \tag{2.36}$$

[2]See for example [MS84] pgs 73-74.

Explicit forms for the Volkov E_p functions are obtained by substituting the explicit forms for the external field 4-potentials to be considered.

$$
\begin{aligned}
E_p(x) &= \left[1+\frac{e}{2(kp)}\left(\not{k}\not{a}_1\cos(kx)+\not{k}\not{a}_2\sin(kx)\right)\right] && \text{circularly polarised} \\
&\times \exp\left[-iqx - ie\frac{(a_1p)}{(kp)}\sin(kx)+ie\frac{(a_2p)}{(kp)}\cos(kx)\right] \\
E_p(x) &= \left[1+\frac{e}{2(kp)}\not{k}\not{a}(kx)\right] && \text{constant crossed} \\
&\times \exp\left[-iqx + i\frac{e^2a^2}{2(kp)}(kx) - i\frac{e(ap)}{2(kp)}(kx)^2 - i\frac{e^2a^2}{6(kp)}(kx)^3\right]
\end{aligned}
\tag{2.37}
$$

A modification of the electron momentum is suggested by gathering together terms such that

$$
q_\mu = p_\mu + \frac{e^2a^2}{2(kp)}\,k_\mu \tag{2.38}
$$

Indeed the Volkov function as a whole can be written in terms of q_μ due to the properties of the external field 4-potential set out in equations 2.27 and 2.29. The fermion momentum modified by the external field can be interpreted as a shift in the fermion mass given by

$$
m^2 + e^2a^2 \equiv m_*^2 \tag{2.39}
$$

2.11 Radiative corrections to the bound electron propagator

The S-matrix expansion allows for radiative corrections proportional to powers of the fine structure constant. For instance Compton scattering can include in its intermediate state the creation of a photon immediately followed by its destruction. This radiative correction is the electron self energy. Inclusion of the electron self energy in the IFQED processes results in a modified bound electron propagator which can be labelled $G^e_{RC}(x,x')$. The electron self energy in the presence of the external field $\Sigma^e(x,x')$ is defined by a product of the bound electron propagator without radiative corrections $G^e(x,x')$ and the free photon propagator $D(x,x')$

$$
\begin{aligned}
\Sigma^e(x,x') &= ie^2\gamma^\mu G^e(x,x')\gamma_\mu D(x,x') \\
\text{where} \qquad D(x,x') &= -\frac{1}{(2\pi)^4}\int d^4k\,\frac{1}{k^2+i\epsilon}\,e^{-ik(x-x')}
\end{aligned}
\tag{2.40}
$$

The radiatively corrected bound electron propagator $G^e_{RC}(x,x')$ is written as the Green's function solution of the equation

$$(\not{p} - e\not{A}^e - m - \Sigma^e(x,x'))G^e_{RC}(x,x') = \delta(x-x') \tag{2.41}$$

The solution to this equation proves cumbersome and a simpler method of including the radiative corrections is obtained by calculating the effect on the intermediate electron energy levels [BM76].

2.12 The external field electron energy shift

Taking radiative corrections into account, electron energy states are quasi-stationary due to a constant interaction between the electron and the cloud of virtual photons that surround it. The energy levels are broadened, gaining a small finite shift $\Delta\epsilon_{p,s}$. For the purposes of this thesis an expression for this energy level shift when the electron also interacts with an external electromagnetic field is required.

The wave function $\psi_V^{\Delta\epsilon_{p,s}}(x_2)$ of an electron of momentum p and spin s at the space-time point x_2 , interacting with a quantised Maxwell field and classical plane wave $A^e(x_2)$ satisfies the equation ([AB65] pg.758)

$$\left(\not{\partial} - ie\not{A}^e(x_2) + m\right)\psi_V^{\Delta\epsilon_{p,s}}(x_2) = -\int d^4x_1\ \Sigma^e(x_2,x_1)\psi_V^{\Delta\epsilon_{p,s}}(x_2) \tag{2.42}$$

The electron energy level shift can be separated from the electron wave function by writing the solution of equation 2.42 as a product of an exponential function and the Volkov wave function

$$\psi_V^{\Delta\epsilon_{p,s}}(x_2) \equiv e^{-i\,\Delta\epsilon_{p,s}\,t_2}\ \psi_V(x_2,p) \tag{2.43}$$

Inserting the general form of the solution expressed by equation 2.43 into equation 2.42, and operating on the right by the adjoint of the Volkov wave function, $\psi_V^\dagger(x_2,p)$

$$-i\,\Delta\epsilon_{p,s}\int d^4x_2\,\psi_V^\dagger(x_2,p)\,\psi_V(x_2,p) = -\int d^4x_1 d^4x_2\,\psi_V^\dagger(x_2,p)\,\Sigma^e(x_2,x_1)\,\psi_V(x_1,p)e^{-i\,\Delta\epsilon_{p,s}\,t_1} \tag{2.44}$$

Using the orthogonality properties of the Volkov functions $E_p(x)$, the integration over space-time variable x_2 on the left hand side of equation 2.44 yields a function of the electron energy, electron mass and the space-time volume $\frac{\epsilon_p}{m}VT$. Assuming that the width of the electron energy levels is small, the substitution $\Delta\epsilon_{p,s} \to 0$ can be made on the right hand side of equation 2.44 and the electron energy level shift can be written

$$\Delta\epsilon_{p,s} = \frac{m}{\epsilon_p}\frac{1}{VT(2\pi)^4}\int d^4x_1 d^4x_2\, \overline{\psi}_V(x_2,p)\,\Sigma^e(x_2,x_1)\,\psi_V(x_1) \tag{2.45}$$

2.13 Non external field regularisation and renormalisation

Calculation of the external field electron energy shift $\Delta\epsilon_{p,s}$ encounters a difficulty due to the presence of divergences in the external field electron self energy. In this section the removal of these divergences in the absence of the external field is considered. A discussion of the impact of the external field is left to chapters 6 and 7.

The removal of divergences is a three step process. Firstly, regularisation involves a modification of QED so that the electron self energy remains finite to all orders of perturbation theory. The momentum dependent electron self energy is written as an integration over photon 4-momentum k_μ [MS84].

$$\Sigma(p) = \frac{e^2}{(2\pi)^4}\int d^4k\,\frac{1}{k^2}\,\frac{2\not{p} - 2\not{k} - 4m}{(p-k)^2 - m^2} \tag{2.46}$$

The integration contains an ultraviolet divergence at its upper bound and an infrared divergence as the momentum reaches the mass shell. Regularisation is the introduction of appropriate limits which allow the integration to proceed. A small ficticious photon mass $i\varepsilon$ is added to the denominators and either a large cut-off is used for the upper bound of the integration or the photon propagator is replaced [PV49, Wei95]

$$\frac{1}{k^2 + i\varepsilon} \to \frac{1}{k^2 - \Lambda^2 + i\varepsilon} \tag{2.47}$$

QED is a renormalisable field theory and renormalisation proceeds from the recognition that the interaction of the Dirac and Maxwell fields modifies the properties of the free fields. The bare field operators (labelled by subscript 'B') are modified such that

$$\begin{aligned} \psi &= Z_2^{-1/2}\psi_B \qquad & A^\mu &= Z_3^{-1/2}A_B^\mu \\ e &= Z_3^{1/2}e_B \qquad & m &= m_B + \delta m \end{aligned} \tag{2.48}$$

The cofactors Z_2, Z_3 and δm are determined from the condition that the propagators of the renormalised fields have identical poles and residues to that of the propagators of the free fields with the absence of interactions. The electron self energy is included in the electron propagator via a sum of loop diagrams, the result being

$$G(p) = (\not{p} - m - \Sigma(p) + i\varepsilon)^{-1} \tag{2.49}$$

The renormalised fields lead to a renormalised electron self energy $\Sigma_{RC}(p)$ and renormalised electron propagator $G_{RC}(p)$

$$\begin{aligned} \Sigma(p) &\rightarrow \Sigma_{RC}(p) = \Sigma(p) - (Z_2 - 1)(\not{p} - m) + Z_2\delta m \\ G(p) &\rightarrow G_{RC}(p) = [Z_2(\not{p} - m) - Z_2\delta m - \Sigma(p)]^{-1} \end{aligned} \tag{2.50}$$

The pole in $G_{RC}(p)$ should occur at $\not{p} = m$ with residue 1. With the aid of L'Hopital's residue rule [Boa83], the renormalisation cofactors are

$$\begin{aligned} Z_2\delta m &= -\Sigma(\not{p} \rightarrow m) \\ Z_2 &= 1 + \Sigma'(\not{p} \rightarrow m) \end{aligned} \tag{2.51}$$

At first inspection Z_2 turns out to contain an infrared divergence. This is dealt with by taking into account emission of soft photons in external lines of the electron self energy process. The ultimate result is that $Z_2 = 1$. The final regularised electron propagator is

$$G_{RC}(p) = (\not{p} - m - \Sigma(p) + \Sigma(\not{p} \rightarrow m) + i\varepsilon)^{-1} \tag{2.52}$$

2.14 The optical theorem

The unitary properties of the S-operator allow a connection to be found between the elastic scattering amplitude[3] of an arbitrary scattering process and the transition probability from initial states $|i\rangle$ to final states $|f\rangle$. This so called optical theorem was developed for quantum scattering from the original expression relating refractive index to forward scattering. In this thesis it will be used to relate electron self energy to Bremsstrahlung in an external field.

Since the S-operator is Hermitian, the following relation holds

$$\langle i'|\, S^\dagger S \,|i\rangle = \sum_f \langle f|\, S^\dagger S \,|i'\rangle^* \, \langle f|\, S^\dagger S \,|i\rangle \tag{2.53}$$

[3] i.e. scattering from an initial state $|i\rangle$ through intermediate states (labelled $|f\rangle$) to final states identical to initial states $|i\rangle$.

The T-matrix can be substituted for for the S-matrix using equation 2.22. If states $|i\rangle$ and $|i'\rangle$ are such that their total momentum is equal, then equation 2.53 becomes

$$\frac{1}{2i}\left[\langle i'|\, T\, |i\rangle - \langle i|\, T\, |i'\rangle^*\right] = \frac{1}{2}\sum_f (2\pi)^4\, \delta(P_f - P_i)\, \langle f|\, T\, |i'\rangle^*\, \langle f|\, T\, |i\rangle \tag{2.54}$$

The final result relating the imaginary part of the elastic scattering amplitude $T_{elastic}$ with the transition probability W, is obtained by identifying $|i\rangle$ with $|i'\rangle$

$$\Im T_{elastic} = \frac{1}{2} W \tag{2.55}$$

Chapter 3

Cross section Calculations

3.1 Introduction

In this chapter analytic expressions are developed for the differential cross sections of two IFQED processes, stimulated Compton scattering (SCS) and stimulated two photon pair production (STPPP) in an external circularly polarised electromagnetic field.

In sections 3.2 - 3.4 analytic expressions are found for the differential cross section of the SCS process without recourse to specific kinematics or restricted energy regimes. The SCS differential cross section is considered in a reference frame in which the initial electron is at rest ($\underset{\sim}{p}_i = 0$), and the Lorentz gauge condition in which the 4th component of the external field 4-potential vanishes. The analytic expressions for both the SCS and the STPPP differential cross sections are lengthy and issues involved with extracting numerical calculations from them are considered in section 3.5.

In section 3.6 the analytic expressions for the SCS differential cross section in two limiting cases are considered. These limiting cases are important for comparison with previous results by other authors. In the limit of vanishing external field the SCS expressions reduce to the Klein-Nishina differential cross section for non external field Compton scattering. The second case limits kinematics such that the initial photon is parallel to the direction of propagation of the external field. This second limiting case was considered by [AM85] and small differences in the analytic expressions, which will prove to be significant, will be found.

In section 3.7 the STPPP process is considered using a centre of mass-like reference frame. A crossing symmetry (see section 2.6) diagrammatically links the SCS and STPPP processes and allows much of the analytic work of sections 3.2 - 3.4 to be reused. The STPPP differential cross section so obtained is considered in the limit of vanishing external field and the analytic expressions reduce to the Breit-Wheeler differential equation for non external field pair production.

The presence of the external field has the effect of shifting the fermion rest mass resulting in a corrected fermion momentum which is a function of external field parameters. In this chapter the corrected momentum of any free fermion p_x is denoted by the symbol q_x.

3.2 The stimulated Compton scattering (SCS) matrix element

Stimulated Compton scattering is the QED process in which a photon k_i together with a discrete number of photons from the external field lk combine with an electron p_i to produce a final state consisting of a photon k_f and an electron p_f. The SCS process can be represented graphically by the two topologically different Feynman diagrams shown in figure 3.2. The double straight lines indicate the electron embedded in the external electromagnetic field.

The matrix element of the scattering process can be written from Wick's theorem with the aid of figure 3.2 and the usual rules for Feynman diagrams.

$$\begin{aligned} S^e_{fi} &= -e^2 \int d^4x_1 d^4x_2 \\ &\times \Big\{ \overline{\psi}_V(x_2,p_f)\overline{\not{A}}_{k_f}(x_2)G^e(x_2,x_1)\not{A}_{k_i}(x_1)\psi_V(x_1,p_i) \\ &+ \overline{\psi}_V(x_2,p_f)\overline{\not{A}}_{-k_i}(x_2)G^e(x_2,x_1)\not{A}_{-k_f}(x_1)\psi_V(x_1,p_i)\Big\} \end{aligned} \tag{3.1}$$

The Volkov wave functions ψ_V and bound electron propagator G^e (section 2.10) and the Maxwell wave functions $A_k(x)$ (equation 2.4), are substituted into equation 3.1. An extra integration over intermediate 4-momentum p appears and the integrand is a function of Volkov E_p functions, 4-momenta and Dirac γ matrices sandwiched between free Dirac bispinors $\bar{u}(p_f)$ and $u(p_i)$.

$$\begin{aligned} S^e_{fi} &= -e^2 \int d^4x_1 d^4x_2 d^4p \\ &\times \ \bar{u}(p_f)\Big\{ \overline{E}_{p_f}(x_2)\not{\epsilon}(k_f)e^{ik_f x_2}E_p(x_2)\left[\frac{\not{p}+m}{p^2-m^2}\right]\overline{E}_p(x_1)\not{\epsilon}(k_i)e^{-ik_i x_1}E_{p_i}(x_1) \\ &+ \ \overline{E}_{p_f}(x_2)\not{\epsilon}(k_i)e^{-ik_i x_2}E_p(x_2)\left[\frac{\not{p}+m}{p^2-m^2}\right]\overline{E}_p(x_1)\not{\epsilon}(k_f)e^{ik_f x_1}E_{p_i}(x_1)\Big\}u(p_i) \end{aligned} \tag{3.2}$$

The integrations over x_1 and x_2 are performed by writing the dependence on x_1 and x_2 in the integrand as an infinite summation of Bessel functions [NR65a]. In that case, x_1 and x_2 appear entirely

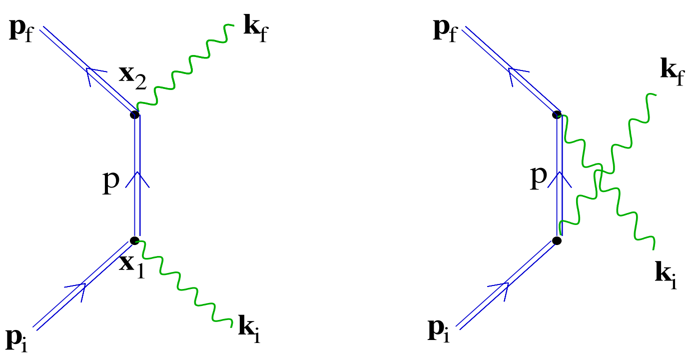

Figure 3.1: **Feynman diagrams for stimulated Compton scattering.**

as an exponential dependence, and the integrations over x_1 and x_2 yield a product of delta functions which contain particle 4-momenta within their arguments. The part of the integrand containing x_1 in equation 3.2 is

$$
\begin{aligned}
\overline{E}_p(x_1)\not{\epsilon}(k_i)E_{p_i}(x_1)e^{-ik_ix_1} &= \left[1+\frac{e}{2(kp)}\not{a}_1\not{k}\cos\phi_1+\frac{e}{2(kp)}\not{a}_2\not{k}\sin\phi_1\right] \\
&\times\ \not{\epsilon}(k_i)\left[1-\frac{e}{2(kp_i)}\not{a}_1\not{k}\cos\phi_1-\frac{e}{2(kp_i)}\not{a}_2\not{k}\sin\phi_1\right]e^{-iF(x_1)} \\
\text{where}\qquad F(x_1) &= \alpha_{1i}\sin\phi_1-\alpha_{2i}\cos\phi_1-qx_1+q_ix_1+k_ix_1 \\
\phi_1 &= (kx_1) \\
\alpha_{1i} &= e\left[\frac{(a_1p_i)}{(kp_i)}-\frac{(a_1p)}{(kp)}\right]
\end{aligned}
\tag{3.3}
$$

Equivalent expressions are found for the part of the integrand containing x_2. Using trigonometric double angle formula to write the function $F(x)$ in the form $z\sin(\phi-\phi_0)$ and using well known properties of Bessel functions [Wat22], the dependence on x_1, x_2 is expanded in a Fourier series [NR65a].

$$
\begin{aligned}
(1,\cos\phi_1,\sin\phi_1)\,e^{-iz_i\sin(\phi_1-\phi_{0i})} &= \sum_{r=-\infty}^{\infty}(M_1,M_2,M_3)e^{-ir\phi_1} \\
(1,\cos\phi_2,\sin\phi_2)\,e^{iz_f\sin(\phi_2-\phi_{0f})} &= \sum_{s=-\infty}^{\infty}(N_1,N_2,N_3)e^{is\phi_2} \\
\text{where}\qquad M_1 &= J_r(z_i)e^{ir\phi_{0i}} \\
M_2 &= \tfrac{1}{2}\left[J_{r-1}(z_i)e^{-i\phi_{0i}}+J_{r+1}(z_i)e^{i\phi_{0i}}\right]e^{ir\phi_{0i}} \\
M_3 &= \tfrac{i}{2}\left[J_{r-1}(z_i)e^{-i\phi_{0i}}-J_{r+1}(z_f)e^{i\phi_{0i}}\right]e^{ir\phi_{0i}} \\
N_1 &= J_s(z_f)e^{-is\phi_{0f}} \\
N_2 &= \tfrac{1}{2}\left[J_{s-1}(z_f)e^{i\phi_{0f}}+J_{s+1}(z_f)e^{-i\phi_{0f}}\right]e^{-is\phi_{0f}} \\
N_3 &= -\tfrac{i}{2}\left[J_{s-1}(z_f)e^{i\phi_{0f}}-J_{s+1}(z_f)e^{-i\phi_{0f}}\right]e^{-is\phi_{0f}}
\end{aligned}
\tag{3.4}
$$

$$
\begin{aligned}
z_i &= \sqrt{\alpha_{1i}^2+\alpha_{2i}^2} & z_f &= \sqrt{\alpha_{1f}^2+\alpha_{2f}^2} \\
\cos\phi_{0i} &= \frac{\alpha_{1i}}{z_i} & \cos\phi_{0f} &= \frac{\alpha_{1f}}{z_f} \\
\sin\phi_{0i} &= \frac{\alpha_{2i}}{z_i} & \sin\phi_{0f} &= \frac{\alpha_{2f}}{z_f}
\end{aligned}
$$

Substituting these Fourier expansions into equation 3.2, grouping together the exponential dependence, and expanding products of 4-vectors, the expression for the matrix element becomes

$$
\begin{aligned}
S^e_{fi} &= -e^2 \sum_{rs} \int d^4x_1\, d^4x_2\, d^4q \\
&\times\ \bar{u}(p_f) \Bigg\{ B_{rs}(\not{\epsilon}(k_f), N, p, p_f) \left[\frac{\not{p} + m}{p^2 - m^2} \right] B_{rs}(\not{\epsilon}(k_i), M, p_i, p) e^{-iG} \\
&+\ B_{rs}(\not{\epsilon}(k_i), N, p, p_f) \left[\frac{\not{p} + m}{p^2 - m^2} \right] B_{rs}(\not{\epsilon}(k_f), M, p_i, p) e^{-iH} \Bigg\} u(p_i) \\
\text{where} \quad G &= (q_i + k_i + rk - q)x_1 - (q_f + k_f + sk - q)x_2 \\
H &= (q_i - k_f + rk - q)x_1 - (q_f - k_i + sk - q)x_2 \\
B(\not{\epsilon}(k_f), N, p, p_f) &= \not{\epsilon}(k_f) N_1 - \frac{e}{2(kp)} \left(\not{\epsilon}(k_f) \not{a}_1 \not{k} N_2 + \not{\epsilon}(k_f) \not{a}_2 \not{k} N_3 \right) \\
+ &\ \frac{e}{2(kp_f)} \left(\not{a}_1 \not{k} \not{\epsilon}(k_f) N_2 + \not{a}_2 \not{k} \not{\epsilon}(k_f) N_3 \right) - \frac{e^2 a^2}{4(kp)(kp_f)} \not{k} \not{\epsilon}(k_f) \not{k} N_1
\end{aligned}
\tag{3.5}
$$

q, q_i and q_f represent the shifted electron momentum ($q = p + \frac{e^2 a^2}{2(kp)} k$). It is convenient to make a transformation of integration variable $d^4p \to d^4q$. This shift has been used before in 2nd order IFQED calculations [Ole68] and the Jacobian of the transformation is unity (see Appendix A).

The transformation $(p, p_i, p_f) \to (q, q_i, q_f)$ is made in the integrand of equation 3.5 with the aid of the orthogonality of 4-vectors $a_{1\mu}, a_{2\mu}$ and k_μ. The following equivalences hold

$$
\begin{aligned}
B(\not{\epsilon}(k_f), N, p, p_f) &\equiv B(\not{\epsilon}(k_f), N, q, q_f) \\
e \left[\frac{(a_n p_m)}{(kp_m)} - \frac{(a_n p)}{(kp)} \right] &\equiv e \left[\frac{(a_n q_m)}{(kq_m)} - \frac{(a_n q)}{(kq)} \right] \ \text{where}\ n = 1, 2 \ \ m = i, f \\
p^2 - m^2 &\equiv q^2 - m_*^2 \ \text{where}\ m_*^2 = m^2 + e^2 a^2 \\
\not{p} + m &\equiv \not{q} - \frac{e^2 a^2}{2(kq)} \not{k} + m
\end{aligned}
\tag{3.6}
$$

Integration over x_1, x_2, q (in that order) yields a single Dirac delta function, the argument of which expresses the conservation of 4-momentum for the SCS process. Mathematically, r external field photons contribute in the initial state and s contribute in the final state. Physically, however, it is the total number $l = r - s$ of external field photons contributing to the process that holds interest. Finally, the matrix element can be written

$$S^e_{fi} = -e^2(2\pi)^8 \sum_{rs} \delta^4(q_i + k_i + (r-s)k - q_f - k_f)\, \bar{u}(p_f)\, Q\, u(p_i)$$

$$\begin{aligned}
\text{where} \quad Q &= B(\not{\epsilon}(k_f), \overline{N}, \bar{q}, q_f) \left[\frac{\bar{\not{q}}_r - \frac{e^2a^2}{2(k\bar{q})}\not{k} + m}{\bar{q}_r^2 - m_*^2}\right] B(\not{\epsilon}(k_i), \overline{M}, q_i, \bar{q}) \\
&+ \; B(\not{\epsilon}(k_i), \overline{\overline{N}}, \bar{\bar{q}}, q_f) \left[\frac{\bar{\bar{\not{q}}}_r - \frac{e^2a^2}{2(k\bar{p})}\not{k} + m}{\bar{\bar{q}}_r^2 - m_*^2}\right] B(\not{\epsilon}(k_f), \overline{\overline{M}}, q_i, \bar{\bar{q}})
\end{aligned} \tag{3.7}$$

$$\text{and} \qquad \bar{q}_r = q_i + k_i + rk$$

$$\bar{\bar{q}}_r = q_i - k_f + rk$$

Notationally, the symbols $\overline{M}, \overline{N}$ and $\overline{\overline{M}}, \overline{\overline{N}}$ refer to the functions M, N defined in equation 3.4, with 4-momentum q replaced by $\bar{q}_r$ and $\bar{\bar{q}}_r$ respectively.

The sum over initial and final states of the square of the S-matrix element $\sum\limits_{if} |S^e_{fi}|^2$ is written as a trace of products of Dirac γ-matrices with the aid of the summation rules for Dirac bispinors and photon polarisations. A factor of $\frac{1}{8m^2}$ is introduced by an average over two electron spin states and the sum over bispinors. An extra factor of $\frac{1}{2}$ is obtained from an average of possible initial photon polarisations. Four infinite summations over indicies r, s, r', s' are introduced. The product of Dirac delta functions leads to $s = s'$. Three infinite summations remain and after making a shift in summation variable $\sum\limits_s \to \sum\limits_l$, the square of the matrix element is

$$\begin{aligned}
\sum_{if} |S^e_{fi}|^2 &= \frac{e^2}{16m^2}(2\pi)^8 \sum_l \delta^4(q_i + k_i + lk - q_f - k_f) \sum_{rr'} \mathrm{Tr}\, Q \\
\text{or} \quad \sum_{if} |T^e_{fi}|^2 &= \frac{e^2}{16m^2} \sum_{lrr'} \mathrm{Tr}\, Q
\end{aligned}$$

$$\text{where} \qquad \mathrm{Tr}\, Q = \mathrm{Tr}\, Q_1(\bar{q}_r, \bar{q}_{r'}) + \mathrm{Tr}\, Q_1(\bar{\bar{q}}_r, \bar{\bar{q}}_{r'}) + \mathrm{Tr}\, Q_2(\bar{q}_r, \bar{\bar{q}}_{r'}) + \mathrm{Tr}\, Q_2^*(\bar{q}_r, \bar{\bar{q}}_{r'})$$

$$\begin{aligned}
\text{and} \quad Q_1(\bar{q}_r, \bar{q}_{r'}) &= (\not{p}_f + m) B(\gamma^\mu, \overline{N}_r, \bar{q}, q_f) \left[\frac{\bar{\not{q}}_r - \frac{e^2a^2}{2(k\bar{q})}\not{k} + m}{\bar{q}_r^2 - m_*^2}\right] B(\gamma^\nu, \overline{M}_r, q_i, \bar{q}) \\
&\times \; (\not{p}_i + m) \tilde{B}(\gamma_\nu, \overline{M}_{r'}, q_i, \bar{q}) \left[\frac{\bar{\not{q}}_{r'} - \frac{e^2a^2}{2(k\bar{q})}\not{k} + m}{\bar{q}_{r'}^2 - m_*^2}\right]^* \tilde{B}(\gamma_\mu, \overline{N}_{r'}, \bar{q}, q_f) \\
Q_2(\bar{q}_r, \bar{\bar{q}}_r') &= (\not{p}_f + m) B(\gamma^\mu, \overline{N}_r, \bar{q}, q_f) \left[\frac{\bar{\not{q}}_r - \frac{e^2a^2}{2(k\bar{q})}\not{k} + m}{\bar{q}_r^2 - m_*^2}\right] B(\gamma^\nu, \overline{M}_r, q_i, \bar{q}) \\
&\times \; (\not{p}_i + m) \widetilde{B}(\gamma_\nu, \overline{\overline{M}}_{r'}, q_i, \bar{\bar{q}}) \left[\frac{\bar{\bar{\not{q}}}_{r'} - \frac{e^2a^2}{2(k\bar{q})}\not{k} + m}{\bar{\bar{q}}_{r'}^2 - m_*^2}\right]^* \widetilde{B}(\gamma_\mu, \overline{\overline{N}}_{r'}, \bar{\bar{q}}, q_f)
\end{aligned} \tag{3.8}$$

The full trace expressions for Tr Q_1 and Tr Q_2 are written down in Appendix B.

3.3 The SCS phase space integral

The calculation of the SCS cross section requires an integration over final states of particle momentum $(\epsilon_f, \underset{\sim}{q}_f)$ and $(\omega_f, \underset{\sim}{k}_f)$. This integration is referred to as the phase space integral

$$\int \frac{d^3\underset{\sim}{k}_f \; d^3\underset{\sim}{q}_f}{\omega_f \; \epsilon_f} \, \delta^4(q_i + k_i + l\,k - q_f - k_f) \tag{3.9}$$

Work done on the first order IFQED processes in circularly polarised field dealt with the phase space integral by making a suitable change of integration variables. Azimuthal symmetry of the scattering process combined with a centre of mass reference frame, resulted in a single integration over a simple function of scalar products [NR65a]. [AM85], in their work on second order external field Compton scattering, also made use of an azimuthal symmetry by restricting their results to a subset of possible kinematics in which the initial photon momentum is collinear with that of the external field. With arbitrary kinematics, however, the second order SCS process in circularly polarised external field does not contain a symmetry with respect to the azimuthal angle φ_f. Additionally, the centre of mass reference frame results in relatively complicated expressions for particle energy-momenta and scattering angles.

A simpler transformation is obtained by considering the laboratory reference frame and defining an element of solid angle $d\Omega_{k_f}(= d\cos\theta_f \; d\varphi_f)$ into which the final SCS photon is scattered. The direction of the scattering is defined by angles θ_f, φ_f depicted in figure 3.2.

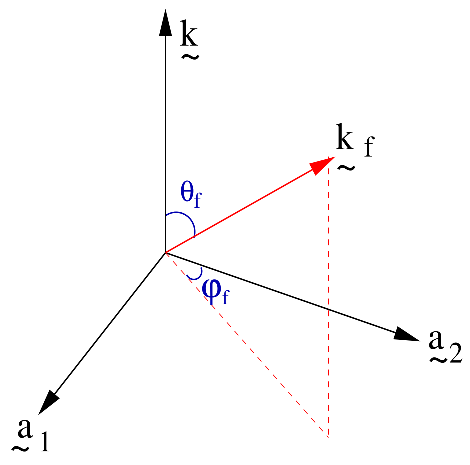

Figure 3.2: **scattering Geometry for stimulated Compton scattering**

An integration variable transformation from free electron 3-momentum to bound electron 3-momentum is required first, using the result that the Jacobian of the 4-vector transformation $d^4p_f \rightarrow d^4q_f$ is unity (see Appendix A)

$$\frac{d^3 p_{\mathcal{L}}}{\epsilon_{p_f}} = 2\int d^4 p_f\ \Theta(\epsilon_{p_f})\,\delta(p_f^2 - m^2) = 2\int d^4 q_f\ \Theta(\epsilon_{q_f})\,\delta(q_f^2 - m_*^2) = \frac{d^3 q_{\mathcal{L}}}{\epsilon_{q_f}} \tag{3.10}$$

and finally the phase space integral transforms as

$$\int \frac{d^3 k_{\mathcal{L}}\ d^3 q_{\mathcal{L}}}{\omega_f\ \epsilon_f}\delta^4(q_i + k_i + l\,k - q_f - k_f) \equiv \int \frac{d\Omega_{k_f}\ \omega_f^2}{m\omega_f + (k_i k_f) + \left[l + \frac{e^2 a^2}{2m\omega}\right](k k_f)} \tag{3.11}$$

3.4 Symbolic evaluation of the SCS cross section

With the results of the last two sections and the knowledge that the relative velocity of the two initial SCS particles p_i and k_i is unity in the laboratory frame, the SCS differential cross section is written with the aid of the general expression (equation 2.25) as

$$\frac{d\sigma}{d\Omega_{k_f}} = \left(\frac{e}{8\pi m}\right)^2\left(\frac{m}{\omega_i}\right)\sum_{lrr'}\frac{\omega_f^2}{m\omega_f + (k_i k_f) + [l + \frac{e^2 a^2}{2(kp_i)}](kk_f)}\ \mathrm{Tr}\ Q \tag{3.12}$$

Before the calculation can proceed further, Tr Q, which was defined in equation 3.8 must be evaluated. This evaluation, though not theoretically difficult, is cumbersome due to its length. A simple algebraic expansion of the 4 traces yields approximately 105,000 terms. Analytic means of simplifying the trace expressions are useful.

The trace of products of large numbers of Dirac γ-matrices and terms like $(\not{p} + m)$ can be simplified by successive application of the Kahane algorithm and the Becker-Schott rule [Kah68]. The calculation of the traces in this thesis was automated with the aid of the computer software package Mathematica, and an add-on package FeynCalc [Mer91].

Performing the entire trace in one pass and using inbuilt functions in Mathematica to simplify results, proved tediously time consuming. The computational time required was shortened by algebraically expanding the trace as a series of trace coefficients of products of the functions M and N denoted as

$$X_{ij}^r \equiv \frac{M_{ir}N_{jr}}{(p_r^2 - m^2)} \qquad \text{where} \qquad i \text{ and } j = 1, 2, 3 \tag{3.13}$$

Using the invariance of a trace of products of Dirac γ-matrices under reversal and cyclic permutation of its elements, many of these trace coefficients are identical under exchange of some of the four-vectors involved in the calculation.

In total, there are 17 independent trace coefficients associated with Tr Q_1 and 15 independent trace coefficients associated with Tr Q_2 . Each independent trace coefficient has, as a co-product, a function of M_{ir} and N_{jr} which can be simplified using well known addition formulae for Bessel functions [NR65a, Wat22] and the relations

$$\begin{aligned}
\alpha_{1i} M_2 + \alpha_{2i} M_3 &= r M_1 \\
\alpha_{1f} N_2 + \alpha_{2f} N_3 &= (r-l) N_1 \\
J_{n-1}(z) + J_{n+1}(z) &= \frac{2n}{z} J_n(z)
\end{aligned} \tag{3.14}$$

It was necessary to develop many relations of the form set out in equation 3.14 in order to complete the full trace calculation. These relations are presented in Appendix C. The trace coefficients themselves, along with the results of their calculation are presented in Appendix B.

In order to obtain numerical values for the SCS differential cross section, it was necessary to write all scalar products in terms of initial state quantities $\omega, \omega_i, l, \theta_i, \nu^2$ and the final state scattering angles θ_f and ϕ_f. From the conservation of momentum for the SCS process, the final electron 4-momentum p_f can be written in terms of other particle 4-momenta, and the energy of the final photon can be written

$$\omega_f = \frac{(q_i k_i) + l(k\bar{p})}{m + \left(\frac{e^2 a^2}{2m} + l\omega\right)(1-\cos\theta_f) + \omega_i\left(1 - \cos\theta_i\,\cos\theta_f\, - \sin\theta_i\,\sin\theta_f\,\cos\phi_f\right)} \tag{3.15}$$

The external field 4-potentials $a_{1\mu}$ and $a_{2\mu}$ appear in the differential cross section expressions in linear combinations of scalar products with other 4-vectors such that the identities of section 2.9 can be applied.

As a consequence, the arguments of the Bessel functions appearing in the differential cross section, which depend on the external field 4-potentials, can be written

$$\begin{aligned}
\bar{z}_i^2 &= \frac{e^2 a^2}{(k\bar{p})^2} \frac{(kk_i)}{(kp_i)} \left[2(q_i k_i) - m_*^2 \frac{(kk_i)}{(kp_i)} \right] \\
\bar{z}_f^2 &= \frac{e^2 a^2}{(k\bar{p})^2} \frac{(kk_f)}{(kp_f)} \left[2(q_f k_f) - m_*^2 \frac{(kk_f)}{(kp_f)} \right] \\
\bar{\bar{z}}_i^2 &= \frac{e^2 a^2}{(k\bar{\bar{p}})^2} \frac{(kk_f)}{(kp_i)} \left[2(q_i k_f) - m_*^2 \frac{(kk_f)}{(kp_i)} \right] \\
\bar{\bar{z}}_f^2 &= \frac{e^2 a^2}{(k\bar{\bar{p}})^2} \frac{(kk_i)}{(kp_f)} \left[2(q_f k_i) - m_*^2 \frac{(kk_i)}{(kp_f)} \right]
\end{aligned} \tag{3.16}$$

3.5 Numerical evaluation of the SCS cross section

The amount of computing time required to complete a numerical calculation of the SCS differential cross section depends, critically, on the convergence of the infinite summations over integers r and r'. Consequently it is of interest to examine the behaviour of the functions $\sum_r X^r$ and $\sum_{r'} X^{r'}$ which mainly account for the appearance of r and r' in the differential cross section expressions.

The r, r' dependence of the functions $X^r, X^{r'}$ obtained by substitution of the expressions for $M, N, \bar{p}$ and $\bar{\bar{p}}$ (equation 3.4, 3.7 and Appendix C) appears in the order of a product of squares of Bessel functions, an exponential dependence in the numerator, and a linear dependence in the denominator

$$\sum_{r=-\infty}^{\infty} J_r(z_i) J_{r-l}(z_f) \frac{e^{-ir\phi}}{r+a} \tag{3.17}$$

These summations were discussed by [Bea79a] in connection with a study of Möller scattering in a circularly polarised electromagnetic field, however no analytic solution is known. It is of interest, then, to discuss the asymptotic forms of the summation. Both the functions $e^{-ir\phi}$ and $\frac{1}{r+a}$ can be expanded in a Taylor series, but neither of these expansions provide any particular benefit. The asymptotic forms of the Bessel functions are determined by the numerical regimes of the order and argument [AS65].

$$\begin{aligned} J_r(z) &\sim \frac{1}{\Gamma(r+1)} \left(\frac{z}{r}\right)^r && \text{where} \quad r \geq 0 \quad \text{and} \quad 0 \leq z \ll r \\ J_r(z) &\sim \sqrt{\frac{2}{\pi z}} \cos\left(z - \frac{r\pi}{2} - \frac{\pi}{4}\right) && \text{where} \quad z \gg r \end{aligned} \tag{3.18}$$

The four Bessel function arguments in equation 3.16 are directly proportional to either ν^2 and $\cos\,\theta_i$, or ν^2 and $\cos\,\theta_f$. Numerical evaluations will include parameter regimes where ν^2 is not small and the angles θ_i and θ_f range fully from 0 to 2π. Therefore the asymptotic forms for the Bessel functions cannot be used. However, the series in equation 3.17 converges rapidly for $|r| > z_i, z_f$ [Bea79a] and this convergence was used to limit the numerical evaluation of the summation over all r.

Any future work in external field QED involving fermion solutions in a circularly polarised electromagnetic plane wave will involve infinite summations of the type discussed here. In QED processes of higher order than those considered in this work the computational time required to complete the summations numerically may become a severely limiting factor. For this reason, in Appendix D, some original work on analytic solutions of infinite summations involving squares of

Bessel functions is presented, in the hope that it may provide some impetus to a future analytic solution of the summation expressed by equation 3.17.

3.6 The SCS cross section in various limiting cases

Previous work done by other authors on the SCS differential cross section has been performed with special kinematics, non relativistic energy regimes and/or asymptotically small external field intensity. For the purposes of comparison and validation it is of interest to examine the general SCS differential cross section developed in the previous sections for various limiting cases.

[AM85] perform most of their work on the SCS process with a linearly polarised external electromagnetic field. They also write down an expression for the square of the matrix element of the SCS process with a circularly polarised external electromagnetic field, though they provide no numerical results. [AM85] consider kinematics in which the direction of propagation of the incoming photon is parallel to the direction of propagation of the external field photons. These kinematics imply that

$$\begin{aligned}
\hat{\underset{\sim}{k}}_i - \hat{\underset{\sim}{k}} &= 0 \\
(kk_i), (a_1 k_i), (a_2 k_i) &= 0 \\
\bar{z}_i = \bar{\bar{z}}_f &= 0 \\
\bar{\bar{z}}_i^2 = \bar{z}_f^2 \; (\equiv z^2) &= \frac{e^2 a^2}{(kp_i)^2} \frac{(kk_f)}{(kp_f)} \left[2(q_f k_f) - \frac{(kk_f)}{(kp_f)} \right]
\end{aligned} \tag{3.19}$$

With application of these relations to the general results obtained in section 3.2 for the square of the SCS S-matrix element, the infinite summations over r and r' can be performed immediately and the resulting expressions are greatly reduced in length.

Small but significant differences were found between analytic expressions of [AM85] and the analytic expressions obtained here. Numerical values obtained from the expressions of [AM85] became negative for certain parameter ranges; a non physical result. In contrast, numerical results from the expressions obtained in this thesis remain positive at all times (see figure 3.6)

The second limiting case to be studied is that of vanishing external field achieved by allowing the external field intensity parameter to approach zero, $\nu^2 \to 0$. In this limit, the SCS process reduces to ordinary Compton scattering [KN28]. As $\nu^2 \to 0$ all four Bessel function arguments $\bar{z}_i, \bar{z}_f, \bar{\bar{z}}_i, \bar{\bar{z}}_f$ reduce to zero, and the infinite summations $\sum_{rr'}$ can be performed immediately. The occurrence of Bessel functions with zero argument in the SCS differential cross section expressions ensure that no laser photons $l = 0$ contribute to the process. The trace expressions reduce to

$$
\begin{aligned}
\mathrm{Tr}\, Q_1(\bar{p}_r, \bar{p}_{r'}) &= 32\{-m^2(p_f\bar{p}) + (p_ik_i)(p_fk_i) + 2m^2(p_ik_i) + 2m^4\} \\
\mathrm{Tr}\, Q_2(\bar{p}_r, \bar{\bar{p}}_{r'}) &= 16m^2[(p_i\bar{p}) + (p_i\bar{\bar{p}}) + (p_f\bar{p}) + (p_f\bar{\bar{p}}) \\
&\quad +(p_ip_f) + (\bar{p}\bar{\bar{p}}) - 2m^4] - 32(\bar{p}\bar{\bar{p}})(p_ip_f)
\end{aligned}
\tag{3.20}
$$

Equation 3.20 is identical with equations (14a) and (14b) of [Ole68] who considered the SCS process with linearly polarised external electromagnetic field in the same limit of vanishing external field.

With substitution of equation 3.20 into the SCS differential cross section (equation 3.12 and 3.8), the Klein-Nishina result for an incoming photon of initial energy ω_i and final energy ω_f scattered through an angle θ_f is obtained.

$$
\begin{aligned}
\frac{d\sigma}{d\Omega} &= \frac{r_o^2}{2}\left(\frac{\omega_f}{\omega_i}\right)^2\left(\frac{\omega_f}{\omega_i} + \frac{\omega_i}{\omega_f} - \sin^2\theta_f\right) \\
\text{where} \qquad r_o &= \frac{e^2}{4\pi m}
\end{aligned}
\tag{3.21}
$$

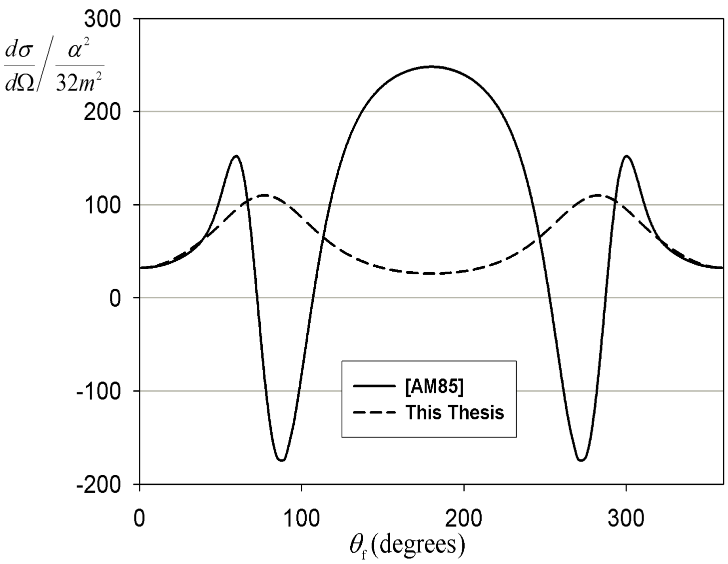

Figure 3.3: **SCS differential cross section comparison between [AM85] and the expressions of Chapter 3 for $\omega = 0.512$ MeV, $\omega_i = 0.41$ MeV, $\theta_i = 0°$ and $\nu^2 = 0.7$.**

3.7 Stimulated Two Photon e^+e^- pair production (STPPP) in an External Field

The stimulated two photon pair production process is the production of a Volkov electron/positron pair, p_- and p_+, by an initial state consisting of two photons, k_1 and k_2, with a number of laser field photons contributing. The STPPP matrix element can be written down from Wick's theorem, and consists of two channels, each of which can be represented by the Feynman diagrams shown in figure 3.4

From the usual rules associated with Feynman diagrams, the STPPP matrix element is

$$\begin{aligned} S^e_{fi} = \quad & -e^2 \int_{-\infty}^{\infty} d^4x_1\, d^4x_2 \left\{ \overline{\psi}^-_V(x_2,p_-)\, \not{A}^+_{k_1}(x_2)\, G^e(x_2,x_1)\, \not{A}^-_{k_2}(x_1)\, \psi^+_V(x_1,p_+) \right. \\ & \left. +\; \overline{\psi}^-_V(x_2,p_-)\, \not{A}^-_{k_2}(x_2)\, G^e(x_2,x_1)\, \not{A}^+_{k_1}(x_1)\, \psi^+_V(x_1,p_+) \right\} \end{aligned} \tag{3.22}$$

$\psi^-_V(x,p_-)$ are the electron Volkov solutions and $\psi^+_V(x,p_+)$ are the positron solutions. Substitution into equation 3.22 of the expressions for the bound electron propagator G^e, the Volkov solutions, ψ_V, and the Maxwell wave functions A_k, yields for the STPPP matrix element

$$\begin{aligned} S^e_{fi} \quad &= -e^2 \int_{-\infty}^{\infty} d^4x_1\, d^4x_2\, d^4q \;\; \bar{u}(p_-)\, \overline{E}_{p_-}(x_2) \\ \times \quad & \left\{ \not{\epsilon}(k_1) e^{-ik_1x_2} E_p(x_2) \left[\frac{\not{p}+m}{p^2-m^2} \right] \overline{E}_p(x_1) \not{\epsilon}(k_2) e^{-ik_2x_1} \right. \\ + \quad & \left. \not{\epsilon}(k_2) e^{-ik_2x_2} E_p(x_2) \left[\frac{\not{p}+m}{p^2-m^2} \right] \overline{E}_p(x_1) \not{\epsilon}(k_1) e^{-ik_1x_1} \right\} E_{-p_+}(x_1) v(p_+) \end{aligned} \tag{3.23}$$

Crossing symmetry (section 2.6) allows the STPPP matrix element to be obtained from the SCS matrix element (equation 3.8) with the following substitutions

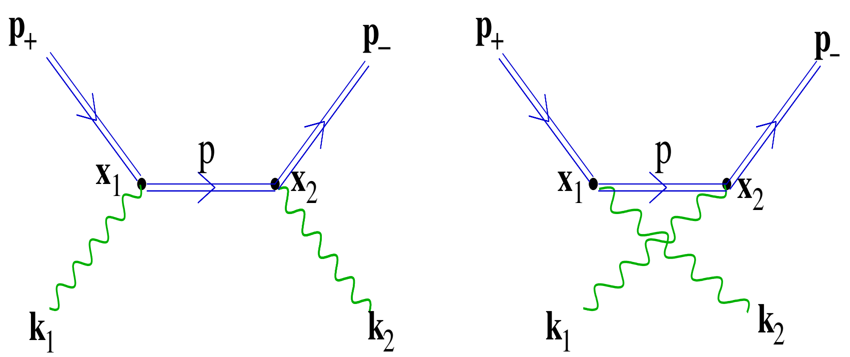

Figure 3.4: **Feynman diagrams for stimulated two photon pair production.**

$$
\begin{array}{cccc}
q_f \leftrightarrow q_- & , \quad q_i \leftrightarrow -q_+ & , \quad k_i \leftrightarrow k_2 & , \quad k_f \leftrightarrow -k_1 \\
e(k_i) \leftrightarrow e(k_2) & , \quad e(k_f) \leftrightarrow e(k_1) & , \quad \bar{u}(p_f) \leftrightarrow \bar{u}(p_-) & , \quad u(p_i) \leftrightarrow v(p_+)
\end{array} \tag{3.24}
$$

The calculation of the square of the STPPP matrix element proceeds in the same fashion as that for the SCS process. Fourier expansions into infinite summations of Bessel functions, integrations over 4-space and 4-momentum variables x_1, x_2, q and the summation over electron spins and photon polarisations are all employed to write down the sum over initial and final states of the square of the matrix element. Alternatively the substitutions in equation 3.24 can be made in the square of the SCS matrix element. A factor of -1 is introduced due to the summation over positron bispinors.

$$
\begin{aligned}
\sum_{if} |S^e_{fi}|^2 \quad &= -\frac{e^2}{16m^2} \sum_l \delta^4(k_1 + k_2 + lk - q_- - q_+) \,\mathrm{Tr}\, Q_{\text{STPPP}} \\
\text{where} \quad \mathrm{Tr}\, Q_{\text{STPPP}} \quad &= \sum_{rr'} [\mathrm{Tr}\ Q_1(\bar{p}_r, \bar{p}_{r\prime}) + \mathrm{Tr}\ Q_1(\bar{\bar{p}}_r, \bar{\bar{p}}_{r\prime}) + \mathrm{Tr}\ Q_2(\bar{p}_r, \bar{\bar{p}}_{r\prime}) + \mathrm{Tr}\ Q_2^*(\bar{p}_r, \bar{\bar{p}}_{r\prime})] \\
\text{and} \quad Q_1(\bar{p}_r, \bar{p}_{r'}) \quad &= (\not{p}_- + m) B(\gamma^\mu, \overline{N}_r, \bar{p}, p_-) \left[\frac{\bar{\not{p}}_r + m}{\bar{p}_r^2 - m^2}\right] B(\gamma^\nu, \overline{M}_r, -p_+, \bar{p}) \\
&\times \ (-\not{p}_+ + m) \widetilde{B}(\gamma_\nu, \overline{M}_{r'}, -p_+, \bar{p}) \left[\frac{\bar{\not{p}}_{r'} + m}{\bar{p}_{r'}^2 - m^2}\right]^* \widetilde{B}(\gamma_\mu, \overline{N}_{r\prime}, \bar{p}, p_-) \\
Q_2(\bar{p}_r, \bar{\bar{p}}_{r'}) \quad &= (\not{p}_- + m) B(\gamma^\mu, \overline{N}_r, \bar{p}, p_-) \left[\frac{\bar{\not{p}}_r + m}{\bar{p}_r^2 - m^2}\right] B(\gamma^\nu, \overline{M}_r, -p_+, \bar{p}) \\
&\times \ (-\not{p}_+ + m) \widetilde{B}(\gamma_\mu, \overline{\overline{M}}_{r'}, -p_+, \bar{\bar{p}}) \left[\frac{\bar{\bar{\not{p}}}_{r'} + m}{\bar{\bar{p}}_{r'}^2 - m^2}\right]^* \widetilde{B}(\gamma_\nu, \overline{\overline{N}}_{r\prime}, \bar{\bar{p}}, p_-) \\
\bar{p}_r \quad &= -p_+ + \frac{e^2a^2}{2} \left[\frac{1}{(kp_+)} + \frac{1}{(k\bar{p})}\right] k + k_2 + rk \\
\bar{\bar{p}}_r \quad &= -p_+ + \frac{e^2a^2}{2} \left[\frac{1}{(kp_+)} + \frac{1}{(k\bar{\bar{p}})}\right] k + k_1 + rk
\end{aligned} \tag{3.25}
$$

The applicability of a crossing symmetry makes the analytic computation of the STPPP simple. The computer programs that generate numerical results for the SCS differential cross section can be used with the appropriate symbolic substitutions. The only additional analytic work required is to choose a reference frame and to transform the STPPP phase space integral.

Choosing the same gauge and coordinate axes to specify the external field 4-vectors, as for the SCS process, the STPPP process geometry is represented in figure 3.5. The bound electron 3-momentum $\underset{\sim}{q}_-$ is scattered into an element of solid angle $d\Omega_{q_-}$ characterised by angles θ_f and φ_f.

The STPPP differential cross section calculation is greatly simplified by use of the centre of mass-like reference frame which includes the contribution from the external field and is expressed by

$$
\begin{aligned}
\underset{\sim}{k}_1 + \underset{\sim}{k}_2 &= \underset{\sim}{q}_- + \underset{\sim}{q}_+ - l\underset{\sim}{k} = 0 \\
\omega_1 + \omega_2 &= \varepsilon_{q_-} + \varepsilon_{q_+} - l\omega
\end{aligned}
\tag{3.26}
$$

The electron and positron energies must each be at least the external field shifted rest mass of the fermion, m_*. With the aid of equation 3.26, a condition for the minimum number of laser photons required to create the e^+e^- pair is

$$
l \geq -\frac{\omega_1}{m}\left(\frac{\omega_1 - m_*}{\omega_1 - \frac{1}{2}m_*}\right) \tag{3.27}
$$

Other parameters in the STPPP differential cross section can be expressed in terms of photon energies ω and ω_1, the number of laser photons l, and the angle θ_f.

$$
\begin{aligned}
\omega_2 &= \omega_1 \\
\varepsilon_{q_+} &= 2\omega_1 - \varepsilon_{q_-} + l\omega \\
\varepsilon_{q_-} &= \frac{1}{2(\mathcal{A}^2 - \mathcal{C}^2)}\left(-2\mathcal{B}\mathcal{C} + \sqrt{(2\mathcal{B}\mathcal{C})^2 + 4(\mathcal{A}^2 - \mathcal{C}^2)(\mathcal{A}^2(1+\nu^2) + \mathcal{B}^2)}\right)
\end{aligned}
\tag{3.28}
$$

where
$$
\begin{aligned}
\mathcal{A} &= l\omega\cos\theta_f \\
\mathcal{B} &= 2\omega_1(\omega_1 + l\omega) \\
\mathcal{C} &= 2\omega_1 + l\omega
\end{aligned}
$$

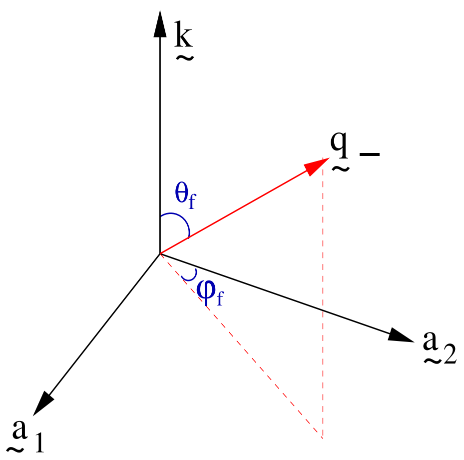

Figure 3.5: **scattering Geometry for stimulated two photon pair production**

The integrations over final particle momenta expressed by the phase space integral can be transformed in a similar fashion to those of the SCS process. The Jacobian of the transformation between free fermion momenta $d\underset{\sim}{p}_-$, $d\underset{\sim}{p}_+$ to corrected fermion momenta $d\underset{\sim}{q}_-$, $d\underset{\sim}{q}_+$ is unity (Appendix A) and the phase space integral transforms into the element of solid angle into which the created bound electron 3-momentum is directed

$$\int \frac{d^3\underset{\sim}{p}_-\, d^3\underset{\sim}{p}_+}{\epsilon_{p_-}\epsilon_{p_+}} \delta^4(P_i - q_- - q_+) = \frac{1}{2}\int d\Omega_{q_-}\, \frac{|\underset{\sim}{q}_-|}{\epsilon_{q_-}} \tag{3.29}$$

The STPPP differential cross section is written with the aid of the square of the STPPP matrix element (equation 3.25), the general differential cross section expression (equation 2.25), the results of the SCS calculation with appropriate substitutions (equation 3.24), and the phase space integral transformation just obtained. The relative velocity of the two initial photons k_1 and k_2 is $v_{ab} = \frac{1}{\omega_1\omega_2}\sqrt{(k_1k_2)^2} = 2$ in the centre of mass frame.

$$\frac{d\sigma}{d\Omega_{q_-}} = -\frac{e^4}{128(2\pi)^2}\sum_{lrr'} \frac{1}{\sqrt{(k_1k_2)^2}}\, \frac{|\underset{\sim}{q}_-|}{2\epsilon_{q_-}}\ \mathrm{Tr}\ Q_{\mathrm{STPPP}} \tag{3.30}$$

In the limit of vanishing external field intensity parameter $\nu^2 \to 0$, the STPPP differential cross section reduces to one term in which no external field photons contribute, $l = 0$. The trace expression reduces to

$$\begin{aligned} \mathrm{Tr}\ Q_{\mathrm{STPPP}} \to \quad & -\frac{16}{(1-\beta^2\cos^2\theta_f)^2}\left[1 - \beta^4\cos^4\theta_f + 2\left(\frac{m}{\omega_1}\right)^2 \beta^2\sin^2\theta_f\right] \\ & \text{where} \qquad \beta^2 = 1 - \frac{m^2}{\omega_1^2} \end{aligned} \tag{3.31}$$

In the same limit of vanishing external field intensity the STPPP differential cross section reduces to the Breit-Wheeler result for non external field two photon pair production in the centre of mass frame [BW34, JR76].

$$\begin{aligned} \frac{d\sigma}{d\Omega_{p_-}} = \quad & \frac{r_0^2}{4}\left(\frac{m}{\omega_1}\right)^2 \frac{\beta}{(1-\beta^2\cos^2\theta_f)^2}\left[1 - \beta^4\cos^4\theta_f + 2\left(\frac{m}{\omega_1}\right)^2\beta^2\sin^2\theta_f\right] \\ & \text{where} \qquad r_0 = \frac{e^2}{4\pi m} \end{aligned} \tag{3.32}$$

Chapter 4

SCS in a circularly polarised electromagnetic field - Results and Analysis

4.1 Introduction

In this chapter we present numerical calculations of the SCS differential cross section analytic expressions obtained in Chapter 3. The numerical results are contained in Section 4.2 and an analysis of these results is contained in Section 4.3. The SCS differential cross section as expressed in equation 3.8 is a triple infinite summation over integer variables l, r and r'. On occasion many of these summation terms contribute significantly to the SCS differential cross section, producing potentially complex behaviour. The task of analysing numerical results is made simpler by dividing figures into two groups.

The first group, contained in Section 4.2.1, represents the summation terms of the SCS differential cross section separately (or summed in part). The analysis for this group of results is contained in Section 4.3.1. The terminology "l contribution" simply means the l summation term in SCS differential cross section. "Longitudinal" and "transverse" are also terms often used in the discussion. When not qualified these refer respectively to directions parallel and perpendicular to the direction of propagation of the external field. The second group of results, presented in Section 4.2.2 (with a corresponding analysis in Section 4.3.2) are those of the complete SCS differential cross section in which all summations have been performed.

The general structure of the analysis will be to introduce a set of figures with common parameter sets, describe the main features and to provide an explanation of how the features arise. The explanation is physical (as opposed to purely mathematical) as often as possible and analogies are sometimes drawn. Sometimes the behaviour of plots is complicated and an appeal to the analytic structure of equations is made. Generally speaking, the variation of the SCS differential cross section with azimuthal angle φ_f is much simpler than the variation with other parameters. Consequently only a couple of figures are devoted to φ_f variation. Elsewhere φ_f is set to zero.

4.2 SCS Plots

4.2.1 Differential Cross section l Contributions

Table 4.1 displays the parameter values of the SCS process investigated in this section. The parameters ω and ω_i are, respectively, the particle energies of the external field and of the initial photon. The initial photon enters the scattering region at an angle of θ_i to the direction of the propagation of the external field, and exits in a direction specified by angles θ_f and φ_f (see figure 3.2). The external field intensity is represented by the parameter $\nu^2 = \frac{e^2 a^2}{m^2}$, which is dimensionless in natural units. The vertical axes of all figures in Sections 4.2.1 and 4.2.2 show the SCS differential cross section divided by a function of the fine structure constant α and electron mass m, and the units are Steradian^{-1}. All angles represented on horizontal axes use units of degrees.

l	r	ν^2	ω(keV)	ω_i(keV)	θ_i	(θ_f, ϕ)	figure(s)
$0 \to 20$	all	$0.1, 0.5, 1.0$	0.001	0.001	$10°$	$(45°, 0°)$	4.1
$0 \to 20$	all	$0.1, 0.5, 1.0$	0.512	0.1	$80°$	$(45°, 0°)$	4.2
$-7 \to 23$	all	$0.1, 0.5, 1.0$	0.512	7.68	$10°$	$(45°, 0°)$	4.3
$-4 \to 12$	all	$0.1, 0.5, 1.0$	0.512	2.047	$30°$	$(45°, 0°)$	4.4
0	0	$0, 0.1, 0.2$ $0.3, 0.4, 0.5$	0.512	$0.409, 0.768$	$0°$	$(0° \to 360°, 0°)$	4.5,4.6
0	0, all	0.1	0.512	$0.409, 0.768$	$0°$	$(0° \to 360°, 0°)$	4.7,4.8
$0, 1$	all	0.1	0.512	25.6	$0°$	$(0° \to 360°, 0°)$	4.9
$0, 1, 2$	all	0.5	0.512	0.768	$0°$	$(0° \to 360°, 0°)$	4.10
$0, 1, 2$	all	0.5	0.512	0.409	$0°$	$(0° \to 360°, 0°)$	4.11
$0, 1, 2$	all	0.2	51.2	5.12	$0°$	$(0° \to 360°, 0°)$	4.12
$0, 1$	all	$0, 0.1, 0.2,$ $0.3, 0.4, 0.5$	0.512	$0.409, 0.768$	$45°$	$(0° \to 360°, 0°)$	$4.13, 4.14$ $4.15, 4.16$
$0, 1, 2$	all	$0.1, 0.5$	0.512	0.768	$45°$	$(0° \to 360°, 0°)$	4.17,4.18
$0, 1, 2$	all	$0.1, 0.5$	0.512	$0.05, 5.12$	$45°$	$(0° \to 360°, 0°)$	4.19,4.20

Table 4.1: **The parameter range for which the SCS differential cross section l and r contributions are investigated.**

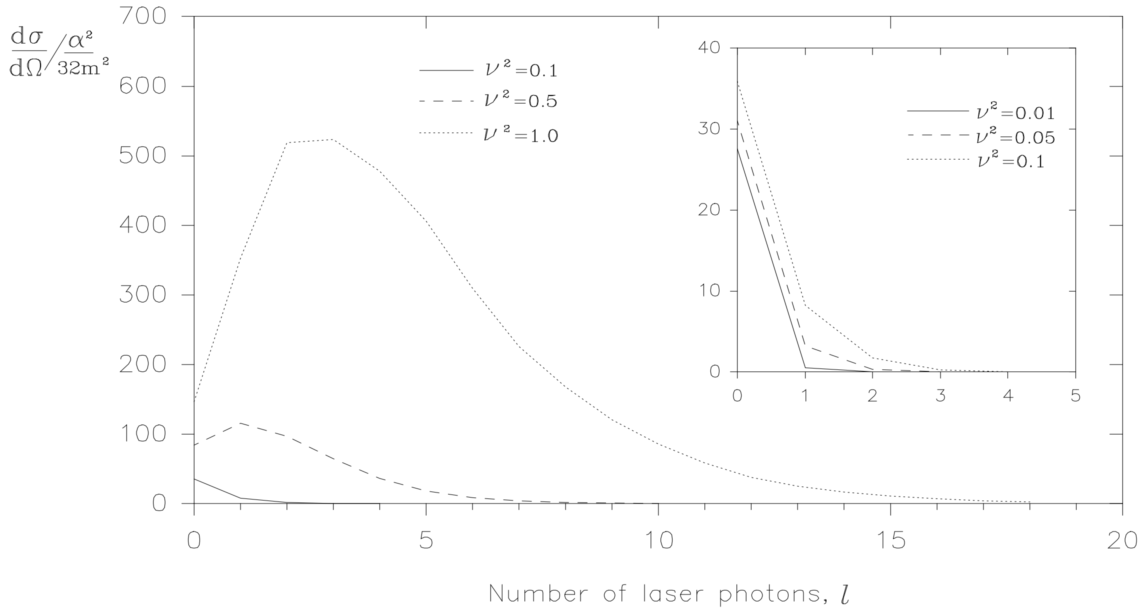

Figure 4.1: **The SCS differential cross section vs l external field photons for $\omega = 0.001$ keV, $\omega_i = 0.001$ keV, $\theta_i = 10°$, $\theta_f = 45°$, $\varphi_f = 0°$ and various ν^2.**

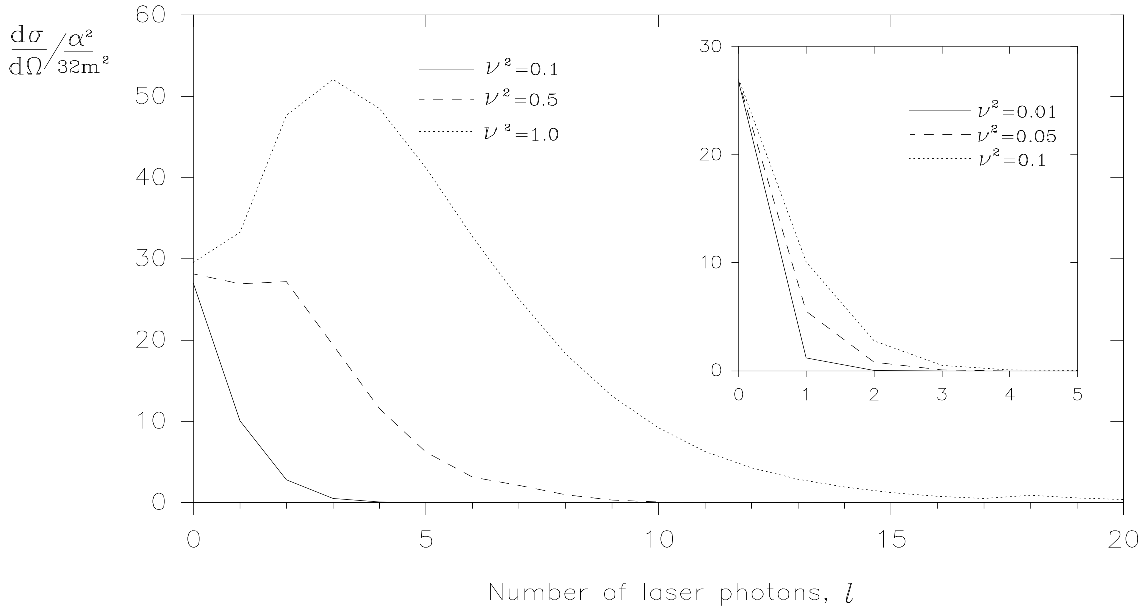

Figure 4.2: **The SCS differential cross section vs l external field photons for $\omega = 0.512$ keV, $\omega_i = 0.1$ keV, $\theta_i = 80°$, $\theta_f = 45°$, $\varphi_f = 0°$ and various ν^2.**

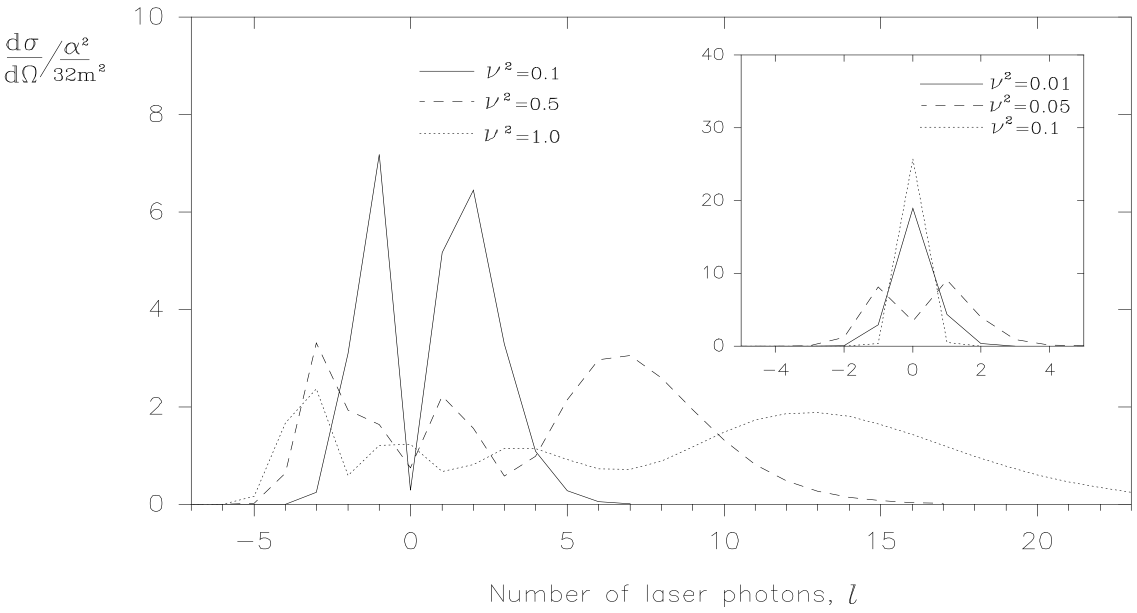

Figure 4.3: **The SCS differential cross section vs l external field photons for $\omega = 0.512$ keV, $\omega_i = 7.68$ keV, $\theta_i = 10°$, $\theta_f = 45°$, $\varphi_f = 0°$ and various ν^2.**

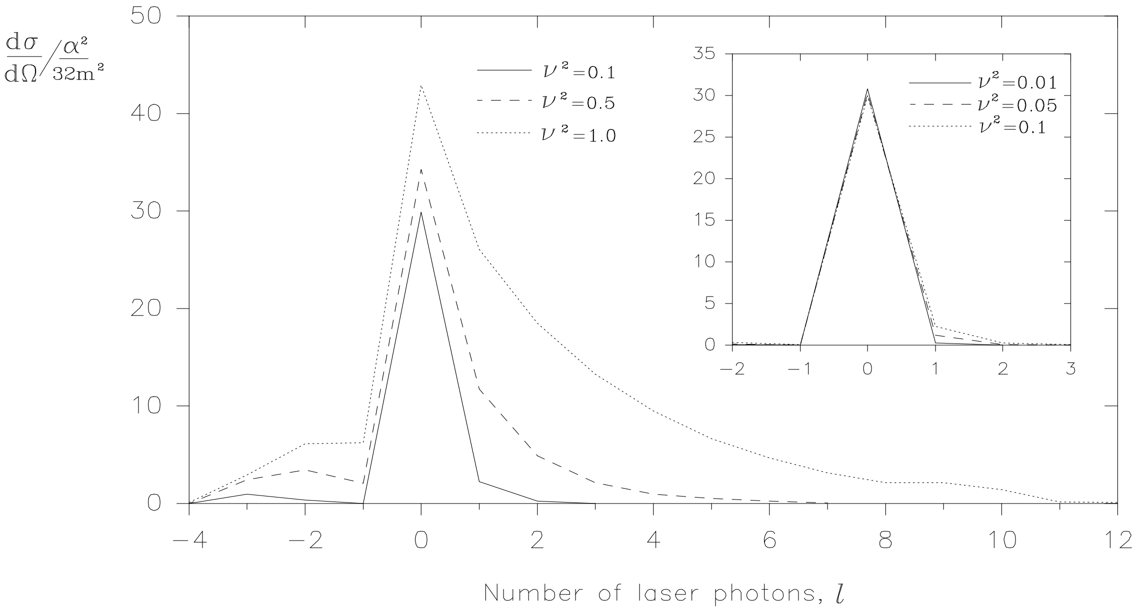

Figure 4.4: **The SCS differential cross section vs l external field photons for $\omega = 0.512$ keV, $\omega_i = 2.047$ keV, $\theta_i = 30°$, $\theta_f = 45°$, $\varphi_f = 0°$ and various ν^2.**

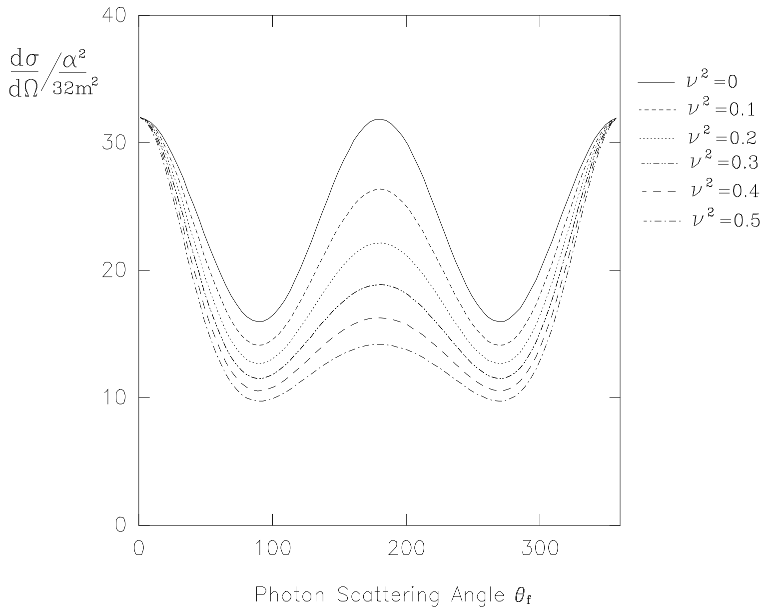

Figure 4.5: **The SCS $l = 0, r = 0$ differential cross section vs θ_f for $\omega = 0.512$ keV, $\omega_i = 0.409$ keV, $\theta_i = 0°$, $\varphi_f = 0°$ and various ν^2.**

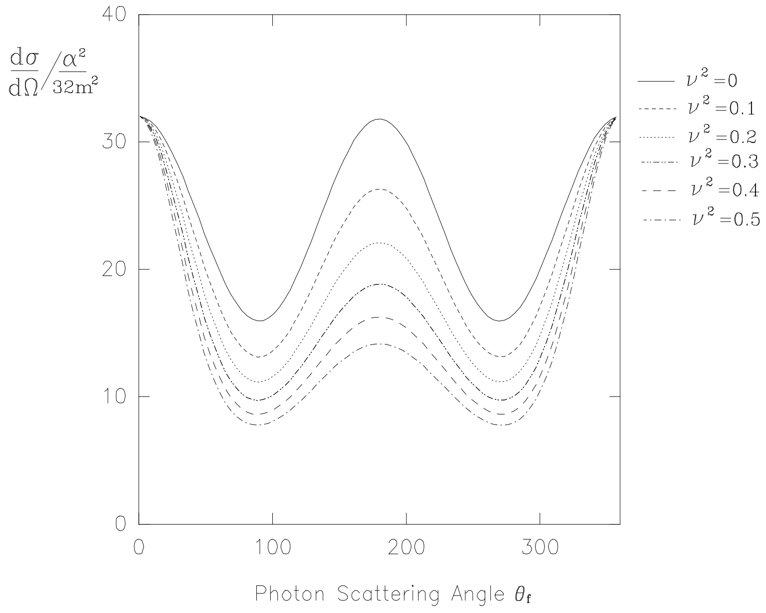

Figure 4.6: **The SCS $l = 0, r = 0$ differential cross section vs θ_f for $\omega = 0.512$ keV, $\omega_i = 0.768$ keV, $\theta_i = 0°$, $\varphi_f = 0°$ and various ν^2.**

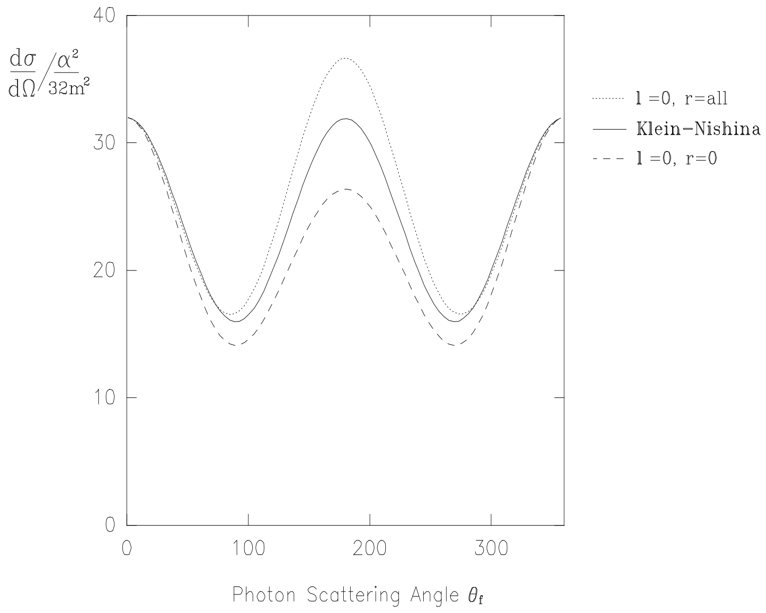

Figure 4.7: **Comparison of The STPPP $l = 0, r = 0$, $l = 0, r =$ all and Klein-Nishina differential cross section vs θ_f for $\omega = 0.512$ keV, $\omega_i = 0.409$ keV, $\theta_i = 0°$, $\varphi_f = 0°$ and $\nu^2 = 0.1$.**

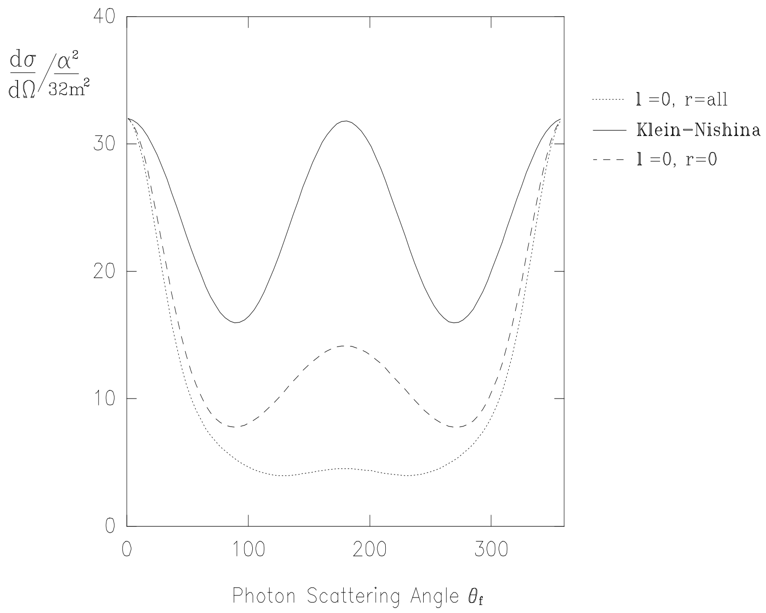

Figure 4.8: **Comparison of The STPPP $l = 0, r = 0$, $l = 0, r =$ all and Klein-Nishina differential cross section vs θ_f for $\omega = 0.512$ keV, $\omega_i = 0.768$ keV, $\theta_i = 0°$, $\varphi_f = 0°$ and $\nu^2 = 0.1$.**

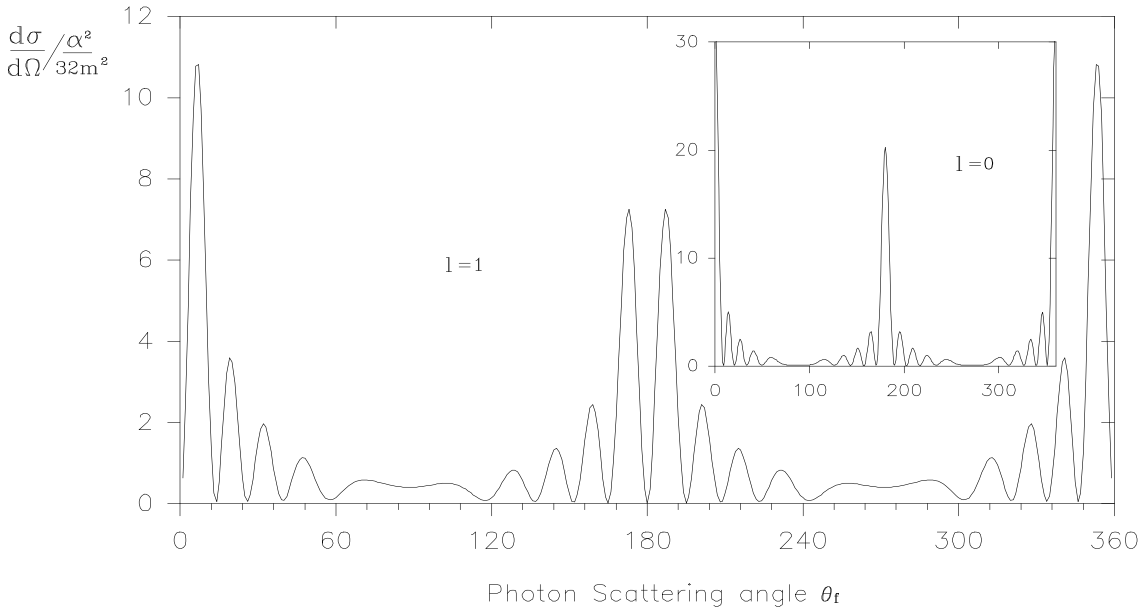

Figure 4.9: **The SCS differential cross section vs θ_f for $\omega = 0.512$ keV, $\omega_i = 2.559$ keV, $\theta_i = 0°$, $\varphi_f = 0°$, $\nu^2 = 0.1$ and various l.**

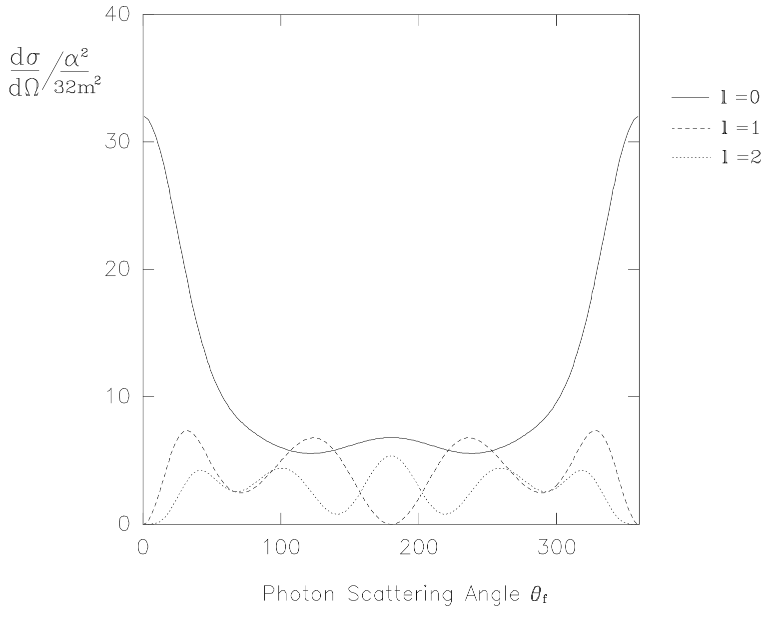

Figure 4.10: **The SCS differential cross section vs θ_f for $\omega = 0.512$ keV, $\omega_i = 0.768$ keV, $\theta_i = 0°$, $\varphi_f = 0°$, $\nu^2 = 0.5$ and various l.**

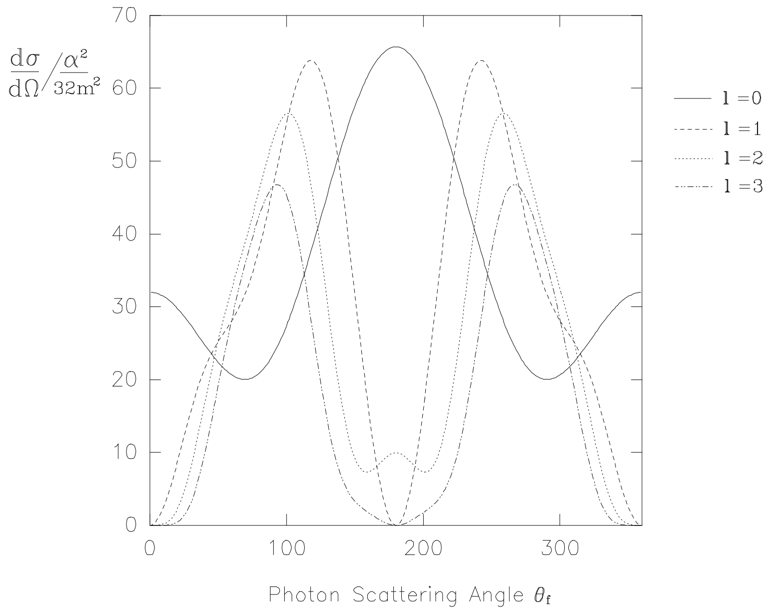

Figure 4.11: **The SCS differential cross section vs θ_f for $\omega = 0.512$ keV, $\omega_i = 0.409$ keV, $\theta_i = 0°$, $\varphi_f = 0°$, $\nu^2 = 0.5$ and various l.**

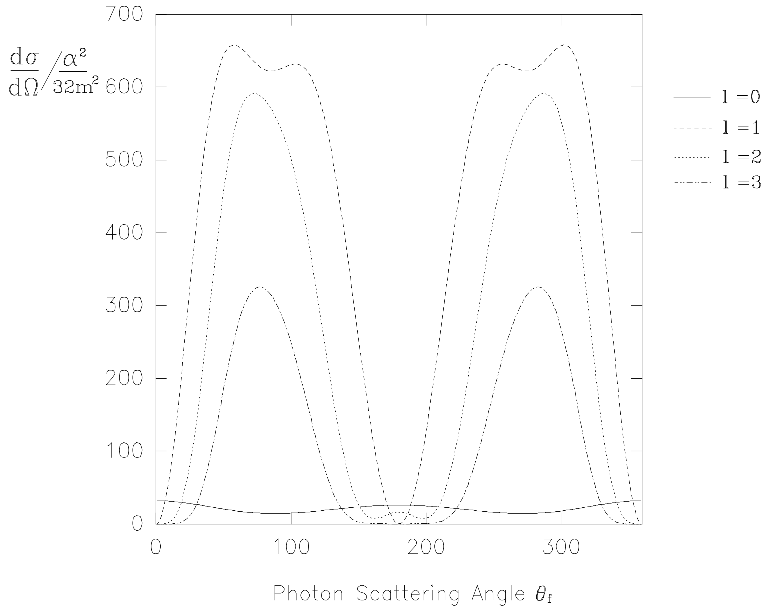

Figure 4.12: **The SCS differential cross section vs θ_f for $\omega = 51.2$ keV, $\omega_i = 5.12$ keV, $\theta_i = 0°$, $\varphi_f = 0°$, $\nu^2 = 0.2$ and various l.**

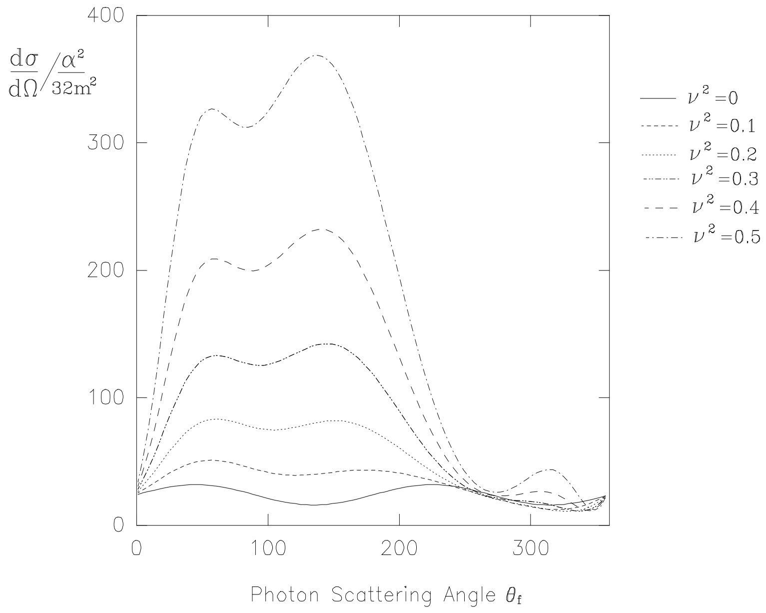

Figure 4.13: **The SCS $l = 0$ differential cross section vs θ_f for $\omega = 0.512$ keV, $\omega_i = 0.409$ keV, $\theta_i = 45°$, $\varphi_f = 0°$ and various ν^2.**

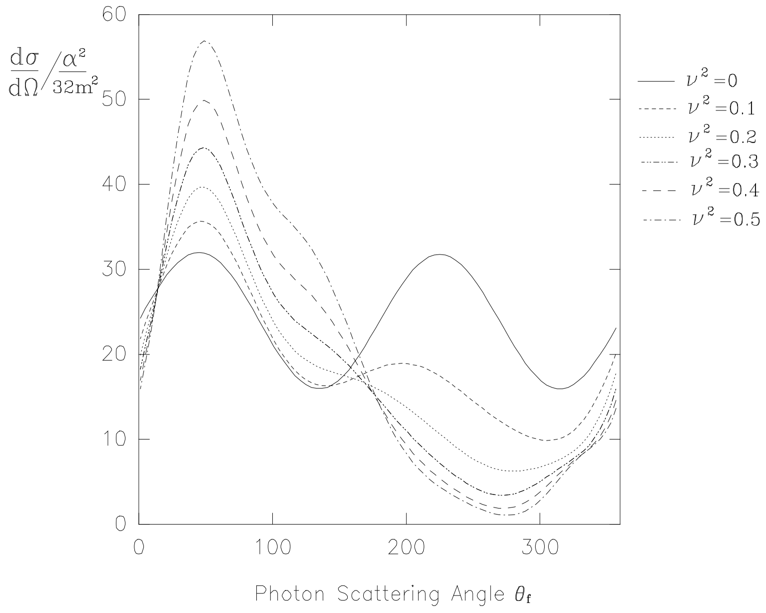

Figure 4.14: **The SCS $l = 0$ differential cross section vs θ_f for $\omega = 0.512$ keV, $\omega_i = 0.768$ keV, $\theta_i = 45°$, $\varphi_f = 0°$ and various ν^2.**

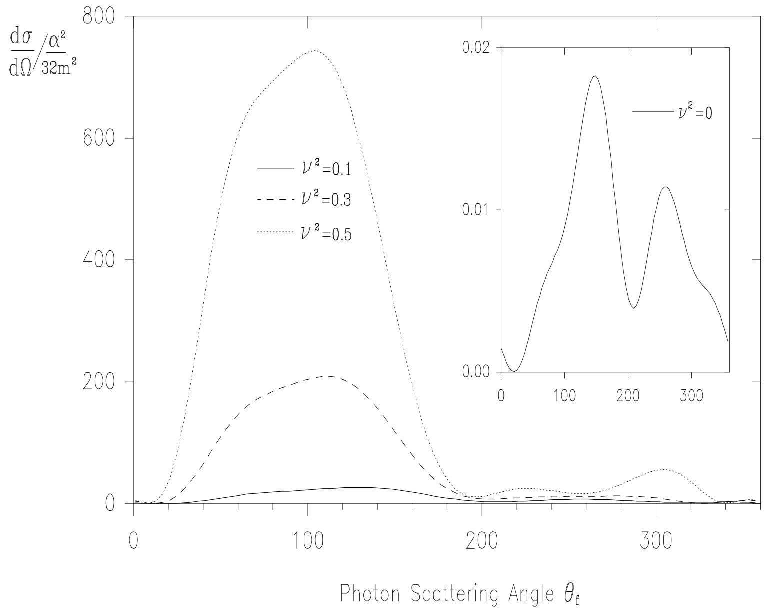

Figure 4.15: **The SCS $l = 1$ differential cross section vs θ_f for $\omega = 0.512$ keV, $\omega_i = 0.409$ keV, $\theta_i = 45°$, $\varphi_f = 0°$ and various ν^2.**

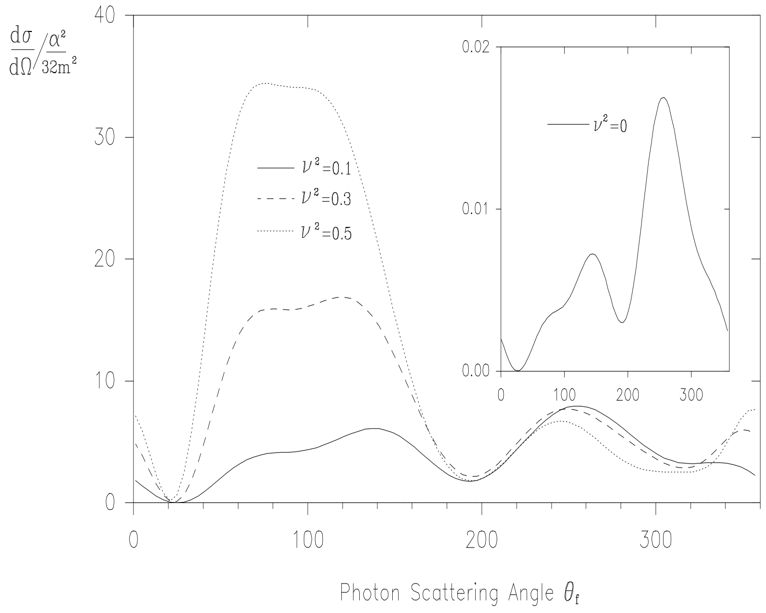

Figure 4.16: **The SCS $l = 0$ differential cross section vs θ_f for $\omega = 0.512$ keV, $\omega_i = 0.768$ keV, $\theta_i = 45°$, $\varphi_f = 0°$ and various ν^2.**

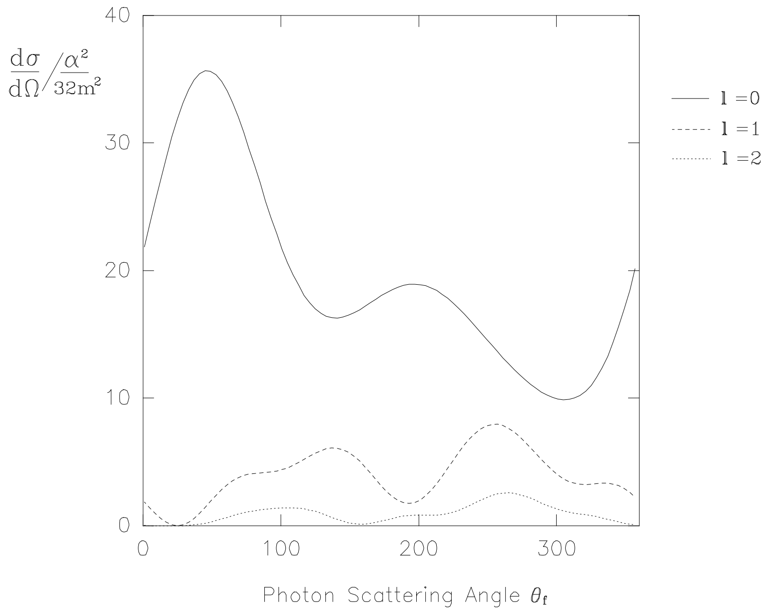

Figure 4.17: **The SCS differential cross section vs** θ_f **for** $\omega = 0.512$ **keV,** $\omega_i = 0.768$ **keV,** $\theta_i = 45°$**,** $\varphi_f = 0°$**,** $\nu^2 = 0.1$ **and various** l**.**

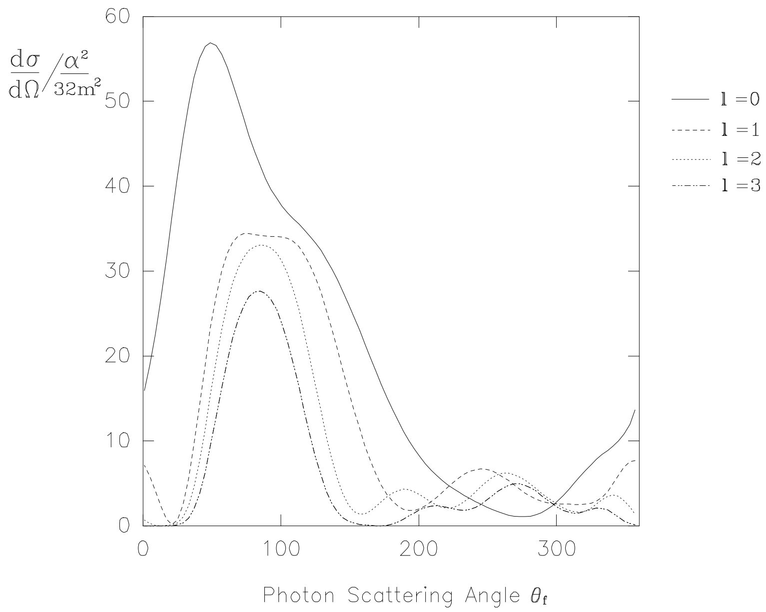

Figure 4.18: **The SCS differential cross section vs** θ_f **for** $\omega = 0.512$ **keV,** $\omega_i = 0.768$ **keV,** $\theta_i = 45°$**,** $\varphi_f = 0°$**,** $\nu^2 = 0.5$ **and various** l**.**

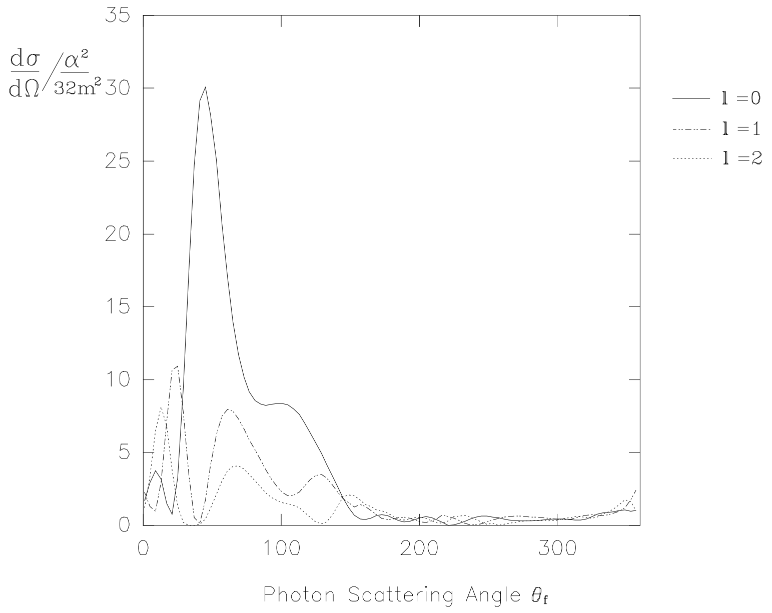

Figure 4.19: **The SCS differential cross section vs θ_f for $\omega = 0.512$ keV, $\omega_i = 5.12$ keV, $\theta_i = 45°$, $\varphi_f = 0°$, $\nu^2 = 0.5$ and various l.**

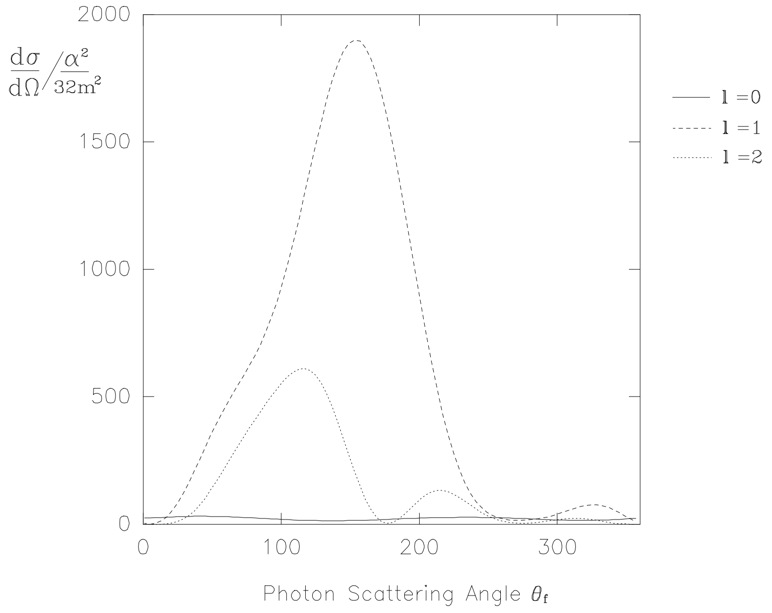

Figure 4.20: **The SCS differential cross section vs θ_f for $\omega = 0.512$ keV, $\omega_i = 0.051$ keV, $\theta_i = 45°$, $\varphi_f = 0°$, $\nu^2 = 0.1$ and various l.**

4.2.2 Differential Cross sections summed over all l

Table 4.2 displays the parameter values of the SCS scattering process investigated in this section. The parameters here have exactly the same meaning as in Section 4.2.1. The integer parameter values l and r are not present in this section due to the summations over these parameters having been performed numerically.

ν^2	$\omega(keV)$	$\omega_i(keV)$	θ_i	(θ_f, ϕ)	figure(s)
$0.1, 0.5, 1.0$	0.005	0.026	$0°, 15°, 30°$	$(0° \to 360°, 0°)$	4.21,4.22,4.23
$0.1, 0.5, 1.0$	0.512	0.409	$0°, 60°, 90°$	$(0° \to 360°, 0°)$	4.24,4.25,4.26
$0, 0.1, 0.2,$ $0.3, 0.4, 0.5$	51.2	10.2	$0°, 45°,$ $90°, 180°$	$(0° \to 360°, 0°)$	$4.27, 4.28,$ $4.29, 4.30$
$0, 0.1, 0.2,$ $0.3, 0.4, 0.5$	0.512	0.768	$0°, 45°,$ $90°, 180°$	$(0° \to 360°, 0°)$	$4.31, 4.32,$ $4.33, 4.34$
$0.1, 0.5, 1.0$	0.512	0.768	$45°$	$(45°, 0° \to 360°)$	4.35
$0.1, 0.3, 0.4$	0.512	0.768	$90°$	$(45°, 0° \to 360°)$	4.36
$0.1, 0.5$	0.512	$2.56, 0.768,$ $0.409, 0.205$	$0°, 45°$	$(0° \to 360°, 0°)$	$4.37, 4.38,$ $4.39, 4.40$
$0 \to 2$	51.2	0.409	$0°, 5°, 10°, 15°$	$(45°, 0°)$	4.41
$0 \to 2$	0.512	0.768	$0°, 15°, 30°, 45°$	$(45°, 0°)$	4.42

Table 4.2: **The parameter range for which the SCS differential cross section summed over all l is investigated.**

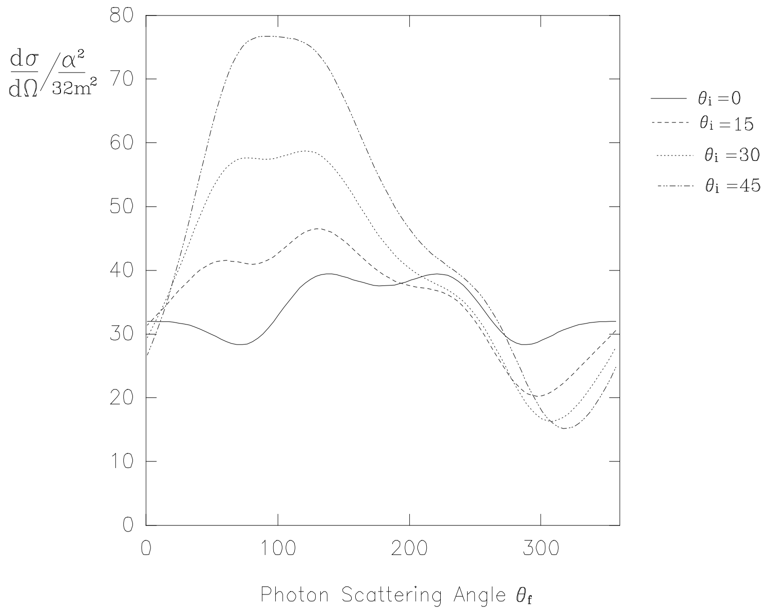

Figure 4.21: **The SCS differential cross section vs θ_f for $\omega = 0.512$ keV, $\omega_i = 0.409$ keV, $\varphi_f = 0°$, $\nu^2 = 0.1$ and various θ_i.**

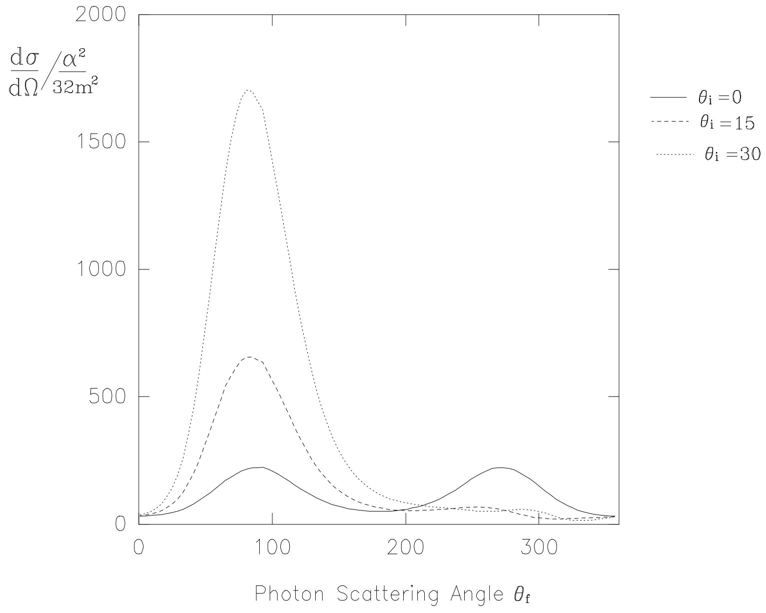

Figure 4.22: **The SCS differential cross section vs θ_f for $\omega = 0.512$ keV, $\omega_i = 0.409$ keV, $\varphi_f = 0°$, $\nu^2 = 0.5$ and various θ_i.**

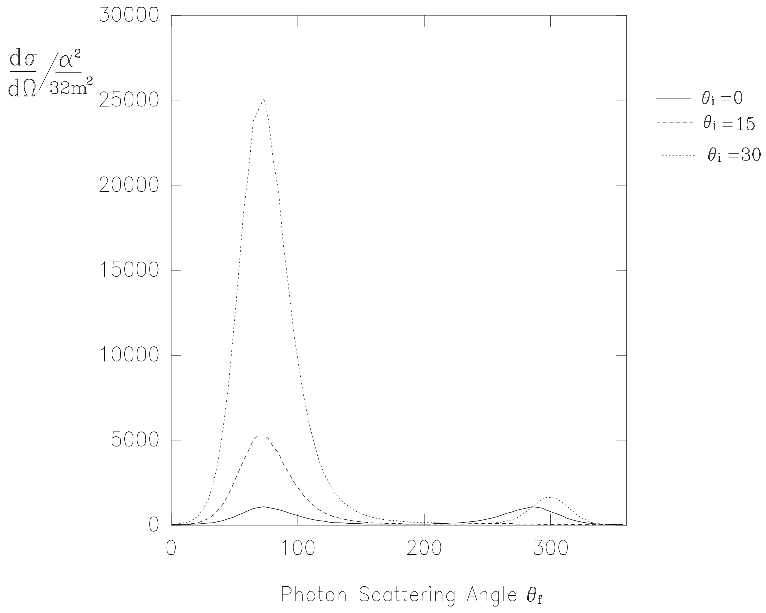

Figure 4.23: **The SCS differential cross section vs θ_f for $\omega = 0.512$ keV, $\omega_i = 0.409$ keV, $\varphi_f = 0°$, $\nu^2 = 1$ and various θ_i.**

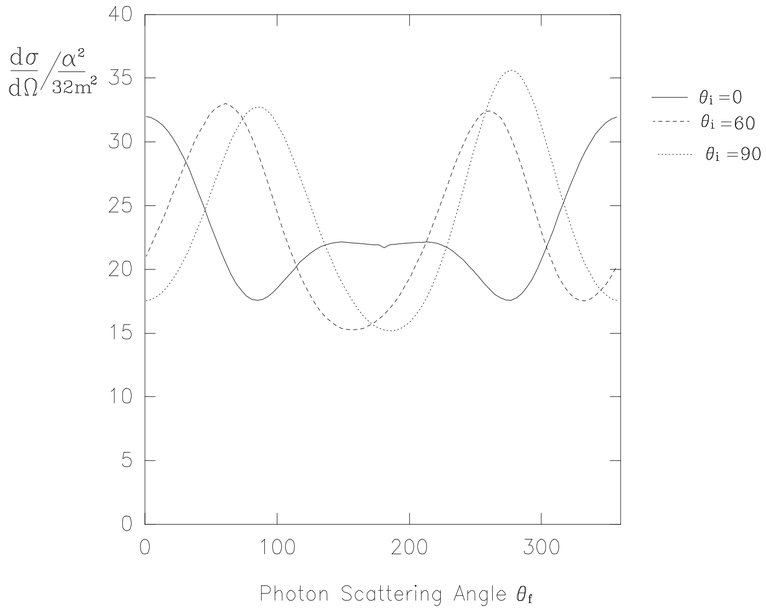

Figure 4.24: **The SCS differential cross section vs θ_f for $\omega = 0.005$ keV, $\omega_i = 0.026$ keV, $\varphi_f = 0°$, $\nu^2 = 0.1$ and various θ_i.**

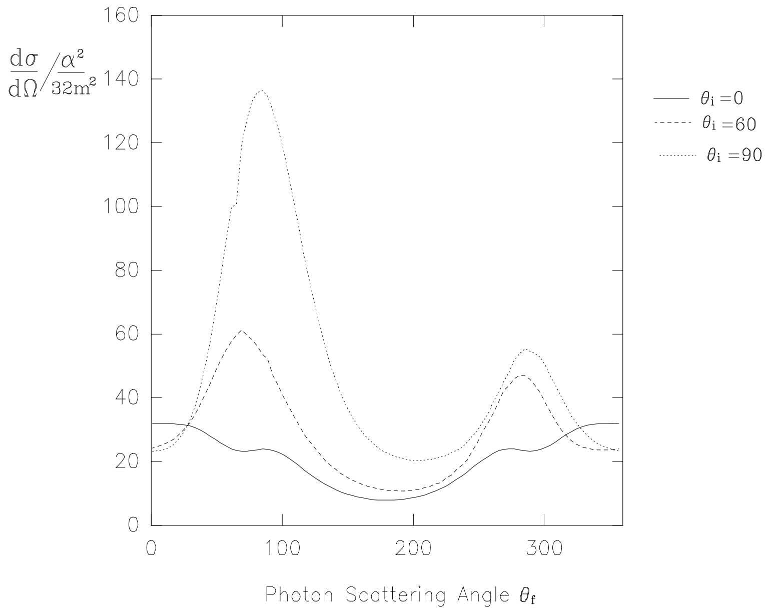

Figure 4.25: **The SCS differential cross section vs θ_f for $\omega = 0.005$ keV, $\omega_i = 0.026$ keV, $\varphi_f = 0°$, $\nu^2 = 0.5$ and various θ_i.**

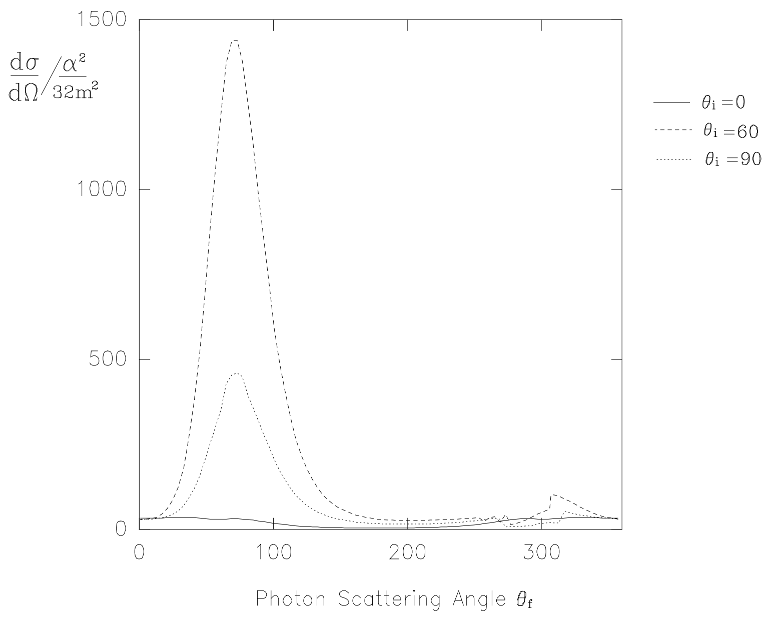

Figure 4.26: **The SCS differential cross section vs θ_f for $\omega = 0.005$ keV, $\omega_i = 0.026$ keV, $\varphi_f = 0°$, $\nu^2 = 1$ and various θ_i.**

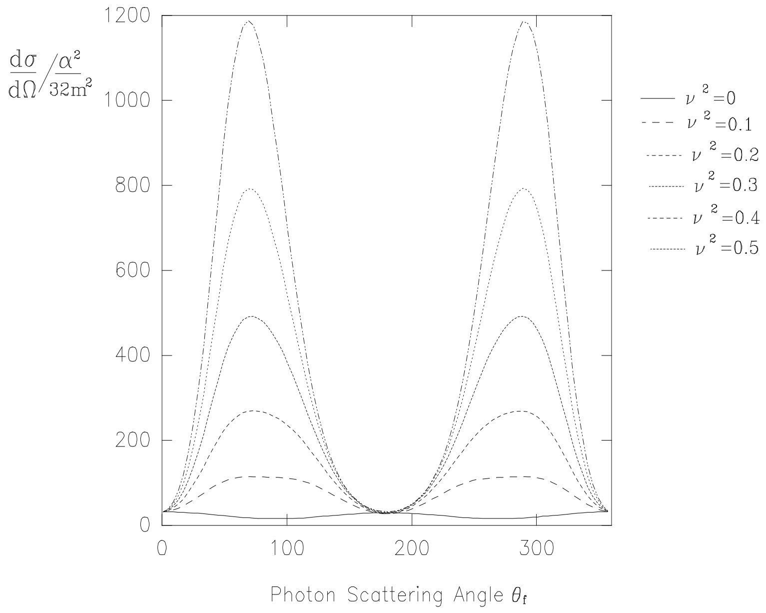

Figure 4.27: **The SCS differential cross section vs θ_f for $\omega = 51.2$ keV, $\omega_i = 10.2$ keV, $\theta_i = 0°$, $\varphi_f = 0°$, and various ν^2.**

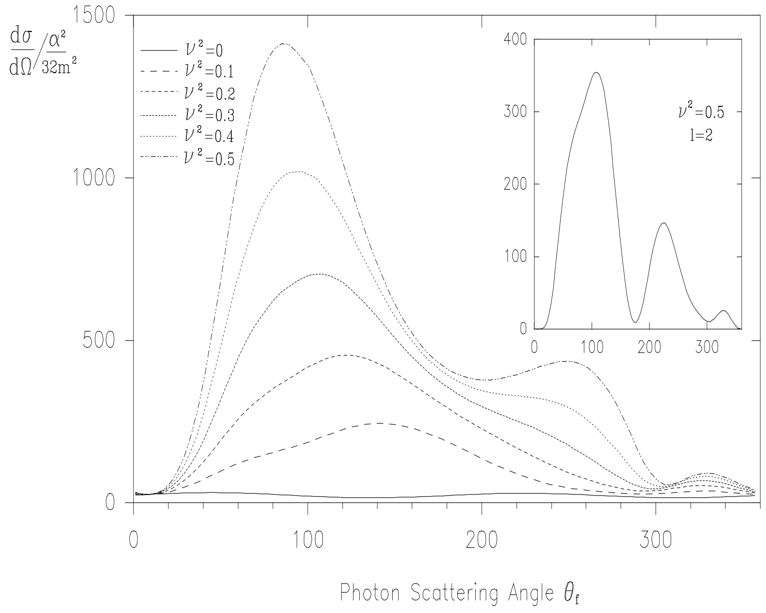

Figure 4.28: **The SCS differential cross section vs θ_f for $\omega = 51.2$ keV, $\omega_i = 10.2$ keV, $\theta_i = 45°$, $\varphi_f = 0°$, and various ν^2.**

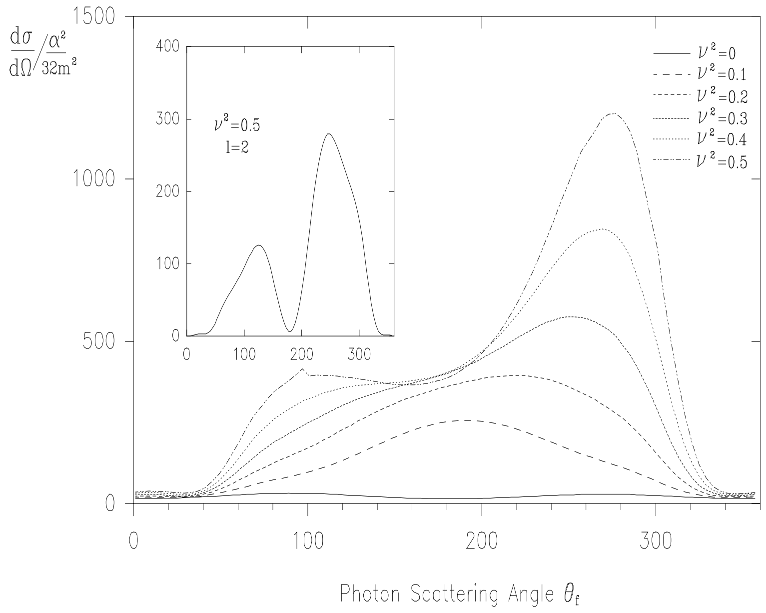

Figure 4.29: **The SCS differential cross section vs θ_f for $\omega = 51.2$ keV, $\omega_i = 10.2$ keV, $\theta_i = 90°$, $\varphi_f = 0°$, and various ν^2.**

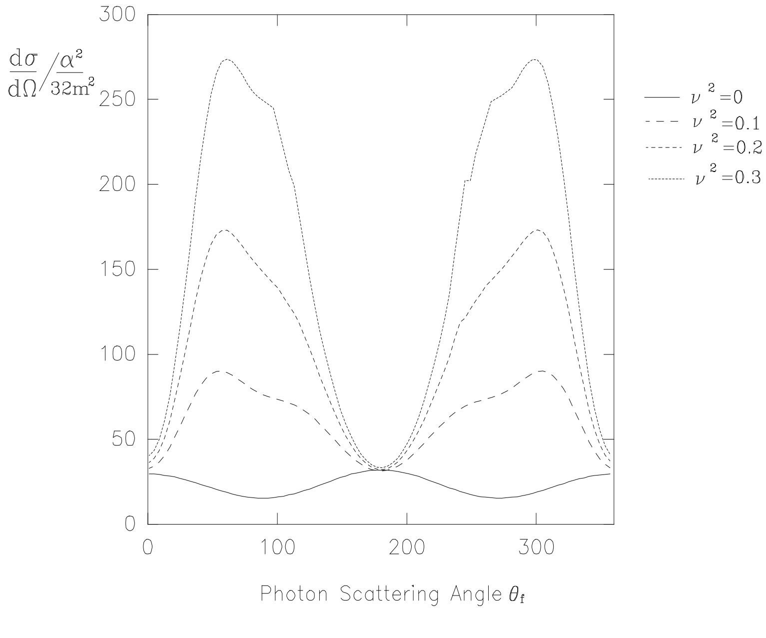

Figure 4.30: **The SCS differential cross section vs θ_f for $\omega = 51.2$ keV, $\omega_i = 10.2$ keV, $\theta_i = 180°$, $\varphi_f = 0°$, and various ν^2.**

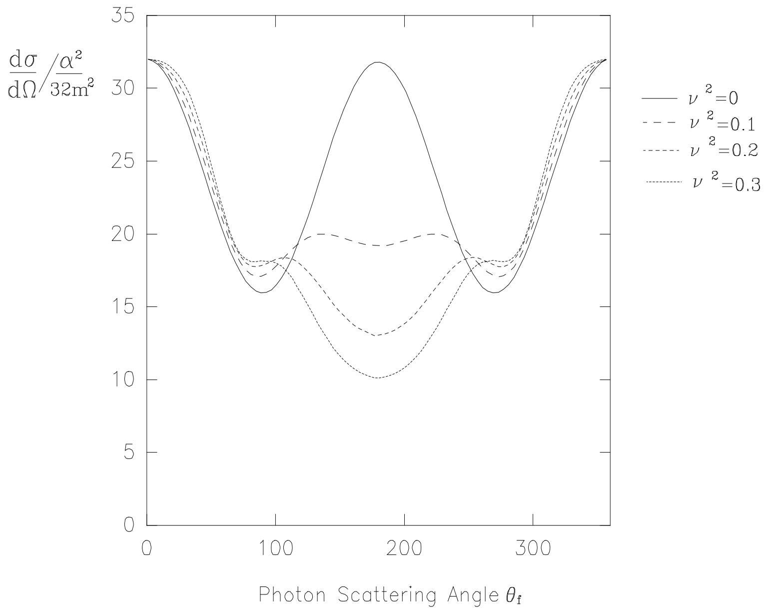

Figure 4.31: **The SCS differential cross section vs θ_f for $\omega = 0.512$ keV, $\omega_i = 0.768$ keV, $\theta_i = 0°$, $\varphi_f = 0°$, and various ν^2.**

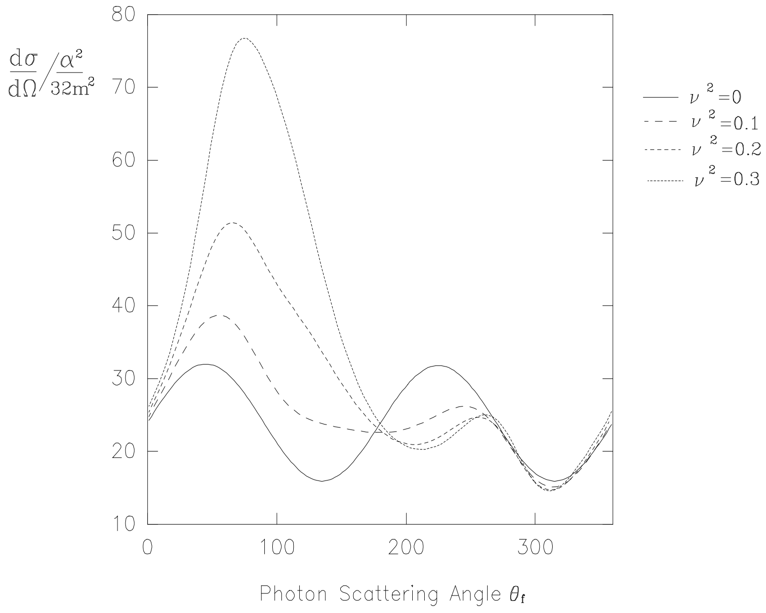

Figure 4.32: **The SCS differential cross section vs θ_f for $\omega = 0.512$ keV, $\omega_i = 0.768$ keV, $\theta_i = 45°$, $\varphi_f = 0°$, and various ν^2.**

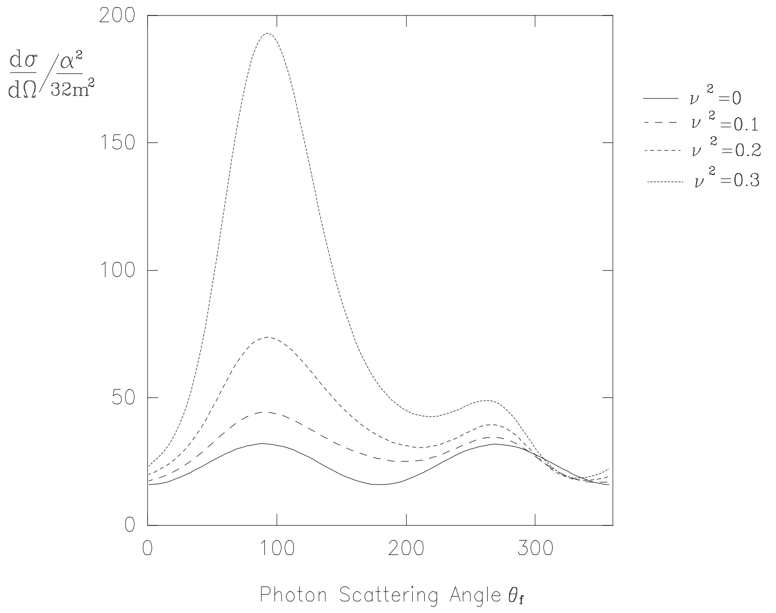

Figure 4.33: **The SCS differential cross section vs θ_f for $\omega = 0.512$ keV, $\omega_i = 0.768$ keV, $\theta_i = 90°$, $\varphi_f = 0°$, and various ν^2.**

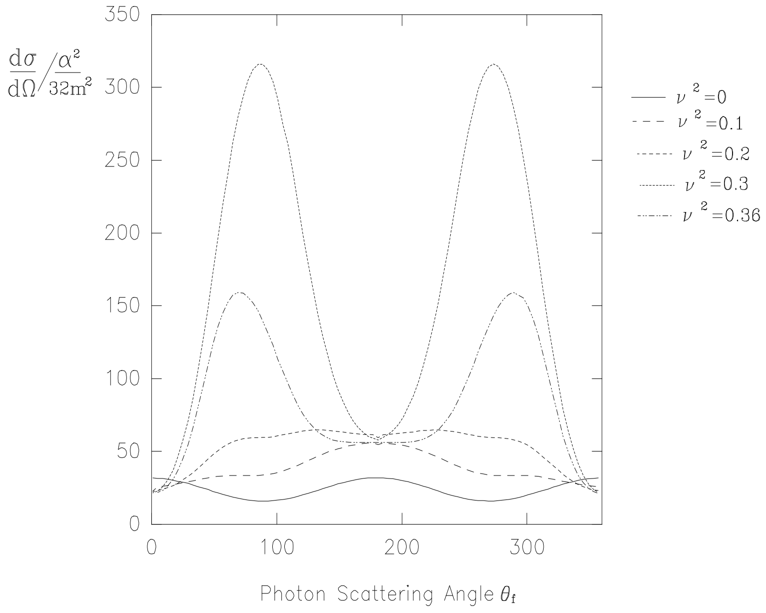

Figure 4.34: **The SCS differential cross section vs θ_f for $\omega = 0.512$ keV, $\omega_i = 0.768$ keV, $\theta_i = 180°$, $\varphi_f = 0°$, and various ν^2.**

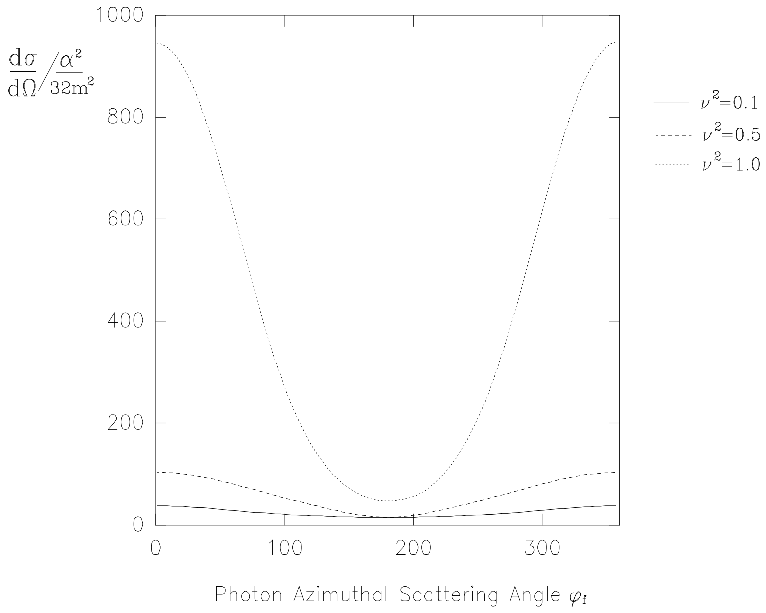

Figure 4.35: **The SCS differential cross section vs φ_f for $\omega = 0.512$ keV, $\omega_i = 0.768$ keV, $\theta_i = 45°$, $\theta_f = 45°$, and various ν^2.**

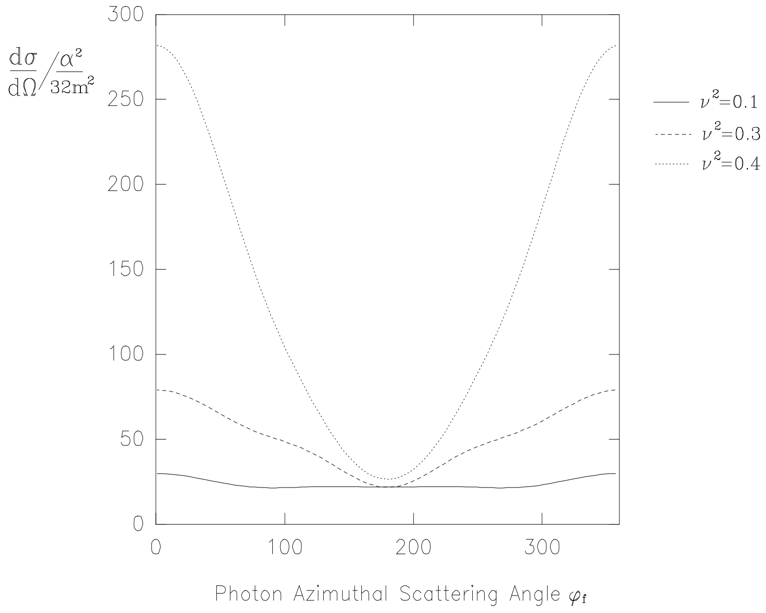

Figure 4.36: **The SCS differential cross section vs φ_f for $\omega = 0.512$ keV, $\omega_i = 0.768$ keV, $\theta_i = 90°$, $\theta_f = 45°$, and various ν^2.**

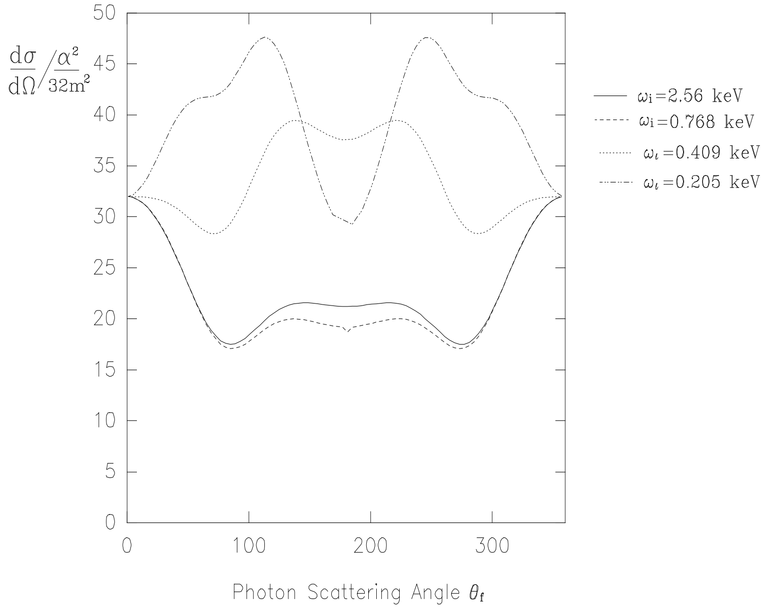

Figure 4.37: **The SCS differential cross section vs θ_f for $\omega = 0.512$ keV, $\theta_i = 0°$, $\varphi_f = 0°$, $\nu^2 = 0.1$ and various ω_i.**

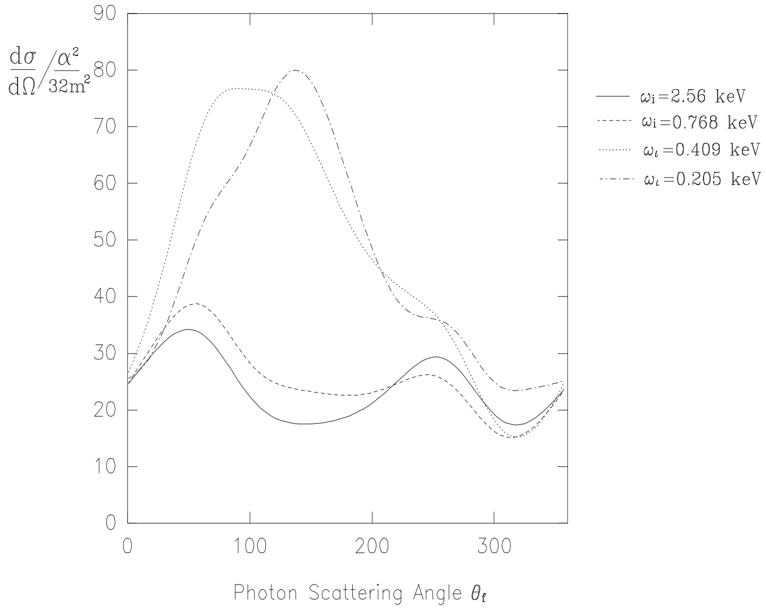

Figure 4.38: **The SCS differential cross section vs θ_f for $\omega = 0.512$ keV, $\theta_i = 45°$, $\varphi_f = 0°$, $\nu^2 = 0.1$ and various ω_i.**

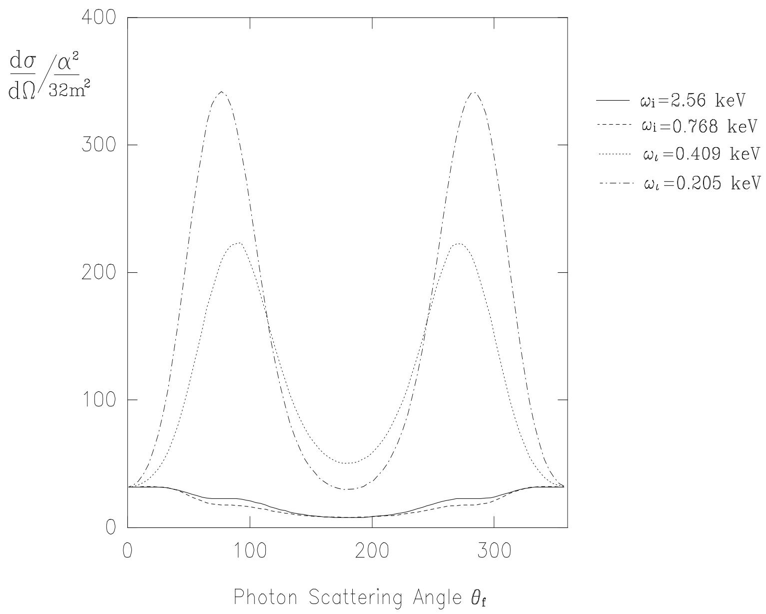

Figure 4.39: **The SCS differential cross section vs θ_f for $\omega = 0.512$ keV, $\theta_i = 0°$, $\varphi_f = 0°$, $\nu^2 = 0.5$ and various ω_i.**

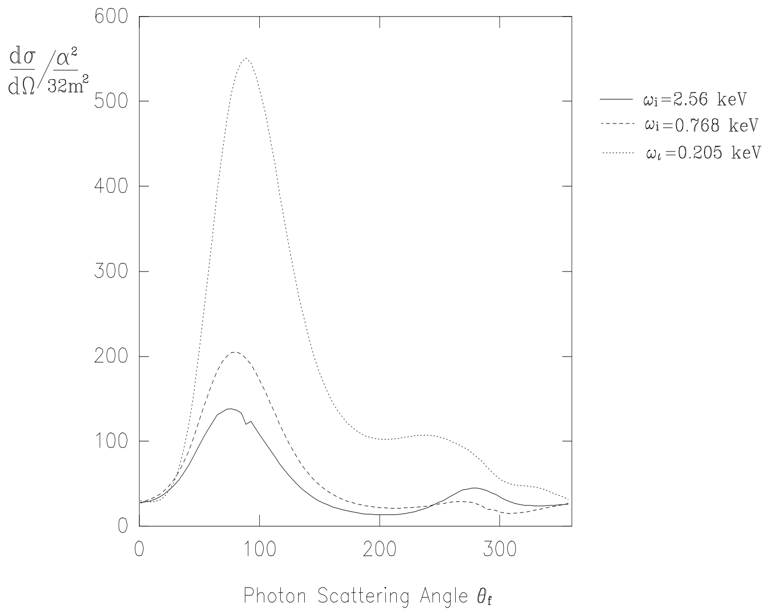

Figure 4.40: **The SCS differential cross section vs θ_f for $\omega = 0.512$ keV, $\theta_i = 45°$, $\varphi_f = 0°$, $\nu^2 = 0.5$ and various ω_i.**

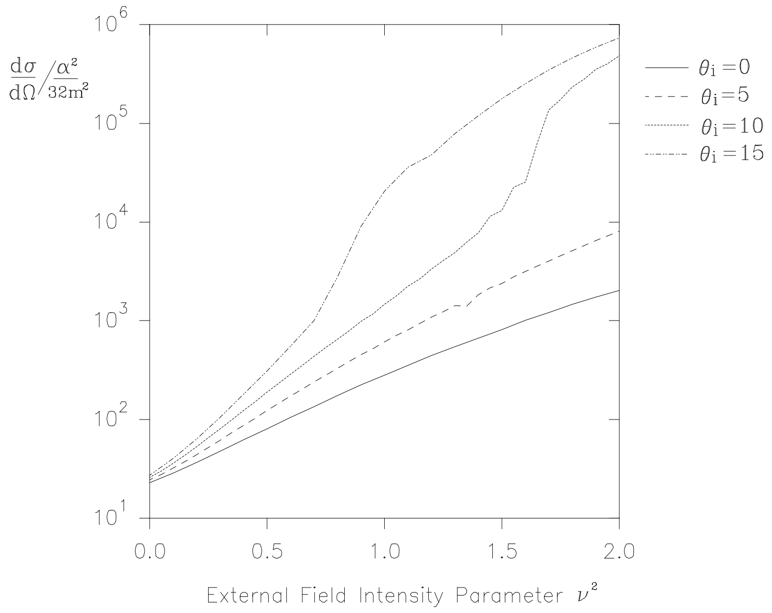

Figure 4.41: **The SCS differential cross section vs ν^2 for $\omega = 51.2$ keV, $\omega_i = 40.9$ keV, $\theta_f = 45°$, $\varphi_f = 0°$ and various θ_i.**

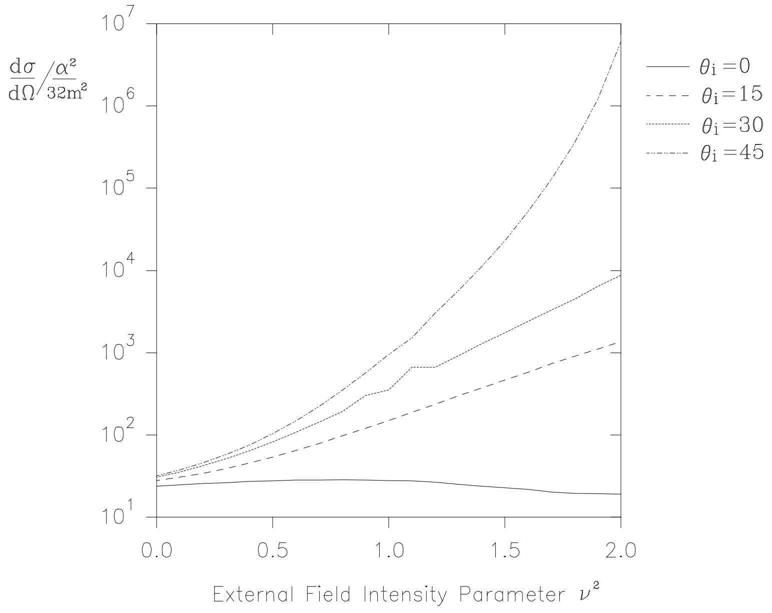

Figure 4.42: **The SCS differential cross section vs ν^2 for $\omega = 0.512$ keV, $\omega_i = 0.768$ keV, $\theta_f = 45°$, $\varphi_f = 0°$ and various θ_i.**

4.3 SCS Analysis

4.3.1 Differential Cross Section l Contributions

Figures 4.1 - 4.4 show the relative contributions of the SCS differential cross section according to the number, l of external field quanta that take part in the scattering process. The differential cross section contributions are calculated for various particle energies, scattering angles and external field intensities ν^2. The insets of figures 4.1 - 4.4 represent the same variation of parameters as their parent plots, except that the parameter ν^2 approaches zero.

We note first of all that the graphs are not "smooth". This is so because of the discrete nature of the horizontal data points and the relatively rapid convergence of the SCS differential cross section with respect to the infinite summation over l for the parameter values considered ($\frac{d\sigma}{d\Omega} \to 0 \quad \text{for} \quad l \leq 25$). Figures 4.1 and 4.2 concern particle parameters for which the initial photon is less energetic than laser photons ($\omega_i < \omega$). The initial state of the scattering process consisting of an electron at rest and the initial photon k_i, does not contain enough energy to allow the emission of a quantum of energy, ω , to the external field. Consequently the only l contributions that are possible are those in which the external field gives up quanta to the initial state of the electron, hence $l \geq 0$. Figures 4.3 and 4.4 on the other hand, concern particle parameters for which the initial photon energy exceeds that of the laser photons ($\omega_i > \omega$). Here the SCS initial state can give up energy to the laser field and differential cross section contributions with $l < 0$ are energetically permitted.

A general feature of all four figures is the "broadening out" of the graphs as ν^2 increases. A greater number of l contributions become significant to the overall SCS differential cross section. This behaviour makes sense physically since there is a direct relationship between ν^2 and the photon number density. With increasing number of external field photons in the fixed region of space in which the SCS process takes place, the probability that a greater number of these photons will combine with the SCS electron also increases.

The insets of figures 4.1 - 4.4 show the opposite effect in that the graphs display a sharpening peak at $l = 0$ with decreasing external field intensity. As ν^2 (and the external field photon number density) decreases to zero, the only significant contribution to the differential cross section is the one in which $l = 0$. The relative value of the l contributions is dependent in part on the scattering angles and particle energies. The region $-4 \leq l \leq 4$ in figure 4.3 displays a more complicated oscillatory behaviour and a more thorough examination of the variation of the SCS differential cross section with scattering angles θ_i and θ_f and photon energies ω and ω_i, which follows in the rest of this chapter, is required.

The behaviour of the SCS differential cross section is simplified for the special kinematic case where the incoming photon is directed parallel to the direction of propagation of the external field $\theta_i = 0°$ and this is investigated in figures 4.5 - 4.12. For these kinematics the SCS process gains an additional symmetry with respect to the azimuthal angle ϕ_f and the form of the differential cross section is considerably simplified. So Figures 4.5 - 4.12 show the $l = 0, 1, 2$ contributions for the initial scattering angle $\theta_i = 0°$ with various values of ν^2 and particle energies ω and ω_i. Each l contribution consists of an infinite number of additional r contributions corresponding to the number of ways in which l external field photons can be included in the scattering process. [1] For example if the net number of external field photons contributing to the process is $l = 0$, then the $r = 2$ contribution corresponds to two external field photons being absorbed by the initial electron and two external field photons being emitted by the final electron.

The SCS differential cross section for $\theta_i = 0°$ was considered in section 3.5 with the important result that the argument of some Bessel functions go to zero. Inspection of the order of the Bessel function co-products of the trace calculations (Appendix B) require then that the only non zero contributions to the differential cross section are those with $r = 0$ (l external field photons contribute to the process), $r = 1$ ($l + 1$ external field photons are absorbed and then one emitted), and $r = -1$ (an external field photon is given up to the field and then $l + 1$ reabsorbed). This result is due to the structure of the Volkov solution in a circularly polarised electromagnetic field. With the initial electron 3-momentum zero the only effect the external field has on initial states is an increase in electron rest mass. However, in the final states, the full range of electron 3-momenta are permitted and the Volkov solution contains contributions corresponding to $r = -1, 0, 1$ from $l - 1$, l or $l + 1$ external field photons.

Figures 4.5 and 4.6 show the variation of the $l = 0, r = 0$ contribution with the final scattering angle θ_f and initial scattering angle $\theta_i = 0°$. Each figure contains several plots corresponding to a variation in intensity parameter ν^2. The central feature is a double peak structure with peaks at $\theta_f = 0°, 180°$. At $\nu^2 = 0$ the peaks are of equal height. As ν^2 increases, the peak at $\theta_f = 180°$ broadens and decreases in height, with the $\theta_f = 0°$ peak narrowing and remaining the same height. Neglecting ν^2, the $l = 0, r = 0$ contribution of the SCS differential cross section is identical to the Klein-Nishina differential cross section and some comments can be made based on its form

$$\frac{d\sigma}{d\Omega} = \frac{r_o^2}{2}\left(\frac{\omega_f}{\omega_i}\right)^2\left(\frac{\omega_f}{\omega_i} + \frac{\omega_i}{\omega_f} - \sin^2\theta_f\right) \quad ; \quad \omega_f = \frac{\omega_i}{1 + \omega_i(1 - \cos\theta_f)} \tag{4.1}$$

When $\omega_f \simeq \omega_i$, the energy of the initial photon is much less than the rest mass of the electron and the angular dependence of the differential cross section is approximately proportional to the term $2 - \sin^2\theta_f$. This is the source of the peaks at $\theta_f = 0°, 180°$. As the energy of the initial electron becomes significant the angular dependence of the $\frac{\omega_f}{\omega_i}$ term, which is a minimum at $\theta_f = 180°$ also becomes significant. The competing angular dependences of terms within the differential cross section results in a reduced peak at $\theta_f = 180°$. The same differential cross section peaks can be

[1] Actually there are two infinite summations over r and r', however for $\theta_i = 0$ these reduce to just one.

determined from physical arguments by considering the electromagnetic field associated with the initial SCS photon.

It is well known that an electron, undergoing simple harmonic motion radiates energy at right angles to its direction of propagation [Jac75]. The electromagnetic wave associated with the initial photon causes the SCS electron to vibrate transversely. Since the differential cross section was summed over all photon polarisations the predominant radiation will be parallel and anti-parallel to the direction of propagation of the initial photon, i.e. $\theta_f = 0°, 180°$. If the energy of the initial photon increases from a low value, a significant amount of forward momentum is transferred to the electron and radiation in the forward direction is more likely. Less final states are available for the scattering and the $\theta_f = 180°$ differential cross section decreases.

When the external field is significant $\nu^2 > 0$ extra momentum is contributed to the electron. The net momentum transferred is the difference between that of the final state electron p_f and that of the initial state electron p_i.

$$\begin{aligned}
\frac{\nu^2}{2(kp_f)}k_\mu - \frac{\nu^2}{2(kp_i)}k_\mu &= \frac{\nu^2}{2}\frac{\omega_f(1-\cos\theta_f)}{\omega(1-\omega_f(1-\cos\,\theta_f))} \\
\text{where} \qquad \omega_f &= \frac{\omega_i + l\omega}{1 + (\frac{\nu^2}{2} + l\omega + \omega_i)(1-\cos\theta_f)}
\end{aligned} \tag{4.2}$$

The net momentum contribution increases with increasing ν^2 as long as $\theta_f \neq 0°$. Consequently at $\theta_f = 0°$ there is no variation of the SCS differential cross section. The maximum increase in net momentum transferred to the electron is at $\theta_f = 180°$. The situation here is equivalent to the Klein-Nishina process in which a not insignificant amount of momentum is transferred to the final electron. Here the momentum comes, not from an energetic initial photon but from the external field. As before, extra momentum transferred to the electron results in a broadened and flattened differential cross section peak at $\theta_f = 180°$, as evidenced from figures 4.5 and 4.6.

Figures 4.7 and 4.8 reveal the effect the external field has on the $l = 0$ contribution for the initial scattering geometry $\theta_i = 0°$. These figures compare the Klein-Nishina differential cross section with the SCS $l = 0, r = 0$ contribution and the SCS $l = 0$ contribution summed over all r contribution ($r = -1, 0, 1$).

The effect is dependent on the particle energy ratio $\frac{\omega_i}{\omega}$ and the $l = 0, r =$all contribution shows an increase in the differential cross section reaching a maximum at $\theta_f = 180°$ when $\frac{\omega_f}{\omega} < 1$ (figure 4.7), and a decrease reaching a minimum at $\theta_f = 180°$ when $\frac{\omega_i}{\omega} > 1$ (figure 4.8).

The behaviour of the $l = 0, r =$ all contribution is clearly different from the $l = 0, r = 0$ contribution. Like the latter, the former can be explained partially by comparison with the Klein-Nishina differential cross section. However the fill explanation requires an appeal to the quasi-level structure of the electron embedded in the external field [Zel67]. The probability of scattering increases if the kinematics are such that the final bound electron energy reaches a quasi-energy level. The quasi-energy levels are given by integer numbers of external field photon energy $n\omega$. For the energies considered in figures 4.7 - 4.8 the first quasi-energy level is 0.512 keV.

In figure 4.7 the incident photon energy at 0.409 keV ($\frac{\omega_i}{\omega} < 1$) supplies energy to the SCS electron just short of the first quasi-energy level. Though momentum is supplied from the external field as described by 4.2, this simply accounts for the increased rest mass of the bound electron. scattering of the SCS photon in the backward ($\theta_f = 180°$) direction becomes more probable because the rebounding final bound electron gains extra energy to carry it closer to the quasi-energy level. In figure 4.8 the energy of the initial photon $\omega_i = 0.768\,\text{keV}$ ($\frac{\omega_i}{\omega} > 1$) exceeds the quasi-energy level. This time, backwards scattering of the SCS photon is suppressed as the gained energy carries the final bound electron away from the quasi-level.

Figures 4.9 - 4.12 compare the angular dependence on the final scattering angle θ_f of the $l = 0, 1, 2$ contributions for various particle energies and external field intensity for the initial scattering geometry $\theta_i = 0°$. Figures 4.9 and 4.10 concern scattering situations in which the initial photon is more energetic than the laser photons. The central feature of figure 4.9 ($\frac{\omega_i}{\omega} = 5$) are oscillatory cross section contributions. Maximum peaks lie in the region around $\theta_f = 0°$ and $\theta_f = 180°$, diminishing in height as the final photon scatters at angles perpendicular to the direction of propagation of the initial photon ($\theta_f = 90°, 270°$).

In figure 4.10 ($\frac{\omega_i}{\omega} = 1.33$), the $l = 0$ contribution has a primary peak at $\theta_f = 0°$ and a second, broadened peak at $\theta_f = 180°$. This angular variation is similar in form to the Klein-Nishina differential cross section where significant momentum has been transferred to the electron in the course of the scattering. Indeed its identical to the plot in figure 4.8. The $l \neq 0$ contributions oscillate and fall to zero at $\theta_f = 0°$. In both figures 4.9 and 4.10, the $l = 0$ contribution exceeds in magnitude the $l \neq 0$ contributions.

Figures 4.11 and 4.12 concern scattering situations in which the laser photon energy exceeds the initial photon energy. In figure 4.11, $\frac{\omega_i}{\omega} = 0.8$ and for figure 4.12 $\frac{\omega_i}{\omega} = 0.1$. Both figures show $l = 0$ contributions with peaks at $\theta_f = 0°, 180°$ (Its difficult to see in figure 4.12 but its there). The $l \neq 0$ contributions show the development of peaks at angles approximately perpendicular to the direction of the initial photon (and the direction of propagation of the external field), $\theta_f = 90°, 270°$. These peaks show evidence of structure, i.e. secondary and tertiary peaks. In figure 4.12 the $l \neq 0$ contributions clearly exceed the $l = 0$ contribution[2], whereas, in figure 4.11, they are of the same order of magnitude.

The peaks associated with the $l = 0$ contribution have already been discussed. The precise form of the peaks associated with the $l \neq 0$ contributions is the result of many terms in the differential cross section equations and cannot be discussed in detail. However general comments can be made

[2]the peak of the $l = 1$ contribution is 20.6 times the magnitude of the $l = 0$ contribution peaks

about the origin of these peaks, approximately where we can expect to find them, and the relative magnitude of the $l = 0$ and $l \neq 0$ contributions.

The origins of the peaks associated with the $l \neq 0$ contributions can be determined by considering the momentum of an electron at space-time x_μ in the presence of the external electromagnetic field $A_\mu(x)$ (see equation 2.29).

$$\Pi_\mu\left(x\right) = p_\mu - eA^e_\mu(x) + k_\mu \left(e\frac{(Ap)}{(kp)} + \frac{e^2A^2}{2(kp)} \right) \tag{4.3}$$

The origin of the term $e\frac{(Ap)}{(kp)}k_\mu$ can be explained with the aid of classical electromagnetic theory. When the electron crosses the plane of vibration of the magnetic field components of the external field the electron momentum gains additional, oscillatory components along the direction of propagation of the external field ($\underset{\sim}{k}$). When the electron momentum is directed along $\underset{\sim}{k}$, there is no intersection with the plane of the magnetic field components and the longitudinal momentum component is zero. The oscillatory nature of the longitudinal momentum component allows it to be written in a Fourier series of discrete external field contributions corresponding to $l = 1, 2, 3, \ldots$. Each contribution is interpreted as the addition of a discrete number of laser field photons, and is proportional to squares of Bessel functions of order l and argument z.

The amplitude of the longitudinal momentum contributions along the direction of propagation of the external field is given by the numerical value of the Bessel function arguments described by

$$z = \sqrt{e^2 \left(\frac{(a_1p)^2}{(kp)^2} + \frac{(a_2p)^2}{(kp)^2} \right)} \tag{4.4}$$

The variation of z with the parameters of the scattering process largely determines the behaviour of the $l \neq 0$ contributions to the SCS differential cross section. For the direct channel (first Feynman diagram in figure 3.2) and exchange channel (second Feynman diagram in figure 3.2) intermediate electrons, z can be written in terms of particle energies, scattering angles and external field intensity

$$\begin{aligned}
\bar{z} &= \nu\frac{\omega_i}{\omega}\left|\sin\,\theta_i\right| && \text{direct channel} \\
\bar{\bar{z}} &= \nu\frac{\omega_f\left|\sin\,\theta_f\right|}{\omega(1-\omega_f(1-\cos\,\theta_f))} && \text{exchange channel} \\
\frac{\omega_f}{\omega} &\simeq \left(\tfrac{\omega_i}{\omega} + l\right)\frac{1}{1+\frac{\nu^2}{2}(1-\cos\,\theta_f)}
\end{aligned} \tag{4.5}$$

The magnitude of longitudinal contributions to the momentum is proportional to the quantities $\frac{\omega_i}{\omega}, \left(\frac{\omega_i}{\omega}+l\right)$. When $\frac{\omega_i}{\omega} > 1$, the maximum value of $\bar{\bar{z}}$ is relatively large as long as ν is not too small [3] ($\bar{z} = 0$ when $\theta_i = 0°$) and many longitudinal contributions have a significant impact on the differential cross section. With variation in θ_f, the associated variation in $\bar{\bar{z}}$ is also relatively large and each longitudinal contribution to the differential cross section oscillates many times (see figure 4.9). This behaviour is a consequence of the mathematical behaviour of the associated Bessel functions.

The oscillatory nature of the differential cross section can be justified physically by an appeal to the quasi-energy level structure. The contribution of incident photon energy such that $\frac{\omega_i}{\omega} = 5$ in figure 4.9 allows the SCS electron to potentially traverse several energy levels corresponding to the differential cross section peaks. The general Klein-Nishina trend of maximum differential cross section in the region of $\theta_f = 0°, 180°$ is still evident.

Conversely in figures 4.11 and 4.12 particle energies are such that $\frac{\omega_i}{\omega} < 1$, the maximum variation in and value of $\bar{\bar{z}}$ is relatively small. [4] Longitudinal momentum contributions and oscillatory behaviour of the differential cross section is also small. The maximum value of the differential cross section occurs at transverse angles when $\bar{\bar{z}}$ is largest ($\theta_f \sim 90°, 270°$). This trend is evident in the $l = 1, 2, 3$ plots of figures 4.11 and 4.12. The $l = 0$ contribution shows Klein-Nishina type longitudinal peaks.

Comparison of figures 4.11 and 4.12 indicate that the differential cross section $l \neq 0$ contributions dominate the $l = 0$ contribution when $\frac{\omega_i}{\omega} \ll 1$. Physical justification for this trend can be made by considering electron motion due to the fields of both the SCS photon and the external field photons.

As already noted, the field of the photon k_i introduces a transverse vibration to the electron which in turn radiates in the $\theta_f = 0°, 180°$ directions (after summing over polarisations) with radiated power proportional to ω_i^2. The circularly polarised wave of the external field photon introduces a circular motion to the electron which in turn radiates in the $\theta_f = 90°, 270°$ direction (provided the electron has no significant forward momentum) with radiated power proportional to $\nu^2\omega^2$ [Jac75]. With the factor $\frac{\omega_i^2}{\nu^2\omega^2} < 1$ ($\frac{\omega_i^2}{\nu^2\omega^2} = 0.05$ in figure 4.12) we expect the radiation produced by the electron subjected to these two fields to be mainly the result of the influence of the external field.

Figures 4.13 - 4.20 show differential cross section variation with various parameters for an initial photon angle $\theta_i = 45°$. Other θ_i values are considered in section 4.3.2. Figures 4.13 and 4.14 show (θ_f) variation of the $l = 0$ contribution for various external field intensities and incident photon energies. The main feature of both figures is a double peak differential cross section structure in the first half of the θ_f parameter range. Figure 4.13 with $\frac{\omega_i}{\omega} = 0.8$ also shows a slight increase in

[3] the maximum value of $\bar{\bar{z}}$ is 1.8 for the $l = 1$ plot of figure 4.9, and 1.44 for the $l = 1$ plot of figure 4.10

[4] the maximum value of $\bar{\bar{z}}$ is 1.0 for the $l = 1$ plot of figure 4.11, and 1.44 for the $l = 0.44$ plot of figure 4.12

the differential cross section with increase in the external field intensity in the second half of the θ_f range. However in the same range figure 4.14 with $\frac{\omega_i}{\omega} = 1.5$ shows a diminution of the differential cross section. At $\nu^2 = 0$ both figures show two peaks of the same height at $\theta_f = 45°, 225°$. These are simply Klein-Nishina type peaks in the forward and backward direction of the initial photon.

An explanation of the features in figures 4.13 and 4.14 is made with the expression for bound electron momentum (equation 4.3). The electron gains two momentum components in the direction of external field propagation, one static and one oscillatory. For the direct channel of the scattering, with ϕ_0 representing a scalar product of particle 4-momenta, they are

$$\begin{aligned} &\frac{\nu^2}{2}\frac{m}{\omega}\,k_\mu && \text{static term} \\ &\nu\frac{\omega_i}{\omega}\,|\sin\,\theta_i|\,\sin(kx+\phi_0)\,k_\mu && \text{oscillatory term} \end{aligned} \tag{4.6}$$

As the magnitude of the external field intensity ν^2 increases, both of these momentum components also increase. The static term favours angles θ_f such that the final electron momentum is more collinear with the propagation direction of the external field. The final photon should carry off the momentum of the initial photon so the differential cross section is maximised in the range $0° < \theta_f < 180°$ and minimised in the range $180° < \theta_f < 360°$. This behaviour has been noted before for the Möller scattering process in the presence of an external field [Bea79a, Bea79b]. The oscillatory term results in radiation perpendicular to its longitudinal direction of oscillation producing peaks in the cross section of equal height at $\theta_f = 90°, 270°$. The momentum requirements of the static term ensure that the $\theta_f = 90°$ peak is enhanced and the $\theta_f = 270°$ peak reduced. Additionally the oscillatory momentum contribution is at least a factor $\frac{\omega_i}{2m\nu}$ smaller than the static term, and for the particle energies considered $\frac{\omega_i}{m} \ll 1$ and ν^2 is not too small. The end result is that the differential cross section peaks in the $0° < \theta_f < 180°$ range dominate.

The dissimilar behaviour of figures 4.13 and 4.14 in the range $180° < \theta_f < 360°$ is due in part to the quasi-energy level structure. Though complicated by the values of ν^2 and θ_i, the determining factor is still the ration $\frac{\omega_i}{\omega}$ which is less than one in figure 4.13 and greater than one in 4.14

Figures 4.15 and 4.16 show the variation of the $l = 1$ contribution with increasing external field intensity for the initial angle $\theta_i = 45°$. The main feature is a general increase in the cross section with an increase in ν^2 for scattering angles $0° < \theta_f < 180°$. This increase has the same explanation as the one given for the $l = 0$ contribution (figures 4.14 and 4.13). Increases in ν^2 shift the electron momentum more nearly parallel to the direction of propagation of the external field. Final photon scattering directions which favour this shift ($0° < \theta_f < 180°$) become more probable, and the cross section increases accordingly.

Figures 4.17 - 4.20 compare the $l = 0$ contributions and the $l \neq 0$ contributions for various values of the external field intensity and particle energies. The relative magnitude is most distinct in figures 4.19 and 4.20. In figure 4.19, with relative particle energies $\frac{\omega i}{\omega} = 10$, the $l = 0$ contribution clearly dominates, whereas in figure 4.20 ($\frac{\omega_i}{\omega} = 0.1$) it is the $l \neq 0$ contributions which are dominant. As in the discussion of figures 4.11 and 4.12, the relative impact of the electromagnetic field of the initial photon compared to the electromagnetic field of the external wave is the physical explanation. The relevant factor $\frac{\omega_i^2}{\nu^2\omega^2}$ is 200 for figure 4.19 which leads to the $\theta_f = theta_i = 45°$ peak in the $l = 0$ contribution and 0.02 for figure 4.20 in which the $l \neq 0$ contributions are largest.

4.3.2 Differential Cross Sections Summed Over All l

Figures 4.21 - 4.26 show the θ_f variation of the complete SCS differential cross section for various initial scattering angles θ_i and external field intensities ν^2. For figures 4.21 - 4.23 an initial photon of energy 0.409 keV is incident on an electron embedded in an 0.512 keV external field. For figures 4.24 - 4.26 a 0.026 keV initial photon is incident on electron embedded in an 0.005 keV external field.

The main feature of all six figures (with the exception of figure 4.24) is the development of a peak at $\theta_f \sim 90°$. Since the differential cross sections here are combinations of $l = 0$ and $l \neq 0$ contributions, much of the previous section's analysis applies. The $l = 0$ contribution produces peaks in the $\theta_f = \theta_i, \theta_i + 180°$ directions, and the $l \neq 0$ contributions in transverse directions. The relative strength of the contributions is once again given by the factor $\frac{\omega_i^2}{\nu^2\omega^2}$, which is smallest where the $\theta_i = 90°$ peak is strongest ($\frac{\omega_i^2}{\nu^2\omega^2} = 0.638$ and maximum peak height ~ 25000 in figure 4.23). The competing trends are complicated by transverse θ_i angles. The $\theta_f = 90°$ peaks increase with increasing θ_i and ν^2 except for figure 4.24 where the influence of the external field is weak. An explanation can be given by considering the longitudinal momentum the SCS electron gains from the field $\frac{\nu^2}{2(kp)}\, k_\mu$. As the longitudinal momentum of the SCS electron increases with ν^2, the probability that it will carry off the transverse momentum supplied by a transverse initial photon decreases. Consequently, the photon has to carry off the transverse momentum of the initial state.

A point of interest is the relative magnitude of the peak maxima for figures 4.21 - 4.23 compared to those for figures 4.24 - 4.26 (table 4.3). For instance, the peak maxima for figure 4.23 is a factor of 17.25 larger than that of figure 4.26. The crucial factor here is the denominator of the electron propagator which expresses the quasi-energy levels of the electron embedded in the external field.

figure	4.21	4.22	4.23	4.24	4.25	4.26
peak maximum	58	1700	25000	32.5	138	1450
ν^2	0.1	0.5	1	0.1	0.5	1

Table 4.3: **Peak maximums for the $\theta_i = 30°$ plots of figures 4.21 - 4.23, and the $\theta_i = 90°$ plots of figures 4.24 - 4.26.**

Figure 4.23 represents a scattering where the addition of an initial photon of energy $409\ keV$ raises the SCS electron to an energy close to its first excited level and the cross section $\theta_f = 90°$ is relatively large. Figure 4.26, in contrast, represents a scattering where the initial photon raises the SCS electron to an energy half way between its 7th and 8th excited level and the cross section $\theta_f = 90°$ peak is relatively small.

Figures 4.27 - 4.34 show the variation of SCS differential cross section with final scattering angle θ_f for various initial scattering angles θ_i, and particle energies ω and ω_i. Each figure contains several plots with differing external field intensity ν^2 allowing ease of comparison with the Klein-Nishina case ($\nu^2 = 0$).

Figures 4.27 - 4.30 show the scattering of a 10.2 keV photon incident on an electron embedded in a 51.2 keV external field for four initial photon angles ($\theta_i = 0°, 45°, 90°, 180°$). The main feature is the development of peaks at $\theta_f \sim 90°, 270°$, which increase with increasing ν^2. In figures 4.27 and 4.30 ($\theta_i = 0°, 180°$) these peaks are of equal height. In figure 4.28 ($\theta_i = 45°$) the $\theta_f \sim 90°$ is dominant, whereas in figure 4.29 ($\theta_i = 90°$) the $\theta_f \sim 270°$ peak is dominant. The factor $\frac{\omega_i^2}{\nu^2\omega^2}$ is less than one for all four figures accounting for the characteristic transverse differential cross section peaks.

Figures 4.28 and 4.29 for transverse θ_i show enhancement of one of the $\theta_f = 90°, 270°$ peaks. Naively we would expect the final photon to carry off the transverse momentum enhancing the $\theta_f = 90°$ peaks in both cases. Figure 4.29 however shows the opposite. A more detailed analysis of the quasi-energy levels in terms of the bound electron propagator is required.

The energy levels can be discussed by considering the expressions for the denominators of electron propagators for the direct and exchange channels of the scattering. Starting from equation 3.7 and expanding scalar products in terms of energy-momenta and scattering angles, the propagator denominator for each of the scattering channels is

$$\begin{aligned} &2(q_i k_i)\left[l\,\frac{\omega}{\omega_i}\frac{1+\omega_i(1-\cos\,\theta_i)}{1+\frac{\nu^2}{2}(1-\cos\,\theta_i)}\;+\;1\right] && \text{direct channel} \\ &2(q_i k_f)\left[l\,\frac{\omega}{\omega_f}\frac{1-\omega_f(1-\cos\,\theta_f)}{1+\frac{\nu^2}{2}(1-\cos\,\theta_f)}\;-\;1\right] && \text{exchange channel} \end{aligned} \tag{4.7}$$

The energy levels of the exchange channel are dependent on the final scattering angle θ_f and the contribution to the values of the differential cross section varies with θ_f variation. For the inset of figure 4.29 ($\theta_i = 90°$) the contribution is 17.2 at $\theta_f = 90°$ and 22.07 at $\theta_f = 277°$. scattering in the $\theta_f \sim 270°$ direction is preferred because the SCS electron moves closer to a quasi-energy level. The relative heights of the $\theta_f \sim 90°$ and $\theta_f \sim 270°$ peaks in figures 4.28 and 4.29 are a result of two competing physical processes. The scattering geometry and momentum contributed by the external field, preferences scattering in the $\theta_f \sim 90°$ direction, whereas the energy level structure of the SCS electron preferences $\theta_f \sim 270°$ scattering.

The same quasi-energy level analysis can be applied to figures 4.31 - 4.34 in which a 0.768 keV photon is incident on an electron embedded in an 0.512 keV external field. Figures 4.32 and 4.33 show the $\theta_i = 45°$ and $90°$ scattering geometries respectively, and reveal a $\theta_f \sim 90°$ peak which increases with increasing ν^2. Figure 4.33 reveals a secondary peak at $\theta_f = 261°$, however its maximum in the $\nu^2 = 0.3$ plot is only 25% that of the $\theta_f \sim 90°$ peak.

The exchange channel propagator denominator is calculated for $l = 2$, $\nu^2 = 0.3$ since this is the dominant term. It contributes a factor of 319.5 to the SCS differential cross section at $\theta_f = 90°$, and 320.7 at $\theta_f = 270°$ for figure 4.32 ($\theta_i = 45°$). For figure 4.33 ($\theta_i = 90°$) the contribution is 289.4 at $\theta_f = 90°$ and 291 at $\theta_f = 270°$. The electron energy level relative weight is approximately even and the dominant scattering is $\theta_f = 90°$ in which the final photon carries the transverse momentum of the initial photon.

Figure 4.31 shows the initial scattering geometry $\theta_i = 0°$, and its main feature is a decrease of the differential cross section with increasing ν^2 in the angular region $90° \leq \theta_f \leq 270°$. The differential cross section is minimum at $\theta_f = 180°$. Here the factor $\frac{\omega_i^2}{\nu^2\omega^2}$ is always greater then unity, [5] the incident photon k_i dominates the process and the θ_f variation of the differential cross section is similar to that of the Klein-Nishina process with significant momentum transferred to the electron in the forward direction ($\theta_f = 0°$).

Figure 4.34 shows the initial scattering geometry $\theta_i = 180°$, and the differential SCS cross section peaks increase as ν^2 increases to =0.3, thereafter decreasing. The $\nu^2 = 0.1$ plot shows characteristic Klein-Nishina scattering with an enhanced $\theta_f = 180°$ peak. The final photon must carry the initial state momentum because bound electron momentum in that direction is inhibited by the propagation direction of the external field. As ν^2 approaches 0.3, the cross section takes on a $\theta_f \sim 90°, 270°$ peak structure characteristic of the SCS electron under the dominant influence of the external field. Examination of the direct channel electron energy levels reveals that $\nu^2 = 0.33$ provides the closest approach to a quasi-energy level. As ν^2 increases beyond this point the scattering cross section begins to decrease again.

Figures 4.35 and 4.36 represent the variation of the SCS differential cross section with the final azimuthal scattering angle ϕ_f for a 0.768 keV photon incident on the SCS electron embedded in a 0.512 keV external field. scattering is most favoured at $\phi_f = 0°$ and least favoured at $\phi_f = 180°$. The variation increases as the external field intensity increases. For these figures the factor $\frac{\omega_i^2}{\nu^2\omega^2}$ is greater than one and the scattering is favoured when the final photon carries the transverse momentum of the initial photon. This condition is most closely met at $\varphi_f = 0°$ and least met at $\varphi_f = 180°$.

Figures 4.37 - 4.40 reveal the effect on the SCS differential cross section of changing the ratio of

[5] $\frac{\omega_i^2}{\nu^2\omega^2} = 22.5$ for $\nu^2 = 0.1$ and $\frac{\omega_i^2}{\nu^2\omega^2} = 7.5$ for $\nu^2 = 0.3$

initial photon energy to external field photon energy. Figures 4.37 and 4.38 show the SCS differential cross section with an external field intensity of $\nu^2 = 0.1$, and initial scattering geometry $\theta_i = 0°$ and $45°$ respectively. Figures 4.39 - 4.40 show the SCS differential cross section with the same parameters as figures 4.37 and 4.38 except for an increased external field intensity $\nu^2 = 0.5$. The pivotal factor is again $\frac{\omega_i^2}{\nu^2\omega^2}$. When $\frac{\omega_i^2}{\nu^2\omega^2}$ is much greater than unity (in the $\omega_i = 12.8$ keV and $\omega_i = 7.68$ keV plots of figures 4.37 and 4.38), the scattering is characteristic of a Klein-Nishina-like process (i.e. primary peak at $\theta_f = \theta_i$ and a flattened, secondary peak at $\theta_f = \theta_i + 180°$). When $\frac{\omega_i^2}{\nu^2\omega^2}$ is much less than unity (in the $\omega_i = 0.409$ keV and $\omega_i = 0.205$ keV plots of figure 4.39 and the $\omega_i = 0.205\ keV$ plot of figure 4.40), the scattering is characteristic of the SCS electron dominated by the circular polarised external field (i.e. double peaks at $\theta_f \sim 90°, 270°$ for $\theta_i = 0°$ and a single peak at $\theta_f \sim 90°$ for $\theta_i = 45°$).

Figures 4.41 and 4.42 represent the variation of the SCS differential cross section with external field intensity ν^2 for various initial photon angles. Figure 4.41 shows a 40.9 keV photon incident on an electron embedded in a $51.2\ keV$ external field. Figure 4.42 shows a 0.768 keV photon incident on an electron embedded in a $0.512\ keV$ external field. The vertical axes of these figures have a logarithmic scale. Except for the $\theta_i = 0°$ plot of figure 4.42, all plots show an increase in the SCS differential cross section with an increase in ν^2. This SCS differential cross section increase is physically justified by the increase in external field photon number density associated with larger values of the external field intensity parameter. The probability that more external field photons will take part in the process also increases.

A limiting factor in all experimental work on these external field phenomena, is the intensity of the external field. It is possible that at the highest external field intensities attainable at present second order IFQED cross sections may become large enough to be experimentally detected. Consideration of the SCS differential cross section for the scattering geometry $\theta_i = 0°$, results in analytic expressions which are considerably simplified [AM85]. However the results of this chapter indicated that the $\theta_i = 0°$ geometry produces small differential cross section values which are least likely to be experimentally detected. Indeed for some scattering geometries the SCS cross section diminishes with increasing external field intensity. Therefore our full analytic expressions and numerical analysis for general kinematics will become important for future experimental work.

Chapter 5

STPPP in a circularly polarised electromagnetic field - Results and Analysis

5.1 Introduction

In this chapter we present numerical calculations of the STPPP differential cross section obtained in section 3.7. The numerical results are contained in section 5.2 and an analysis of these results is contained in section 5.3.

We preface our remarks in this chapter by drawing a comparison with the data and analysis presented for the SCS process. The order of data presented and the phenomena highlighted is similar to that presented in Chapter 4. This is the case because the external electromagnetic field is identical and the STPPP process is related to the SCS process through the Substitution Law.

Also in similarity to the SCS process, the STPPP differential cross section is expressed as a triple infinite summation over integer variables l, r and r'. Analysis is again facilitated by dividing figures into two groups; those representing summation terms of the STPPP differential cross section separately or summed in part (section 5.2.1 with the accompanying analysis in section 5.3.1), and those in which all contributions have been summed over (section 5.2.2 with the accompanying analysis in section 5.3.2). Sets of figures with common parameter presentations will be introduced and analysed in turn.

A FORTRAN program was used to perform calculational work in this chapter. It was constructed from a similar FORTRAN program used in chapter 4 using the Substitution Law to make a simple reassignment of program variables.

5.2 STPPP Plots

5.2.1 Differential cross section l contributions

Table 5.2.1 displays the parameter values of the STPPP process investigated in this section. The parameter ω is the energy of external field quanta. The parameters ω_1 and ω_2 are the particle energies of the initial photons and are of equal magnitude for the centre of mass reference frame in which the STPPP differential cross section expressions were calculated. The initial photon $\underset{\sim}{k}_1$ enters the interaction region at an angle of θ_1 to the direction of the propagation of the external field. The direction of the created electron $\underset{\sim}{q}_-$ is specified by the final polar angle θ_f and the final azimuthal scattering angle ϕ_f. The external field intensity is represented by the parameter $\nu^2 = \frac{e^2a^2}{m^2}$.

The vertical axes of all figures in Sections 5.2.1 and 5.2.2 show the STPPP differential cross section divided by a function of the fine structure constant α and electron mass m, and the units are Steradian^{-1}. All angles represented on horizontal axes use units of degrees.

l	r	ν^2	ω(MeV)	$\omega_{1,2}$(MeV)	θ_1	(θ_f, ϕ_f)	figure(s)
$0 \to 6$	all	$0.1, 0.3, 0.5$	2.56	0.768	$0°$	$(45°, 0°)$	5.1
$1 \to 9$	all	$0.1, 0.3, 0.5$	1.024	0.512	$45°$	$(45°, 0°)$	5.2
$-3 \to 15$	all	$0.1, 0.3, 0.5$	0.102	0.768	$0°$	$(45°, 0°)$	5.3
$0 \to 7$	all	$0.1, 0.3, 0.5$	0.256	0.614	$45°$	$(45°, 0°)$	5.4
0	0	$0, 0.1, 0.2$ $0.3, 0.4, 0.5$	$2.56, 0.102$	0.768	$0°$	$(0° \to 360°, 0°)$	5.5,5.6
0	all	$0.5, 1.0,$ 2.0	0.256	2.56	$0°$	$(0° \to 360°, 0°)$	5.9
0	all	$0.1, 0.5,$ $1.0, 2.0$	1.024	2.56	$0°$	$(0° \to 360°, 0°)$	5.10
0	all	$0.1, 0.5,$ $1.0, 2.0$	1.024	0.409	$0°$	$(0° \to 360°, 0°)$	5.11
0	all	$0.1, 0.5,$ 1.0	5.12	0.768	$0°$	$(0° \to 360°, 0°)$	5.12
$0, 1, 2$	all	0.5	$0.05, 0.77$ $1.28, 2.56$	1.024	$0°$	$(0° \to 360°, 0°)$	$5.13, 5.13$ $5.15, 5.16$
$0, 1$	all	$0, 0.1,$ $0.2, 0.3$	0.256	1.024	$45°, 90°$	$(0° \to 360°, 0°)$	$5.17, 5.18$ $5.19, 5.20$
$0, 1, 2$	all	0.1	0.256	1.024	$45°, 90°$	$(0° \to 360°, 0°)$	5.21,5.22

Table 5.1: **The parameter range for which the STPPP differential cross section l and r contributions are investigated.**

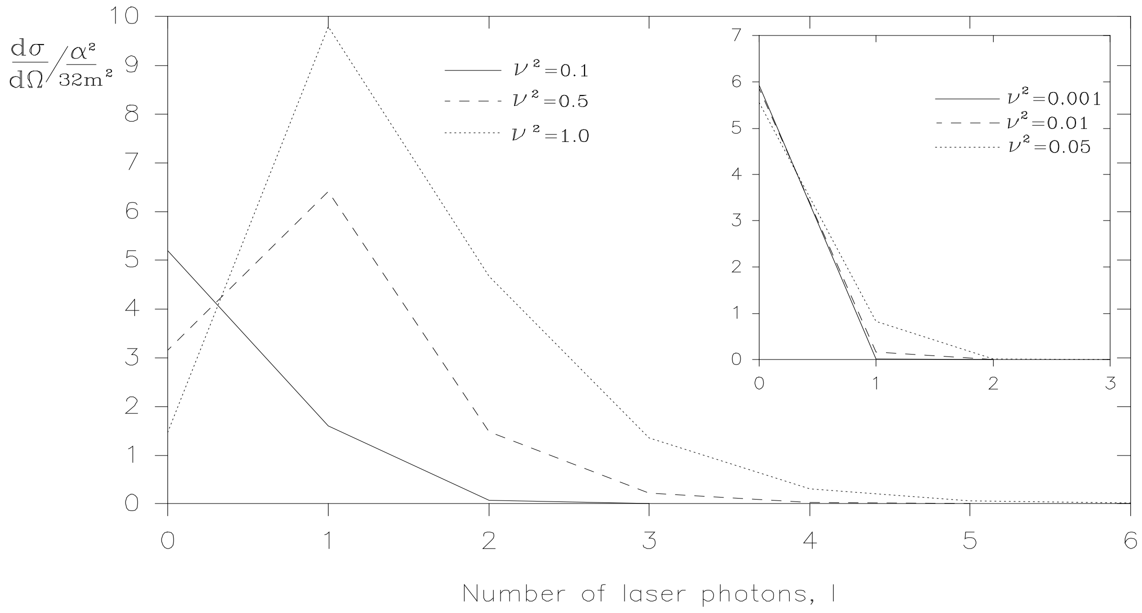

Figure 5.1: **The STPPP differential cross section vs l external field photons for $\omega = 2.56$ MeV, ω_1,$\omega_2 = 0.768$ MeV, $\theta_1 = 0°$, $\theta_f = 45°$, $\varphi_f = 0°$ and various ν^2.**

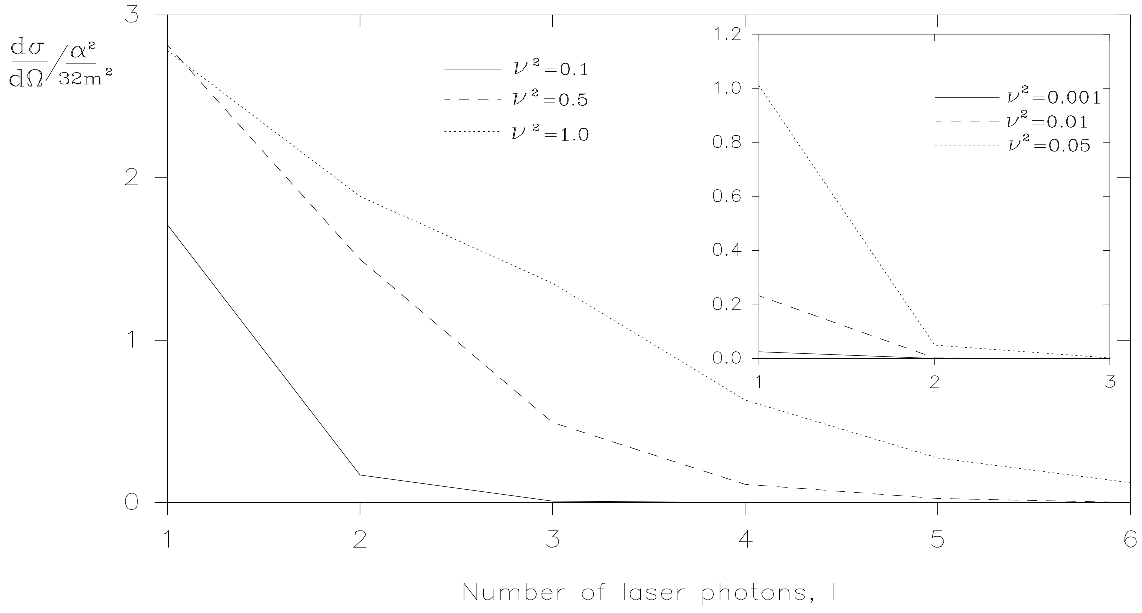

Figure 5.2: **The STPPP differential cross section vs l external field photons for $\omega = 1.024$ MeV, ω_1,$\omega_2 = 0.512$ MeV, $\theta_1 = 45°$, $\theta_f = 45°$, $\varphi_f = 0°$ and various ν^2.**

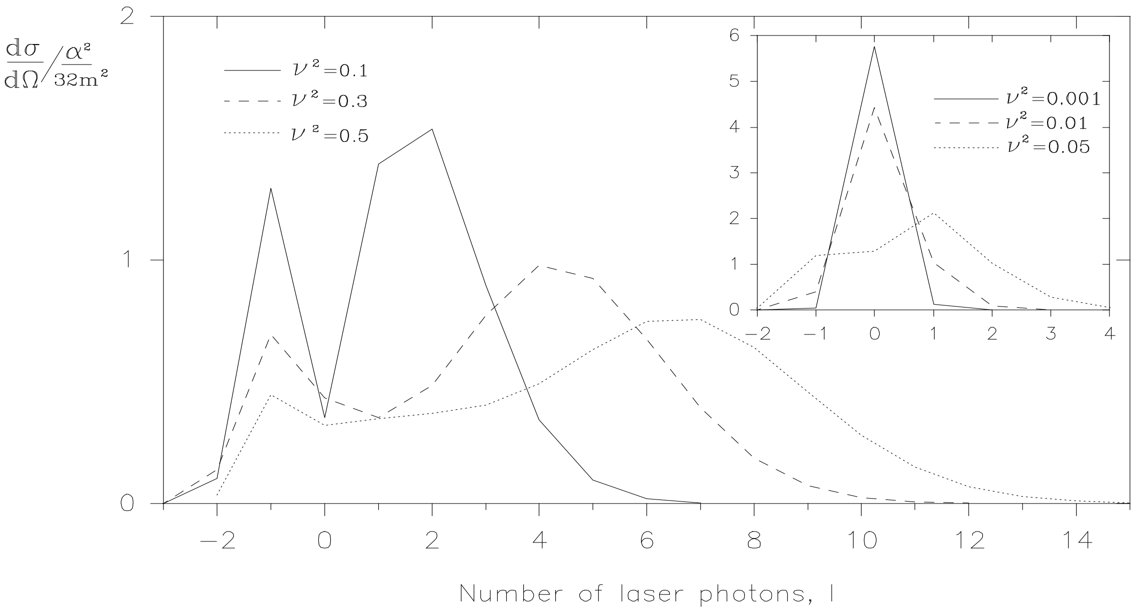

Figure 5.3: **The STPPP differential cross section vs l external field photons for $\omega = 0.102$ MeV, ω_1,$\omega_2 = 0.768$ MeV, $\theta_1 = 0°$, $\theta_f = 45°$, $\varphi_f = 0°$ and various ν^2.**

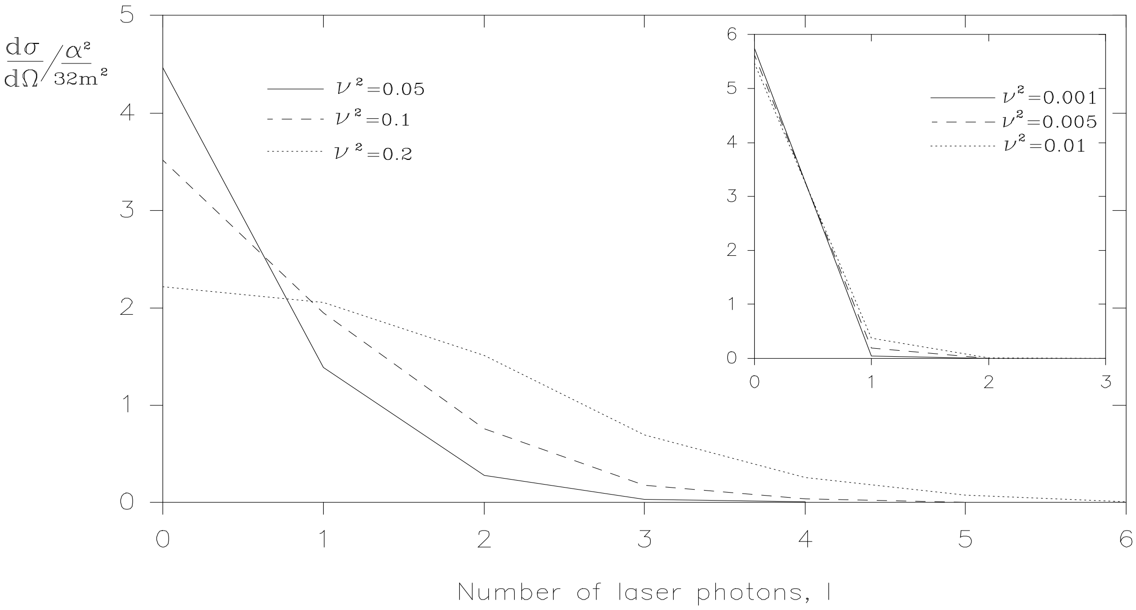

Figure 5.4: **The STPPP differential cross section vs l external field photons for $\omega = 0.256$ MeV, ω_1,$\omega_2 = 0.614$ MeV, $\theta_1 = 45°$, $\theta_f = 45°$, $\varphi_f = 0°$ and various ν^2.**

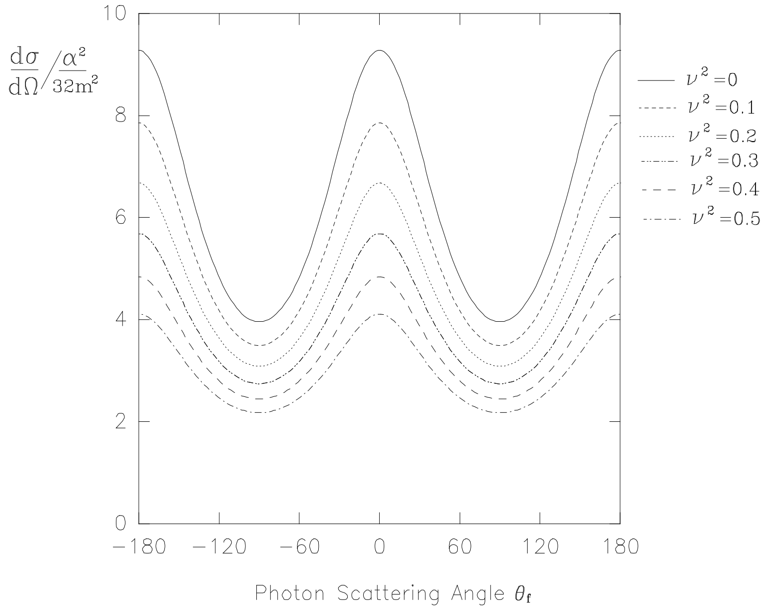

Figure 5.5: **The STPPP $l = 0, r = 0$ differential cross section vs θ_f for $\omega = 2.56$ MeV, ω_1,$\omega_2 = 0.768$ MeV, $\theta_1 = 0°$, $\varphi_f = 0°$ and various ν^2.**

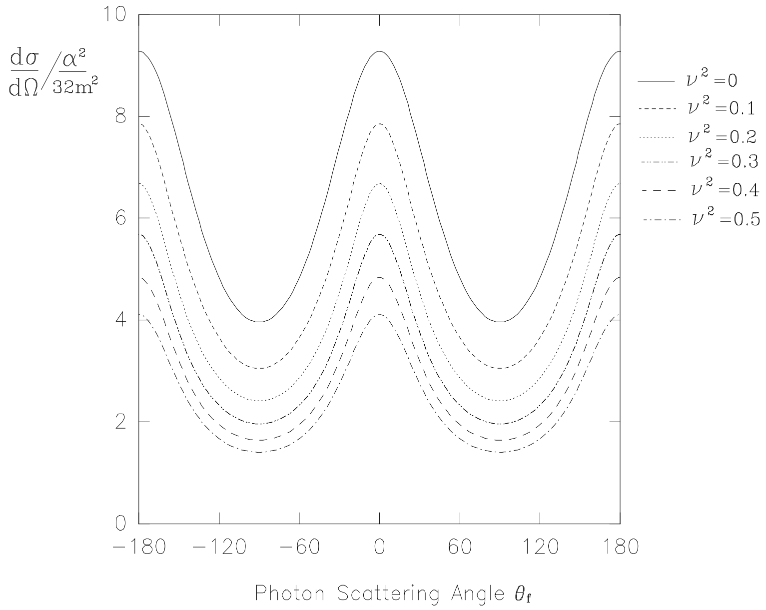

Figure 5.6: **The STPPP $l = 0, r = 0$ differential cross section vs θ_f for $\omega = 0.102$ MeV, ω_1,$\omega_2 = 0.768$ MeV, $\theta_1 = 0°$, $\varphi_f = 0°$ and various ν^2.**

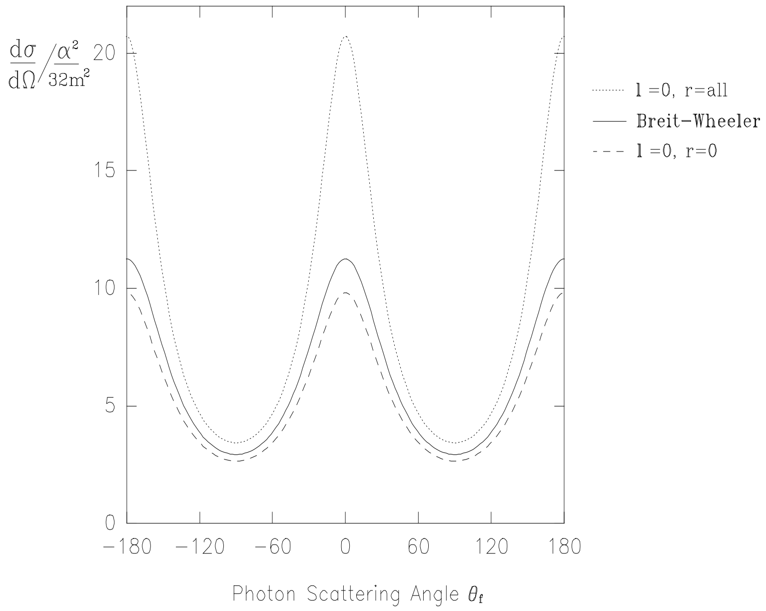

Figure 5.7: **Comparison of The STPPP $l = 0, r = 0$, $l = 0, r =$ all and Breit-Wheeler differential cross section vs θ_f for $\omega = 2.56$ MeV, ω_1,$\omega_2 = 0.768$ MeV, $\theta_1 = 0°$, $\varphi_f = 0°$ and $\nu^2 = 0.1$.**

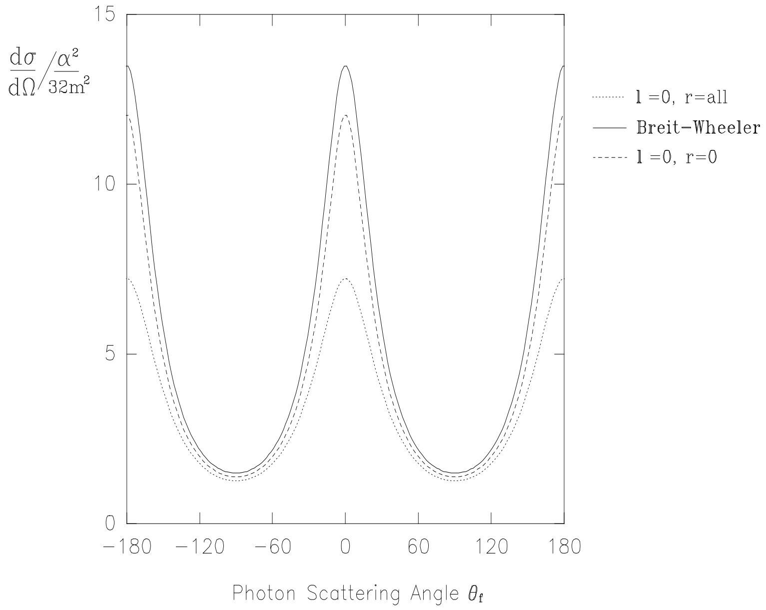

Figure 5.8: **Comparison of The STPPP $l = 0, r = 0$, $l = 0, r =$ all and Breit-Wheeler differential cross section vs θ_f for $\omega = 0.102$ MeV, ω_1,$\omega_2 = 0.768$ MeV, $\theta_1 = 0°$, $\varphi_f = 0°$ and $\nu^2 = 0.1$.**

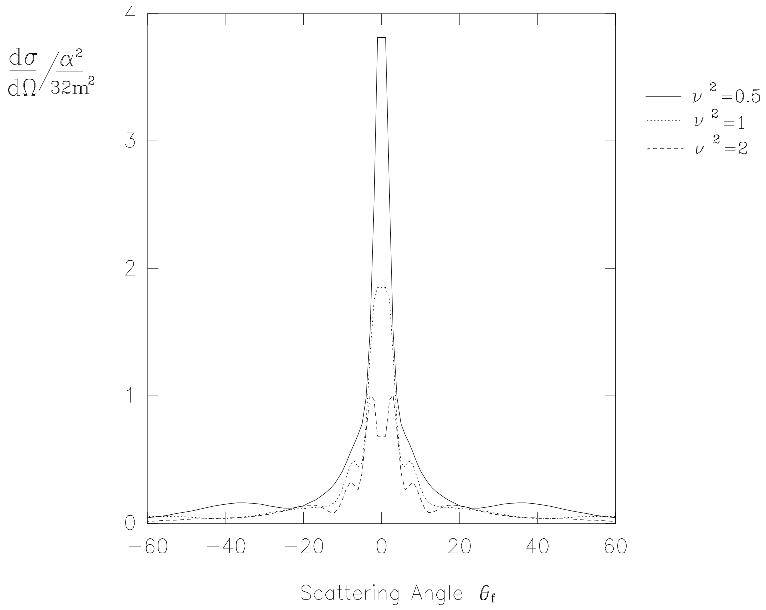

Figure 5.9: **The STPPP $l = 0$ differential cross section vs θ_f for $\omega = 0.256$ MeV, ω_1,$\omega_2 = 2.56$ MeV, $\theta_1 = 0°$, $\varphi_f = 0°$ and various ν^2.**

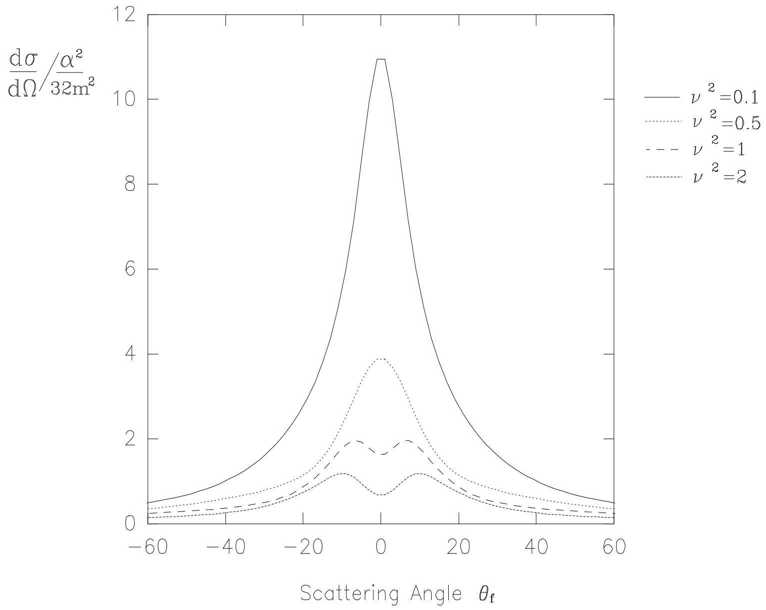

Figure 5.10: **The STPPP $l = 0$ differential cross section vs θ_f for $\omega = 1.02$ MeV, ω_1,$\omega_2 = 2.56$ MeV, $\theta_1 = 0°$, $\varphi_f = 0°$ and various ν^2.**

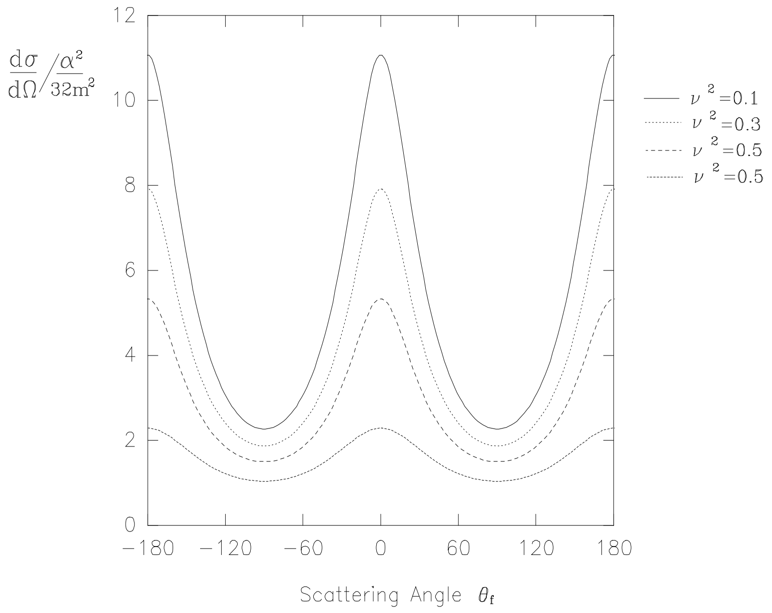

Figure 5.11: **The STPPP $l = 0$ differential cross section vs θ_f for $\omega = 1.02$ MeV, ω_1,$\omega_2 = 0.409$ MeV, $\theta_1 = 0°$, $\varphi_f = 0°$ and various ν^2.**

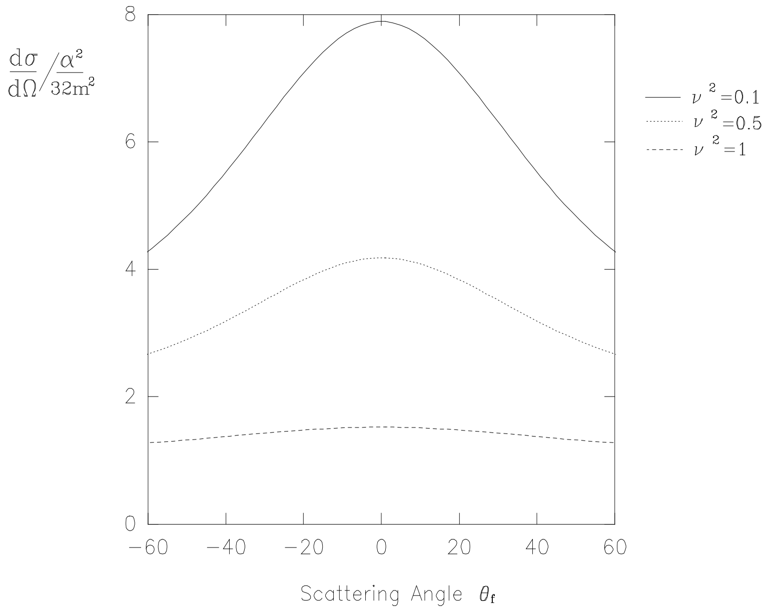

Figure 5.12: **The STPPP $l = 0$ differential cross section vs θ_f for $\omega = 5.12$ MeV, ω_1,$\omega_2 = 0.768$ MeV, $\theta_1 = 0°$, $\varphi_f = 0°$ and various ν^2.**

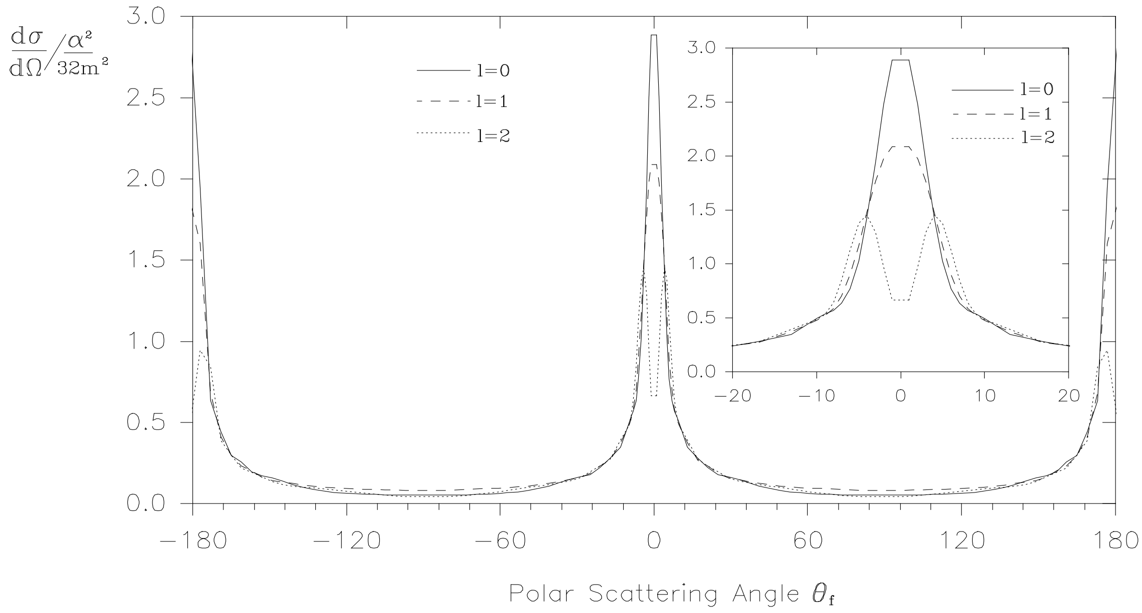

Figure 5.13: **The STPPP differential cross section vs θ_f for $\omega = 0.05$ MeV, ω_1,$\omega_2 = 1.024$ MeV, $\theta_1 = 0°$, $\varphi_f = 0°$ $\nu^2 = 0.5$ and various l.**

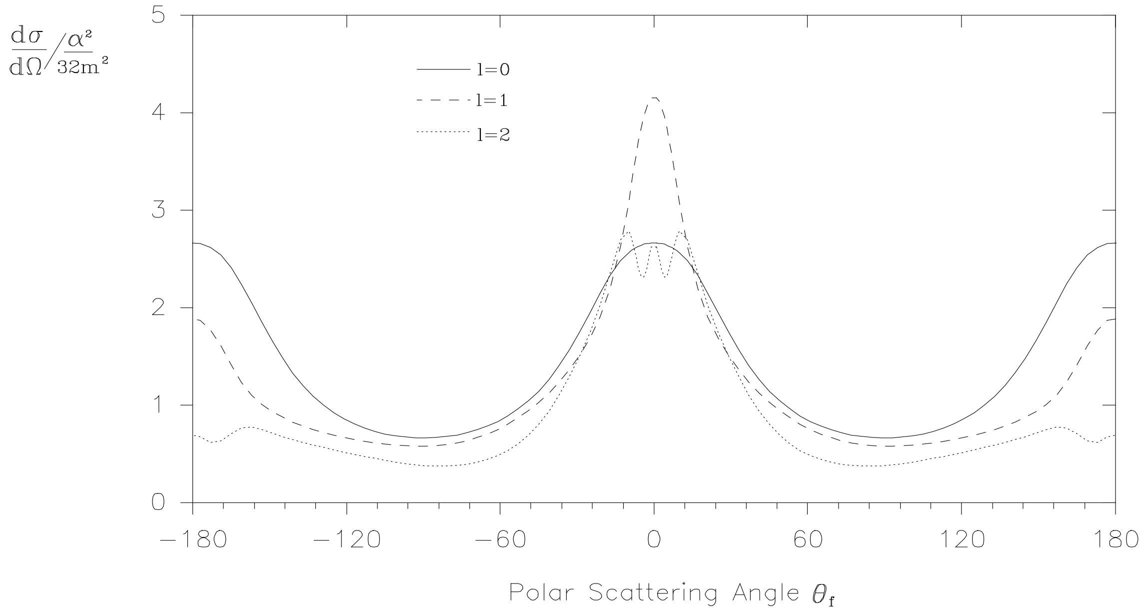

Figure 5.14: **The STPPP differential cross section vs θ_f for $\omega = 0.41$ MeV, ω_1,$\omega_2 = 1.024$ MeV, $\theta_1 = 0°$, $\varphi_f = 0°$ $\nu^2 = 0.5$ and various l.**

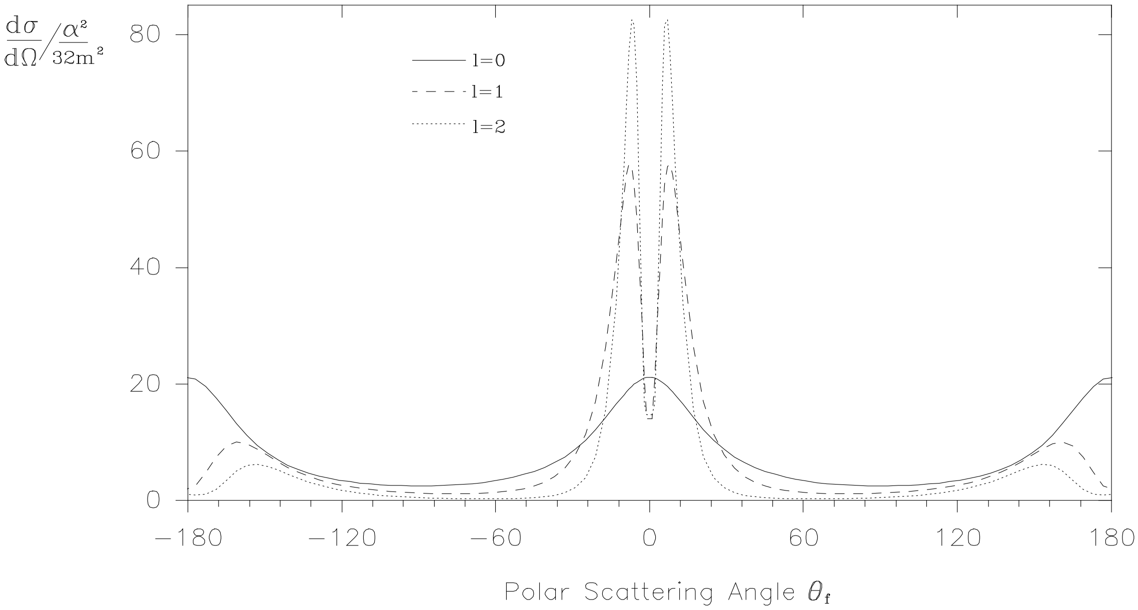

Figure 5.15: **The STPPP differential cross section vs** θ_f **for** $\omega = 1.28$ **MeV,** ω_1**,**$\omega_2 = 1.024$ **MeV,** $\theta_1 = 0°$**,** $\varphi_f = 0°$ $\nu^2 = 0.5$ **and various** l**.**

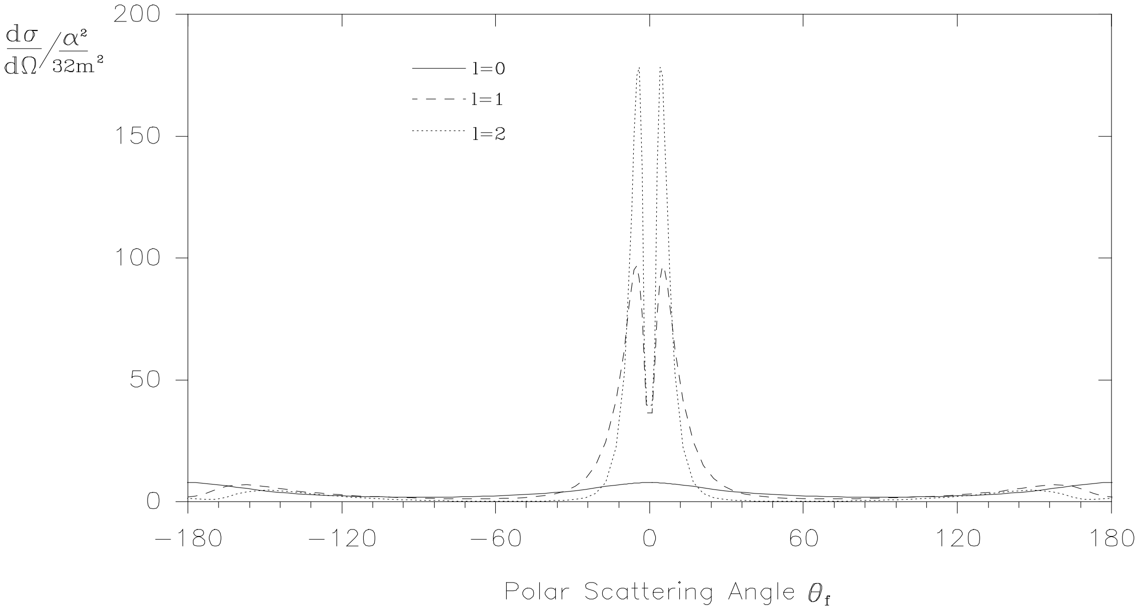

Figure 5.16: **The STPPP differential cross section vs** θ_f **for** $\omega = 2.56$ **MeV,** ω_1**,**$\omega_2 = 1.024$ **MeV,** $\theta_1 = 0°$**,** $\varphi_f = 0°$ $\nu^2 = 0.5$ **and various** l**.**

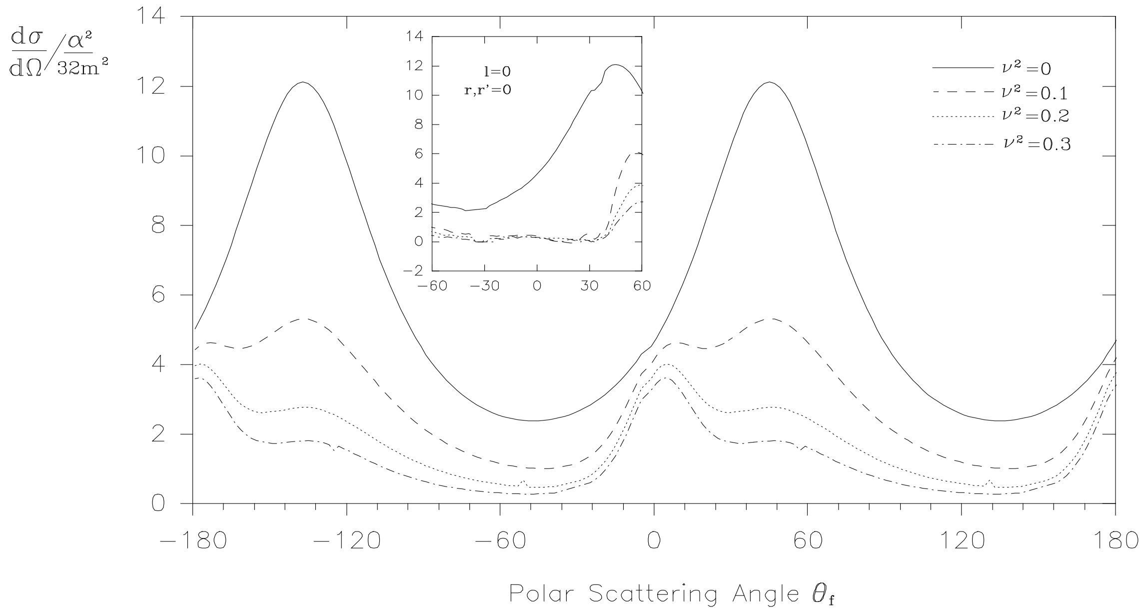

Figure 5.17: **The STPPP $l = 0$ differential cross section vs θ_f for $\omega = 0.256$ MeV, ω_1,$\omega_2 = 1.024$ MeV, $\theta_1 = 45°$, $\varphi_f = 0°$ and various ν^2.**

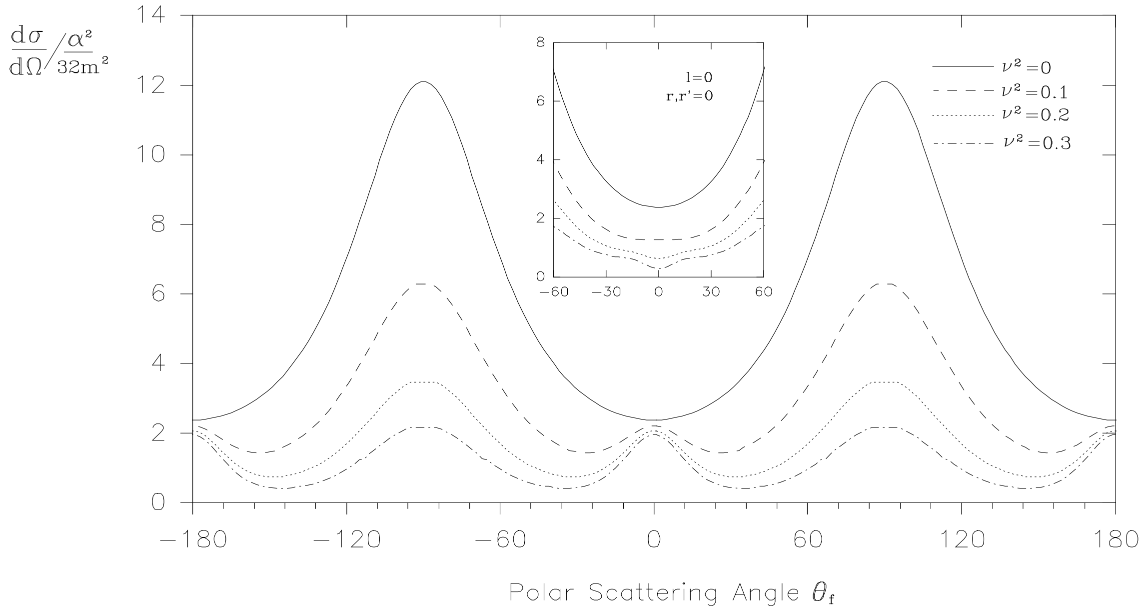

Figure 5.18: **The STPPP $l = 0$ differential cross section vs θ_f for $\omega = 0.256$ MeV, ω_1,$\omega_2 = 1.024$ MeV, $\theta_1 = 90°$, $\varphi_f = 0°$ and various ν^2.**

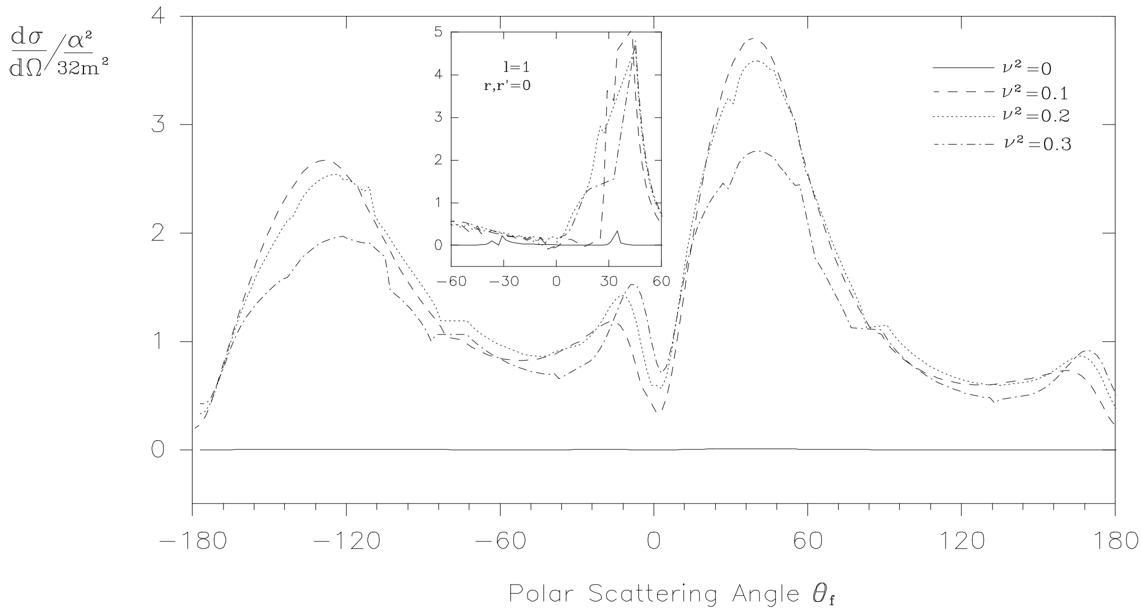

Figure 5.19: **The STPPP $l = 1$ differential cross section vs θ_f for $\omega = 0.256$ MeV, ω_1,$\omega_2 = 1.024$ MeV, $\theta_1 = 45°$, $\varphi_f = 0°$ and various ν^2.**

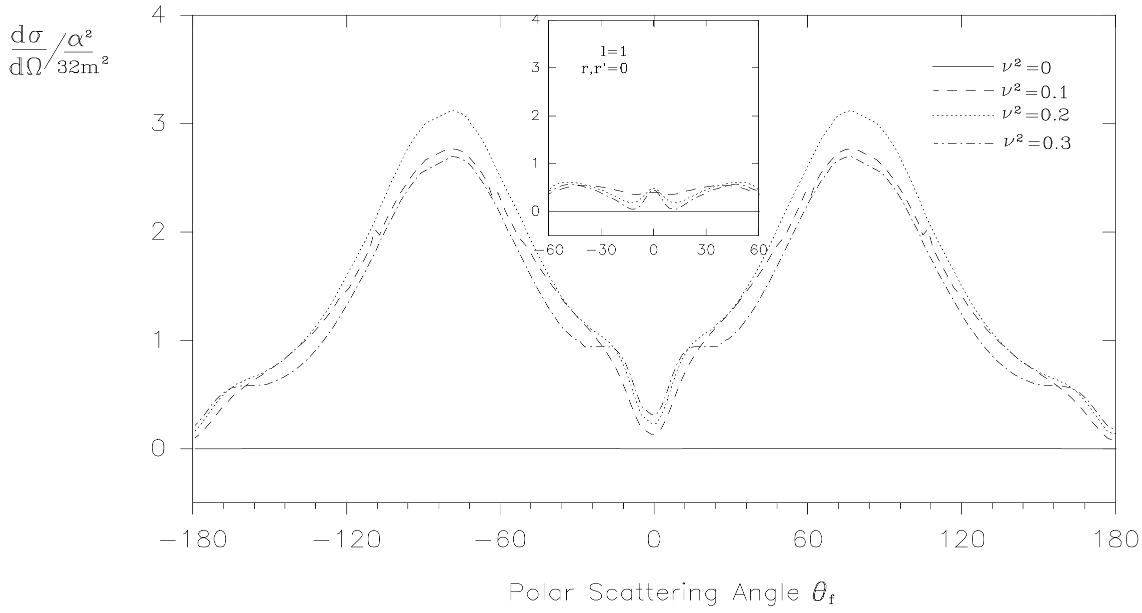

Figure 5.20: **The STPPP $l = 1$ differential cross section vs θ_f for $\omega = 0.256$ MeV, ω_1,$\omega_2 = 1.024$ MeV, $\theta_1 = 90°$, $\varphi_f = 0°$ and various ν^2.**

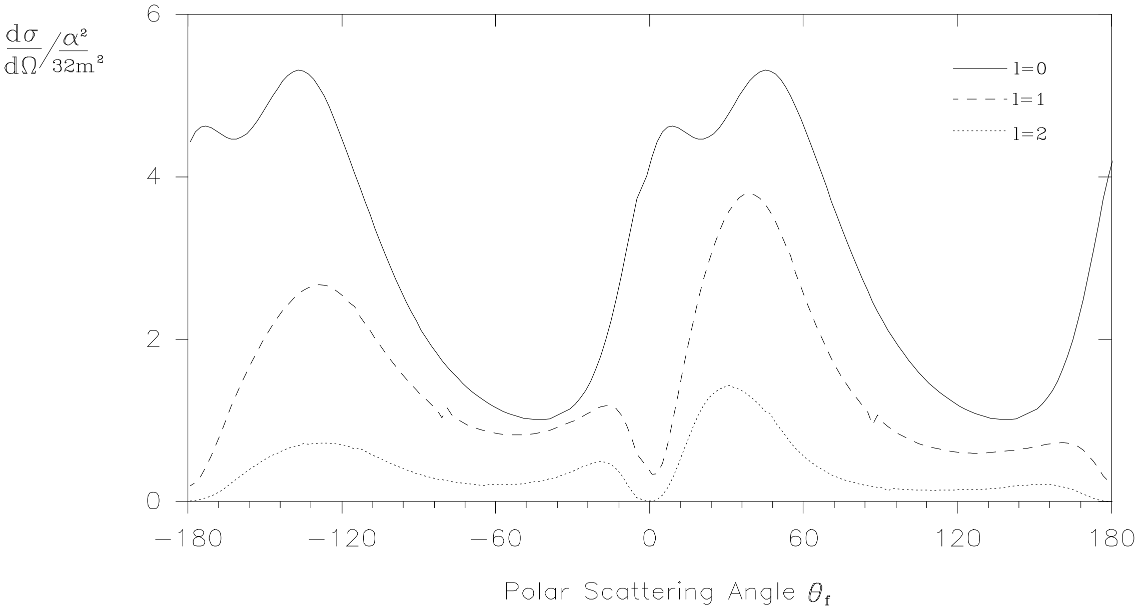

Figure 5.21: **The STPPP differential cross section vs θ_f for $\omega = 0.256$ MeV, ω_1,$\omega_2 = 1.024$ MeV, $\theta_1 = 45°$, $\varphi_f = 0°$, $\nu^2 = 0.1$ and various l.**

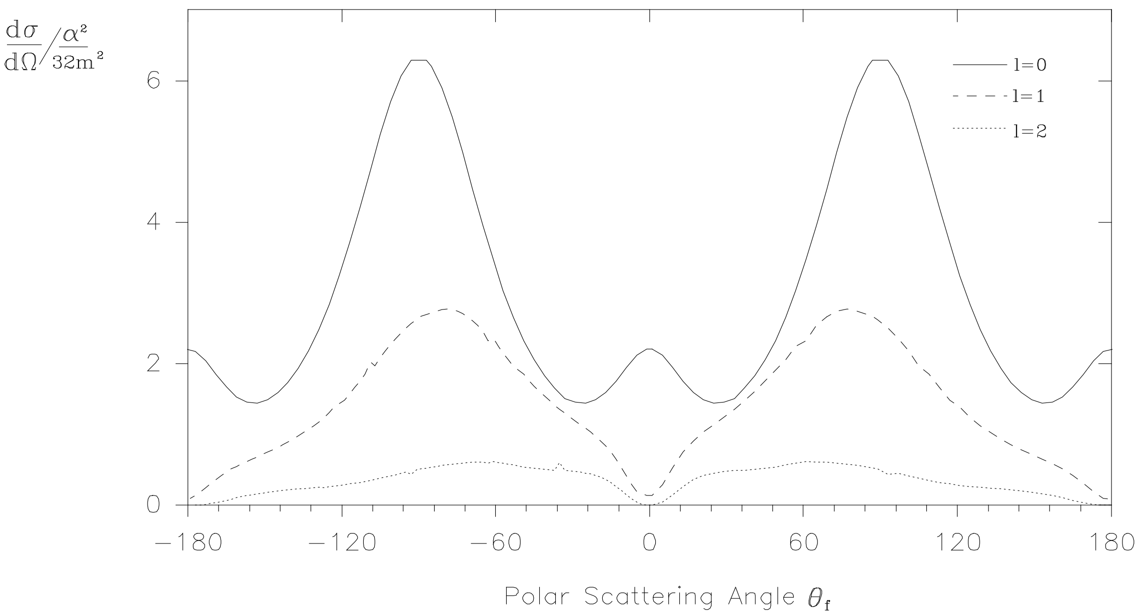

Figure 5.22: **The STPPP differential cross section vs θ_f for $\omega = 0.256$ MeV, ω_1,$\omega_2 = 1.024$ MeV, $\theta_1 = 90°$, $\varphi_f = 0°$, $\nu^2 = 0.1$ and various l.**

5.2.2 Differential Cross sections summed over all l

Table 5.2 displays the parameter values of the STPPP scattering process investigated in this section. The parameters here have exactly the same meaning as in Section 5.2.1. The STPPP differential cross section has been summed over all values l and r.

ν^2	$\omega(MeV)$	$\omega_1, \omega_2(MeV)$	θ_1	(θ_f, ϕ_f)	figure(s)
$0.00001, 0.1$	2.56	0.512	$0°, 45°,$ $90°, 180°$	$(0° \to 360°, 0°)$	5.23, 5.24
$0.0001, 0.1$	0.256	1.024	$0°, 45°,$ $90°, 180°$	$(0° \to 360°, 0°)$	5.25,5.26
$0, 0.1, 0.2, 0.3$	0.256	1.024	$0°, 45°$	$(0° \to 360°, 0°)$	5.27,5.28
$0, 0.05,$ $0.1, 0.2$	1.024	0.512	$0°, 45°$	$(0° \to 360°, 0°)$	5.29,5.30
$0, 0.1, 0.5$	0.256	1.024	$0°, 45°$	$(45°, 0° \to 360°)$	5.31,5.32
0.0001	1.024	$5.12, 2.56,$ $0.768, 0.563$	$0°, 30°$	$(0° \to 360°, 0°)$	5.33,5.34
0.1	1.024	$5.12, 2.56,$ $0.768, 0.563$	$0°, 30°$	$(0° \to 360°, 0°)$	5.35,5.36
$0 \to 1.5$	1.536	0.512	$0°, 20°, 45°$	$(45°, 0°)$	5.37
$0 \to 1.5$	0.973	1.024	$0°, 20°, 45°$	$(45°, 0°)$	5.38
$0 \to 1.5$	0.563	0.061	$0°$	$(45°, 0°)$	5.39,5.40

Table 5.2: **The parameter range for which the STPPP differential cross section summed over all l is investigated.**

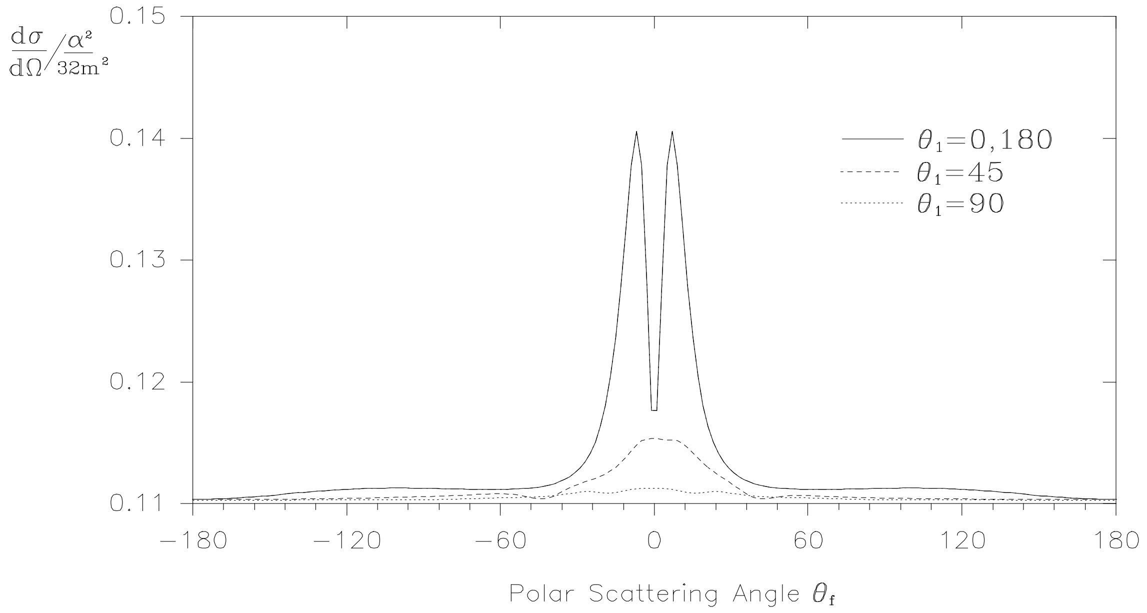

Figure 5.23: **The STPPP differential cross section vs θ_f for $\omega = 2.56$ MeV, ω_1,$\omega_2 = 0.512$ MeV, $\varphi_f = 0°$, $\nu^2 = 0.00001$ and various θ_1.**

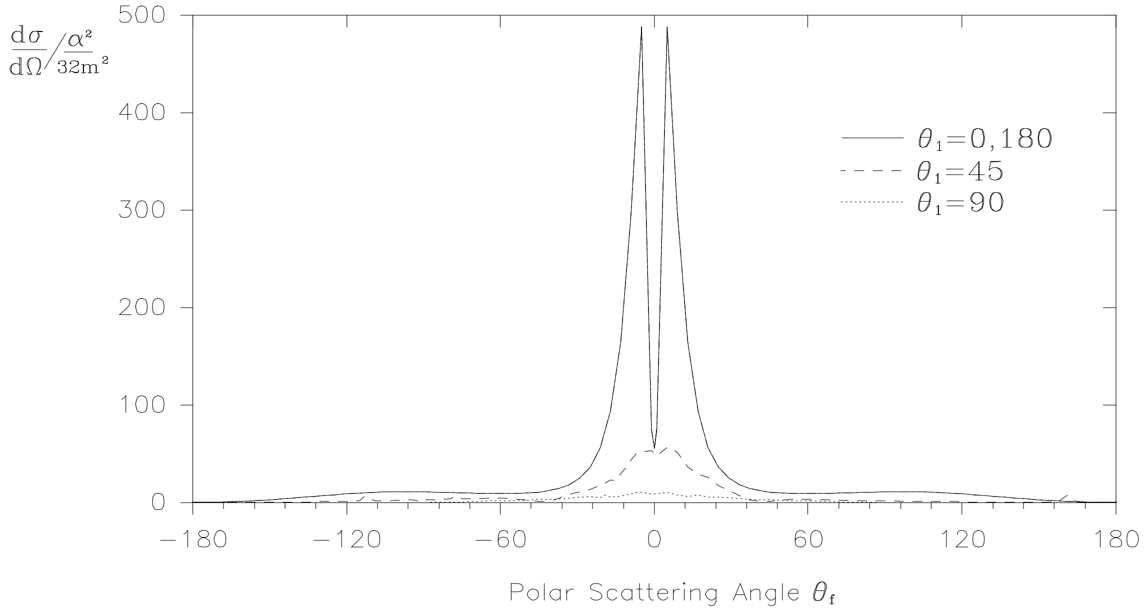

Figure 5.24: **The STPPP differential cross section vs θ_f for $\omega = 2.56$ MeV, ω_1,$\omega_2 = 0.512$ MeV, $\varphi_f = 0°$, $\nu^2 = 0.1$ and various θ_1.**

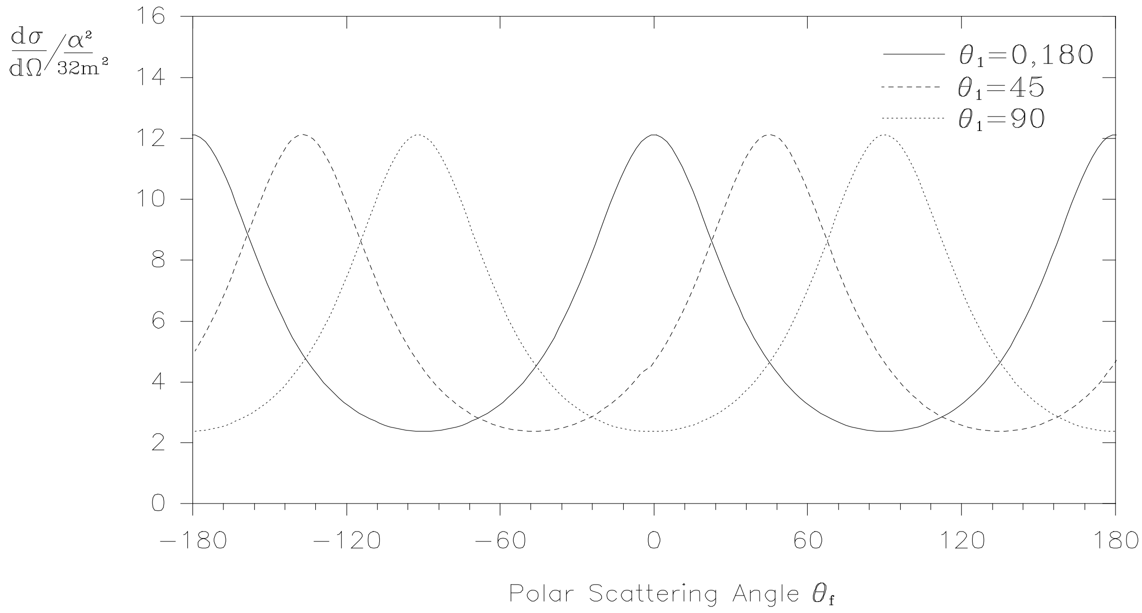

Figure 5.25: **The STPPP differential cross section vs θ_f for $\omega = 0.256$ MeV, ω_1,$\omega_2 = 1.024$ MeV, $\varphi_f = 0°$, $\nu^2 = 0.0001$ and various θ_1.**

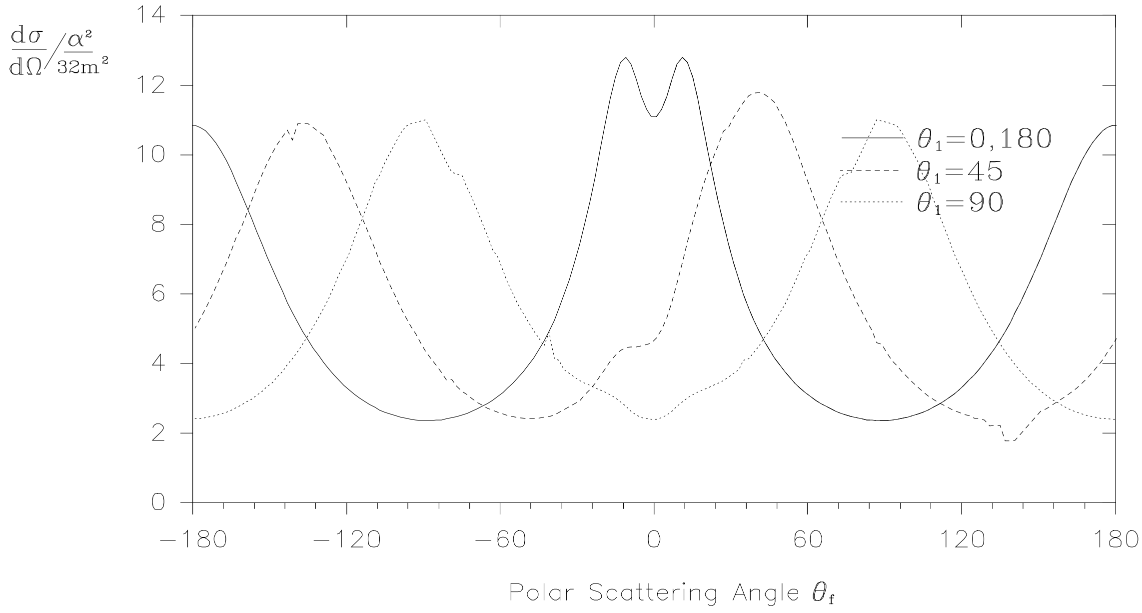

Figure 5.26: **The STPPP differential cross section vs θ_f for $\omega = 0.256$ MeV, ω_1,$\omega_2 = 1.024$ MeV, $\varphi_f = 0°$, $\nu^2 = 0.1$ and various θ_1.**

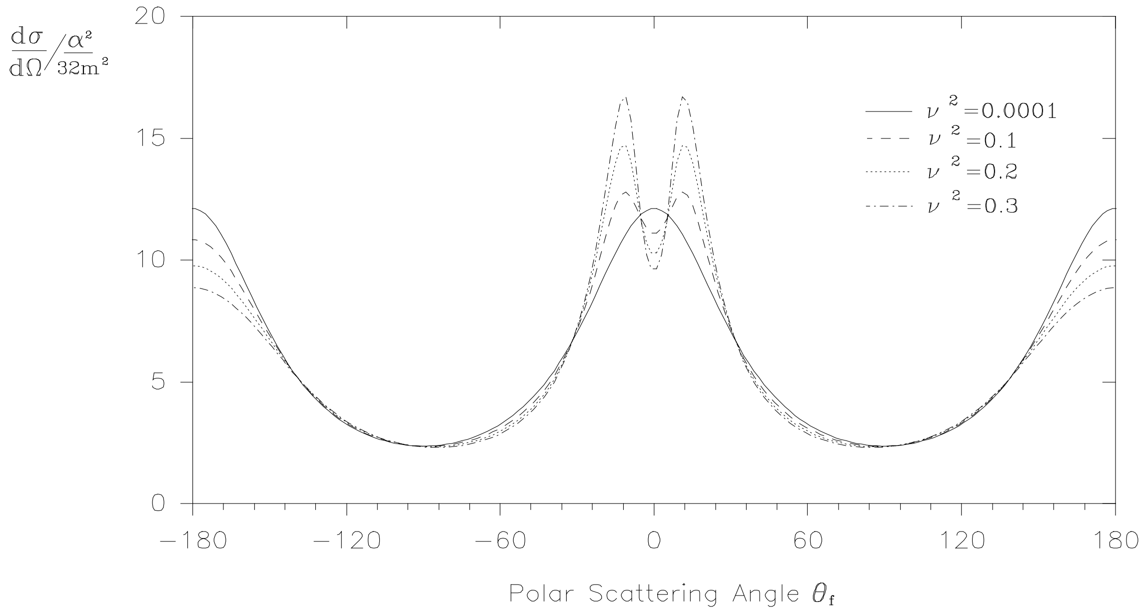

Figure 5.27: **The STPPP differential cross section vs θ_f for $\omega = 0.256$ MeV, ω_1,$\omega_2 = 1.024$ MeV, $\theta_1 = 0°$, $\varphi_f = 0°$ and various ν^2.**

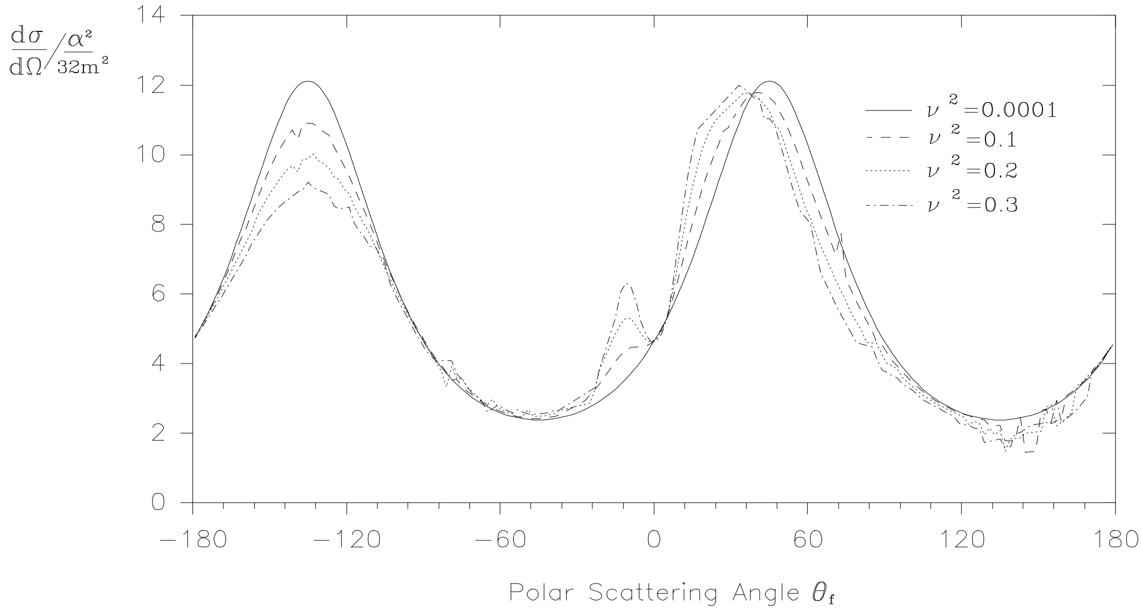

Figure 5.28: **The STPPP differential cross section vs θ_f for $\omega = 0.256$ MeV, ω_1,$\omega_2 = 1.024$ MeV, $\theta_1 = 45°$, $\varphi_f = 0°$ and various ν^2.**

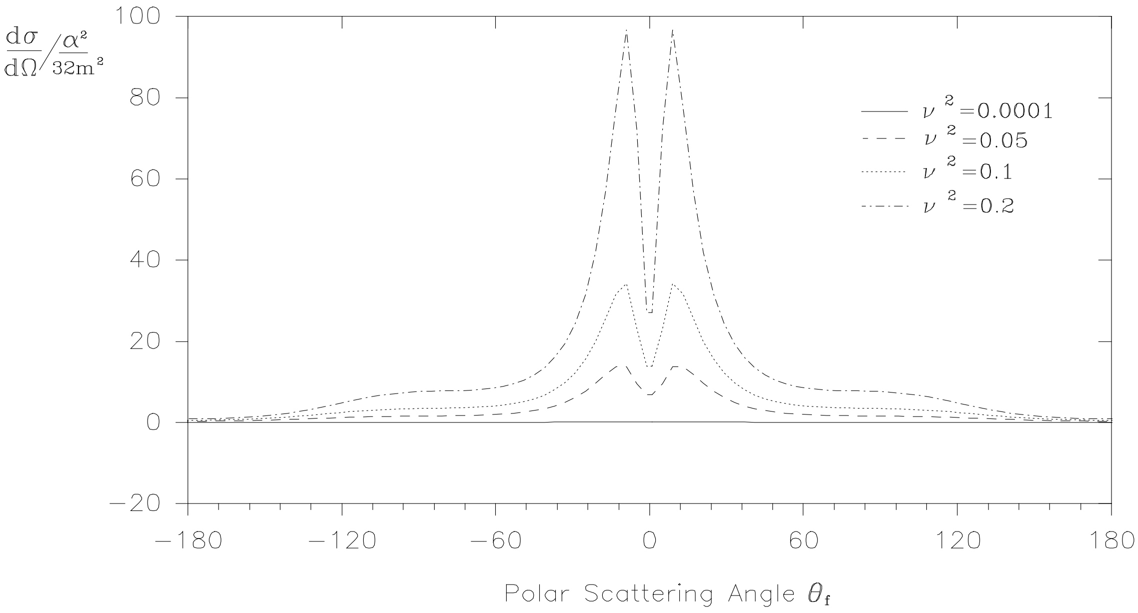

Figure 5.29: **The STPPP differential cross section vs θ_f for $\omega = 1.024$ MeV, ω_1,$\omega_2 = 0.512$ MeV, $\theta_1 = 0°$, $\varphi_f = 0°$ and various ν^2.**

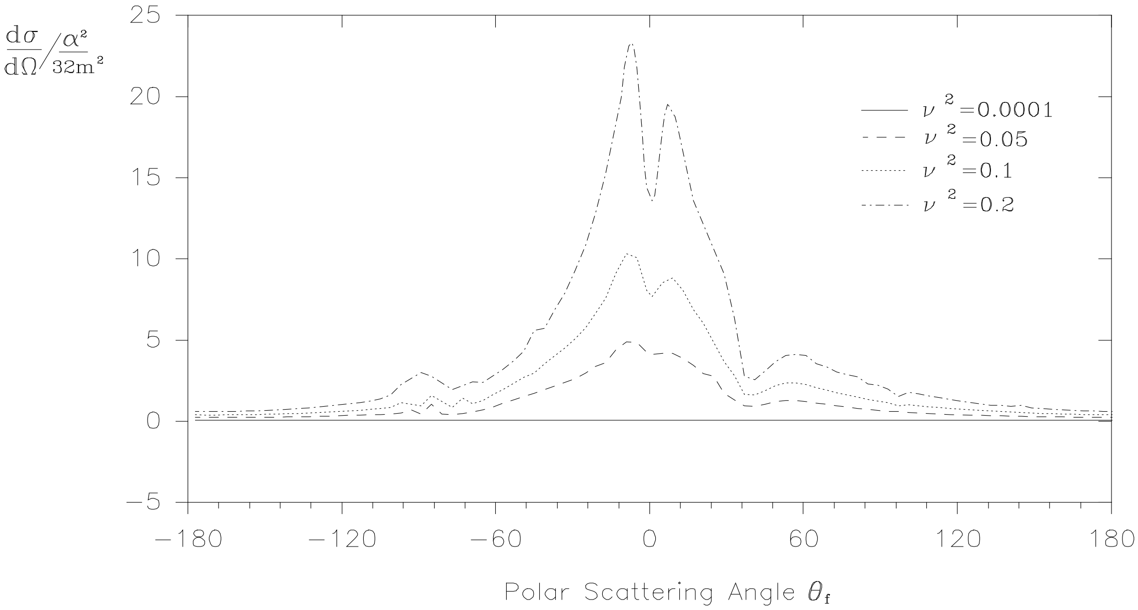

Figure 5.30: **The STPPP differential cross section vs θ_f for $\omega = 1.024$ MeV, ω_1,$\omega_2 = 0.512$ MeV, $\theta_1 = 45°$, $\varphi_f = 0°$ and various ν^2.**

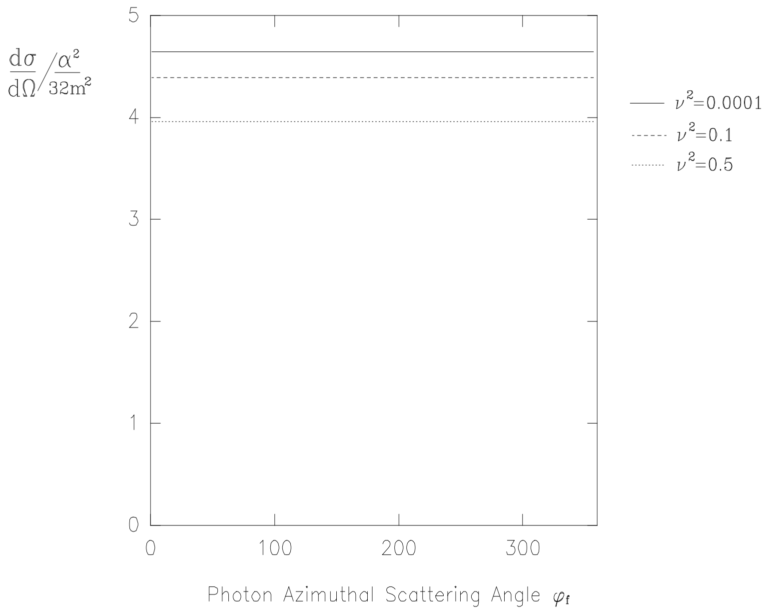

Figure 5.31: **The STPPP differential cross section vs φ_f for $\omega = 0.256$ MeV, ω_1,$\omega_2 = 1.024$ MeV, $\theta_1 = 0°$, $\theta_f = 45°$ and various ν^2.**

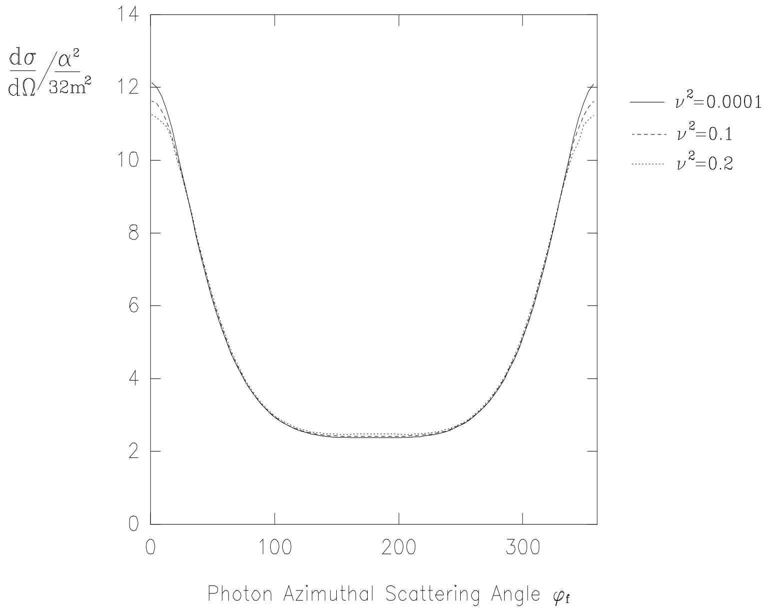

Figure 5.32: **The STPPP differential cross section vs φ_f for $\omega = 0.256$ MeV, ω_1,$\omega_2 = 1.024$ MeV, $\theta_1 = 45°$, $\theta_f = 45°$ and various ν^2.**

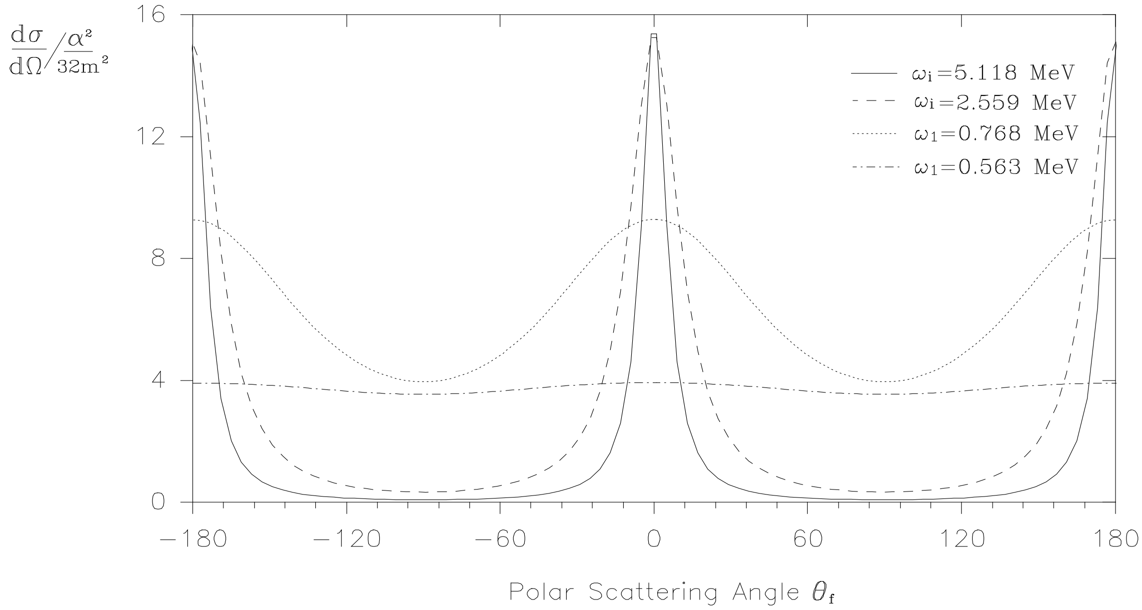

Figure 5.33: **The STPPP differential cross section vs θ_f for $\omega = 1.024$ MeV, $\theta_1 = 0°$, $\varphi_f = 0°$, $\nu^2 = 0.0001$ and various ω_1.**

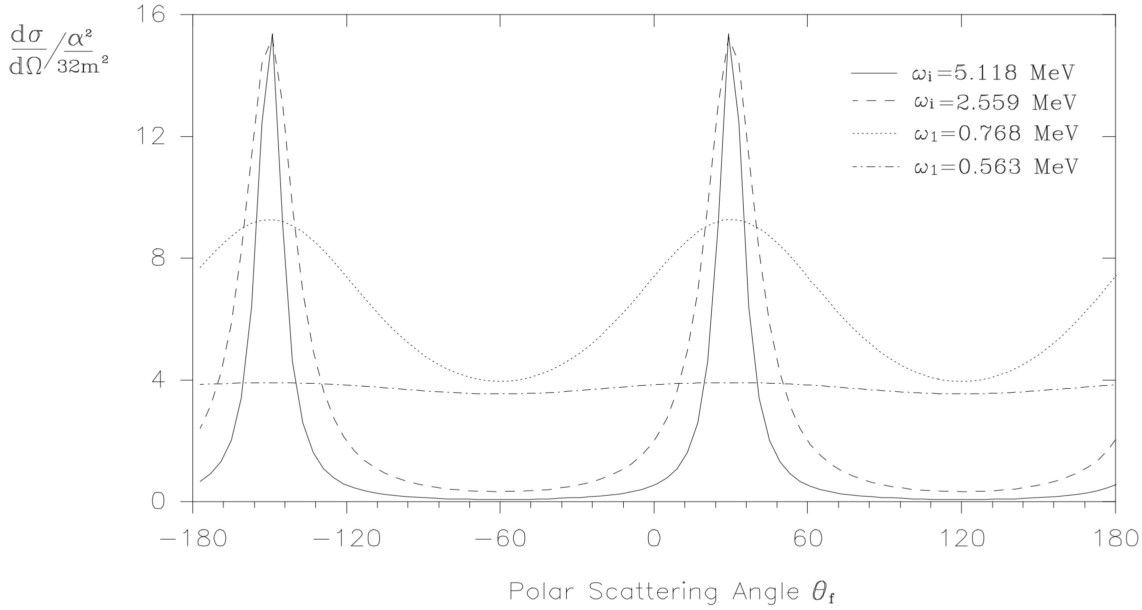

Figure 5.34: **The STPPP differential cross section vs θ_f for $\omega = 1.024$ MeV, $\theta_1 = 30°$, $\varphi_f = 0°$, $\nu^2 = 0.0001$ and various ω_1.**

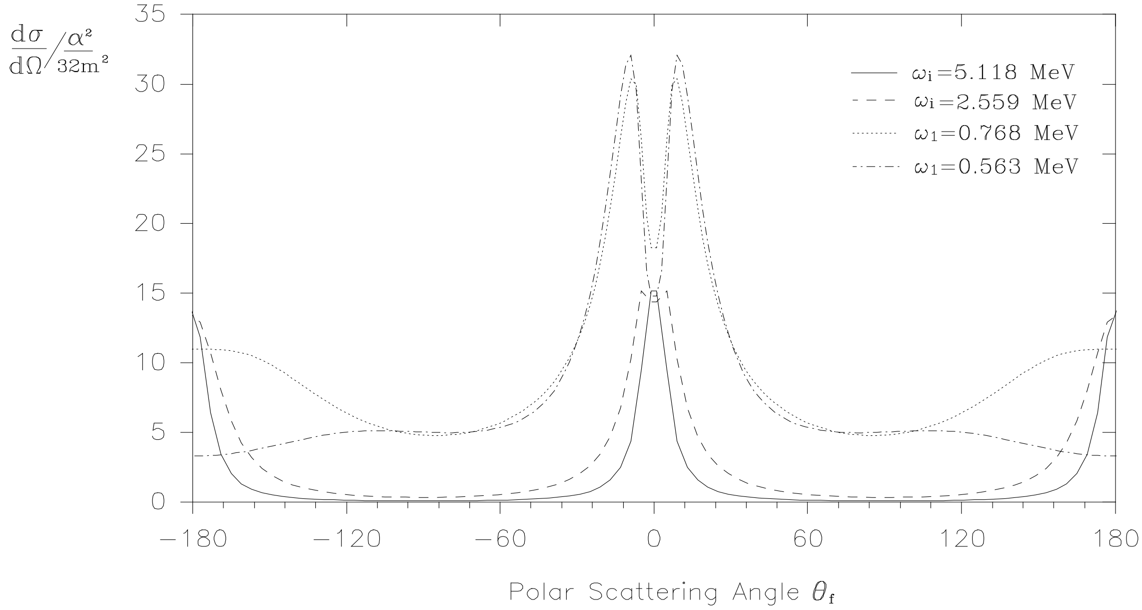

Figure 5.35: **The STPPP differential cross section vs θ_f for $\omega = 1.024$ MeV, $\theta_1 = 0°$, $\varphi_f = 0°$, $\nu^2 = 0.1$ and various ω_1.**

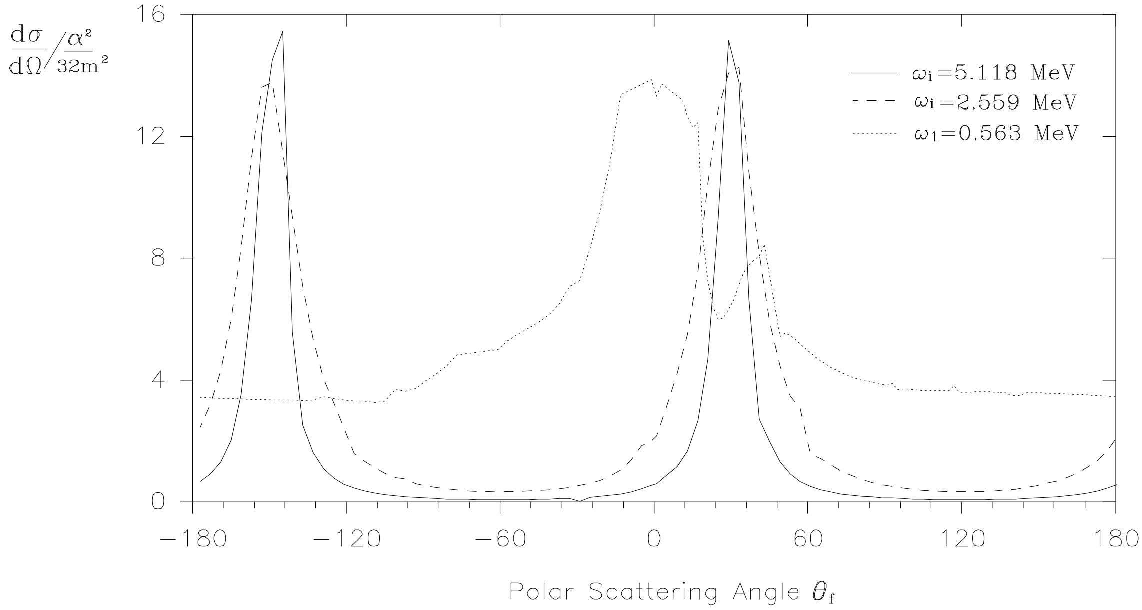

Figure 5.36: **The STPPP differential cross section vs θ_f for $\omega = 1.024$ MeV, $\theta_1 = 30°$, $\varphi_f = 0°$, $\nu^2 = 0.1$ and various ω_1.**

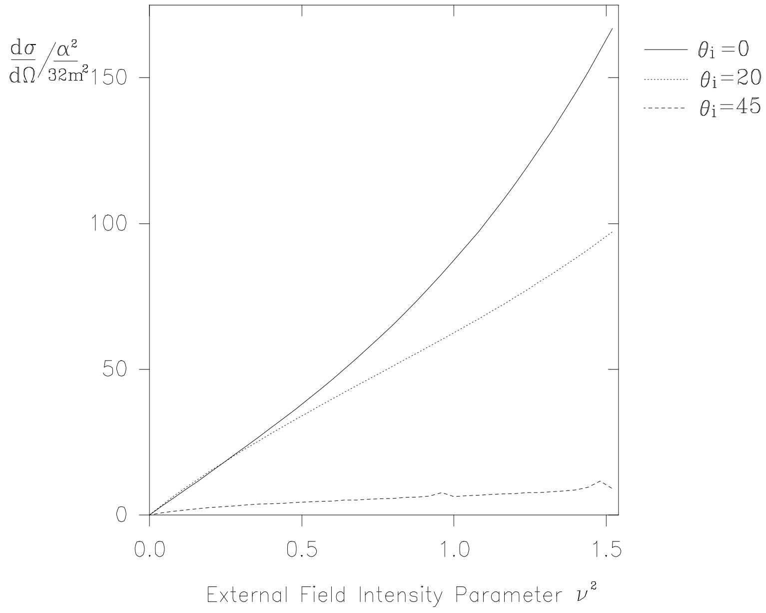

Figure 5.37: **The STPPP differential cross section vs ν^2 for $\omega = 1.536$ MeV, ω_1,$\omega_2 = 0.512$ MeV, $\theta_f = 45°$, $\varphi_f = 0°$ and various θ_1.**

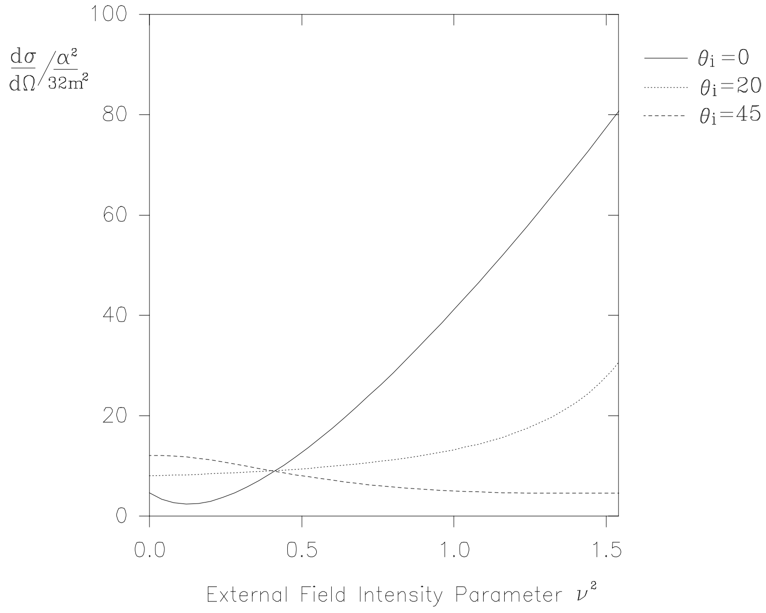

Figure 5.38: **The STPPP differential cross section vs ν^2 for $\omega = 0.973$ MeV, ω_1,$\omega_2 = 1.024$ MeV, $\theta_f = 45°$, $\varphi_f = 0°$ and various θ_1.**

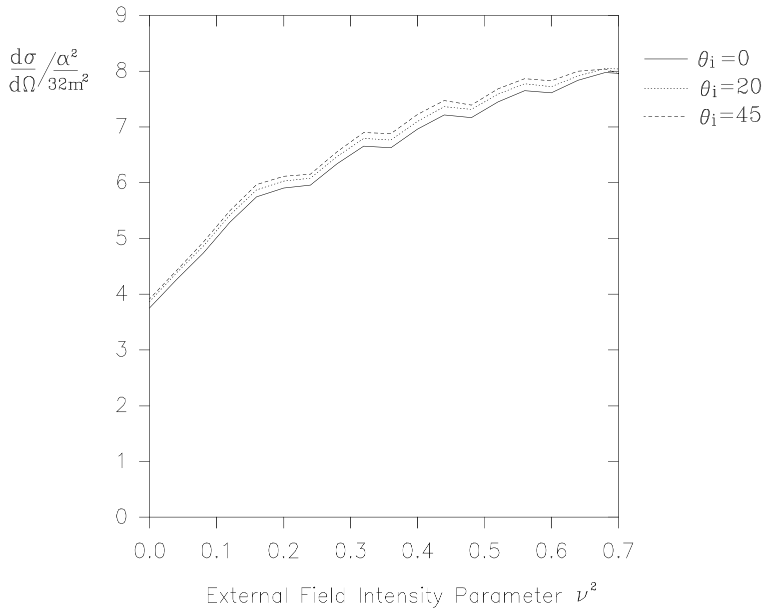

Figure 5.39: **The STPPP differential cross section vs ν^2 for $\omega = 0.061$ MeV, ω_1,$\omega_2 = 0.563$ MeV, $\theta_f = 45°$, $\varphi_f = 0°$ and various θ_1.**

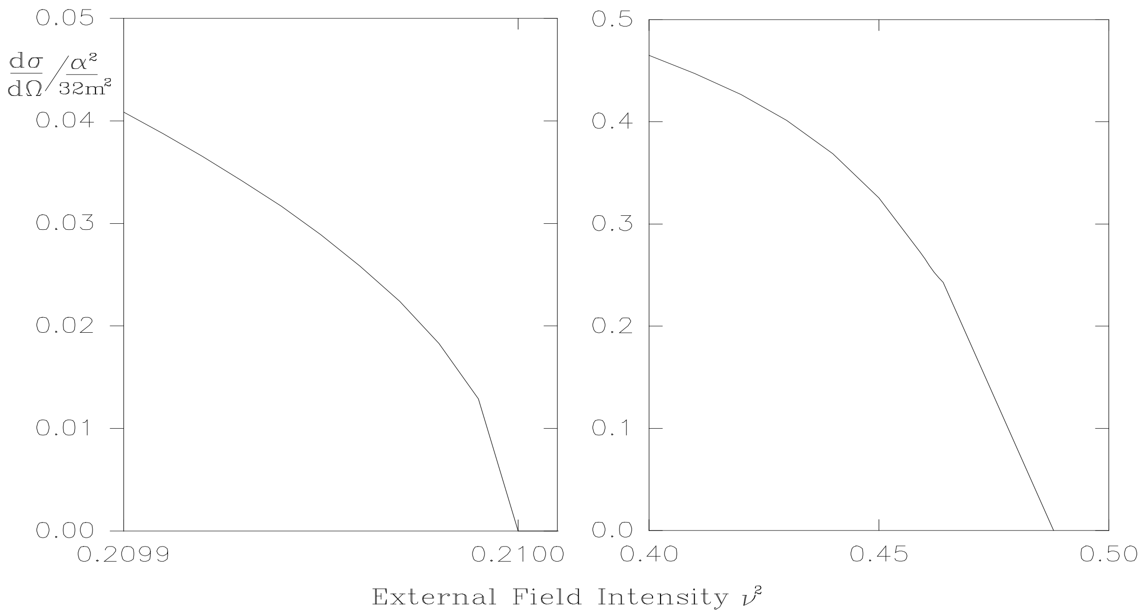

Figure 5.40: **The STPPP $l = 0$ and $l = 2$ differential cross section vs ν^2 for $\omega = 0.061$ MeV, ω_1,$\omega_2 = 0.563$ MeV, $\theta_1 = 0°$, $\theta_f = 45°$, $\varphi_f = 0°$.**

5.3 STPPP Analysis

5.3.1 Differential Cross Section l Contributions

Figures 5.1-5.4 show the variation of the STPPP differential cross section with the number l of external field photons that contribute to the process. Each figure includes several plots corresponding to different values of the external field intensity parameter ν^2.

Figures 5.1-5.2 deal with particle energies such that the ratio of initial photon energy to external field energy, $\frac{\omega_1}{\omega}$, is less than one. [1] Under these conditions the only STPPP process permitted is one in which $l \geq 0$. Conversely, Figures 5.3-5.4, for which $\frac{\omega_1}{\omega}$ is greater than unity, permit STPPP processes in which quanta is given up to the external field as long as sufficient energy is left to create the e^+e^- pair. The precise requirement for the number of laser photons energetically permitted to take part in the STPPP process is given by the inequality

$$l \geq 2\frac{\sqrt{1+\nu^2}}{\omega/m} - 2\frac{\omega_1}{\omega} \tag{5.1}$$

Figures 5.1-5.4 show the same general broadening with increasing ν^2 as the equivalent figures of Chapter 4 (figures 4.1-4.4). Increasing ν^2 leads to increasing external field photon number density and it is more likely that l external field quanta will contribute to the STPPP process.

For a fixed value of ν^2 however, figures 5.1-5.4 reveal an optimum value for l at which the differential cross section is a maximum and beyond which the differential cross section decreases [2].

This is entirely reasonable since no matter how large the external field photon density may be, it is still finite and the contribution of a still larger number of external field photons is unlikely.

The variation of the parameter ν^2 is not the sole determining factor of the variation in differential cross section with the number of laser quanta l taking part in the STPPP process. To proceed, the simplest initial scattering geometry in which the initial photons are collinear with the direction of propagation of the external field ($\theta_1 = 0°$), is considered.

Figures 5.5-5.16 consider the variation of the $l = 0, 1, 2$ STPPP differential cross section contributions with other parameters for $\theta_1 = 0°$. As was the case for the SCS process, the condition $\theta_1 = 0°$ leads to the two infinite summations over r and r' in the STPPP analytic expressions shrinking to one. The only non zero contributions to the STPPP differential cross section come from the $r = -1, 0, 1$ terms.

Figures 5.5-5.6 show the $l = 0$, $r = 0$ contribution to the STPPP differential cross section when $\theta_1 = 0°$ at different values of the initial particle energy-momenta, ω and ω_1. Each figure

[1] Due to the reference frame used the energies of the two incident photons are identical.

[2] $l = 1$ for the $\nu^2 = 0.5, 1.0$ plots and $l = 0$ for the $\nu^2 = 0.1$ plot of figure 5.1. $l = 1$ for all plots of figure 5.2. $l = 2$ for the $\nu^2 = 0.1$ plot, $l = 4$ for the $\nu^2 = 0.3$ plot, and $l = 6$ for the $\nu^2 = 0.5$ plot of figure 5.3. $l = 0$ for all plots of figure 5.4.

contains several plots corresponding to different values of the external field intensity parameter ν^2. The main feature is a $\theta_f = -180°, 0°, 180°$ peak structure, with differential cross section minimums occurring at $\theta_f = -90°, 90°$. As ν^2 increases from zero, the differential cross section generally decreases while maintaining the same peak structure. The greatest rate of decrease of the cross section occurs at $\theta_f = -180°, 0°, 180°$. The $\nu^2 = 0$ plot of figures 5.5-5.6 corresponds to two photon pair production in the absence of an external field. The $\theta_f = -180°, 0°, 180°$ peak structure can be explained by the Breit-Wheeler equation in the centre of mass reference frame

$$\frac{d\sigma}{d\Omega_{p_-}} = \frac{r_0^2}{4}\left(\frac{m}{\omega_1}\right)^2 \frac{\beta}{(1-\beta^2\cos^2\theta_f)^2}\left[1-\beta^4\cos^4\theta_f + 2\left(\frac{m}{\omega_1}\right)^2\beta^2\sin^2\theta_f\right] \tag{5.2}$$

The e^+e^- pair are most likely created such that their 3-momenta are collinear with the initial photon 3-momenta. That peaks of equal height occur at $\theta_f = -180°, 180°$ as well as $\theta_f = 0°$ is due to the identical energy of the initial photons in the centre of mass frame. As the external field intensity ν^2 increases, the e^+e^- pair gain extra momentum due to their interaction with the field of the external electromagnetic wave. At $\theta_1 = 0°$ the net momentum gained is given by

$$\frac{\nu^2}{\omega\omega_1}\frac{1}{1-(1-\frac{1+\nu^2}{\omega_1^2})\cos^2\theta_f} \tag{5.3}$$

Since the $l = 0$ term of the STPPP differential cross section does not involve a momentum contribution from external field quanta, then the momentum required to produce the e^+e^- pair embedded in the external field must come from the initial photon momenta. Less energy is available to create the pair and the result is a decrease in the differential cross section. That this decrease is not constant for all final scattering geometries is due to the angular dependence of equation 5.3. At $\theta_f = -180°, 0°, 180°$ the net momentum gain due to the external field is a maximum, and for fixed ν^2, ω_1 and ω, the decrease in the differential cross section is also a maximum. The converse is true at $\theta_f = -90°, 90°$.

Figures 5.7-5.8 compare the $l = 0$, $r = 0$ and $l = 0$, $r =$all contributions to the STPPP differential cross section with the Breit-Wheeler differential cross section for initial scattering angle $\theta_1 = 0°$. The main feature is the $\theta_f = -180°, 0°, 180°$ peak structure, the origin of which has been discussed previously. Comparison of figure 5.7 to figure 5.8 reveals that the magnitude of the differential cross section seems to depend on the ratio $\frac{\omega_1}{\omega}$. Figure 5.7 with $\frac{\omega}{\omega_1} = 3.3$ displays a $l = 0$, $r =$ all contribution in excess of the Breit-Wheeler plot, and figure 5.8 with $\frac{\omega}{\omega_1} = 0.13$ displays a $l = 0$, $r =$all plot of lower magnitude than the Breit-Wheeler plot. As the external field is switched on, the e^+e^- pair produced in the STPPP process require a greater initial momentum to be created, consequently the $l = 0$, $r = 0$ plots of figures 5.7-5.8 lie below the Breit-Wheeler plots.

The contribution from the $l = 0$, $r = \pm 1$ plots is actually dependent on the comparative values of ω, ω_1 and m_*. In figure 5.7 the initial photon does not have enough energy to create the pair and enable a quantum to be given up to the external field. So the $r = -1$ contribution is suppressed and the $r = 1$ contribution alone increases the $\theta_f = -180°, 0°, 180°$ peaks due to the availability of extra momentum. In figure 5.8 there is more than enough energy for quanta to be given up. The $r = -1$ contribution outweighs the effect of the $r = 1$ contribution and there is a diminished momentum available for the e^+e^- pair.

Figures 5.9-5.12 display the effect on the total $l = 0$ contribution of increasing the external field intensity for differing values of the ratio of particle energy $\frac{\omega_1}{\omega}$. The main feature of all four figures is a central peak centred at $\theta_f = 0°$ which diminishes in height as the external field intensity increases. Peak widths vary with $\frac{\omega_1}{\omega}$, the narrowest obtained for figure 5.9 with $\frac{\omega_1}{\omega} = 10$ increasing in size to the largest width in figure 5.12 with $\frac{\omega_1}{\omega} = 0.15$. Another feature dependent on the value of $\frac{\omega_1}{\omega}$ is a secondary and more complicated peak structure. [3]

The behaviour here can be explained by examination of the arguments of the Bessel functions which are nonzero when fermions involved in the scattering process propagate in directions other than the direction of propagation of the external field. The fermion momenta gain a longitudinal oscillatory components which can be interpreted as the contribution of external field quanta to the STPPP process. With $l = 0$, $\theta_i = 0°$ and $F(\cos\theta_f)$ being a function that is minimised at $\theta_f = -180°, 0°, 180°$, the Bessel function arguments are

$$\begin{aligned} \bar{z} &= \nu \frac{\omega_1}{\omega} F(\cos\theta_f) && \text{direct channel} \\ \bar{\bar{z}} &= 0 && \text{exchange channel} \end{aligned} \tag{5.4}$$

The onset of secondary (and more complicated) peak structure in figures 5.9-5.10 coincides with large $\frac{\omega_1}{\omega}$ (and therefore large $\bar{z}$). In the range $-60° < \theta_f < 60°$ $\bar{z}$ varies greatly and the Bessel function along with the differential cross section is oscillatory. This oscillatory behaviour is enhanced by increasing external field intensity due to the direct relationship between $\bar{z}$ and ν.

Where the ratio $\frac{\omega_1}{\omega}$ is small ($\frac{\omega_1}{\omega} = 0.4$ for figure 5.11 and $\frac{\omega_1}{\omega} = 0.15$ for figure 5.12) the argument $\bar{z}$ achieves a small maximum value and the form of the differential cross section is a single peak centred at $\theta_f = 0°$.

Figures 5.13-5.16 compare the $l = 0, 1, 2$ contributions to the STPPP differential cross section for a field intensity of $\nu^2 = 0.5$ and varying particle energies. The main features of these figures are the development of a dual $\theta_1 \sim 0°$ peak structure for higher values of l, peak heights which become larger at $\theta_f \sim 0°$ than at $\theta_f = -180°, 180°$ when l increases, and relative l contributions to the differential cross section which vary with the value of $\frac{\omega_1}{\omega}$.

[3] the $\nu^2 = 1, 2$ plots of figure 5.9 ($\frac{\omega_1}{\omega} = 10$) and figure 5.10 ($\frac{\omega_1}{\omega} = 2.5$) display a twin peak structure.

We examine the differing $\theta_f = -180°, 0°, 180°$ peak heights first. The e^+e^- pair are more likely produced with 3-momenta collinear with initial photon momenta. When external field quanta contribute to the STPPP process momentum is available for fermion production and the differential cross section peak increases in the direction of propagation of the external field ($\theta_f = 0°$). The disparity between peak heights increases as the energy of external field quanta increase relative to the energy of the initial photons (i.e. $\frac{\omega_1}{\omega}$ decreases) and the disparity is larger for the $l = 2$ contributions than for the $l = 1$ contributions. Table 5.3 displays the trend.

Mathematically the dual peak arises from the numerical value of $\bar{z}$ (equation 5.4) which is related to longitudinal components of fermion momentum obtained from interaction with the external field. $\bar{z}$ is small at $\theta_f = -180°, 0°, 180°$. The dual peak structure at $\theta_f \sim 0°$ is evidence of two competing trends. On one hand extra momentum is available for fermion production. On the other, momentum is not absorbed from the external field very well at $\theta_f = -180°, 0°, 180°$. The two trends have different angular spreads resulting in a dual peak. This dual peak also appears in figures 5.13-5.16 at $\theta_f \sim -180°, 180°$ however its diminished by the preferential direction of propagation of the external field.

The relative contributions to the STPPP differential cross section for $l = 0, 1$ or 2 external field quanta contributing to the scattering process, can only be determined precisely by a numerical calculation of the complete differential cross section expressions. However a correlation can be established between the number of final states available for the scattering process and the relative peak heights of figures 5.13-5.16 in the $\theta_f = 0°$ region (see Table 5.4).

STPPP processes for angles other than $\theta_1 = 0°$ are now considered. Differential cross section peaks are generally broad so only $\theta_1 = 45°, 90°$ are considered. In order to avoid resonances (which are studied in Chapters 6 and 7) ω_1 was chosen to be considerably larger than ω.

Figures 5.17, 5.19 and 5.21 consider the STPPP process at $\theta_1 = 45°$. Figure 5.17 and 5.19 show the variation of the $l = 0$ and $l = 1$ contributions for various ν^2, and figure 5.21 compares the $l = 0$, $l = 1$ and $l = 2$ contribution when $\nu^2 = 0.1$. Figures 5.18, 5.20 and 5.22 are identical to figures 5.17, 5.19 and 5.21 except that $\theta_1 = 90°$. The insets of each of figures 5.17-5.20 show the $l = 0$, $r, r' = 0$ contributions to the STPPP process in the region $-60° \leq \theta_f \leq 60°$ for the same

figure	$l = 1 : l = 0$	$l = 2 : l = 0$	$\frac{\omega}{\omega_1}$
5.13	0.723	0.5	0.05
5.14	1.56	1.046	0.4
5.15	2.77	3.96	1.25
5.16	12.26	22.52	2.5

Table 5.3: **The ratio of peak heights and particle energies for figures 5.13 - 5.16.**

parameters considered in the parent plots. For all six figures 2 MeV initial photons combine with 0.5 MeV external field quanta to produce the e^+e^- pair.

The main feature of figures 5.17-5.18 is a twin transverse peak structure ($\theta_f = -135°, 45°$ for figure 5.17 and $\theta_f = -90°, 90°$ for figure 5.18) which diminishes as ν^2 increases. Secondary to both figures is the appearance of a smaller longitudinal ($\theta_f = -180°, 0°, 180°$) peak structure as ν^2 increases from zero. As ν^2 reaches 0.3 the longitudinal peak structure dominates, having approximately twice the height of the transverse peaks. The origin of the transverse peaks is due to the likelihood that the e^+e^- pair will be created with 3-momenta collinear to that of the initial photons. As ν^2 increases so does the e^+e^- rest mass and the initial energy required to produce the pair, and there is a general decrease in the differential cross section.

The emergence of the $\theta_f = -180°, 0°, 180°$ peaks have their origin in differential cross section terms other than the $r, r' = 0$ contribution. This is indicated by the insets of figures 5.17 and 5.18. Once again these peaks are due to the net momentum gained by the e^+e^- pair due to exchange of quanta with the external field (equation 5.3). The effect is enhanced as ν^2 increases.

Figures 5.19 and 5.20 which display the $l = 1$ contribution reveal a zero differential cross section when $\nu^2 = 0$. This is a trivial result relating to the inability of the external field to contribute quanta to the STPPP process when the field intensity is zero. Limits of computational accuracy were reached whilst generating the $\nu^2 \neq 0$ plots resulting in small "jittery" features. These can be ignored. The main feature of these figures is a transverse peak structure with the $\theta_f = 45°$ peak approximately 1.4 times the height of the $\theta_f = -135°$ peak for figure 5.19, and $\theta_f = -90°, 90°$ peaks of equal height for figure 5.20. The contribution of quanta from the external field ensures that scattering in the forward direction ($-90° \leq \theta_f \leq 90°$) is preferred. A second feature of both figures is a localised decrease or trough at $\theta_f = -180°, 0°, 180°$ regions. This is related once again to the ability of the fermions to absorb external field quanta at these points.

Figures 5.21 and 5.22, which compare the $l = 0$, $l = 1$ and $l = 2$ contributions at $\nu^2 = 0.1$

figure	$l = 1$:$l = 0$ density of final states	$l = 1$:$l = 0$ differential cross section	$l = 2$:$l = 1$ density of final states	$l = 2$:$l = 1$ differential cross section	$l = 2$:$l = 0$ density of final states	$l = 2$:$l = 0$ differential cross section
5.13	1.077	0.72	1.071	0.7	1.154	0.5
5.14	1.59	1.56	1.35	0.67	2.14	1.05
5.15	2.74	2.74	1.59	1.43	4.36	3.91
5.16	4.36	12.27	1.73	1.84	7.55	22.54

Table 5.4: **A comparison of the number of final states and the differential cross section values for various ratios of l contributions for the STPPP process represented in figures 5.13 - 5.16.**

show all the features discussed in the previous four figures. It is reasonably clear that summing the contributions together will produce dual longitudinal peaks and transverse peaks collinear with the initial photons. The next section will examine total STPPP differential cross sections for all l contributions added together.

5.3.2 Differential Cross Sections Summed Over All l

Figures 5.23-5.26 show the effect on the STPPP process of varying the initial angle θ_1. Each figure contains several plots corresponding to $\theta_1 = 0°, 45°, 90°$ and $180°$. Figures 5.23-5.24 show a STPPP process in which 0.512 MeV photons combine in a 2.56 MeV external field for $\nu^2 = 0.00001$ and $\nu^2 = 0.1$ respectively.

The main feature of both figures is a peak structure centered around $\theta_f = 0°$. For both figures the $\theta_1 = 0°$ plot (identical to the $\theta_1 = 180°$ plots in the centre of mass reference frame) has a double peak at $\theta_f \sim 0°$. The $\theta_1 = 45°$ and $\theta_1 = 90°$ plots reveal a single, flattened peak. The $\theta_1 = 0°, 180°$ plot peaks are of greatest height, having a value of 0.14 in figure 5.23 and approximately 500 in figure 5.24. The $\theta_1 = 45°$ and $\theta_1 = 90°$ plots show a large diminishment in peak height, with the $\theta_f = 0°$ peak almost vanishing for the $\theta_1 = 90°$ plots. We note that the vertical axis of figure 5.23 has a minimum bound of 0.11.

The energy of initial photons, being precisely the rest mass of the e^+e^- pair in the absence of the external field, do not create the e^+e^- pair in the presence of the external field due to the higher fermion rest mass required. Consequently the only non zero contributions to the STPPP differential cross section are those in which one or more external field quanta are absorbed. In figure 5.23, which represents an STPPP process in which the external field intensity is very small, the probability of the external field giving up quanta to the STPPP process is correspondingly small and differential cross section peaks don't exceed 0.14. The STPPP process represented in figure 5.24, with higher external field intensity, has a correspondingly higher probability.

The $\theta_f = 0°$ location of differential cross section peaks no matter what the value of θ_1 is explained by the momentum contribution from external field quanta which dominate the STPPP process in figures 5.23 and 5.24. Since the initial photons k_1 contribute no momentum to the fermion pair, the most likely direction of both electron and positron 3-momenta is parallel to the direction of propagation of the external field. The double peak structure of the $\theta_1 = 0°$ plots of both figures is explained by a combination of two competing factors. On one hand the probability of pair production is increased in directions parallel to the 3-momenta of external field quanta ($\theta_f = 0°$). On the other hand, when $\theta_1 = 0°$ there is a decreased probability that external field quanta will participate in the STPPP process when the e^-e^+ pair are co-linear with the direction of propagation of the external field ($\theta_f = 0°$).

For an analysis of relative peak heights the Breit-Wheeler equation for two photon pair production in the centre of mass frame is of use (equation 5.2) For energetic photons the Breit-Wheeler differential cross section is large but strongly dependent on how collinear the produced fermions are with initial photons. The external field supplies plenty of energy to create the pair, but the momenta of external field quanta require the pair be created at $\theta_f = 0°$. Consequently the STPPP process is highly favoured for $\theta_1 = 0°$ and disfavoured elsewhere.

Figures 5.25-5.26 show a STPPP process in which 1.024 MeV photons combine with 0.256 MeV external field quanta to produce the e^+e^- pair. For this ratio of particle energies ($\frac{\omega_1}{\omega} = 4$), $l = 0$ contributions to the differential cross section dominate the $l \neq 0$ contributions.

Figure 5.25 shows a STPPP process with a very low intensity external field ($\nu^2 = 0.0001$) and is essentially a Breit-Wheeler process with a differential cross section that peaks whenever the e^+e^- 3-momenta is collinear with the 3-momenta of initial photons. As θ_1 changes, the differential cross section θ_f peaks shift by the same amount and remain the same height. This indicates the negligible impact of the external field on the STPPP process in this case.

By comparison, figure 5.26 with an external field intensity parameter of 0.1 reveals the effect of switching on the external field. The $\theta_1 = 0°$ plot of figure 5.26 reveals a $\theta_f = -180°, 0°, 180°$ peak structure with the $\theta_f = -180°, 180°$ peaks diminished due to the direction of propagation of the external field. The $\theta_f \sim 0°$ twin peak is generally enhanced due to the contribution of external field quanta, but diminished at $\theta_f = 0°$ due to the lower probability that the external field will contribute quanta at that point. In comparison with the behaviour of the $\theta_1 = 0°$ STPPP differential cross section in the $\theta_f = 0°$ region of figures 5.23-5.24, the double peak behaviour of figure 5.26 is minimal. This is again due to relative particle energies. The other plots of figure 5.26 show a similarly small impact from the external field. The $\theta_1 = 45°$ plot shows a slight enhancement of the $\theta_f = 45°$ peak relative to the $\theta_f = -135°$ peak, due to components of the external field quanta 3-momenta contributing positively in the $\theta_f = 45°$ direction. The $\theta_1 = 90°$ plot shows peaks of equal height shifted slightly in the forward direction ($\theta_f = -88°, 88°$).

Figures 5.27-5.30 show the effect of increasing external field intensity in more detail. Figures 5.27-5.28 show a STPPP process in which 1.024 MeV photons are incident on a 0.256 MeV external field. In figure 5.27 the incident photons are collinear with the direction of propagation of the external field, in figure 5.28 their 3-momenta intersect at $45°$. Figures 5.29-5.30 have the same respective θ_1 values but with 0.512 MeV photons incident on a 1.024 MeV external field.

The $\nu^2 = 0.0001$ plots of all four figures displays the differential cross section θ_f variation expected of the Breit-Wheeler process. Figures 5.27-5.28 with incident photons twice the energy of the e^+e^- pair rest mass, display the usual peaks collinear with initial photons. Figures 5.29-5.30 show a STPPP process in which the initial photons have just sufficient energy to create the e^+e^- pair, and the $\nu^2 = 0.0001$ plot is consequently very close to zero.

The main feature of figures 5.27 and 5.29 ($\theta_1 = 0°$) is the development of a twin peak structure in the $\theta_f \simeq 0°$ region. As has been discussed previously, this behaviour is attributable to contributions to the STPPP process from external field quanta. This feature is more marked in figure 5.29 [4] which has relative particle energies ($\frac{\omega_1}{\omega} = 0.5$) in which external field quanta contributions dominate. Figure 5.27 shows a differential cross section that diminishes with increasing ν^2 at $\theta_f = -180°, 0°, 180°$. This is due to a combination of increasing e^+e^- rest mass and low probability of $l \neq 0$ contributions when $\frac{\omega_1}{\omega} > 1$.

Figures 5.28 and 5.30 display a loss of azimuthal symmetry associated with initial scattering geometries in which $\theta_1 \neq 0°$. The main feature of figure 5.28 is the development of a dual asymmetric $\theta_f \sim 0°$ peak. The positive θ_f peak merges with the $\theta_f = 45°$ peak collinear with initial photons, seemingly shifting it. The ratio $\frac{\omega_1}{\omega} > 1$ and the dual longitudinal peaks are small.

The diminishment of the $\theta_f \simeq -135°$ peak height is again due to the 3-momenta of external field quanta, components of which diminish the electron 3-momenta for scattering geometries in which the electron travels in backward directions. [5] The "noisy" behaviour of the $\nu^2 = 0.1, 0.2$ and 0.3 plots in the region $120° < \theta_f < 170°$ is not a feature of the STPPP process. It's origin lies in the accuracy restrictions imposed on the computation of the differential cross section.

The main feature dominating figure 5.30 is the development of a dual peak centered at $\theta_f = 0°$, which is to be expected for the energy regime in which external field quanta are more energetic than the initial photons. The twin peak is not symmetrical, with the $\theta_f = -7°$ peak of greater height than the $\theta_f = 7°$ peak. The $\theta_f = -135°, 45°$ peaks have been shifted towards the forward direction under the impact of the relatively more energetic external field quanta. The $\theta_f = -135°$ peak shifts to $\theta_f = -90°$ and the $\theta_f = 45°$ peak is partially obscured by the positive θ_f peak. A secondary feature of figure 5.30 is the development of a smaller peak at $\theta_f \simeq 55°$.

The asymmetric $\theta_f \sim 0°$ dual peak is explained by competing factors. Positive θ_f pair production is enhanced because its more nearly collinear with initial photons. However when the electron is directed to negative θ_f directions ($\theta_f \sim -7°$) and further away from the collinear direction, the probability of external field quanta contributing to the process increases. This is so because with $\theta_1 \neq 0$ the relations expressing the longitudinal fermion momentum contributions (equation 5.4) become asymmetric with respect to θ_f. In the relative particle energy regime considered, the second factor outweighs the first and the $\theta_f \sim -7°$ peaks are of greater height than the $\theta_f \sim 7°$ peaks.

The $\theta_f \sim 55°$ peak is explained by the expression for the net momentum gained by the e^+e^- pair due to the interaction with the external field, an expression considerably more complicated than that for the $\theta_1 = 0°$ case. A numerical evaluation reveals that the net momentum is at its minimum at $\theta_f = -53°$ and $\theta_f = 53°$ for the $l = 1$ contribution, and at these points the probability of pair

[4] The $\nu^2 = 0.2$ plot of figure 5.27 reaches a maximum height of 14.72 whereas the $\nu^2 = 0.2$ plot of figure 5.29 reaches a maximum height of 96.74.

[5] i.e. whenever $-180° \leq \theta_f \leq -90°$ and $90° \leq \theta_f \leq 180°$.

production is consequently maximised. The effect is small with only the $\theta_f \simeq 55°$ peak visible due to the positive contribution from external field quanta at that point.

Figures 5.31-5.32 show the azimuthal (ϕ_f) variation of the STPPP differential cross section for 1.024 MeV photons incident on a 0.256 MeV external field. For figure 5.31 $\theta_1 = 0°$ and $\theta_f = 45°$. With this geometry, the differential cross section is unchanged as ϕ_f ranges from $0°$ to $360°$. This is due to the circular polarisation of the external field which, along with $\theta_1 = 0°$ initial photons remain unchanged by rotation through azimuthal angles. That the differential cross section decreases with increasing ν^2 is due to the increase in the e^+e^- pair rest mass.

Figure 5.32 examines azimuthal variation when $\theta_1, \theta_f = 45°$ The STPPP process is most favourable at $\phi_f = 0°$, and least favourable at $\phi_f = 180°$. The explanation here is a geometrical one. At $\phi_f = 0°$ the e^+e^- pair and the initial photons are collinear, and at $\phi_f = 180°$ perpendicular.

Figures 5.33-5.36 show the effect of varying the ratio of initial photon energy to the energy of external field quanta. Each figure contains four plots with incident photons of varying energy incident on a 1.024 MeV external field. Figures 5.33-5.34 show a STPPP process with a very small external field intensity $\nu^2 = 0.0001$ and an incident angle of $\theta_1 = 0°$ and $\theta_1 = 30°$ respectively. Figures 5.35-5.36 have the same scattering geometry with an external field intensity $\nu^2 = 0.1$.

The main feature of figures 5.33-5.34 is a Breit-Wheeler, collinear peak structure ($\theta_f = -180°, 0°, 180°$ for $\theta_1 = 0°$ and at $\theta_f = -150°, 30°$ for $\theta_1 = 30°$). The peaks broaden out and decrease in height as ω_1 approaches the rest mass of the STPPP fermion (0.512 MeV for figure 5.33, and 0.537 MeV for figure 5.34).

That the STPPP differential cross section behaves like that of the Breit-Wheeler process is due to the very low external field intensity which ensures that the external field plays little part. The peak structure is due to the 3-momenta of the initial photons, and the decrease in peak height with decreasing ω_1 is a consequence of the decrease in 3-momenta available to the e^+e^- pair from the initial photons.

Figures 5.35-5.36 have the same parameters as the previous two figures but with significant external field intensity. The main feature of figure 5.35 is $\theta_f = -180°, 0°, 180°$ peaks which take on a $\theta_f \sim 0°$ dual peak structure as ω_1 decreases. The $\theta_f = -180°, 180°$ peaks decrease. As we have seen previously, the probability of participation from external field quanta is dependent on the ratio $\frac{\omega_1}{\omega}$, increasing the differential cross section in the propagation direction of the external field ($\theta_f \simeq 0°$) and decreasing it at $\theta_f = -180°, 180°$. The development of the dual peak structure is once again due to the probability of participation of external field quanta which remains low at $\theta_f = 0°$ but increases in the region near $\theta_f = 0°$.

Figure 5.36 displays $\theta_f = -150°, 30°$ peaks for the $\omega_1 = 5.12$ MeV and $\omega_1 = 2.56$ MeV plots in which the ratio $\frac{\omega_1}{\omega}$ is greater than unity and the STPPP process is dominated by the 3-momenta of the initial photons. For the $\omega_1 = 0.563$ MeV plot in which external field quanta contributions dominate, a $\theta_f = 0°$ peak develops. The small secondary peak at $\theta_f = 44°$ is due to the angular dependence of the net momentum obtained by the e^-e^+ pair from the external field, which falls to its minimum value, and therefore maximises the differential cross section at that point. We note that the $\omega_1 = 0.768$ MeV plot has not been included in figure 5.36. This is due to the onset of resonance behaviour which is to be considered in chapter 7.

Figures 5.37-5.40 show the variation of the STPPP differential cross section with external field intensity for various θ_1. Figures 5.37-5.39 consider different values for ω, ω_1 and figure 5.40 shows the $l = 0$ and $l = 2$ contributions of figure 5.39. For all figures $\theta_f = 45°$ and $\varphi_f = 0°$.

The main feature of figures 5.37-5.38 is a differential cross section that generally increases with increasing ν^2. The increase is greatest for $\theta_1 = 0°$ and least for $\theta_1 = 45°$. At work here are two competing tendencies. An increasing ν^2 increases the rest mass of the e^-e^+ pair and diminishes the STPPP differential cross section. However an increasing ν^2 increases the probability that the external field quanta will contribute to the process thereby increasing the differential cross section. For most of the plots of figures 5.37-5.38, the second tendency is dominant and the differential cross section increases. For the $0 \leq \nu^2 \leq 0.12$ region of the $\theta_1 = 0°$ plot and the entire $\theta_1 = 45°$ plot of figure 5.38, the first tendency is dominant and the differential cross section decreases. That the $\theta_1 = 0°$ plots of figures 5.37-5.38 show the greatest increase in differential cross section is due to the contribution of external field quanta which for the relative particle energy regime considered $\frac{\omega_1}{\omega} \leq 1$, favour scattering geometries in which initial photons are collinear with the propagation direction of the external field.

Figure 5.39 shows an increase in differential cross section that proceeds in a series of ”steps”. This phenomena has been observed before in computations of the OPPP process [NR65a, Lyu75] and relates to the existence of a threshold for pair production (expressed by equation 5.1). For the particle energies represented by figure 5.39, an increase in ν^2 increases the e^-e^+ pair rest mass and increases the number of external field quanta required to create the pair. For instance in the region $0 < \nu^2 < 0.21$ no external field quanta are required, in the region $0.21 < \nu^2 < 0.35$ one external field quanta is required, and in the region $0.35 < \nu^2 < 0.49$ two external field quanta are required.

Whether or not the differential cross section is discontinuous at the ”steps” is a matter of concern. However, figure 5.40, which shows the $l = 0$ and $l = 2$ contributions at their respective ”cut-off” points, reveals that the differential cross section approaches zero as the cut-off point is reached. This is as it should be since a STPPP process with an initial state which contains just enough energy to create the e^-e^+ pair, but no energy to provide the pair with a non zero 3-momenta, yields a zero probability that e^-e^+ 3-momenta will be observed.

Chapter 6

External Field Electron Propagator Radiative Corrections

6.1 Introduction

Both the SCS and STPPP differential cross sections contain resonant infinities corresponding to the points where the denominator of the electron propagator goes to zero. These infinities arise because the interaction of the electrons with the cloud of virtual photons has not been taken into account. This interaction gives rise to a ”spreading” of electron energy levels, i.e. they gain a finite width. The width, containing both an imaginary and a real part, has the effect of restricting the cross section to finite values at points of resonance. A calculation of this resonance width requires a calculation of the electron self energy, or mass operator as it is also known.

The electron mass operator in the presence of a circularly polarised electromagnetic field was calculated by [BS75b]. They use an operator technique to derive the mass operator. After taking an operator average, they write the imaginary part as a double integration with upper bounds at infinity. [BM76] perform a more complete calculation by obtaining the corrected electron propagator in the external field via a calculation of the electron self energy using Schwinger's proper-time electron Green's functions, choosing the Feynman gauge for the radiation field and using light-like coordinates. The corrected propagator so obtained contains modifications in both numerator and denominator and, as has been recognised by the authors, is too complex to be included in other external field processes (see also [AK87]).

[BM76] approximate the corrected propagator by expanding both numerator and denominator in powers of the fine structure constant α. They obtain a mass correction in the denominator containing both imaginary and real parts which are functions of the parameter $\rho = \frac{2(kp)}{m^2}$. The form of these mass corrections are the same as those obtained by [BS75a], i.e. a double integration with infinite upper bounds.

[BM76] write down a further approximation to the imaginary and real parts of the mass correction as a simple algebraic function of the parameter ρ and the external field intensity ν^2. These further approximations are only valid for a restricted range of parameter values ($0.1 \leq \rho \leq 0.3$ and $\nu^2 \leq 0.1$). Moreover, [BM76] find their expansion invalid for the real part whenever $\rho \leq \alpha (= \frac{1}{137})$. This condition falls within the range of parameter values to be considered.

In this chapter the calculations are repeated using a different approach. The external field electron energy shift (EFEES) is calculated directly by using Schwinger's well know equation for an electron interacting with a quantised Maxwell field and a classical plane wave [Sch54]. The EFEES is simply the external field electron self energy (EFESE)[1] sandwiched between Dirac bispinors. The form of the bound electron propagator to be used is that obtained by [Rit72] and real and imaginary parts of the EFEES are separated by use of dispersion relations. An EFEES expression that is an infinite summation of terms corresponding to the number of external field photons that contribute to the self energy process will be obtained.

This calculation is necessary for two reasons. Firstly, the EFEES is to be inserted into the expressions for the SCS and STPPP cross sections considerably lengthening the computational time required to obtain a numerical result.[2] The expressions obtained in this chapter for the EFEES require considerably less computational time than the expressions obtained by [BS75b, BM76].[3] It is possible to obtain the representation for the EFEES derived here from that obtained by [BM76], by using several transformations [BS75a]. However these are not immediately obvious and the representation in terms of an infinite summation is not written down in the literature.

Secondly, these calculation lend themselves to physical insights not obvious in other calculations. This is the case because, from the outset, the influence of the external field upon the process is expressed as a series of contributions corresponding to the number of external field photons that take part. As [Zel67] and others have shown, IFQED processes are best understood by transitions between electron energy levels characterised by exchange of external field quanta. The work performed in this chapter take as a starting point the calculation of the electron energy shift in the absence of an external field ([IZ80] pg.329) and the mass operator in a constant crossed electromagnetic field [Rit72].

The full gamut of external field radiative corrections, though important in their own right, were not considered in this work. This is purely in regards to limitation of space. Calculation of the EFEES alone is sufficient to obtain the important characteristics of the resonant cross section and serves as a good first approximation to the nonlinear effect of the external field on the SCS and STPPP cross sections.

[1] Please note the difference - EFEES and EFESE are two different acronyms

[2] The EFEES must be recalculated at each data point in the plots presented in Chapters 4,5

[3] This is due largely to the rapid convergence of the summation

6.2 The external field electron energy shift in a circularly polarised external field

The general form of the energy shift $\Delta\epsilon_{p,s}$ of an electron of momentum p and spin s in the presence of the external field, is the external field electron self energy (EFESE) in the external field sandwiched between Dirac bi-spinors (see section 2.12).

$$\Delta\epsilon_{p,s} = \frac{m}{\epsilon_p}\,\overline{u}_{p,s}\,\Sigma^e(p)\,u_{p,s} \tag{6.1}$$

The EFESE in momentum space is a Volkov transform of the EFESE in position space [BM76]. This representation can be obtained directly from the orthogonality and completeness properties of the Volkov function $E_p(x)$.

$$\begin{gathered}\Sigma^e(p) = \frac{1}{VT(2\pi)^4}\int d^4x_1 d^4x_2\,\overline{E}_p(x_2)\,\Sigma^e(x_2,x_1)\,E_p(x_1)\\ \Sigma^e(x_2,x_1) = ie^2\gamma^\mu\,G^e(x_2,x_1)\gamma_\nu\,D_{\mu\nu}(x_2-x_1)\end{gathered} \tag{6.2}$$

The precise form of this representation can be written with the aid of the EFESE Feynman diagram (Figure 6.1) and the expressions for the fermion propagator in the external field $G^e(x_2,x_1)$ and the free photon propagator $D_{\mu\nu}(x_2-x_1)$.

$$\begin{aligned}\Sigma^e(p) &= \frac{i4e^2}{VT(2\pi)^4}\int d^4x_1\,d^4x_2\,d^4k'\,d^4q'\\ &\times\ \overline{E}_p(x_2)\gamma^\mu\,E_{p'}(x_2)\left(\not{q}' + \frac{e^2a^2}{2(kq')}\not{k} + m\right)\overline{E}_{p'}(x_1)\gamma_\mu\,E_p(x_1)\,\frac{1}{q'^2-m_*^2}\,\frac{1}{k'^2}\,e^{ik'(x_2-x_1)}\end{aligned} \tag{6.3}$$

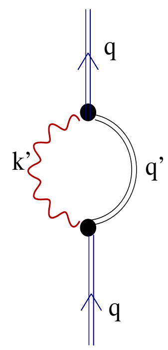

Figure 6.1: **Feynman diagram for the electron self-energy in an external field.**

A representation is extracted from equation 6.3 in terms of a discrete number of external field contributions in direct analogy with the procedure in Chapters 4 and 5 for the SCS and STPPP processes. The exponential functions are grouped together, oscillatory functions expanded in an infinite summation of Bessel functions and the orthogonality properties of the 4-vectors a_1, a_2, k are used to write

$$
\begin{aligned}
\Sigma^e(p) &= \frac{i4e^2}{VT(2\pi)^4}\sum_{bc}\int d^4x_1\, d^4x_2\, d^4k'\, d^4q'\, A(\gamma^\mu, C, q', q)\left(\not{q}' + \tfrac{e^2a^2}{2(kq')}\not{k} + m\right)\\
&\times\; A(\gamma_\mu, B, q', q)\frac{1}{q'^2 - m_*^2}\,\frac{1}{k'^2}\; e^{i(q-q'+k'+ck)x_2}\, e^{i(q'-q-bk)x_1}
\end{aligned}
$$

$$
\begin{aligned}
\text{where}\quad & A(\gamma_\mu, C, q', q) = \gamma_\mu C_1 - \frac{e}{2(kq')}\left(\gamma_\mu \not{a}_1\not{k} C_2 + \gamma_\mu\not{a}_2\not{k}C_3\right)\\
+\quad & \frac{e}{2(kq)}\left(\not{a}_1\not{k}\gamma_\mu\, C_2 + \not{a}_2\not{k}\gamma_\mu\, C_3\right) - \frac{e^2a^2}{4(kq')(kq)}\not{k}\gamma_\mu\not{k}C_1\\
& B_1 = J_b(z)e^{ib\phi_0}\\
& B_2 = \frac{1}{2z}\left[J_{b-1}(z)\left(\alpha_1 - i\alpha_2\right) + J_{b+1}(z)\left(\alpha_1 + i\alpha_2\right)\right]e^{ib\phi_0}\\
& B_3 = \frac{1}{2z}\left[J_{b-1}(z)\left(\alpha_2 + i\alpha_1\right) + J_{b+1}(z)\left(\alpha_2 - i\alpha_1\right)\right]e^{ib\phi_0}\\
& C_1 = J_c(z)e^{-ic\phi_0}\\
& C_2 = \frac{1}{2z}\left[J_{c-1}(z)\left(\alpha_1 + i\alpha_2\right) + J_{c+1}(z)\left(\alpha_1 - i\alpha_2\right)\right]e^{-ic\phi_0}\\
& C_3 = \frac{1}{2z}\left[J_{c-1}(z)\left(\alpha_2 - i\alpha_1\right) + J_{c+1}(z)\left(\alpha_2 + i\alpha_1\right)\right]e^{-ic\phi_0}\\
\text{and}\quad & z = \sqrt{\alpha_1^2 + \alpha_2^2}\quad;\quad \alpha_1 = e\left[\frac{(a_1p)}{(kp)} - \frac{(a_1p')}{(kp')}\right]\quad;\quad \alpha_2 = e\left[\frac{(a_2p)}{(kp)} - \frac{(a_2p')}{(kp')}\right]\\
& \cos\phi_0 = \frac{\alpha_1}{z}\quad;\quad \sin\phi_0 = \frac{\alpha_2}{z}
\end{aligned}
\tag{6.4}
$$

Integrations over x_1, x_2 and q' yield a single delta function $\delta^4(bk - ck)$ and the EFESE is only non zero if $b = c$. The number of infinite summations reduces to one, and the following holds

$$
C_1 = B_1^* \quad;\quad C_2 = B_2^* \quad;\quad C_3 = B_3^* \tag{6.5}
$$

Proceeding with the calculation at this stage presents a problem in that the EFESE contains the term $\frac{1}{VT}$ which goes to zero as all space-time is included. This can be resolved by setting $b = c$ at the outset. The integrations over x_1 and x_2 are then transformed into integrations over $x_1 - x_2$

and $x_1 + x_2$, with the first yielding a delta function expressing conservation of 4-momentum for the process, and the other yielding a space-time volume VT.

$$\begin{aligned}\Sigma^e(p) &= \frac{i4e^2}{(2\pi)^4}\sum_b \int d^4k'\, d^4q'\, \delta^4(q'-q-k'-bk) \\ &\times\; A(\gamma^\mu, B^*, q', q)\left(\not{q}' + \tfrac{e^2a^2}{2(kq')}\not{k} + m\right) A(\gamma_\mu, B, q', q)\,\frac{1}{q'^2-m_*^2}\,\frac{1}{k'^2}\end{aligned} \tag{6.6}$$

The EFESE is a summation of contributions corresponding to the number of external field photons b that contribute to the process. There is no lower limit on b as was the case for the summations involved with the SCS and STPPP processes.[4] This is so because the initial and final states of the EFESE electron are virtual, permitting energy states to reach negative values.

An average over electron spins in equation 6.1 leads to the appearance of a trace expression. The spin averaged EFEES is

$$\begin{aligned}\Delta\epsilon_p &= \frac{1}{2}\sum_{s=1}^{2}\Delta\epsilon_{p,s} \\ &= \frac{i4e^2}{(2\pi)^4}\frac{m}{\epsilon_p}\sum_b \int d^4k'\, d^4q'\, \delta^4(q'-q-k'-bk) \\ &\times\; \frac{1}{4m}\,\mathrm{Tr}\left\{(\not{p}'+m)\,Q(B,q,q')\right\}\,\frac{1}{q'^2-m_*^2}\,\frac{1}{k'^2}\end{aligned} \tag{6.7}$$

$$\text{where} \qquad Q(B,q,q') = A(\gamma^\mu, B^*, q', q)\left(\not{q}' + \tfrac{e^2a^2}{2(kq')}\not{k} + m\right) A(\gamma_\mu, B, q', q)$$

In equation 6.7 the integrations over k' and q' are performed, and real and imaginary parts are extracted using a dispersion relation method outlined in Appendix E. Introducing new 4-vectors K_μ, D_μ and defining θ to be the angle between $\underset{\sim}{K}$ and $\underset{\sim}{k}$, the real and imaginary parts of the EFEES are (see equation E.7)

[4] A negative value for b corresponds to energy being given up to the field.

$$\begin{aligned}
\Re\Delta\epsilon_p(D^2) &= \frac{1}{\pi} P \int_{-\infty}^{\infty} \frac{\Im\Delta\epsilon_p(\sigma^2)}{\sigma^2 - D^2} d\sigma^2 \\
\Im\Delta\epsilon_p(D_\mu) &= \frac{e^2 m^2}{16\pi\epsilon_p} \sum_b \int_{-1}^{1} d\cos\theta \left(1 - \frac{m_*^2}{D^2}\right) \\
&\times \left\{ -2\, J_b^2(z) + \nu^2 \left(1 + \tfrac{1}{2}\tfrac{[(kD)-(kK)]^2}{(kD)(kK)}\right) \right. \\
&\times \left. J_{b-1}^2(z) + J_{b+1}^2(z) - 2J_b^2(z) \right\} \Theta\left(D^2 - m_*^2\right)
\end{aligned} \tag{6.8}$$

$$\begin{aligned}
\text{where} \quad z &= \sqrt{\tfrac{e^2 a^2}{(kK)}(D^2 + m_*^2)\left[\tfrac{1}{(kD)} - \tfrac{1}{(kK)}\right]} \\
D_\mu &\equiv q_\mu + b\, k_\mu \\
K_\mu &\equiv q'_\mu + \tfrac{1}{2}\, k_\mu
\end{aligned}$$

The form of the real part of the EFEES requires the imaginary part to be written in terms of a length D^2. However the imaginary part of equation 6.8 contains vector dependences (kD). The EFEES is to be inserted in propagator denominators and becomes important at resonance $q^2 = m_*^2$ and can be neglected elsewhere. The resonance condition allows the replacement

$$\frac{1}{(kD)} \to \frac{2b}{D^2 - m_*^2} \tag{6.9}$$

The imaginary part of the EFEES becomes dependent only on D^2. A shift of integration variable can be made and the EFEES is

$$\begin{aligned}
\Re\Delta\epsilon_p(D^2) &= \frac{1}{\pi} P \int_{(m_*+\epsilon)^2}^{\infty} \frac{\Im\Delta\epsilon_p(\sigma^2)}{\sigma^2 - D^2} d\sigma^2 \\
\Im\Delta\epsilon_p(D^2) &= \frac{e^2 m^2}{16\pi\epsilon_p} \sum_b \int_0^{u(D^2)} \frac{du}{(1+u)^2} \\
&\times \left\{ -4\, J_b^2(z) + \nu^2 \left(2 + \frac{u^2}{1+u}\right) \left(J_{b-1}^2(z) + J_{b+1}^2(z) - 2J_b^2(z)\right) \right\} \\
&\times .\Theta\left(D^2 - m_*^2\right)
\end{aligned} \tag{6.10}$$

$$\begin{aligned}
\text{where} \quad u(D^2) &= \frac{D^2}{m_*^2} - 1 \\
z(D^2) &= \sqrt{\nu^2(1+\nu^2)\tfrac{m^4}{(kp)^2}\, u\left(u(D^2) - u\right)}
\end{aligned}$$

The lower bound, $(m_* + \epsilon)^2$, on the integration in the real part of the EFEES is due to the step function $\Theta(D^2 - (m_* + \epsilon)^2)$ in the imaginary part. Self energy calculations in QED are prone to divergences. Indeed it is known that the electron self energy in the absence of the external field is divergent. Taking the limit of vanishing external field intensity, $\nu^2 \to 0$, and a contribution of zero external field photons, $b = 0$, a logarithmic divergence appears

$$\begin{aligned} \Im\Delta\epsilon_p(D^2, \nu^2 \to 0, b = 0) &= \frac{e^2 m^2}{4\pi\varepsilon_p}\left(\frac{m^2}{D^2} - 1\right) \\ \Re\Delta\epsilon_p(\nu^2 \to 0, b = 0) &= -\frac{e^2 m^2}{4\pi^2\varepsilon_p}\int_{m^2}^{\infty}\frac{\mathrm{d}\sigma^2}{\sigma^2} \end{aligned} \tag{6.11}$$

A regularisation procedure is required. In [BM76]'s study of the electron self energy in a circularly polarised external field, divergences were found to exist only in unregularised expressions that contained no dependence on the external field. [Rit72] found a similar result for the case of a constant crossed external electromagnetic field. Indeed, numerical evaluation of equation 6.10 reveals that divergences are only present in the field free parts. The regularisation procedure for the EFEES consequently reduces to the regularisation procedure for the same process in the absence of the external field.

Renormalisation allows the divergences of the EFEES to be absorbed into the physical mass of the electron. A discussion of renormalisation with the external field present is left to section 7.2. Assuming here that the EFEES has already been properly renormalised, the regularised EFEES, $\Delta\epsilon_p^R(D^2)$ is simply the difference between the unregularised EFEES and the $b = 0$ term of the unregularised EFEES at the mass shell, $p^2 = m^2$

$$\Delta\epsilon_p^R(D^2) = \Delta\epsilon_p(D^2) - \Delta\epsilon_p(D^2, p^2 = m^2, b = 0) \tag{6.12}$$

As it stands, the divergent part $\Delta\epsilon_p(\sigma^2, \nu^2 \to 0, b = 0)$ is also undefined since the argument of the Heaviside step function goes to zero at that point. A small photon mass (cf. equation D.5) is inserted to avoid the pole so that

$$\begin{gathered} \Theta(D^2 - m_*^2) \to \Theta(D^2 - (m_* + \epsilon)^2) \\ q^2 = m_*^2\,,\, b = 0 \Rightarrow D^2 = m_*^2 \end{gathered} \tag{6.13}$$

The argument of the step function ensures that the lower bound of the summation is $b = 1$. Transforming the integration variable in the real part to $y \equiv \sqrt{1 - \dfrac{m_*^2}{\sigma^2}}$, the regularised EFEES near the resonance ($q^2 \sim m_*^2$) is

$$
\begin{aligned}
\Re\Delta\epsilon_p^R(D^2) &= \frac{e^2m^2}{16\pi^2\epsilon_p}\sum_{b=1}^{\infty}\int_0^1 \frac{dw}{w}\,\frac{q^2-m_*^2}{m_*^2w^2+2b(kp)(1-w^2)}\int_0^{u(w^2)}\frac{du}{(1+u)^2} \\
&\times \left\{-4\,J_b^2(z)+\nu^2\left(2+\frac{u^2}{1+u}\right)\left(J_{b-1}^2(z)+J_{b+1}^2(z)-2J_b^2(z)\right)\right\} \\
\Im\Delta\epsilon_p^R(D^2) &= \frac{e^2m^2}{16\pi\epsilon_p}\sum_{b=1}^{\infty}\int_0^{u(D^2)}\frac{du}{(1+u)^2} \\
&\times \left\{-4\,J_b^2(z)+\nu^2\left(2+\frac{u^2}{1+u}\right)\right. \\
&\times \left. J_{b-1}^2(z)+J_{b+1}^2(z)-2J_b^2(z)\right\}\Theta\left(D^2-(m_*+\epsilon)^2\right)
\end{aligned}
\tag{6.14}
$$

Confirmation of the expression obtained for the regularised imaginary part can be found by use of the optical theorem which connects the regularised imaginary part with the probability for emission of a photon from an electron embedded in the external electromagnetic field [Rit72]. Equation 6.14 indeed agrees with the HICS transition probability in a circularly polarised field W^e_{brem} [NR65a], and

$$W^e_{brem} = \frac{1}{2}\Im\Delta\epsilon_p^R(D^2) \tag{6.15}$$

A numerical investigation and analysis will be made in section 6.3 and 6.4. Numerical comparison will also be made with the expressions obtained by [BS75b, BM76] which are only valid in certain limits. The real part of the EFEES will be neglected since it reduces to zero at the mass shell. The imaginary part on the other hand, plays a vital role in determining the SCS and STPPP resonant differential cross sections which will investigated in Chapter 7.

6.3 EFEES Plots

The regularised imaginary part of the EFEES is investigated in this section for the parameter range set out in Table 6.1 expressed by equation 6.14. The integer variable b corresponds to the number of external field photons that contribute to the process. $\rho = \frac{2(kp)}{m^2}$ is a scalar product function of the external field and electron 4-momenta. The external field intensity is represented by the parameter $\nu^2 = \frac{e^2a^2}{m^2}$. Both ρ and ν^2 are dimensionless in natural units. Figures 6.8 - 6.13 represent a comparison between approximation formulae obtained by [BM76] and the expression contained in equation 6.14.

The vertical axes of all figures in this sections show the regularised imaginary part of the EFEES multiplied by a factor $\frac{2\epsilon_p}{\alpha}$ where α is the fine structure constant and ϵ_p the electron energy. Generally, the summation over b converges rapidly and the typical computational time required to generate a single plot containing 50 data points was of the order of 10 seconds. However plots representing parameter values at the high end of ρ and ν^2 required approximately 10 minutes of computational time.

b	ν^2	ρ	figure(s)
$1 \to 20$	$0.1, 0.5, 1.0$	0.001	6.2
$1 \to 20$	$0.1, 0.5, 1.0$	0.1	6.3
all	$0 \to 0.1$	$0.001, 0.01, 0.1$	6.4
all	$0 \to 0.2$	$0.001, 0.01, 0.1$	6.8,6.9, 6.10
all	$0 \to 2.0$	$0.001, 0.01, 0.1$	6.5,6.11, 6.12,6.13
all	$0.1, 0.5, 1.0$	$0 \to 0.1$	6.6
all	$0.1, 0.5, 1.0$	$0.1 \to 3.0$	6.7

Table 6.1: **The parameter range for which the regularised imaginary part of the EFEES is investigated.**

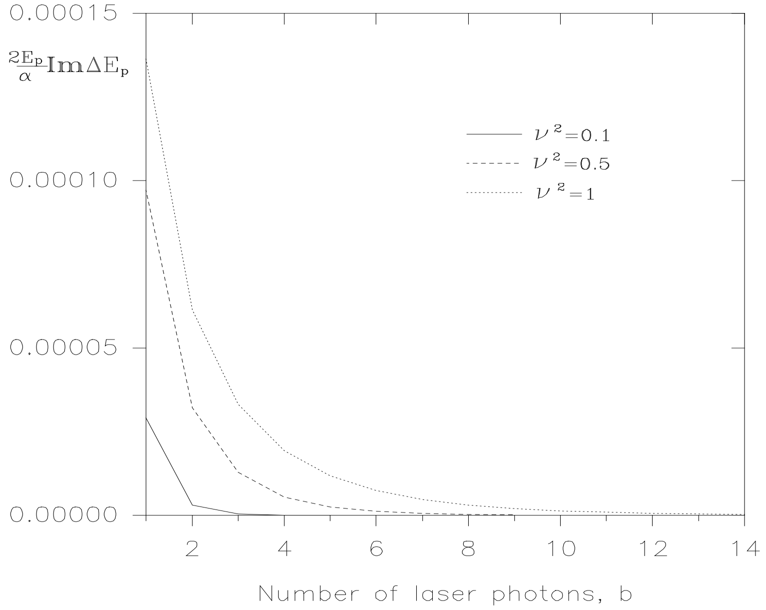

Figure 6.2: **The EFEES imaginary part vs b external field photons for $\rho = 0.001$ and various ν^2.**

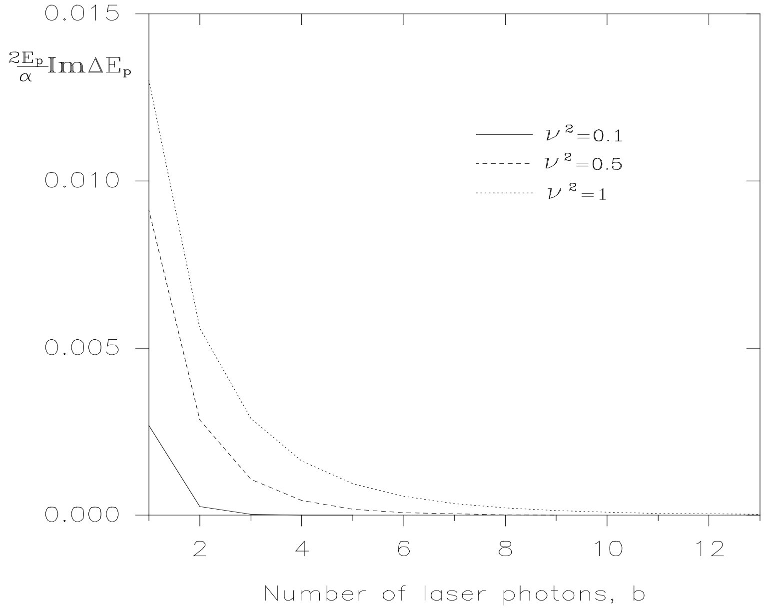

Figure 6.3: **The EFEES imaginary part vs b external field photons for $\rho = 0.1$ and various ν^2.**

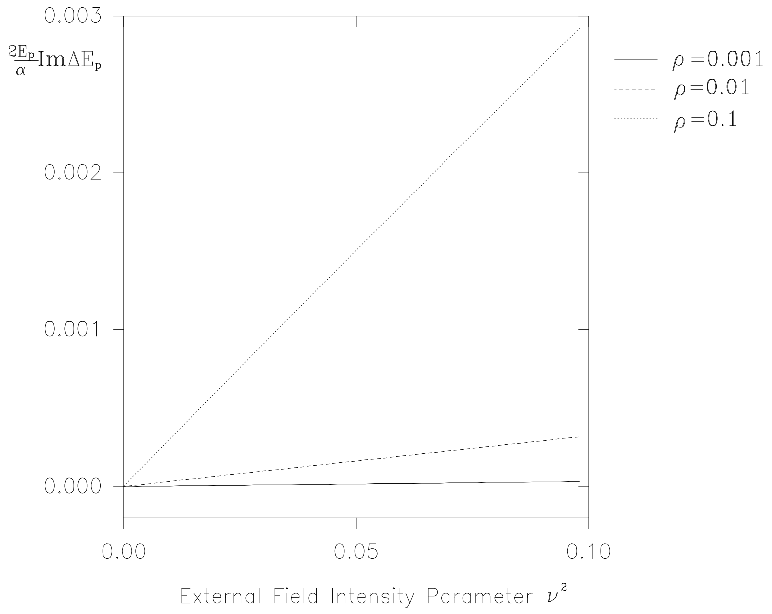

Figure 6.4: **The EFEES imaginary part vs $\nu^2 < 0.1$ for various ρ.**

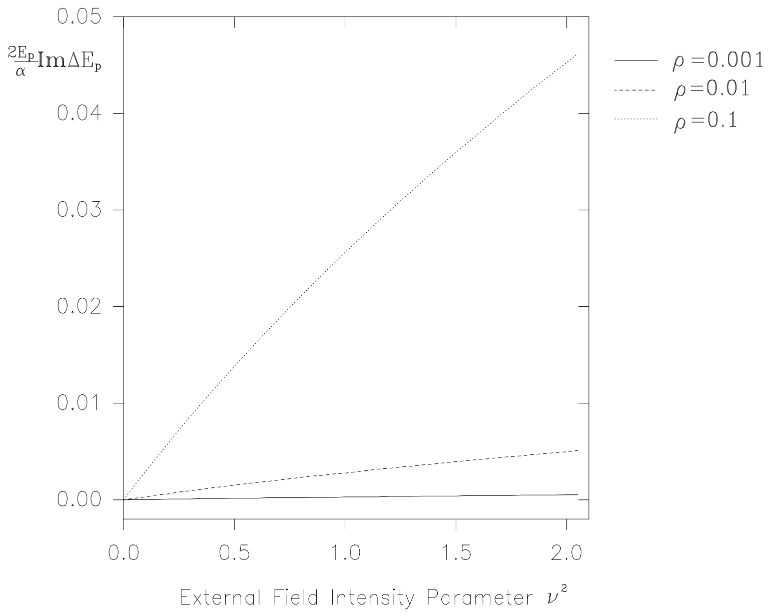

Figure 6.5: **The EFEES imaginary part vs $\nu^2 < 2$ for various ρ.**

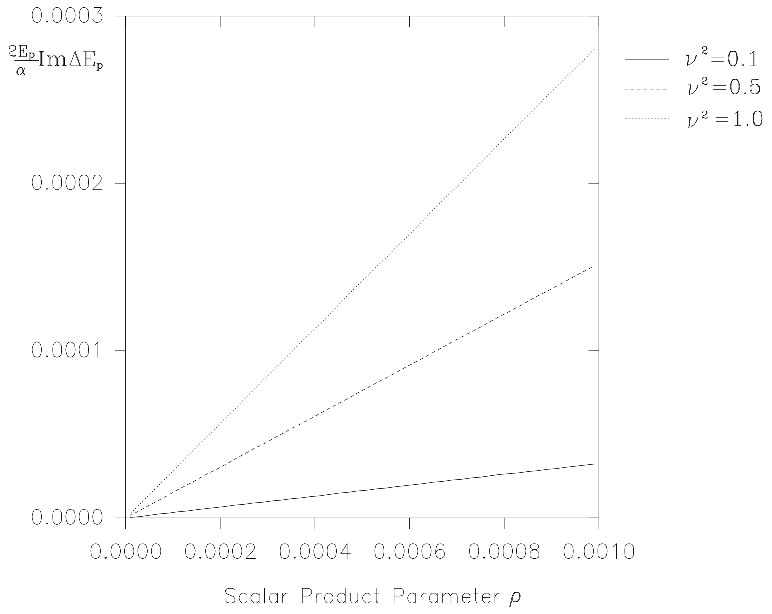

Figure 6.6: **The EFEES imaginary part vs $\rho < 0.001$ for various ν^2.**

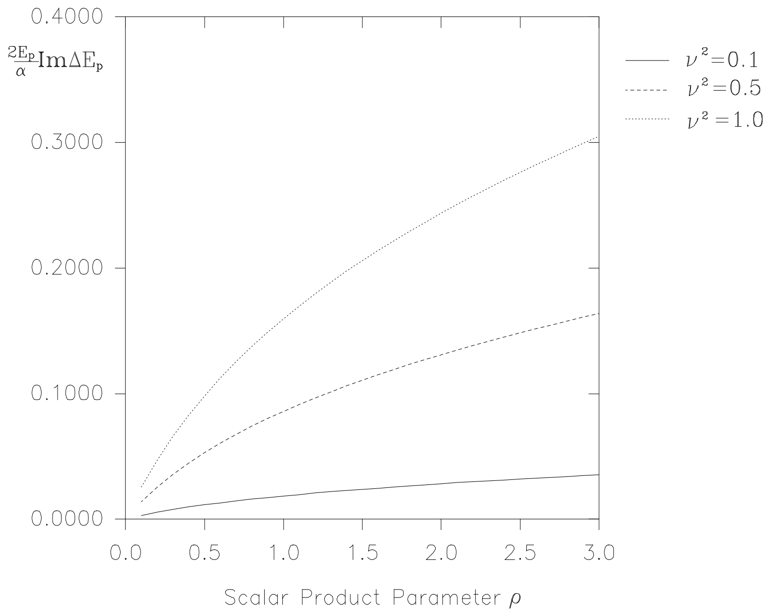

Figure 6.7: **The EFEES imaginary part vs $\rho < 3$ for various ν^2.**

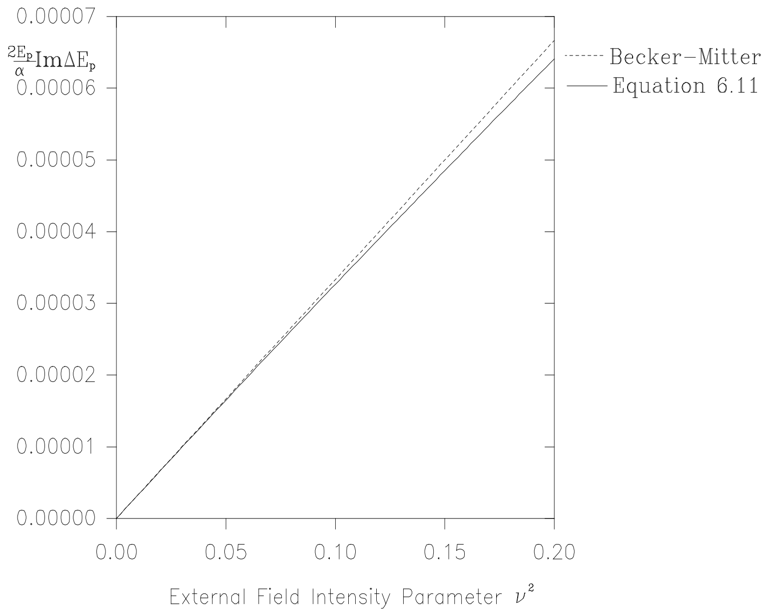

Figure 6.8: **Comparison of the EFEES imaginary part of Chapter 6 and that of [BM76] vs ν^2 for $\rho = 0.001$.**

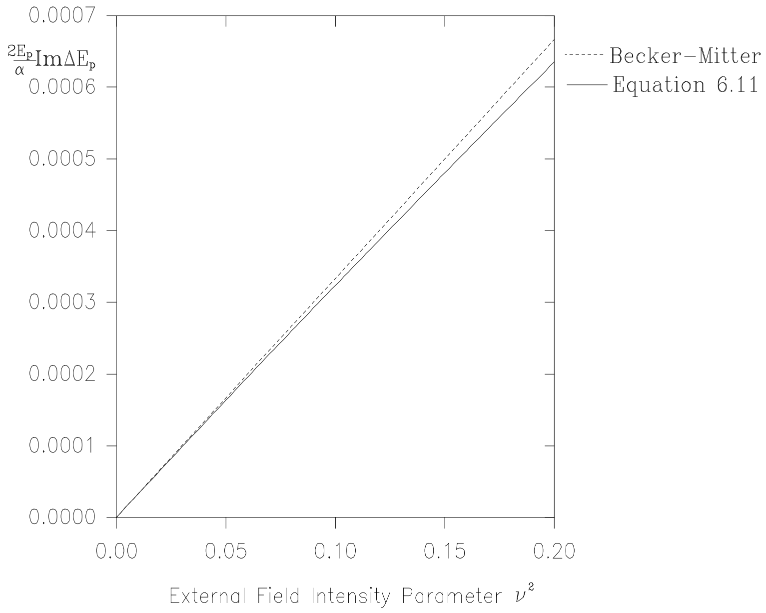

Figure 6.9: **Comparison of the EFEES imaginary part of Chapter 6 and that of [BM76] vs ν^2 for $\rho = 0.01$.**

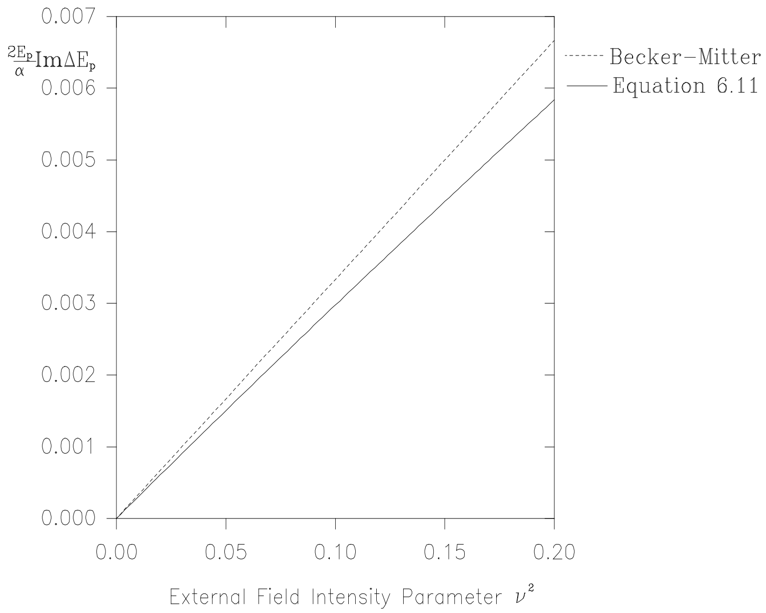

Figure 6.10: **Comparison of the EFEES imaginary part of Chapter 6 and that of [BM76] vs ν^2 for $\rho = 0.1$.**

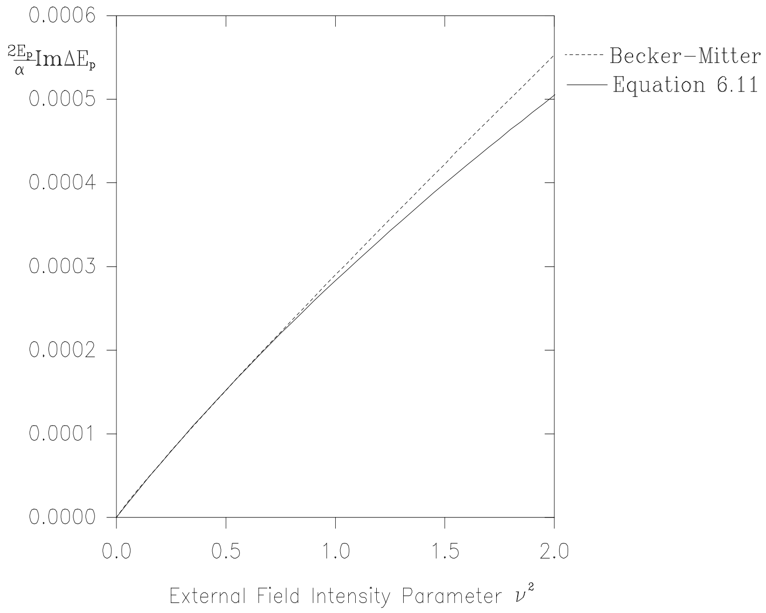

Figure 6.11: **Comparison of the EFEES imaginary part of Chapter 6 and that of [BM76] vs ν^2 for $\rho = 0.001$ and $\nu^2 < 2$.**

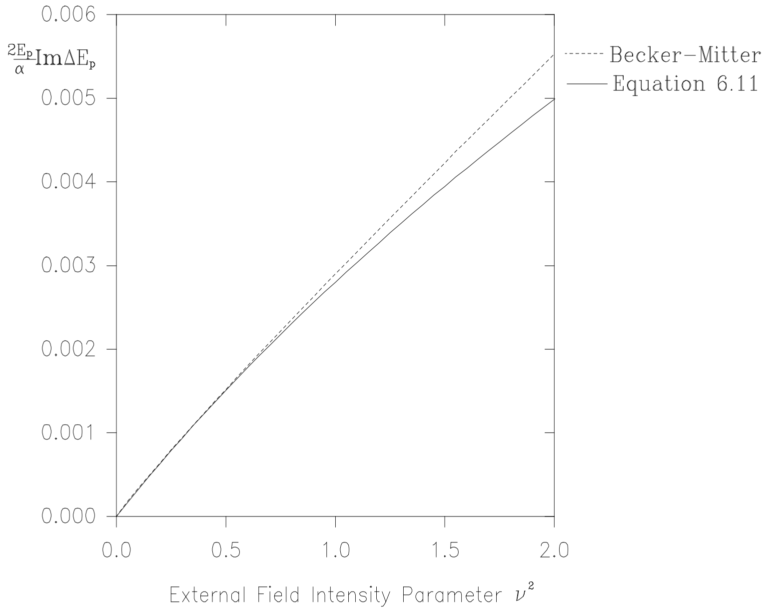

Figure 6.12: **Comparison of the EFEES imaginary part of Chapter 6 and that of [BM76] vs ν^2 for $\rho = 0.01$ and $\nu^2 < 2$.**

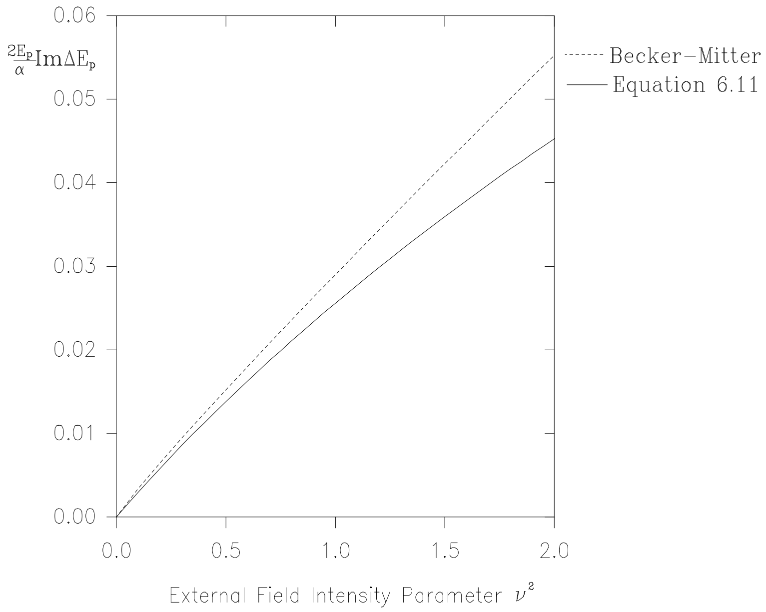

Figure 6.13: **Comparison of the EFEES imaginary part of Chapter 6 and that of [BM76] vs ν^2 for $\rho = 0.1$ and $\nu^2 < 2$.**

6.4 EFEES Analysis

The variation of the imaginary part of the EFEES displayed in the figures of section 6.3 is analysed here. The main purpose in calculating the imaginary part of the EFEES is to include it in the propagator denominators of the SCS and STPPP differential cross sections. Therefore only brief remarks are made about the physical origin of the variation in magnitude of the EFEES imaginary part and the relevance of the numerical range of the parameters considered.

Figures 6.2 - 6.3 show the variation of the EFEES imaginary part with the number of external field photons b that contribute to the process. The figures display several plots corresponding to the differing values of the scalar product parameter ρ and the external field intensity ν^2. The horizontal scale of both figures has $b = 1$ as its lowest value. This point corresponds to the minimum value of contributing external field photons required for the regularised EFEES to be non zero.

The main feature of both figures is a seemingly inverse relationship between the EFEES imaginary part and the parameter b. Maximum values are obtained at $b = 1$, decreasing towards zero as b increases. The parameter ρ has little bearing on the EFEES imaginary part variation with ν^2, though it increases its magnitude in figure 6.3 ($\rho = 0.1$) by a factor of approximately 100 compared with its magnitude in figure 6.2 ($\rho = 0.001$).

The discussion makes use of the optical theorem (equation 6.15) which allows interpretation of the behaviour of the EFEES imaginary part to be given in terms of the probability of emission of radiation from the electron embedded in the external field. The discussion is facilitated by drawing a comparison with the probability of radiation by an electron in the field of a nucleus, which bears an inverse relationship to the recoil momentum of the external field ([Nac90] p.153, [Hei54] p.246). It is assumed here that a similar relationship exists when the external field is electromagnetic.

The probability of emission of an electron in an external field has an inverse relationship to the recoil momentum ([MS84] p.167). The recoil momentum is the energy of the emitted photon ω_f which has a dependence on ν^2, b, ρ and the angle θ its 3-momentum makes with the direction of propagation of the external field. This relation can be obtained from equation 3.15 by setting $\underset{\sim}{k}_i, \omega_i$ to zero and substituting b for l

$$\omega_f = \frac{\rho\, b}{1 + (b\omega + \frac{\nu^2}{2})(1 - \cos\,\theta)} \tag{6.16}$$

At least one external field photon contributes and the process can be considered a Compton scattering. The contributed photon is most likely scattered collinear to its initial state ($\theta \sim 0°$) and the probability it does so increases as ν^2 (see Chapter 4). At $\theta \sim 0°$ the recoil momentum is almost directly proportional to b and therefore the probability of emission (which is equivalent to the vertical axes of figures 6.2 and 6.3) should be inversely proportional to b.

Figures 6.4 and 6.5 show the variation of the EFEES imaginary part with external field intensity for different values of the scalar product parameter ρ. The relationship between the EFEES imaginary part and ν^2 appears to be linear. However its not quite so for the $\rho = 0.1$ plot of figure 6.5. The behaviour can be justified again by considering the recoil momentum (equation 6.16). All else being constant, an increasing ν^2 decreases ω_f and therefore increases the probability of emission. An understanding of the relationship with ν^2 is also gained by considering an electron accelerated by the circularly polarised external field. The power radiated (and probability of emission) is directly proportional to the square of the electron acceleration [Jac75].

The variation of the EFEES imaginary part with the scalar product parameter ρ is considered in figures 6.6 and 6.7 which shows a seemingly linear relationship when ρ is small (figure 6.6) though non linear when ρ is large (figure 6.7). A linear relationship is suggested for the recoil momentum which is directly proportional to ρ. However a closer examination of the analytic expressions for the imaginary part of the EFEES reveal terms which are not linear. The two tendencies combine to produce the numerical variation shown.

Figures 6.8 - 6.13 contain a comparison between numerical values for the EFEES imaginary part and the two approximation formulae given by [BM75, BM76] in their treatment of the same process. These figures are divided in two groups.

Figures 6.8 - 6.10 consider the variation of the EFEES imaginary part for $0 \leq \nu^2 \leq 0.2$ and contain a comparison with the second of [BM76] approximation formulae which are quoted as valid for $\nu^2 \leq 0.1$ and $\rho \leq 0.1$. For this range of parameters, in figures 6.8 and 6.9, good agreement is obtained with [BM76]. Variation is obtained as expected where [BM76] is no longer valid at $\nu^2 > 0.1$ and $\rho = 0.1$ (figure 6.10).

Figures 6.11 - 6.13, which contain a comparison with the first of [BM76]'s approximation formulae valid for $0.1 \leq \nu^2 \leq 1.0$ and $\rho \leq 0.1$, consider the variation of the EFEES imaginary part for $0 \leq \nu^2 \leq 2.0$. Again, good agreement is obtained whenever the parameters considered fall within the range of validity for [BM76]'s expressions. The variation obtained with [BM76] shows the necessity of using the expressions for the EFEES imaginary part (equation 6.14) in further calculations of SCS and STPPP resonances. At the $\nu^2 = 1.0$ point in figure 6.13, the variation obtained represents a 13.4% error in the heights of resonant peaks which have an inverse square relationship to the EFEES imaginary part.

A potential problem emerges as $\nu^2 \to 0$. Here the imaginary part of the EFEES falls to zero resulting in potentially resonant cross sections again becoming infinite. However resonances do not occur in the SCS and STPPP differential cross sections when $\nu^2 \sim 0$. A detailed examination follows in Chapter 7.

Chapter 7

SCS and STPPP Resonance Cross sections

7.1 Introduction

As will be seen in this chapter, the virtual particle exchanged in both the SCS and STPPP processes reaches the mass shell. Uncorrected, the SCS and STPPP cross sections would contain resonant infinities at those points. The results of chapter 6 for the electron self energy will be used to render these resonant infinities finite. The one loop electron self energy is only one of many radiative corrections, including the vertex correction, the correction of particle wave functions and the propagator corrections, that chould be calculated and included in the SCS and STPPP cross sections. However there are constraints imposed by the difficulties of performing these corrections in the presence of the external electromagnetic field. Also, computational restrictions require radiative corrections of immediate concern to be prioritised. So the focus in this chapter is on the insertion of the imaginary part of the EFEES into the bound fermion propagator present in both the SCS and STPPP processes.

In section 7.2 the regularisation and renormalisation procedures required to deal with the divergences present in the electron self energy are revisited. The regularisation and renormalisation procedure in the presence of the external field reduces to the equivalent one in the absence of the external field [BM76]. The insertion of the EFEES into the denominator of the bound fermion propagator yields expressions identical to those of [BM76]'s fully corrected propagator to order one in the fine structure constant.

The possible experimental detection of QED processes in external electromagnetic fields is of great interest. In the last decade experimental apparatus has been developed which allows observation of some first order IFQED processes. At resonance however, the detection of the second order IFQED processes may become more likely. With possible experimental detection in mind, sections 7.3 - 7.6 are devoted to the calculation of the SCS and STPPP differential cross sections at points of resonance. In section 7.3 analytic expressions for the widths, locations, spacings and heights of the resonant differential cross sections are obtained. In section 7.4 numerical results are presented for SCS and STPPP resonances which are analysed in section 7.5. Finally in section 7.6 the likely experimental constraints in the detection of these resonances are discussed.

7.2 Renormalisation in the external field

The exact, radiatively corrected fermion propagator embedded in the external field can be obtained from an infinite series in direct analogy to the procedure used to obtain the exact fermion propagator in the absence of the external field. The Dyson equation can be used to write the exact external field propagator $G^e_{SE}(x_2, x_1)$ as a function of the external field electron self energy $\Sigma^e(x_2, x_1)$ and the external field fermion propagator in the absence of radiative corrections $G^e(x_2, x_1)$. The expression is contained in equation 7.1 and can be written down directly from the series of Feynman diagrams represented in figure 7.1.

$$\begin{aligned} G^e_{SE}(x_2, x_1) &= G^e(x_2, x_1) \\ &+ \int d^4x_a\, d^4x_b G^e(x_2, x_a)\Sigma^e(x_a, x_b)G^e(x_b, x_1) \\ &+ \int d^4x_a\, d^4x_b\, d^4x_c\, d^4x_d\, G^e(x_2, x_a)\Sigma^e(x_a, x_b)G^e(x_b, x_c)\Sigma^e(x_c, x_d)G^e(x_d, x_1) \\ &+ \ldots \end{aligned} \tag{7.1}$$

The integrations over space-time points can be absorbed by using the expression for the momentum space EFESE, $\Sigma^e(p)$ and the series becomes

$$\begin{aligned} G^e_{SE}(x_2, x_1) &= \int d^4p\; E_p(x_2)\frac{1}{\not{p} - m}\overline{E}_p(x_1) \\ &+ \int d^4p\; E_p(x_2)\frac{1}{\not{p} - m}\Sigma^e(p)\frac{1}{\not{p} - m}\overline{E}_p(x_1) \\ &+ \ldots \end{aligned} \tag{7.2}$$

The sum in equation 7.2 can be reduced and the momentum space EFESE, $\Sigma^e(p)$ appears in the denominator of the propagator

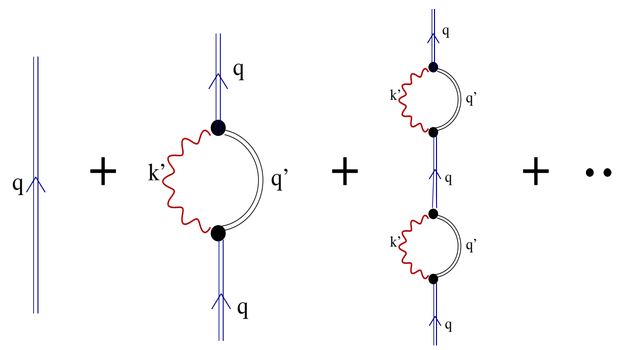

Figure 7.1: **Feynman diagrams for the external field electron self energy series.**

$$G^e_{SE}(x_2, x_1) = \int d^4p \; E_p(x_2) \frac{1}{\not{p} - m - \Sigma^e(p)} \overline{E}_p(x_1) \tag{7.3}$$

The EFESE $\Sigma^e(p)$ contains divergences and a renormalisation procedure is required. The exact bound bound fermion propagator $G^e_{SE}(x_2, x_1)$ is the exact fermion propagator in the absence of the external field sandwiched between Volkov $E_p(x)$ functions. A renormalisation procedure equivalent to that of the field free case is suggested. Renormalisation of the fermion mass and charge is obtained by an expansion of the field free electron self energy as a function of the slash vector $\not{p}$. However with the external field present, the EFESE has vector dependencies on external field parameters $\not{a}_1, \not{a}_2, \not{k}$ as well as a dependence on the electron momentum vector $\not{p}$.

[BM76] used the axial symmetry of a circularly polarised external field and gauge invariance to find that the divergences present in the EFESE have no dependence on external field parameters. This result was made use of in Chapter 6 and is so used again here. The EFESE $\Sigma^e(p)$ is separated into a non external field part $\Sigma^0(p)$ and an external field dependent part $\Sigma^L(p, a_1, a_2, k)$.

$$\Sigma^e(p) = \Sigma^0(p) + \Sigma^L(p, a_1, a_2, k) \tag{7.4}$$

The divergences present in $\Sigma^0(p)$ are dealt with by the standard regularisation and renormalisation procedure in the absence of the external field (section 2.13). The regularised EFESE is

$$\Sigma^e_R(p) = \Sigma^0(p) - \Sigma^0(p, p^2 = m^2) + \Sigma^L(p, a_1, a_2, k) \tag{7.5}$$

In Chapter 6, the external field electron energy shift (EFEES) was calculated. The EFEES can be inserted into the electron energy in the propagator denominator. However before doing so, it is necessary to show that the procedure is equivalent to the insertion of the EFESE as in equation 7.3. In previous work the general structure of the EFESE was obtained and expansions to order α used [BM76].

The general structure of the EFESE can be constructed from products of the slash vectors $\not{p}, \not{a}_1, \not{a}_2, \not{k}$. Taking linear combinations of these with the aim of achieving orthogonality, the EFESE can be reduced to a dependence on products of three slash vectors

$$\not{p} \quad ; \quad \not{F}_1 = \not{a}_1 - \frac{(a_1 p)}{(kp)} \not{k} \quad ; \quad \not{F}_2 = \not{a}_2 - \frac{(a_2 p)}{(kp)} \not{k} \tag{7.6}$$

Each of the slash vectors defined in equation 7.6 are orthogonal in the sense that a scalar product of any two of these is zero. In general the EFESE can be written

$$\Sigma^e(p) = A_1\not{p} + A_2\not{F}_1 + A_3\not{F}_2 + A_4\not{p}\not{F}_1 + A_5\not{p}\not{F}_2 + A_6\not{F}_1\not{F}_2 + A_7\not{p}\not{F}_1\not{F}_2 + A_8 \tag{7.7}$$

Furry's theorem ([JR76], pg.160) requires that $\Sigma^e(p)$ be an even function of the 4-vectors F_1 and F_2. Because of orthogonality then

$$A_2, A_3, A_4, A_5 = 0 \tag{7.8}$$

Since F_1, F_2 can only appear in the remaining coefficients in a scalar product with itself (i.e. as $F_1^2 = F_2^2 = a^2$) then the coefficients A_1, A_6, A_7, A_8 must be independent of vectors a_1 and a_2. Equation 7.7 can be simplified further by performing an operation in which the 4-vectors a_1 and a_2 are exchanged. Examination of the complete expression of the EFESE (see equation 6.4) reveals that the effect of swapping a_1 and a_2 is to obtain the complex conjugate of $\Sigma^e(p)$. The remaining A coefficients of equation 7.7 can then be written

$$\begin{aligned} A_6 &= -A_6^* \\ A_7 &= -A_7^* \\ A_1 &= A_1^* \\ A_8 &= A_8^* \end{aligned} \tag{7.9}$$

With the restrictions on the coefficients A_i contained in equations 7.8 and 7.9, the general expression for the EFESE contained in equation 7.7 can be rewritten in terms of coefficients Y_i which are functions of real quantities and are each proportional to the fine structure constant α.

$$\Sigma^e(p) = Y_1\not{p} + iY_2\not{F}_1\not{F}_2 + iY_3\not{p}\not{F}_1\not{F}_2 + Y_4 \tag{7.10}$$

Insertion of the EFESE into the exact electron propagator (equation 7.3) is achieved by separating $\Sigma^e(p)$ into a vector part and a scalar part, and operating twice on the numerator and denominator by the conjugate of the denominator. The result for the propagator denominator, to first order in the fine structure constant is

$$(p^2 - m^2)^2 + 2(p^2 - m^2)(2p^2Y_1 + 2mY_4) \tag{7.11}$$

Alternatively, the EFEES can be inserted into the electron energy contained in the denominator of the external field propagator, $p^2 - m^2 = \epsilon_p^2 - \left(|\underset{\sim}{p}|^2 + m^2\right)$. After squaring and expanding to first order in the fine structure constant, the denominator becomes

$$(p^2 - m^2)^2 + 2(p^2 - m^2)2\epsilon_p \Delta\epsilon_p \tag{7.12}$$

The equivalence of equations 7.11 and 7.12 is obtained by use of the expression relating the EFESE and the EFEES (see equations 6.1 and 6.6)

$$\begin{aligned} 2\epsilon_p \Delta\epsilon_p &= m \sum_{s=1}^{2} \bar{u}_{p,s}\, \Sigma^e(p)\, u_{p,s} \\ &= \tfrac{1}{2}\mathrm{Tr}\left\{(\not{p} + m)\Sigma^e(p)\right\} \\ &= 2p^2 Y_1 + 2mY_4 \end{aligned} \tag{7.13}$$

The regularised EFEES $\Delta\epsilon_p^R$ (which is equivalent to the regularised EFESE), is inserted into the denominator of the external field propagator to produce, finally, an expression for the exact external field electron propagator (to first order in the fine structure constant)

$$G^e_{SE}(x_2, x_1) = \int d^4p\; E_p(x_2) \frac{\not{p} + m}{p^2 - m^2 + 2\epsilon_p \Delta\epsilon_p^R} \overline{E}_p(x_1) \tag{7.14}$$

7.3 Resonance Conditions

The replacement of the bare fermion propagator in the SCS and STPPP differential cross sections with the corrected fermion propagator obtained in Section 7.2 (equation 7.14) has the effect of rendering the resonant infinities present in the uncorrected cross sections finite. The corrected propagator denominator, from equation 7.14, is

$$p^2 - m^2 + 2\epsilon_p \Re\Delta\epsilon_p^R + i2\epsilon_p \Im\Delta\epsilon_p^R \tag{7.15}$$

For the purposes of experimental detection of the SCS and STPPP differential cross sections, the characteristics of the resonant peaks, particularly the location, separation, height and width of the peaks are of interest. For numerical evaluation of these characteristics the precise value of the imaginary part of the regularised EFEES is of central importance. The real part provides only a small correction to the peak location and for the sake of simplicity can be neglected.

Analytic expressions developed for resonance locations and resonance widths proved useful computationally. Resonance heights were determined numerically by running the computer programs that generated the results of Chapters 4 and 5 at the resonant parameter region indicated by analytic expressions. The resonance peaks locations, obtained from the mass shell condition $p^2 = m^2$, are determined by the solution of two equations corresponding to the direct channel and the exchange channel of the scattering. For the SCS process, using the same notation as Chapter 3, these are

$$\begin{aligned} 2(q_i k_i) + 2r\left[(kp_i) + (kk_i)\right] &= 0 \qquad \text{direct channel} \\ -2(q_i k_f) + 2r\left[(kp_i) - (kk_f)\right] &= 0 \qquad \text{exchange channel} \end{aligned} \tag{7.16}$$

For a particular set of particle energy-momenta, external field intensity and summation variables r and l, equation 7.16 yields expressions for the resonant scattering angles θ_i^{res} and θ_f^{res}

$$\begin{aligned} \cos\,\theta_i^{res} &= 1 + \frac{1 + r\frac{\omega}{\omega_i}}{\frac{1}{2}\nu^2 + r\omega} \\ \cos\,\theta_f^{res} &= \frac{1}{2(b^2+c^2)}\left(2ab \pm \sqrt{4c^2(b^2+c^2) - 4a^2c^2}\right) \\ \text{where} \qquad a &= r\omega + \tfrac{\nu^2}{2} + 1 - \frac{r\omega}{(q_i k_i) + l(k\bar{p})}(1 + \tfrac{\nu^2}{2} + l\omega + \omega_i) \\ b &= r\omega + \tfrac{\nu^2}{2} - \frac{r\omega}{(q_i k_i) + l(k\bar{p})}(\tfrac{\nu^2}{2} + l\omega + \omega_i) \\ c &= -\frac{r\omega\omega_i \sin\theta_i \cos\phi_f}{[1 + \frac{\nu^2}{2}(1 - \cos\theta_i)]} \end{aligned} \tag{7.17}$$

For the STPPP process, the two equations to be solved for resonant scattering angles are

$$\begin{aligned} (r-l)\frac{\omega}{\omega_1}\,\frac{\epsilon_{q_-} - |q_-|\cos\theta_f - \omega_1(1-\cos\theta_1)}{\epsilon_{q_-} - |q_-|\left(\cos\theta_1\cos\theta_f - \sin\theta_1\sin\theta_f\cos\phi_f\right)} &= 1 \qquad \text{direct channel} \\ (r-l)\frac{\omega}{\omega_1}\,\frac{\epsilon_{q_-} - |q_-|\cos\theta_f - \omega_1(1+\cos\theta_1)}{\epsilon_{q_-} + |q_-|\left(\cos\theta_1\cos\theta_f - \sin\theta_1\sin\theta_f\cos\phi_f\right)} &= 1 \qquad \text{exchange channel} \end{aligned} \tag{7.18}$$

After substituting the expressions for the electron energy-momenta (see equation 3.28), equation 7.18 yields a polynomial to 4th order in $\cos\,\theta_i^{res}$ and $\cos\,\theta_f^{res}$. The solution is most easily achieved numerically.

The angular spacing between resonances ($\delta\,\theta_i$ and $\delta\,\theta_f$) is obtained by solving equations 7.17 and 7.18 for different values of the summation variables r and l. For instance, assuming that the SCS direct channel resonance condition is satisfied for $r = n$, the location of the closest resonant peak is determined by the solution of equation 7.17 for $r = n+1$ (or $r = n-1$). The resonance spacing is obtained by a solution of the equation set

$$\begin{aligned} \cos(\theta_i^{res} + \delta\,\theta_i) &= 1 + \frac{1 + (n+1)\frac{\omega}{\omega_i}}{\frac{1}{2}\nu^2 + (n+1)\omega} \\ \cos\,\theta_i^{res} &= 1 + \frac{1 + n\frac{\omega}{\omega_i}}{\frac{1}{2}\nu^2 + n\omega} \end{aligned} \tag{7.19}$$

The combination of values obtained for resonance spacing and resonance width determine whether or not resonance peaks can be resolved using currently available experimental apparatus, and whether or not resonances overlap. By definition, the angular resonance width $\Delta\theta$ is obtained by the condition that the differential cross section at the points $\theta = \theta^{res} \pm \Delta\theta$ be half its resonant value at $\theta = \theta^{res}$.

Generally, the differential cross section for either the SCS or STPPP process is of the form

$$\frac{d\sigma}{d\Omega} \sim \left| \sum_{r=-\infty}^{\infty} \left(\frac{A}{\bar{p}_r^2 - m^2 + i2\epsilon_p \Im\Delta\epsilon_p^R(\bar{\rho})} + \frac{B}{\bar{\bar{p}}_r^2 - m^2 + i2\epsilon_p \Im\Delta\epsilon_p^R(\bar{\bar{\rho}})} \right) \right|^2 \tag{7.20}$$

where the notation $\bar{p}_r$ and $\bar{\rho}$ refer to the direct channel scattering, and $\bar{\bar{p}}_r$ and $\bar{\bar{\rho}}$ the exchange channel scattering. Assuming the resonance width is small, the quantities A and B can be considered constant over the range of angles $\theta^{res} - \Delta\theta < \theta < \theta^{res} + \Delta\theta$. The resonance width is then determined by a solution of

$$\begin{aligned} \left|\bar{p}_r^2 - m^2\right| &= \left|2\epsilon_p \Im\Delta\epsilon_p^R(\bar{\rho})\right| \qquad \text{direct channel} \\ \left|\bar{\bar{p}}_r^2 - m^2\right| &= \left|2\epsilon_p \Im\Delta\epsilon_p^R(\bar{\bar{\rho}})\right| \qquad \text{exchange channel} \end{aligned} \tag{7.21}$$

For the SCS process, assuming that a resonance occurs for parameters ω, ω_i, ν^2 and r, the θ_i resonance width is approximately given by

$$\cos\,\Delta\theta_i \approx \left| 1 - \frac{2\epsilon_p \Im\Delta\epsilon_p^R(\bar{\rho})}{\omega_i(\frac{1}{2}\nu^2 + r\omega) + \omega_i + r\omega} \right| \tag{7.22}$$

The SCS θ_f resonance width and the equivalent expressions for the STPPP process are considerably more complicated and are not written down here. However these are easily determined computationally. From the analysis of Chapter 6 the numerical value of $\frac{2\epsilon_p \Im\Delta\epsilon_p^R(\bar{\rho})}{\omega_i(\frac{1}{2}\nu^2 + r\omega) + \omega_i + r\omega}$ is much less than unity, assuming that $\frac{\omega_i}{m}$ and $\frac{\omega}{m}$ are not too small. Therefore the numerical value of $\Delta\theta_i$ is also very small. Whether the resonances are too narrow to be experimentally detected requires the precise results of section 7.4.

It is worthwhile comparing the second order SCS and STPPP resonant differential cross sections with the differential cross sections of the equivalent first order process. For the SCS process the equivalent process is HICS, and for the STPPP process it is the OPPP process. With an external field consisting of a circularly polarised electromagnetic wave, the transition probability for the HICS and OPPP processes is due to [NR65a]. To convert to a differential cross section the flux density of incoming particles is required. This is the reciprocal of the three dimensional volume V for one incident photon (OPPP) or one incident electron at rest (HICS).

For the HICS process, an incident electron combines with s external field quanta of energy ω to produce a scattered photon of energy ω_f. The differential cross section is

$$\begin{aligned}
\frac{d\sigma}{d\Omega_{k_f}} &= \frac{\alpha^2}{2m^2}\sum_{s=1}^{\infty}\frac{1}{s}\left(\frac{\omega_f}{\omega}\right)^2\left[-\frac{4}{\nu^2}J_s^2(z)+(2u-1)\left(J_{s-1}^2(z)+J_{s+1}^2(z)-2J_s^2(z)\right)\right] \\
\text{where}\quad z &= \nu^2\frac{m}{\omega}\sqrt{(1+\nu^2)u(u_s-u)} \\
u &= \frac{(kk_f)}{(kp_f)} \quad ; \quad u_s=\frac{2s\omega}{1+\nu^2}
\end{aligned} \tag{7.23}$$

For the OPPP process, an incident photon of energy ω_1 combines with s external field quanta ω to produce an electron-positron pair of 4-momenta q_- and q_+. The differential cross section is

$$\begin{aligned}
\frac{d\sigma}{d\Omega_{q_-}} &= \frac{2\alpha^2}{m^2}\sum_{s>s_0}\left(\frac{m^2}{\omega\omega_1}\right)\frac{|q_-|}{\omega_1+s\omega}\left[\frac{2}{\nu^2}J_s^2(z)+(2u-1)\left(J_{s-1}^2(z)+J_{s+1}^2(z)-2J_s^2(z)\right)\right] \\
\text{where}\quad z &= 4\nu^2\sqrt{1+\tfrac{1}{\nu^2}}\frac{m^2}{(kk_1)}\sqrt{u(u_s-1)} \\
u &= \frac{(kk_1)^2}{4(kq_-)(kq_+)} \quad ; \quad u_s=\frac{s(kk_1)}{2m_*^2} \quad ; \quad s_0=\frac{2m_*^2}{(kk_1)}
\end{aligned} \tag{7.24}$$

7.4 Resonance Figures

The figures contained within section 7.4 are divided into two main groups. The SCS resonances are investigated in section 7.4.1 and the STPPP process in section 7.4.2. Tables 7.4.1 and 7.4.2 present the range of parameters to be investigated. These parameters were defined in chapters 4 and 5. The majority of the figures presented in section 7.4 show the angular location and differential cross section height of resonance peaks. The remaining figures show the variation of resonance height and width with the external field intensity parameter ν^2. Vertical axes representing differential cross sections unless otherwise labelled are understood to be the differential cross section $\frac{d\sigma}{d\Omega}\Big/\frac{\alpha^2}{32m^2}$ in units of steradian^{-1}. Resonant differential cross sections are generally large and vary greatly in height. Consequently a logarithmic scale is used. Resonances arise in specific summation terms, characterised by the l and r, r' parameters, of the SCS and STPPP differential cross section expressions. Some figures show specific summation terms. Most however are summed over all permissible values. At the end of each subsection a full cross section is presented. This was obtained by numerically integrating over final angles using the DIVONNE implementation in the numerical integration library CUBA [Hah05]. The usefulness of this implementation is that assistance is accepted from initial specification of peak locations. This proved particularly useful for the STPPP cross-section which contained only narrow peaks.

7.4.1 SCS Resonances

$\boldsymbol{l}$	$\boldsymbol{r}, r'$	$\boldsymbol{\nu^2}$	$\boldsymbol{\omega}(keV)$	$\boldsymbol{\omega}_i(keV)$	$\boldsymbol{\theta}_i$	(θ_f, ϕ_f)	**figure(s)**
all	all	0.1	$25.6, 61.4$	51.2	$90°$	$(0° \to 360°, 0°)$	7.2,7.3
all	all	1	$25.6, 61.4$	51.2	$90°$	$(0° \to 360°, 0°)$	7.4,7.5
all	all	1	61.4	51.2	$0° \to 360°$	$(0°, 0°)$	7.6
all	all	1	61.4	51.2	$0° \to 360°$	$(45°, 0°)$	7.7
all	all	1	61.4	51.2	$0° \to 360°$	$(90°, 0°)$	7.8
all	all	1	61.4	51.2	$0° \to 360°$	$(180°, 0°)$	7.9
$3, 4$	$6, 7$		61.4	51.2	$90°$		7.10,7.12
$3, 4$	$6, 7$		61.4	51.2		$45°$	7.11,7.13
all	all	$0.05 \to 0.6$	25.6	51.2		$90°$	7.14

Table 7.1: **The parameter range for which the SCS cross section resonances are investigated.**

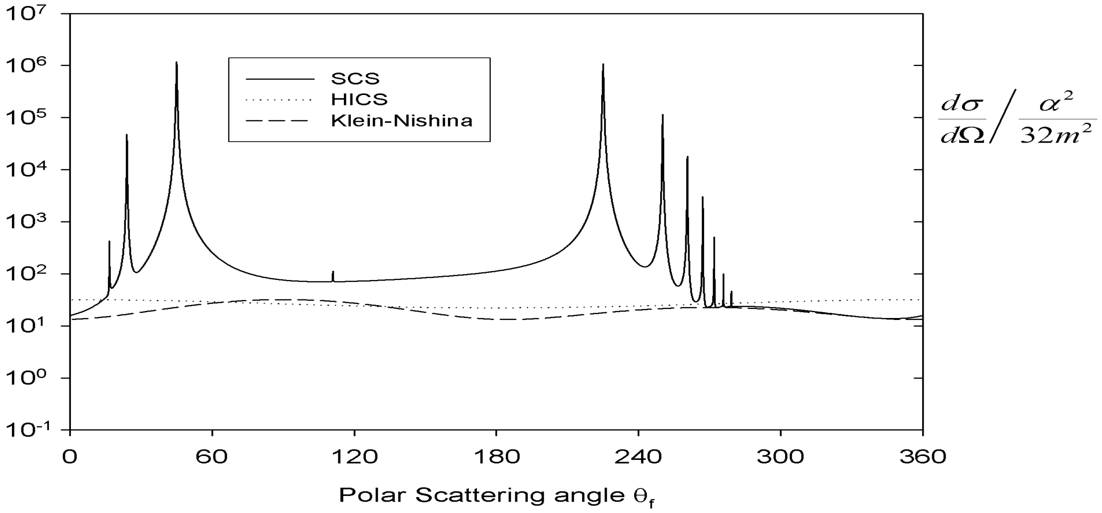

Figure 7.2: **Comparison of the Klein-Nishina, HICS and SCS differential cross section resonances vs θ_f for $\omega = 25.6$ keV, $\omega_i = 51.2$ keV, $\theta_i = 90°$, $\varphi_f = 0°$ and $\nu^2 = 0.1$.**

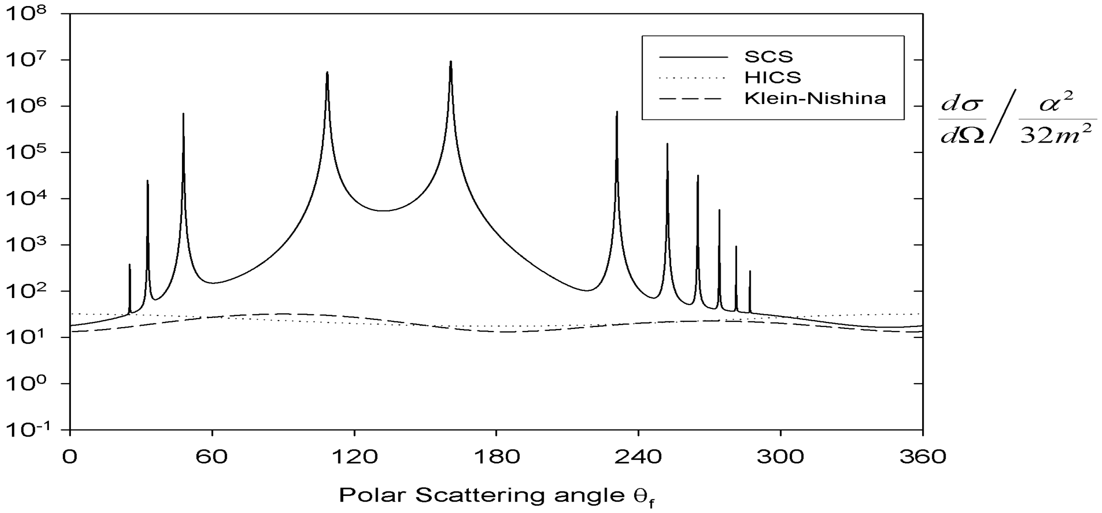

Figure 7.3: **Comparison of the Klein-Nishina, HICS and SCS differential cross section resonances vs θ_f for $\omega = 61.4$ keV, $\omega_i = 51.2$ keV, $\theta_i = 90°$, $\varphi_f = 0°$ and $\nu^2 = 0.1$.**

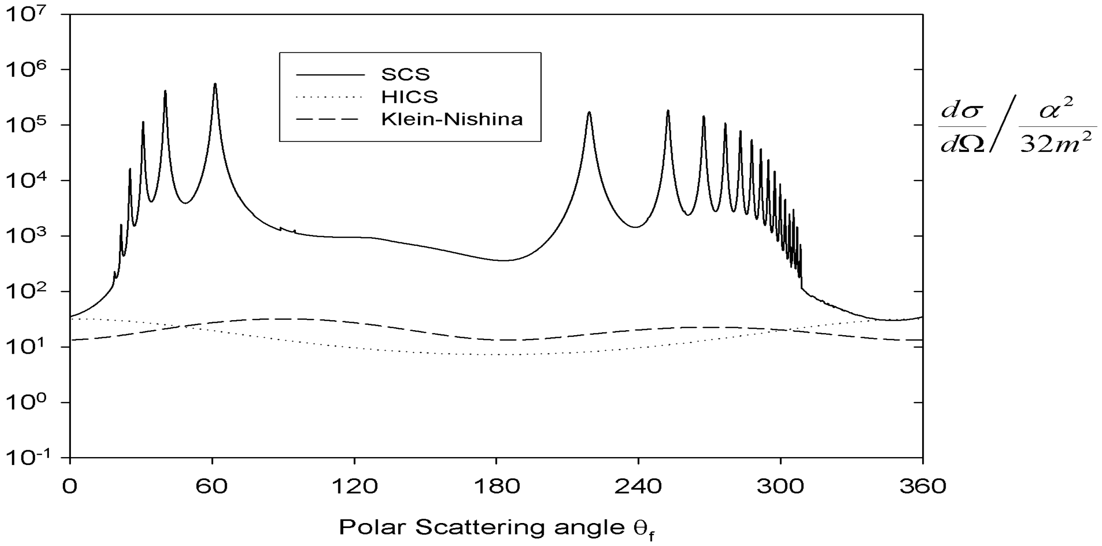

Figure 7.4: **Comparison of the Klein-Nishina, HICS and SCS differential cross section resonances vs θ_f for $\omega = 25.6$ keV, $\omega_i = 51.2$ keV, $\theta_i = 90°$, $\varphi_f = 0°$ and $\nu^2 = 1$.**

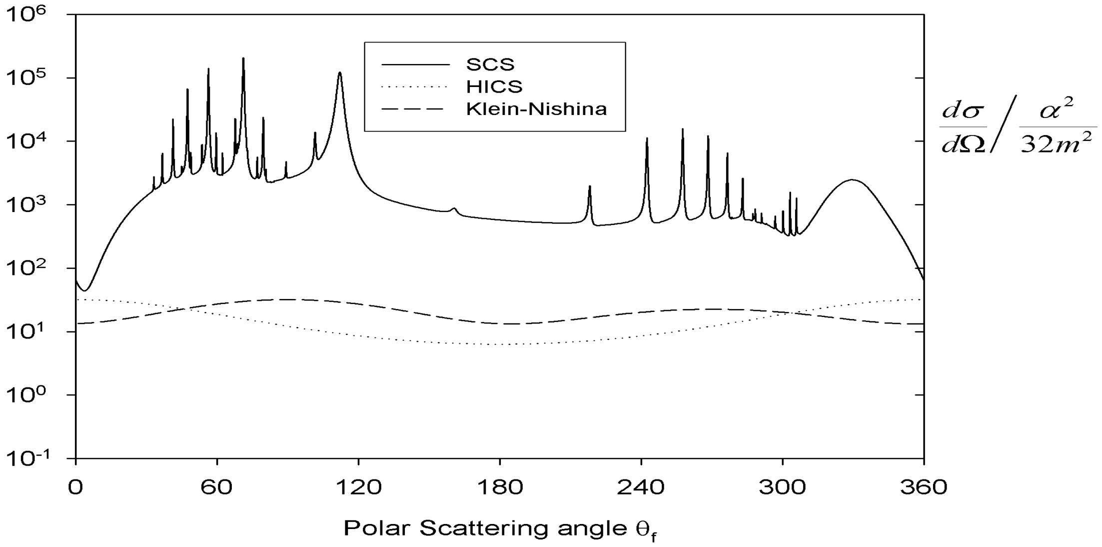

Figure 7.5: **Comparison of the Klein-Nishina, HICS and SCS differential cross section resonances vs θ_f for $\omega = 61.4$ keV, $\omega_i = 51.2$ keV, $\theta_i = 90°$, $\varphi_f = 0°$ and $\nu^2 = 1$.**

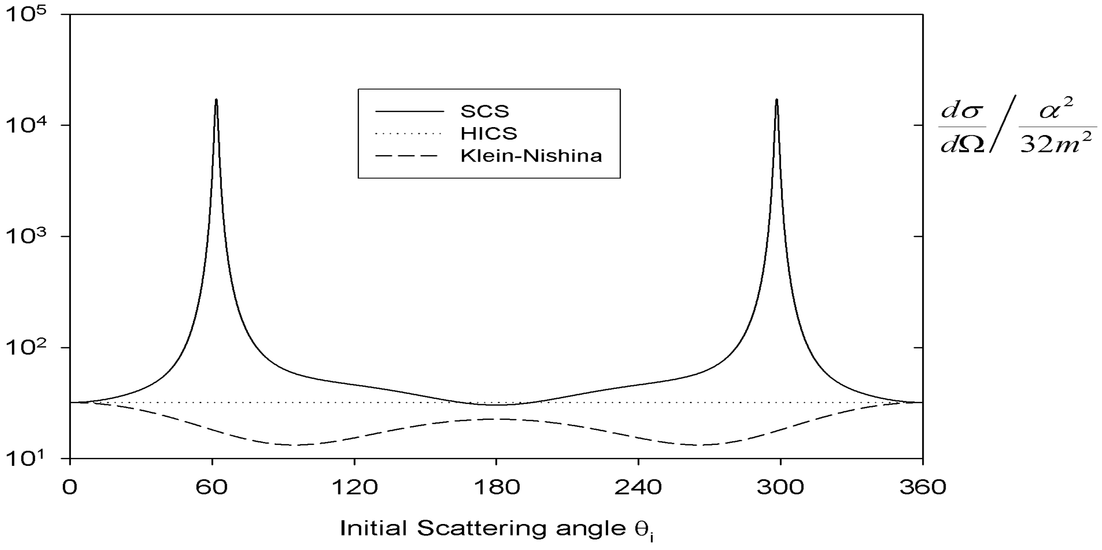

Figure 7.6: **Comparison of the Klein-Nishina, HICS and SCS differential cross section resonances vs θ_f for $\omega = 25.6$ keV, $\omega_i = 51.2$ keV, $\theta_i = 0°$, $\varphi_f = 0°$ and $\nu^2 = 1$.**

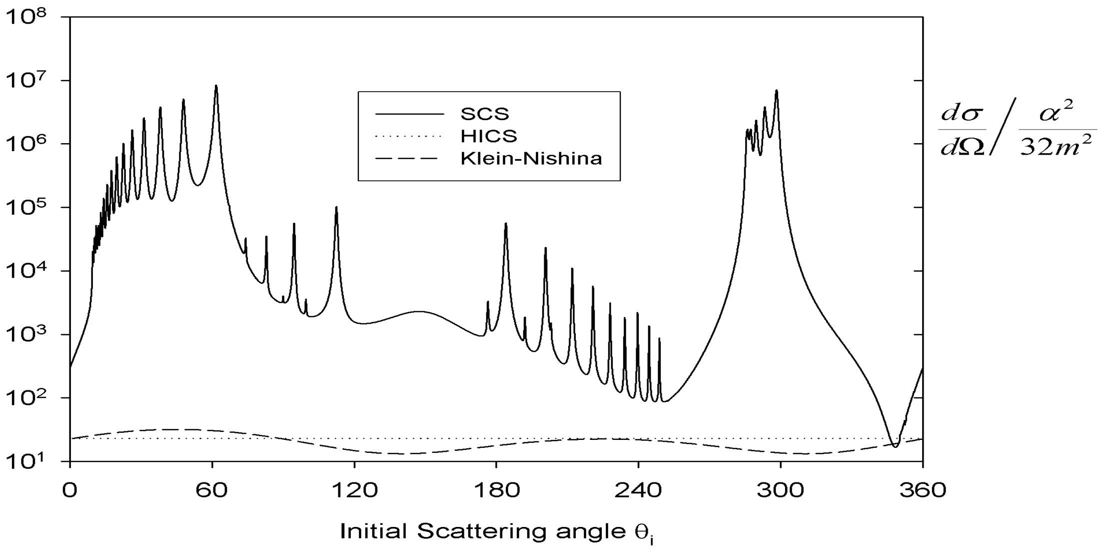

Figure 7.7: **Comparison of the Klein-Nishina, HICS and SCS differential cross section resonances vs θ_f for $\omega = 25.6$ keV, $\omega_i = 51.2$ keV, $\theta_i = 45°$, $\varphi_f = 0°$ and $\nu^2 = 1$.**

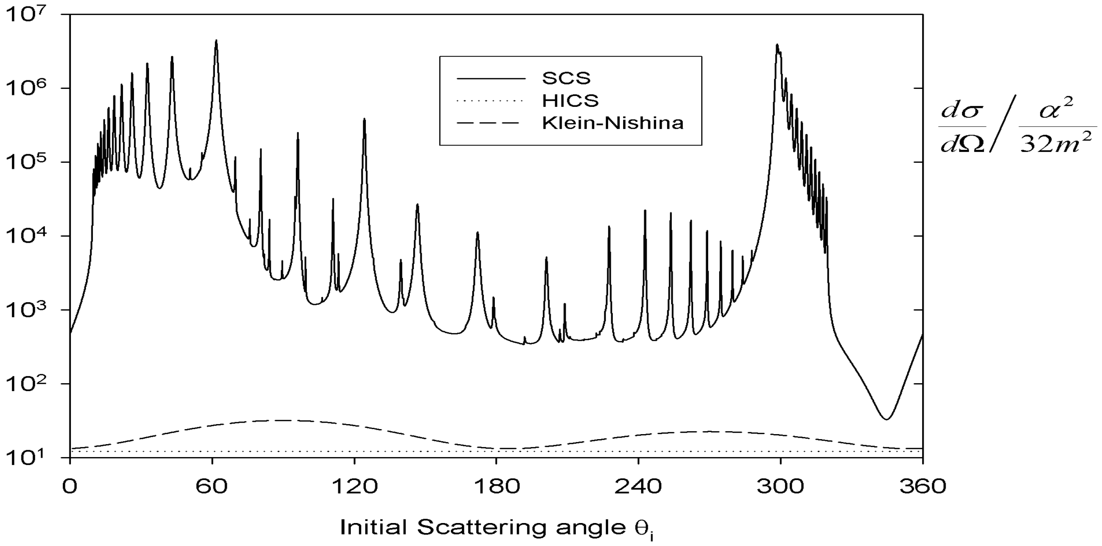

Figure 7.8: **Comparison of the Klein-Nishina, HICS and SCS differential cross section resonances vs θ_f for $\omega = 25.6$ keV, $\omega_i = 51.2$ keV, $\theta_i = 90°$, $\varphi_f = 0°$ and $\nu^2 = 1$.**

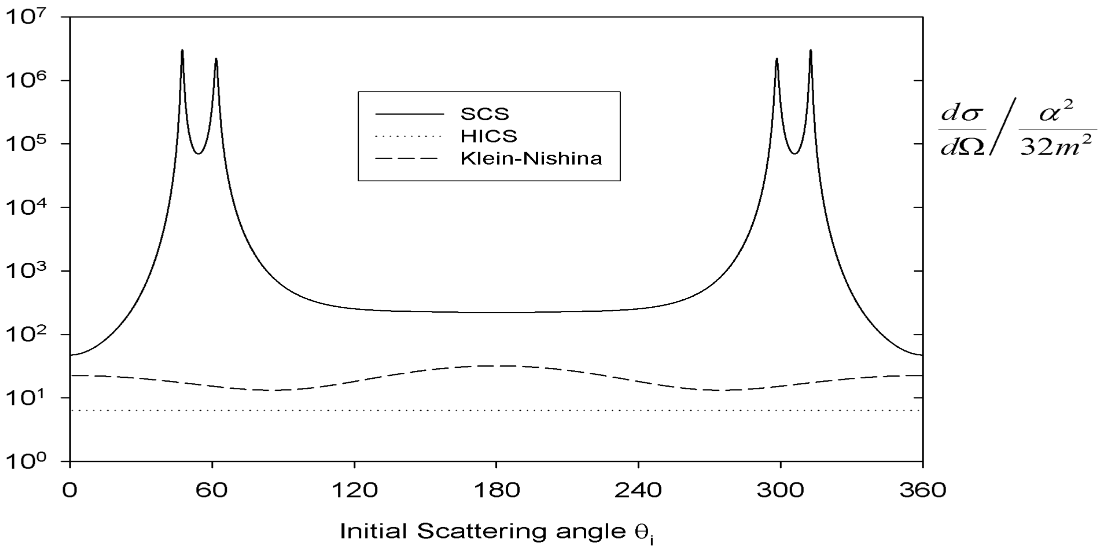

Figure 7.9: **Comparison of the Klein-Nishina, HICS and SCS differential cross section resonances vs θ_f for $\omega = 25.6$ keV, $\omega_i = 51.2$ keV, $\theta_i = 180°$, $\varphi_f = 0°$ and $\nu^2 = 1$.**

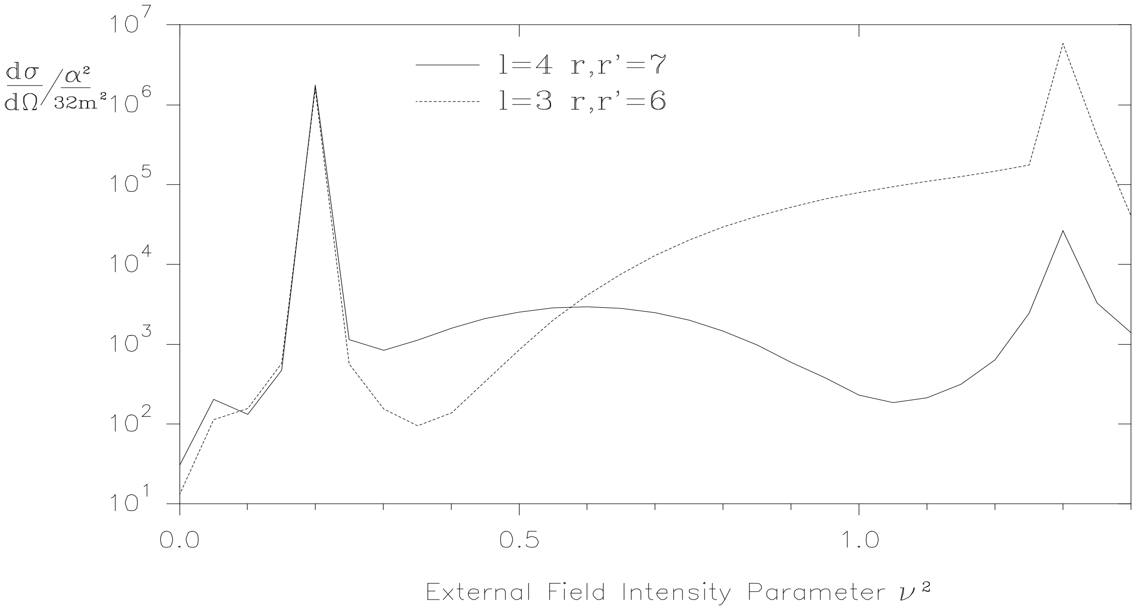

Figure 7.10: **SCS differential cross section resonances vs ν^2 for $\omega = 25.6$ keV, $\omega_i = 51.2$ keV, $\theta_i = 90°$, $\varphi_f = 0°$ and various l, r, r' terms.**

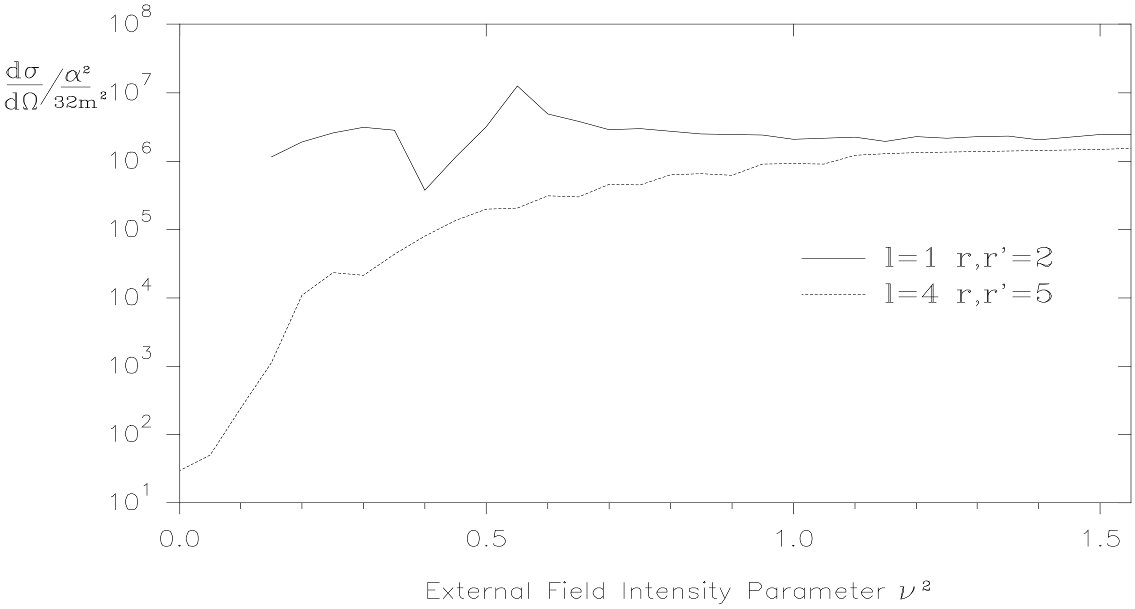

Figure 7.11: **SCS differential cross section resonances vs ν^2 for $\omega = 61.4$ keV, $\omega_i = 51.2$ keV, $\theta_f = 45°$, $\varphi_f = 0°$ and various l, r, r' terms.**

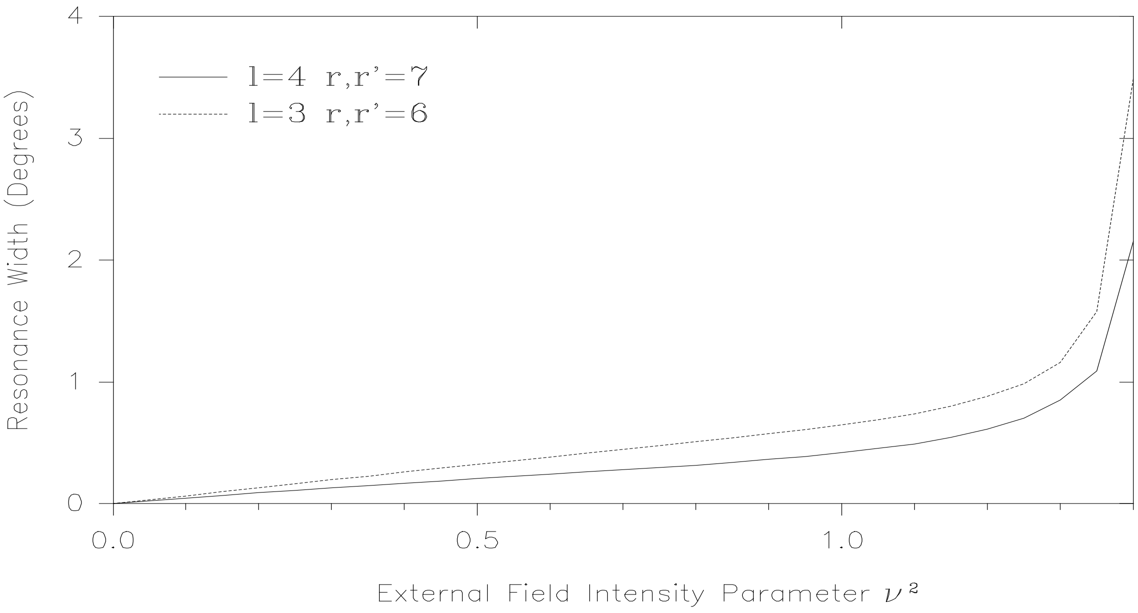

Figure 7.12: **SCS differential cross section resonances vs ν^2 for $\omega = 25.6$ keV, $\omega_i = 51.2$ keV, $\theta_f = 45°$, $\varphi_f = 0°$ and various l, r, r' terms.**

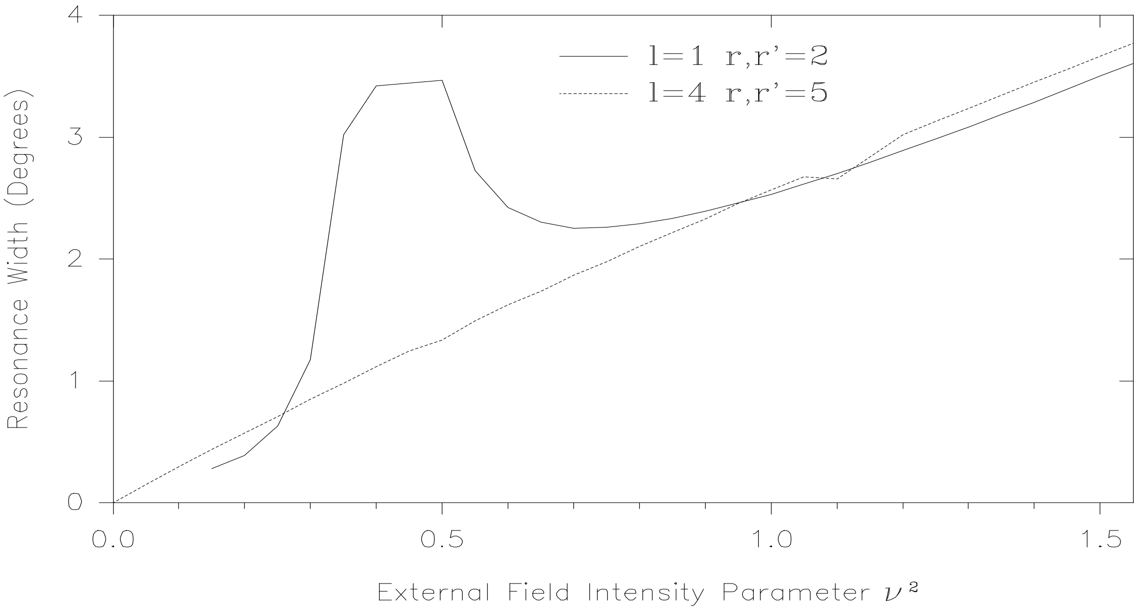

Figure 7.13: **SCS differential cross section resonances vs ν^2 for $\omega = 61.4$ keV, $\omega_i = 51.2$ keV, $\theta_i = 90°$, $\varphi_f = 0°$ and various l, r, r' terms.**

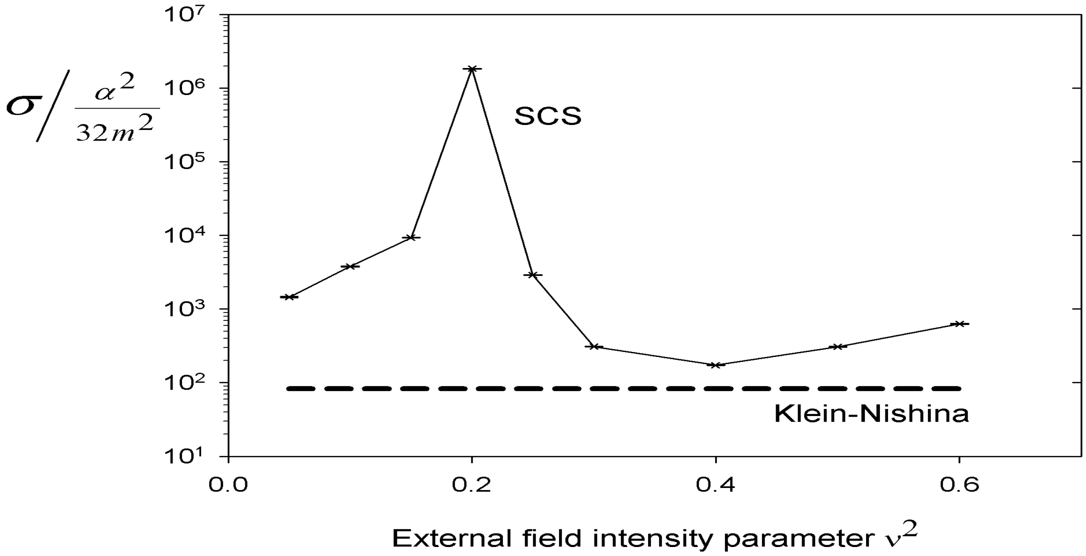

Figure 7.14: **Comparison of the full Klein-Nishina and SCS cross sections vs ν^2 for $\omega = 1.28$ MeV,$\omega_1, omega_2 = 0.92$ MeV, $\theta_f, = 45°$ and $\varphi_f = 0°$.**

7.4.2 STPPP Resonances

l	r, r'	ν^2	ω(MeV)	$\omega_{1,2}$, (MeV)	θ_1	(θ_f, ϕ_f)	figure(s)
all	all	0.1	$0.409, 1.28$	0.768	$45°$	$(0° \to 360°, 0°)$	7.15,7.16
all	all	0.5	$0.409, 1.28$	0.768	$45°$	$(0° \to 360°, 0°)$	7.17,7.18
all	all	0.5	1.024	0.768	$0° \to 360°$	$(0°, 0°)$	7.19
all	all	0.5	1.024	0.768	$0° \to 360°$	$(45°, 0°)$	7.20
all	all	0.5	1.024	0.768	$0° \to 360°$	$(90°, 0°)$	7.21
all	all	0.5	1.024	0.768	$0° \to 360°$	$(180°, 0°)$	7.22
2	$3, -1$		0.768	0.409	$45°$		7.23,7.25
1	$-1, 2$		1.024	0.768		$45°$	7.24,7.26
all	all	$0.05 \to 1.0$	1.28	0.92	$45°$		7.27

Table 7.2: **The parameter range for which the STPPP cross section resonances are investigated.**

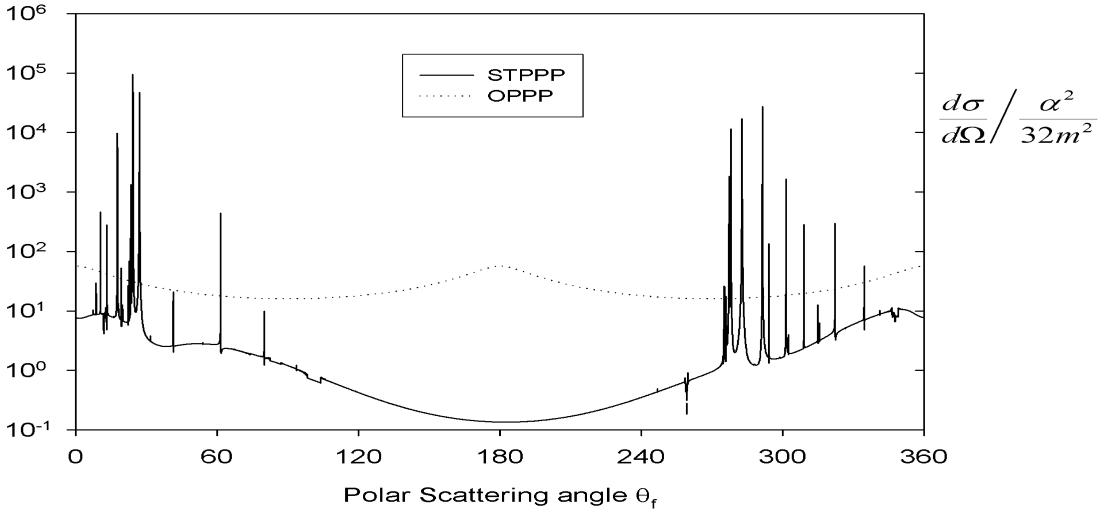

Figure 7.15: **Comparison of the OPPP and STPPP differential cross section resonances vs θ_f for $\omega = 0.409$ MeV, $\omega_1, \omega_2 = 0.768$ MeV, $\theta_1 = 45°$, $\varphi_f = 0°$ and $\nu^2 = 0.1$.**

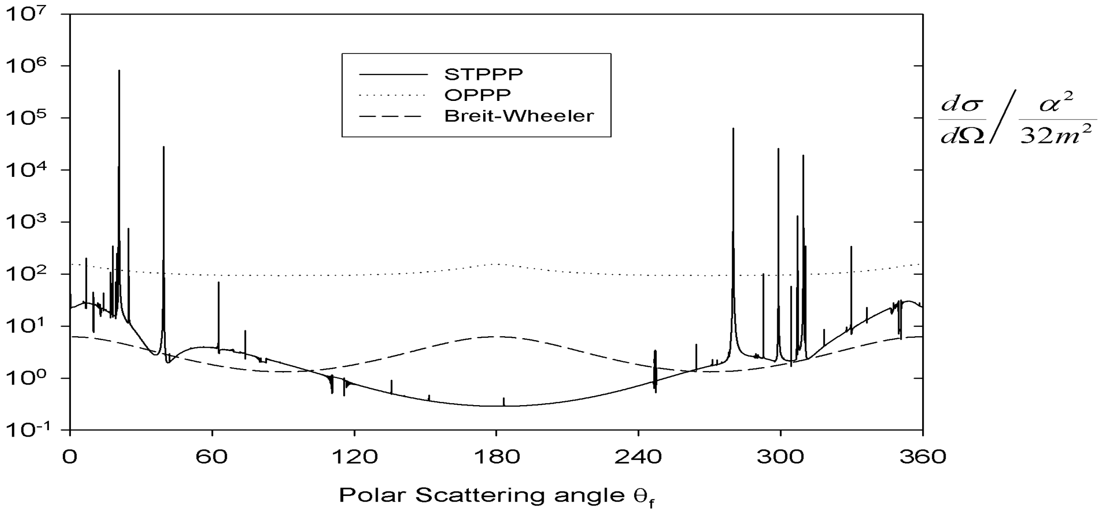

Figure 7.16: **Comparison of the Breit-Wheeler, OPPP and STPPP differential cross section resonances vs θ_f for $\omega = 0.409$ MeV, $\omega_1, \omega_2 = 1.28$ MeV, $\theta_1, = 45°$, $\varphi_f = 0°$ and $\nu^2 = 0.1$.**

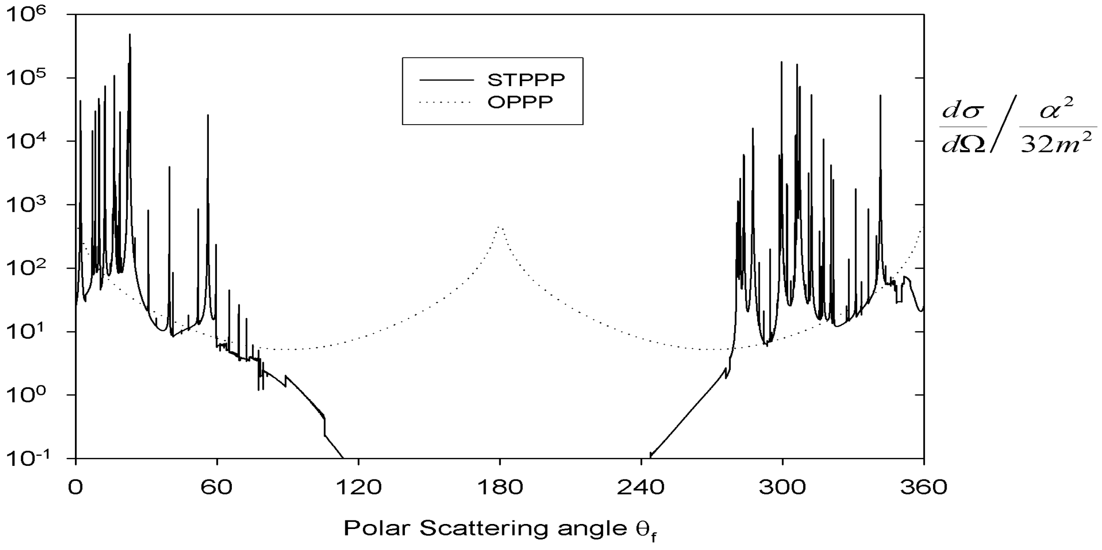

Figure 7.17: **Comparison of the OPPP and STPPP differential cross section resonances vs θ_f for $\omega = 0.409$ MeV, $\omega_1, \omega_2 = 0.768$ MeV, $\theta_1, = 45°$, $\varphi_f = 0°$ and $\nu^2 = 0.5$.**

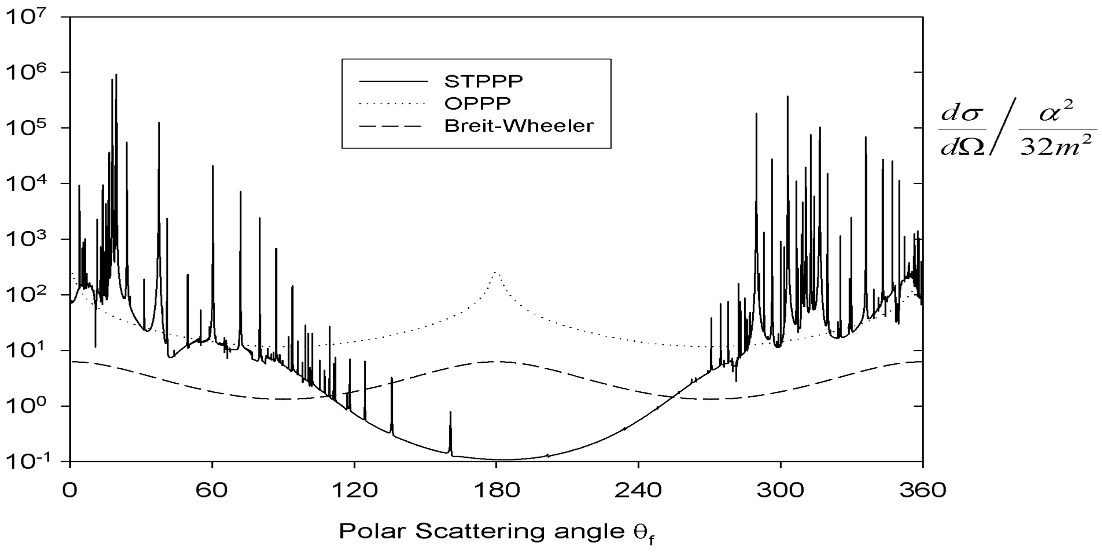

Figure 7.18: **Comparison of the Breit-Wheeler, OPPP and STPPP differential cross section resonances vs θ_f for $\omega = 0.409$ MeV, $\omega_1, \omega_2 = 1.28$ MeV, $\theta_1, = 45°$, $\varphi_f = 0°$ and $\nu^2 = 0.5$.**

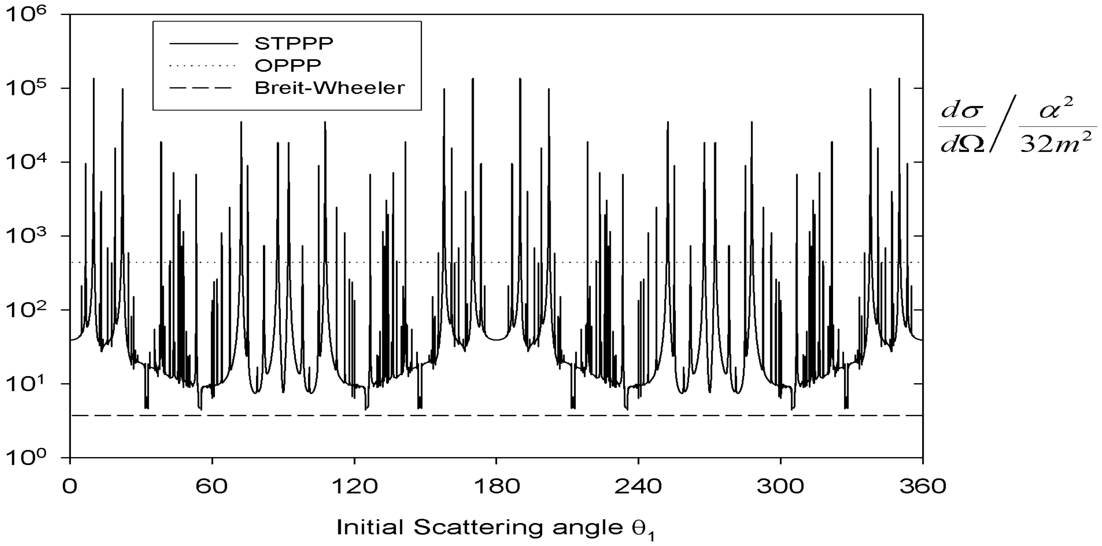

Figure 7.19: **Comparison of the Breit-Wheeler, OPPP and STPPP differential cross section resonances vs θ_1 for $\omega = 1.024$ MeV, $\omega_1, \omega_2 = 0.768$ MeV, $\theta_f, = 0°$, $\varphi_f = 0°$ and $\nu^2 = 0.5$.**

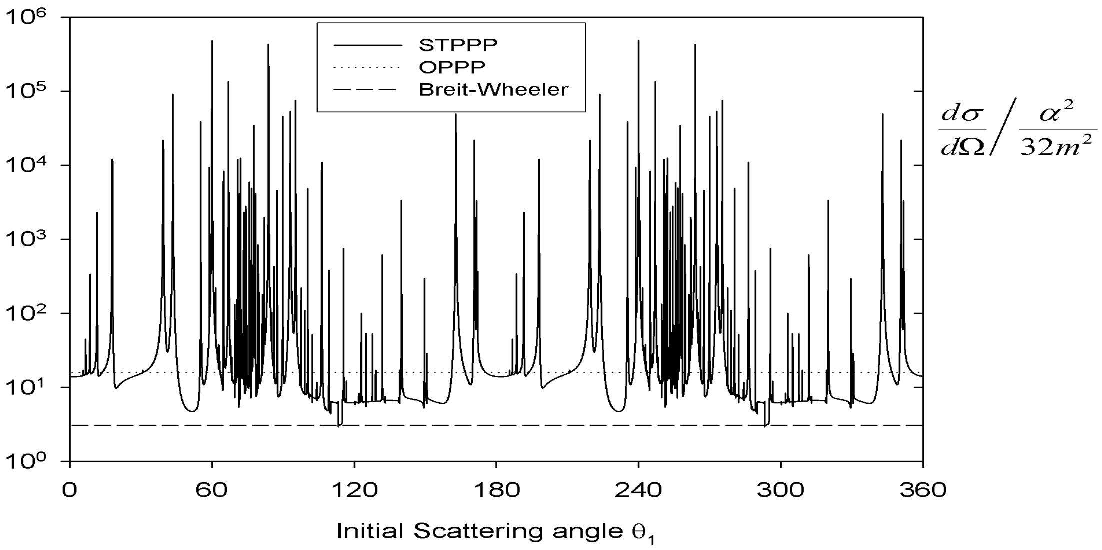

Figure 7.20: **Comparison of the Breit-Wheeler, OPPP and STPPP differential cross section resonances vs θ_1 for $\omega = 1.024$ MeV, $\omega_1, \omega_2 = 0.768$ MeV, $\theta_f, = 45°$, $\varphi_f = 0°$ and $\nu^2 = 0.5$.**

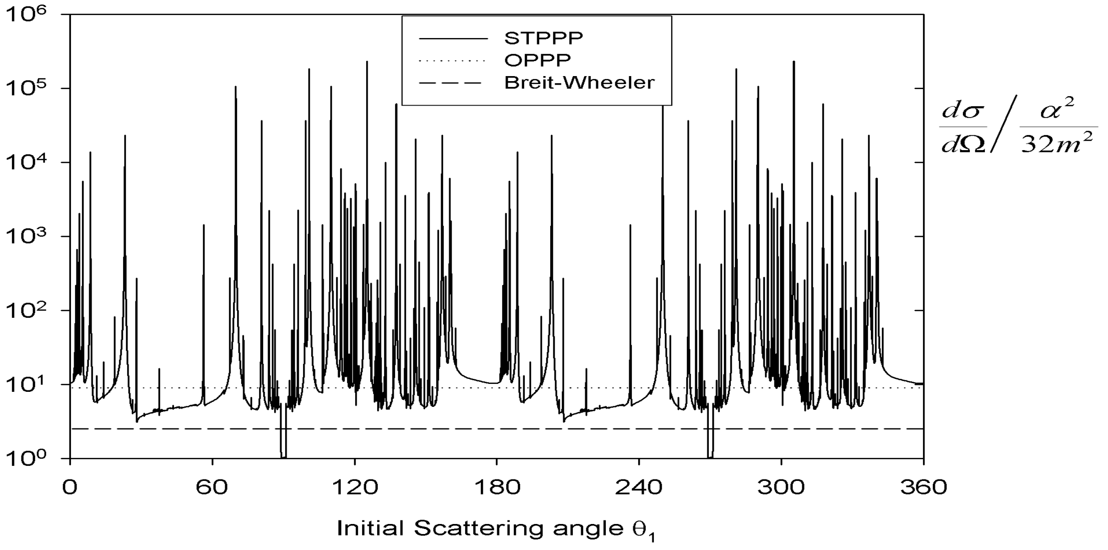

Figure 7.21: **Comparison of the Breit-Wheeler, OPPP and STPPP differential cross section resonances vs θ_1 for $\omega = 1.024$ MeV, $\omega_1, \omega_2 = 0.768$ MeV, $\theta_f, = 90°$, $\varphi_f = 0°$ and $\nu^2 = 0.5$.**

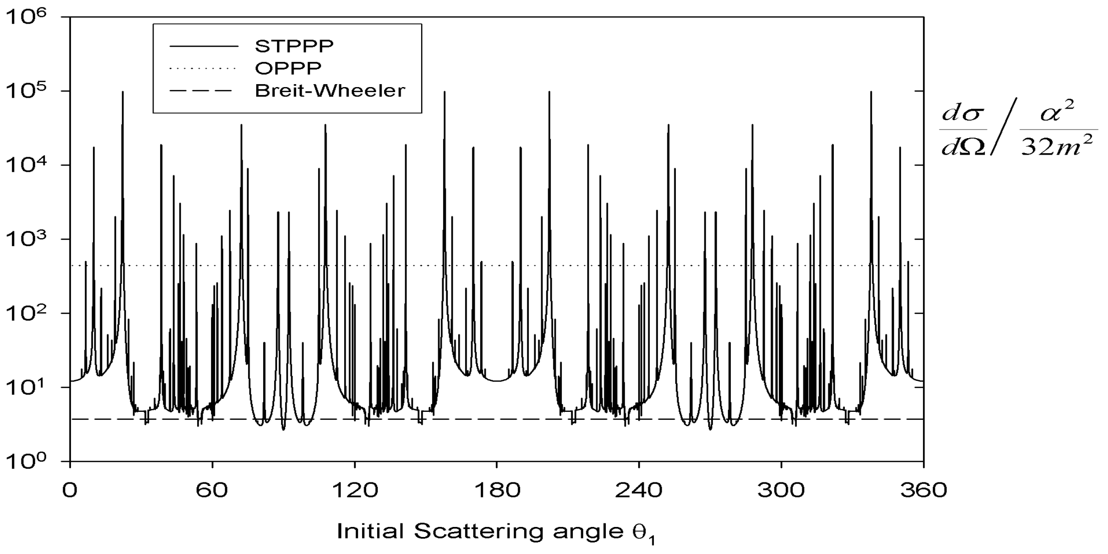

Figure 7.22: **Comparison of the Breit-Wheeler, OPPP and STPPP differential cross section resonances vs θ_1 for $\omega = 1.024$ MeV, $\omega_1, \omega_2 = 0.768$ MeV, $\theta_f, = 180°$,$\varphi_f = 0°$ and $\nu^2 = 0.5$.**

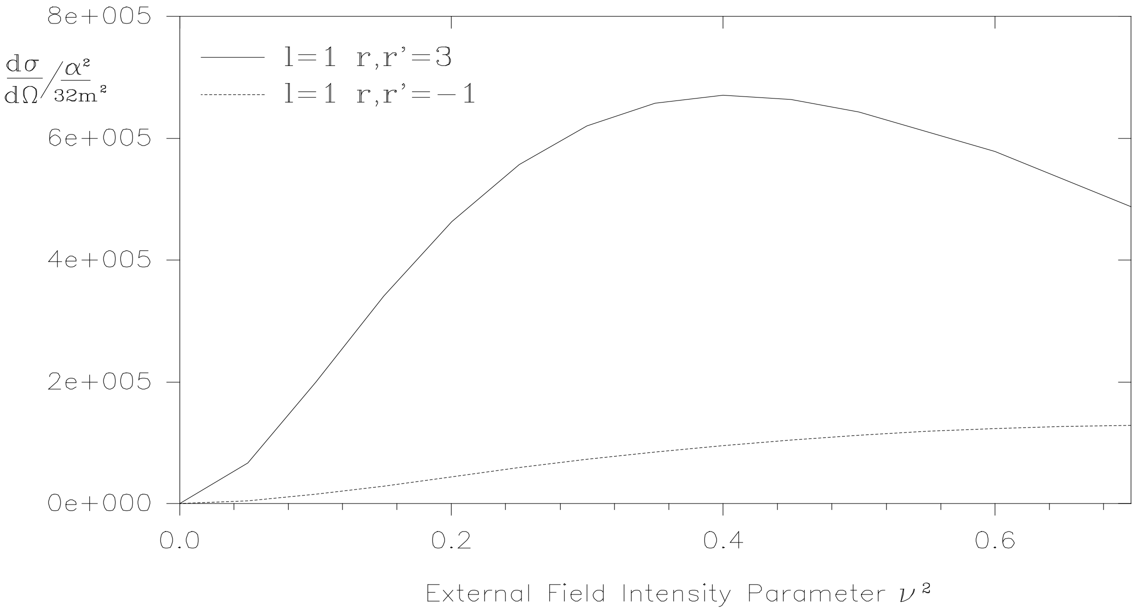

Figure 7.23: **The STPPP differential cross section resonances vs** ν^2 **for** $\omega = 0.768$ **MeV,** $\omega_1, \omega_2 = 0.409$ **MeV,** $\theta_1, = 45°$**,** $\varphi_f = 0°$ **and various** l, r, r' **terms.**

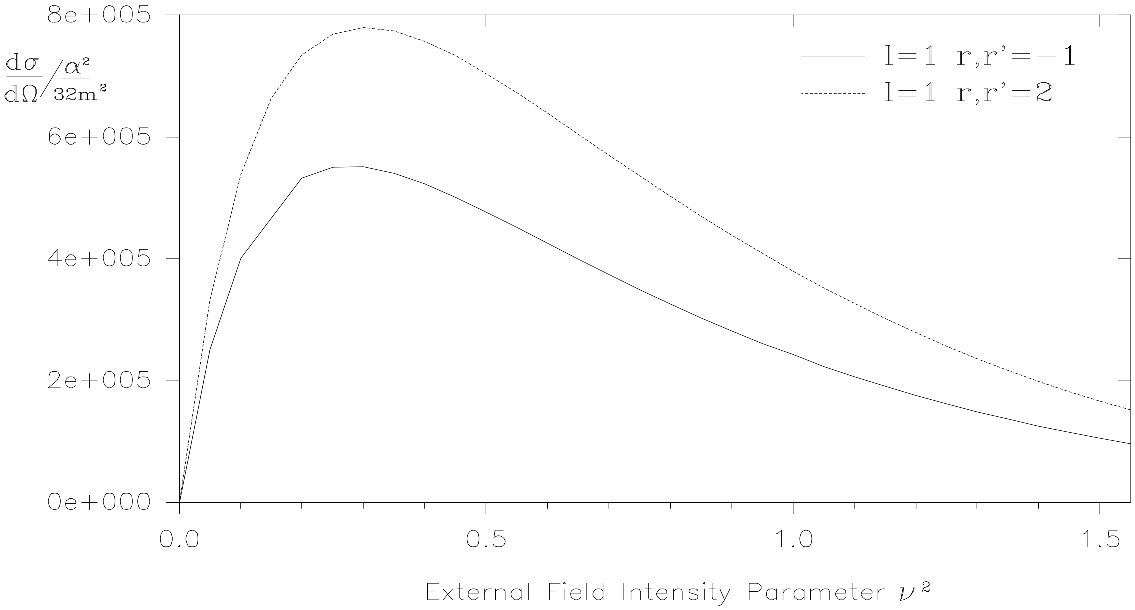

Figure 7.24: **The STPPP differential cross section resonances vs** ν^2 **for** $\omega = 1.024$ **MeV,** $\omega_1, \omega_2 = 0.768$ **MeV,** $\theta_f, = 45°$**,** $\varphi_f = 0°$ **and various** l, r, r' **terms.**

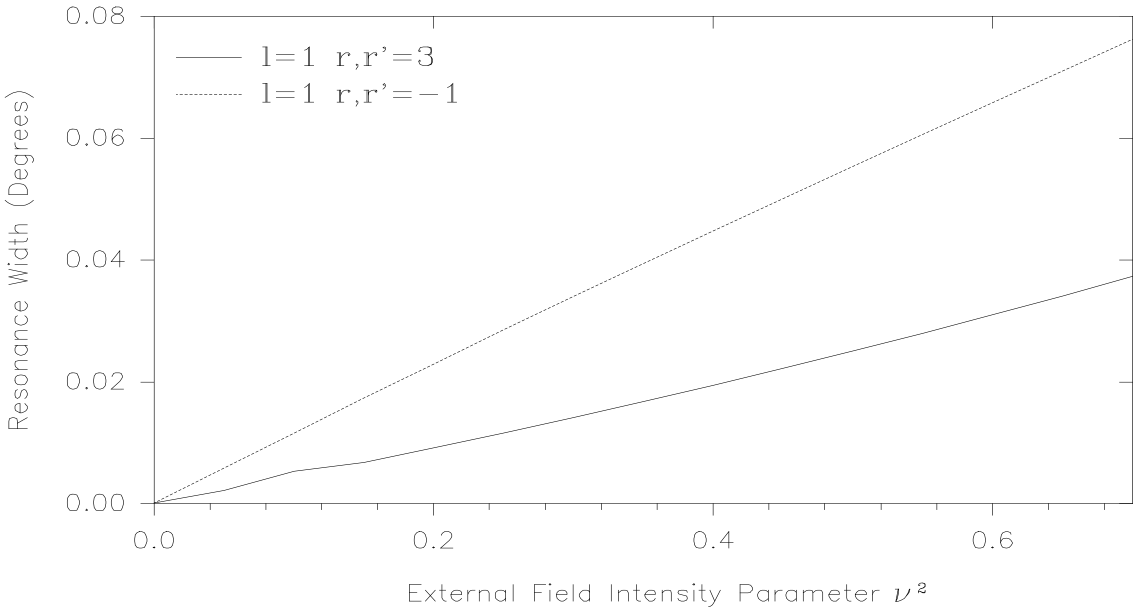

Figure 7.25: **The STPPP differential cross section resonances vs ν^2 for $\omega = 0.768$ MeV, $\omega_1, \omega_2 = 0.409$ MeV, $\theta_1, = 45°$, $\varphi_f = 0°$ and various l, r, r' terms.**

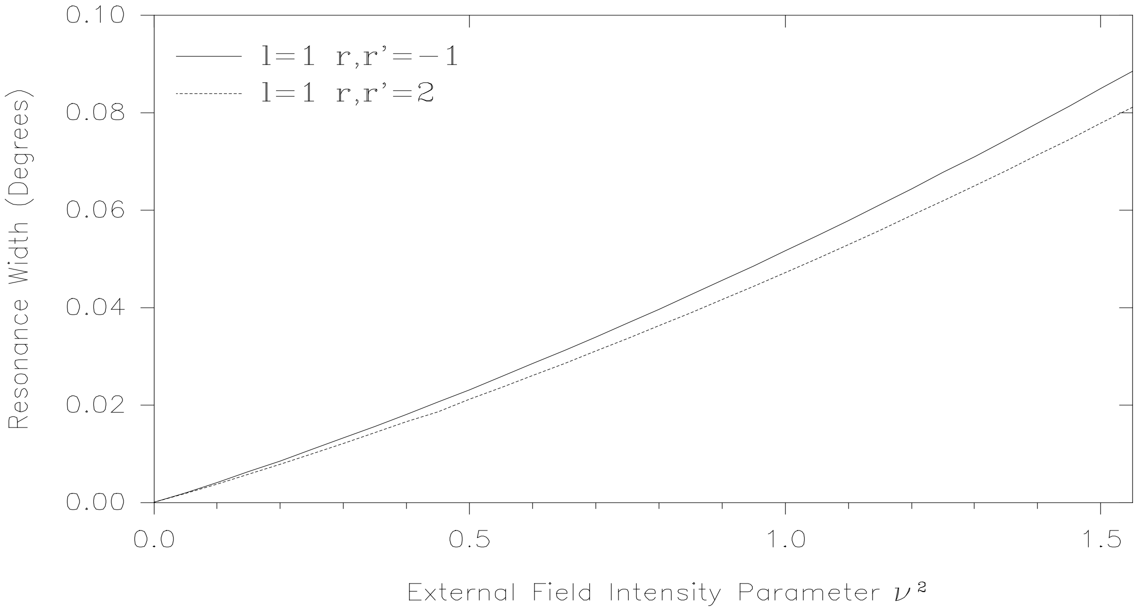

Figure 7.26: **The STPPP differential cross section resonances vs ν^2 for $\omega = 1.024$ MeV, $\omega_1, \omega_2 = 0.768$ MeV, $\theta_f, = 45°$, $\varphi_f = 0°$ and various l, r, r' terms.**

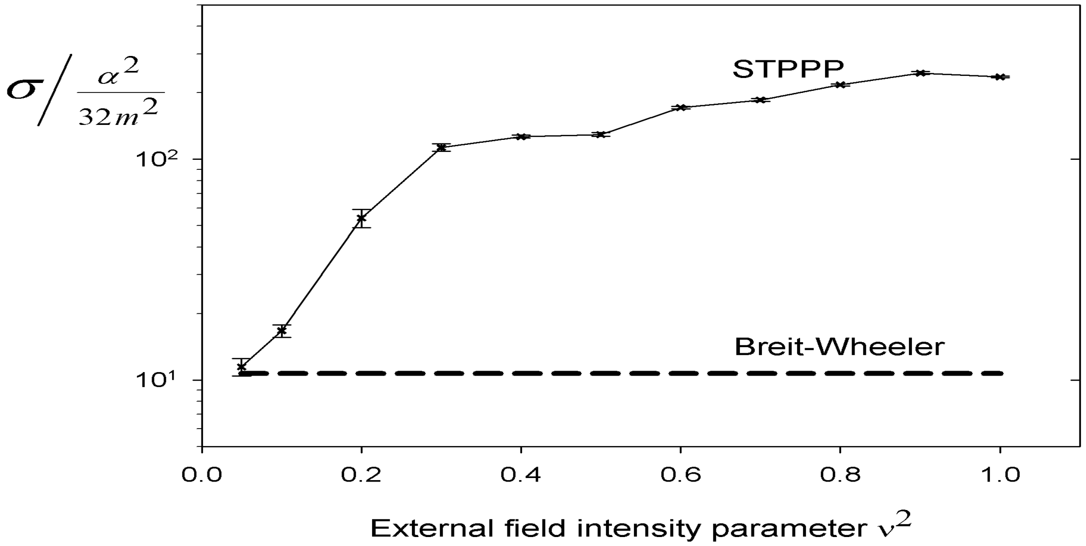

Figure 7.27: **Comparison of the full Breit-Wheeler and STPPP cross sections vs ν^2 for $\omega = 1.28$ MeV, $\omega_1, \omega_2 = 0.92$ MeV, $\theta_f, = 45°$ and $\varphi_f = 0°$.**

7.5 Analysis of Resonance Plots

The differential cross section resonances of both the SCS and STPPP processes are discussed in this section. Analysis is in terms of the four quantities considered in section 7.3, namely resonance height, width, spacing and location. Generally the analysis follows the figure order - SCS resonances first, and STPPP following. However comparison is made between groups of SCS resonance figures and groups of STPPP resonance figures. The figures showing variation with respect to ν^2 for both SCS and STPPP processes are discussed at the end of the section. The variation of the full cross section with ν^2 for both processes will also be discussed.

The θ_f distribution of resonance peaks of the SCS (figures 7.2 - 7.9 and STPPP (figures 7.15 - 7.22) processes are discussed first. The logarithmic scale on all vertical axes of figures 7.2 - 7.9 and figures 7.15 - 7.22, facilitates comparison of the SCS and STPPP resonances with the corresponding first order external field processes and the corresponding second order process in the absence of the external field. The SCS resonance differential cross section is compared with the differential cross sections of the HICS process (equation 7.23) and the Klein-Nishina process (equation 3.21) in the reference frame in which the initial electron is stationary. The resonant STPPP differential cross section is compared with the differential cross section of the OPPP process in the reference frame in which the sum of initial photon 3-momentum and the 3-momenta sum total of contributing external field quanta is zero (equation 7.24), and the differential cross section of the Breit-Wheeler process (equation 3.32).

Each of figures 7.2 - 7.9 display several resonances of differing heights. Figures 7.2 and 7.3 show an external field intensity parameter of $\nu^2 = 0.1$ at relative particle energies such that the ratio $\frac{\omega_i}{\omega}$ is above and below unity.[1] The maximum resonances of figure 7.3 reach a value of approximately 10^7 compared to approximately 10^6 for figure 7.2. This result appears consistent with the analysis of chapter 4 which found, generally, that the SCS differential cross section is enhanced for a relative particle energy regime in which $\frac{\omega_i}{\omega} < 1$. On the other hand, figures 7.4 - 7.5 with an external field intensity $\nu^2 = 1$, reveal a reverse behaviour. The maximum resonance of figure 7.4 with $\frac{\omega_i}{\omega} = 2$ is larger in value than the maximum resonance of figure 7.5 with $\frac{\omega_i}{\omega} = 0.83$. This is due to the appearance of the maximum resonance in differing summation terms. The maximum resonance of figure 7.4 occurs in the $l = -1$ contribution which is more probable than the $l = 3$ contribution in which the maximum resonance of figure 7.5 appears. Generally, the resonance heights of figures 7.4 and 7.5 are lower than those of figures 7.2 and 7.3. This is due to the increase of the EFEES imaginary part with increased ν^2 (see figures 6.4 and 6.5).

Figures 7.6 - 7.9 show the SCS resonances with variation in θ_i. The maximum resonances of all four figures occur at $\theta_i = 61.726°$ indicating that the resonance occurs in the direct channel of the scattering, which has a dependence only on initial state quantities. The $\theta_i = 61.726°, 298.271°$

[1] $\frac{\omega}{\omega_1} = 2$ for figure 7.2 and $\frac{\omega}{\omega_1} = 0.83$ for figure 7.3.

resonance peaks dominate in each of figures 7.6 - 7.9 since they appear in every l contribution of the SCS differential cross section.

Figures 7.15 - 7.22 display the resonances of the STPPP process with a similar grouping of parameters as figures 7.2 - 7.9 for the SCS process. The heights of maximum STPPP resonance peaks fall in the range $10^5 \leq \frac{d\sigma}{d\Omega} \Big/ \frac{\alpha^2}{32m^2} \leq 10^6$. That the resonance peaks generally differ greatly in height, is due to the summation terms of the STPPP differential cross section in which they appear and whether they appear in the direct or exchange channel of the process.

The point of greatest interest in the consideration of resonance peak heights of both the SCS and STPPP processes is that they exceed by several orders of magnitude the differential cross sections of the equivalent first order processes. Naively it would be expected that the first order process cross sections which are proportional to the fine structure constant α would dominate the second order processes which are proportional to α^2. Indeed most experimental attempts to detect QED processes in the external electromagnetic field of similar form to that considered in this thesis have dealt with the first order processes. However the second order processes at resonance provide a much more likely candidate for experimental detection. For the range of parameters considered in section 7.4, the maximum resonant differential cross sections expressed as a percentage increase over the equivalent first order processes are

$$\begin{array}{ll} 1.19 \times 10^8\ \% & \text{for the } \theta_i = 61.726^\circ \text{ SCS resonance of figure 7.6} \\ 4.49 \times 10^6\ \% & \text{for the } \theta_1 = 239.95^\circ \text{ STPPP resonance of figure 7.19} \end{array} \tag{7.25}$$

For the purposes of experimental detection the number of resonances that occur and their angular location, is also of interest. The number of resonances that occur for a particular set of parameters and all possible scattering geometries ($0^\circ \leq \theta_f \leq 360^\circ$ and $0^\circ \leq \theta_i \leq 360^\circ$) is generally larger for the STPPP resonances. An examination of the energy level structure of the electron embedded in the external field reveals why this should be the case. For an electron of 4-momentum q embedded in an external field of intensity ν^2 and 4-momentum k, the nth energy level is characterised by

$$(q + nk)^2 = m^2(1 + \nu^2) \tag{7.26}$$

Using the notation of chapters 4 and 5, the energy levels of the intermediate SCS and STPPP electron with l external field quanta contributing can be written

$$\begin{aligned} n-l &= \frac{(q_ik_i)}{(kp_i)+(kk_i)} && \text{SCS direct channel} \\ n-l &= \frac{-(q_ik_f)}{(kp_i)-(kk_f)} && \text{SCS exchange channel} \\ n-l &= \frac{(q_-k_1)}{(kp_-)-(kk_1)} && \text{STPPP direct channel} \\ n-l &= \frac{(q_-k_2)}{(kp_-)-(kk_2)} && \text{STPPP exchange channel} \end{aligned} \tag{7.27}$$

The number of resonances available for any given set of parameters is related to the number of energy levels the intermediate electron can traverse, which is dependent on the numerical value of the right hand side of equation 7.27. These are, in full

$$\begin{aligned} \frac{(q_ik_i)}{(kp_i)+(kk_i)} &= \frac{\omega_i}{\omega}\frac{1+\frac{\nu^2}{2}(1-\cos\theta_i)}{1+\omega_i(1-\cos\theta_i)} && \text{SCS direct channel} \\ \frac{-(q_ik_f)}{(kp_i)-(kk_f)} &= -\frac{\omega_f}{\omega}\frac{1+\frac{\nu^2}{2}(1-\cos\theta_f)}{1-\omega_f(1-\cos\theta_f)} && \text{SCS exchange channel} \\ \frac{(q_-k_1)}{(kp_-)-(kk_1)} &= \frac{\omega_1}{\omega}\frac{\epsilon_{q_-}-|q_-|\left(\cos\theta_1\cos\theta_f-\sin\theta_1\sin\theta_f\cos\phi_f\right)}{\epsilon_{q_-}-|q_-|\cos\theta_f-\omega_1(1-\cos\theta_1)} && \text{STPPP direct channel} \\ \frac{(q_-k_2)}{(kp_-)-(kk_2)} &= \frac{\omega_1}{\omega}\frac{\epsilon_{q_-}+|q_-|\left(\cos\theta_1\cos\theta_f-\sin\theta_1\sin\theta_f\cos\phi_f\right)}{\epsilon_{q_-}-|q_-|\cos\theta_f-\omega_1(1+\cos\theta_1)} && \text{STPPP exchange channel} \end{aligned} \tag{7.28}$$

The energy levels correspond to points where the numerical value of the expressions of equation 7.28 are integer values. Using figure 7.6 for the SCS process and figure 7.19 for the STPPP process as examples

$$\begin{aligned} 0.833 &\leq \frac{(q_ik_i)}{(kp_i)+(kk_i)} \leq 1.389 && \text{SCS direct channel} \\ -6.389 &\leq \frac{-(q_ik_f)}{(kp_i)-(kk_f)} \leq -0.833 && \text{SCS exchange channel} \\ -47 &\leq \frac{(q_-k_1)}{(kp_-)-(kk_1)} \leq 132 && \text{STPPP direct channel} \\ -47 &\leq \frac{(q_-k_2)}{(kp_-)-(kk_2)} \leq 132 && \text{STPPP exchange channel} \end{aligned} \tag{7.29}$$

The STPPP intermediate electron traverses a greater number of energy levels and can therefore reach more points of resonance.

The expressions of equation 7.28 suggest a greater number of resonances when the ratio $\frac{\omega_i}{\omega}, \frac{\omega_1}{\omega}$ is large. The validity of that suggestion can be established by comparing pairs of figures with similar parameter sets (table 7.5)

Figure 7.6, with $\theta_f = 0°$, shows a special case for the SCS process. For this final scattering geometry the direct channel resonance terms reduce to a dependence purely on the ratio $\frac{\omega_i}{\omega}$. Since this ratio is never unity, no direct channel resonances exist. Of note also for the SCS process, is that no resonances exist when $\theta_i = 0°$, except when the ratio $\frac{\omega_i}{\omega}$ is integral. This is confirmed by the work of [AM85].

Figures 7.10 - 7.13 (SCS process) and figures 7.23 - 7.26 (STPPP process) show the variation of resonance height and widths with external field intensity ν^2. The trend for figure 7.10 which shows $l = 3, r = 6$ and $l = 4, r = 7$ SCS resonant peak heights is difficult to determine due to the existence of sharp peaks at $\nu^2 = 0.2$ and $\nu^2 = 1.3$. These points correspond to instances in which direct channel resonances coincide with the exchange channel resonance considered.

Figure 7.11 shows increasing $l = 4$ $r, r' = 5$ peak height up to $\nu^2 = 1.5$ and remaining approximately constant thereafter. The $l = 1$ peak of the same figure, apart from the coincidence of an exchange channel resonance peak at $\nu^2 = 0.55$, remains approximately constant throughout the range of ν^2 values considered. There are two competing tendencies at work in figures 7.10 and 7.11. The SCS differential cross section increases with increasing ν^2 and resonance heights diminish with increasing resonance width.

The SCS resonance widths of figures 7.12 and 7.13 also increase with increasing ν^2. Exchange channel resonance widths (figure 7.12) reach a value of approximately $0.5°$ at $\nu^2 = 1$, and direct channel resonance widths reach approximately $2.5°$ at $\nu^2 = 1$. Resonances of this width should easily be resolved experimentally.

The ν^2 variation of STPPP resonance peak heights represented in figures 7.23 and 7.24 reveal an increase up until an optimum ν^2 value, thereafter decreasing. Maximum resonance peak heights are obtained at $\nu^2 = 0.4$ for the $l = 1$ $r, r' = 3$ resonance of figure 7.23, $\nu^2 \sim 0.25$ for the

Figure	$\frac{\omega_i}{\omega}, \frac{\omega_1}{\omega}$	number of resonances
7.4	2	8
7.5	0.83	4
7.15	1.67	169
7.16	0.53	58
7.17	1.67	186
7.18	0.53	86

Table 7.3: **Variation of the number of SCS and STPPP resonances with $\frac{\omega_i}{\omega}, \frac{\omega_1}{\omega}$.**

$l = 1\ r, r' = -1$ resonance of figure 7.24, and $\nu^2 \sim 0.3$ for the $l = 1\ r, r' = 2$ resonance of figure 7.24. The $l = 1\ r, r' = -1$ peak height of figure 7.23 has no maximum, but begins to flatten off at upper limits. The angular widths of the same resonances, considered in figures 7.25 and 7.26 show an almost linear increase with ν^2. At $\nu^2 = 0.5$ the $l = 1\ r, r' = 3$ and $l = 1\ r, r' = -1$ resonance widths of figure 7.25 are approximately $0.02°$ and $0.05°$ respectively, while the $l = 1\ r, r' = -1$ and $l = 1\ r, r' = 2$ resonance widths of figure 7.26 are both about $0.02°$ at the same ν^2. Generally STPPP resonances are much narrower than the SCS resonances.

The variation of the full cross section of the SCS process with external field intensity ν^2 is considered in figure 7.14. The initial photon has an energy of 51.2 keV and the external field photon energy is 25.6 keV. These are the same parameters as those considered for the ν^2 variation of figure 7.10 and the same trend of a large peak at $\nu^2 = 0.2$ is obtained. The full SCS cross section exceeds the Klein-Nishina cross section by 5 to 6 orders of magnitude at that point and the extent of the increase is generally due to the fact that the SCS differential cross section resonances are broad. A full STPPP cross section variation with ν^2 is shown in figure 7.27. This plot displays a much more moderate increase in cross section with increasing ν^2 which is due to the generally narrower resonances of the STPPP differential cross section. The STPPP cross section increases more rapidly at low values of ν^2 with the increase levelling off as ν^2 increases. This has the same explanation as the ν^2 variation of figures 7.23-7.24. The increase of the STPPP cross section over the Breit-Wheeler process is slightly more than an order of magnitude by $\nu^2 = 0.5$.

7.6 Experimental Considerations

In this section all results obtained thus far for the SCS and STPPP differential cross sections are discussed in light of experimental work due to [Bea99] and [ER83]. A numerical comparison between parameters used in this work with those that have been used experimentally is pertinent.

The initial photon energies employed in calculation of SCS differential cross sections ranges from UV ($\omega_i = 26$ eV) to x-rays ($\omega_i = 10.2$ keV), whereas those employed in STPPP differential cross section calculation, the requirement being that they must be at least the electron rest mass, range from low energy gamma rays ($\omega_1 = 0.512$ MeV) to high energy gamma rays ($\omega_1 = 5.12$ MeV). Since the photon beam containing the initial photons does not need to be ultra intense, there is no experimental difficulty in producing a full range of initial photon energies. These can be produced in the IR [Sea91], UV [Lea89, Bea99] or x-ray [Mea91] directly from a laser source, or higher energy photons are obtained by the scattering of lower energy photons from high energy electron beams. Using this method [Fea80] have obtained 80 MeV photons from a 1.5 GeV electron beam and more recently [Bea99] obtained 36.5 GeV photons from an incident UV ($\lambda = 350$ nm) laser pulse and a 50 GeV electron beam.

Due to computational time restrictions the external field energies considered were never smaller than initial photon energies divided by a factor of 10. The number of l contribution terms required to obtain data points is roughly proportional to twice the ratio $\frac{\omega_i}{\omega}$, $\frac{\omega_1}{\omega}$. The external field energies examined range from the visible ($\omega = 5$ eV) to x-rays ($\omega = 51.2$ keV) for the SCS process, and from hard x-rays ($\omega = 0.256$ MeV) to gamma rays ($\omega = 5.12$ MeV) for the STPPP process. However, ultra high intensity lasers operate at much lower photon energies. The TableTop Terawatt (T^3) generation of lasers produce 3.55 eV photons at an intensity of 4×10^{17} W cm^{-2} [McD91] or 5 eV photons at an intensity of 2×10^{19} W cm^{-2}. Higher photon energy lasers are available but at lower intensity. 50-1200 keV photons can be produced with an intensity of $6.1 \times 10^{15} - 1.5 \times 10^{17}$ W cm^{-2} [Sea92].

The T^3 lasers which produce the greatest energy flux are considered the most interesting for investigating QED processes in the external field. For these lasers the external field intensity parameter ν^2 approaches unity, at which point perturbative QED is of limited validity [Bea99]. Further, the cross sections of the first order external field QED processes are optimal when the parameter $\frac{1}{4}(\frac{\omega}{m})^2\nu^2 \sim 1$ [Bec91].[2] The second order processes investigated here, however, return large differential cross section values at points of resonance. The figures of section 7.4 reveal resonance differential cross sections several orders of magnitude in excess of those of first order processes for external field intensities as low as $\nu^2 = 0.1$. Available laser intensity is more than adequate for experimental detection of the SCS and STPPP resonances.

Another parameter of experimental significance is the momentum of incoming particles. Experiments use relativistic electron beams or electron plasmas [Bec91]. The SCS calculations in this thesis were performed in the laboratory frame and there is little difficulty in repeating calculations with a non zero initial electron momentum. The STPPP differential cross section calculations, performed in the centre of mass frame of incoming photons, are immediately amenable to experimental study due to the availability of counter propagating photon beams.

In determining the observability of the second order IFQED processes values for the full cross section and the number density of incident particles are required. The cross section calculation can proceed in one of two ways. Assuming that the resonant differential cross section dominates, we can calculate the contribution to the total cross section from each resonant peak can be calculated, or alternatively the probability of detection of a particular resonant peak by a real particle detector of finite aperture in a fixed position can be determined. The second alternative is considered here.

[ER83] use an experimental setup such that their particle detector aperture subtends 0.024 of the total solid angle, which translates to a $5.66°$ angular resolution for a circular detector aperture. In [McD91] an angular resolution of $4 \times 10^{-5\,\circ}$ is obtained. Assuming angular resolution is such that the top 50% of one resonant peak falls within the aperture of a detector in a fixed position, the cross section measured is obtained by an integration of the differential cross section across the range

[2] Based on the electron embedded in the external field being in its ground state.

of angles subtended by the detector's aperture.[3]

$$\sigma_{\text{detector}} = \int_{-\frac{1}{2}\Delta\Gamma}^{\frac{1}{2}\Delta\Gamma} d\phi_f \int_{-\Delta\cos\Gamma}^{\Delta\cos\Gamma} d\cos\theta_f \left.\frac{d\sigma}{d\Omega}\right|_{\text{resonance}} \tag{7.30}$$

Taking, as a first approximation, a linear relationship between the differential cross section near resonance and the cosine of the polar angle θ_f, and no variation of the differential cross section with the azimuthal angle ϕ_f near resonance,[4] the cross section measured by the detector is the resonant differential cross section multiplied by the factor

$$\frac{3}{4}\Delta\Gamma\,\Delta\cos\Gamma \tag{7.31}$$

Choosing the largest resonance peaks for the SCS and STPPP processes and including the conversion factor from natural units to SI units, the cross section measured by the detector is

$$\begin{aligned} \sigma_{\text{detector}} &= 1.528\times10^{-21}\ \text{cm}^2 \qquad \text{SCS process} \\ \sigma_{\text{detector}} &= 5.95\times10^{-25}\,\text{cm}^2 \qquad \text{STPPP process} \end{aligned} \tag{7.32}$$

To convert these into the number of particles detected per second the number density of incoming particles is required. Real photon sources are pulsed and only one detection per pulse is possible [McD91]. The number density is calculated from the flux density of the photon source I, pulse length Δt and photon energy ω

$$\text{number density} = \frac{I\,\Delta t}{\omega} \tag{7.33}$$

For the maximum resonances of the SCS and STPPP processes considered ($\omega_i = 51.2$ keV and $\omega_1 = 0.768$ MeV respectively) an incident photon source in the hard x-ray/low energy gamma ray range is required. Such a source with a photon number density of 2.4×10^{14} per pulse is available at a pulse repetition rate of 1 Hz [McD91].

The number of events per second (which is a product of the cross section and particle number density) is increased by introducing the second incident particle (electron for the SCS process and photon for the STPPP process) via a particle beam. For the purposes of the SCS process, a 50 GeV pulsed electron beam at $10^9 - 10^{10}$ electrons per pulse is available. The consequent increase in the

[3] $\Delta\Gamma$ is the resonance width and $\Delta\cos\Gamma$ is difference in cosine angles across the resonance width.

[4] This is not a bad assumption since, generally, the SCS and STPPP differential cross section vary much more slowly with ϕ_f than with θ_f.

event rate cannot be included here since a recalculation of the SCS differential cross section allowing for initial electron 3-momentum, is required. For the STPPP process two counter propagating photon beams of similar energy is easily achieved experimentally. For two incident particle beams a factor of 10^{-2} is assumed as a loss due to the spatial coincidence of the beams and the detector efficiency [McD91].

The event rates obtained for the SCS and STPPP maximum resonances are

$$\begin{array}{rc} 3.7\times 10^{-7}\ \mathrm{s}^{-1} & \text{SCS process} \\ 342.72\ \mathrm{s}^{-1} & \text{STPPP process} \end{array} \tag{7.34}$$

As it stands, the event rate obtained for the maximum resonant peak of the SCS process is too low to be experimentally observable. For the first order HICS process, however, the allowance for an initial electron 3-momentum can lead to an enhancement of the differential cross section [DT95, Gea83a]. A factor of $10^7 - 10^8$ for the electron number density plus spatial coincidence of particle beams can be included, leading to an observable SCS event rate. The STPPP event rate is easily observable and in fact larger than the OPPP event rate [McD91].

In order to achieve maximum photon flux densities, laser beams are focused resulting in a non plane wave electromagnetic field. To determine the relevance of our results we need to estimate the extent to which SCS and STPPP differential cross section calculations performed in a plane wave external field and a non plane wave focused field differ.

No work in a focused external field has been performed for the second order processes considered in this work, however the first order HICS and OPPP processes in which one external field quanta participates has been considered. The plane wave external field constitutes a valid approximation to the focused external field whenever the energy of the quanta associated with the field is several orders of magnitude less than that of other incident particles. When particle energies are equivalent, differential transition rates obtained with the focused external field are 40% smaller than those obtained with a plane wave external field [DT95].

An estimate of the effect on second order processes can be obtained by examining the focused field equations and the extent to which they differ from a plane wave. If a focussed laser beam can be considered Gaussian, then in the paraxial approximation (which neglects longitudinal components of the electric and magnetic fields), the equation governing the radius of curvature of the wavefront $R(z)$ is simple. The relationship is in terms of the beam waist width w_0, laser wavelength λ and the longitudinal distance from the beam waist, z. This relationship reveals that the beam is a plane wave ($R=\infty$) at the focal plane ($z=0$) ([Ald02] p.999-1013).

$$R(z) = z\left[1+\left(\frac{\pi w_0^2}{z\lambda}\right)^2\right] \tag{7.35}$$

However the QED calculations consider Volkov wave functions far from the focal plane. The paraxial approximation again provides relatively simple expressions however now the wave fronts are curved. Corrections to the paraxial approximation have been made [LM75, Dav79] and the most general expression of the electromagnetic field at the focus of a lens were provided by [BW65]. In the general expression the electric and magnetic field strengths at a point P near the focus of an ideal lens are given by

$$\begin{aligned} E(P,t) &= Re\left[e(P)\, e^{-i\omega t}\right] \\ H(P,t) &= Re\left[h(P)\, e^{-i\omega t}\right] \end{aligned} \tag{7.36}$$

$$\text{where} \quad \begin{aligned} e_x(P) &= -i\alpha\,(I_0 + I_2\,\cos 2\phi) & h_x(P) &= -i\alpha\, I_2\,\sin 2\phi \\ e_y(P) &= -i\alpha\, I_2\,\sin 2\phi & h_y(P) &= -i\alpha\,(I_0 - I_2\,\cos 2\phi) \\ e_z(P) &= -2\alpha\, I_1\,\cos\phi & h_z(P) &= -2\alpha\, I_1\,\sin\phi \end{aligned}$$

Here $\alpha = k\,f\,E_0$, E_0 is the amplitude of the electric field strength in the incident plane wave, f is the focal length of the lens, $k = \frac{\omega}{c}$. With J_μ a Bessel function of order μ, $\theta_0 = \arctan\frac{d}{2f}$, d the lens diameter, and (ρ, z, ϕ) are the coordinates of a point in the cylindrical coordinate system with centre at the focus and polar axis coinciding with the optical axis of the lens, the functions I_μ are described by

$$I_\mu(k\rho, kz, \theta_0) = 4\int_0^{\theta_0} d\theta\,\cos^{1/2}\theta\,\sin^{\mu+1}\left(\tfrac{\theta}{2}\right)\cos^{3-\mu}\left(\tfrac{\theta}{2}\right) J_\mu(k\rho\,\sin\theta)\, e^{i\,kz\,\cos\theta} \tag{7.37}$$

With the use of a $\frac{f}{d} = 3$ lens, a focused laser beam of spot size 2.8λ ($\lambda = 1054$ nm) for which the parameter $k\rho$ varies from 0 to 17.59 can be obtained [McD91]. The extent to which the focused field can be approximated by a plane wave is the extent to which the function I_0 is sinusoidal and the functions I_1 and I_2 are negligible. The plane wave approximation for the focused field is best for low $k\rho$ (i.e. near the centre of the focused laser beam), and for the upper limit of $k\rho$ considered by [McD91] the approximation remains reasonably valid.

The SCS and STPPP differential cross section results in this thesis were obtained with laser quanta of $0.061 - 1.024$ MeV. The beam spot sizes available for these laser sources result in the range of parameters $0 \leq k\rho \leq 1.52 \times 10^8$ for which a plane wave approximation cannot be expected to remain valid. What is required is a more tightly focused high energy laser beam or a recalculation of the SCS and STPPP differential cross sections at lower laser quanta energies.

Chapter 8

STPPP in the Beam Field of an e^+e^- Collider

8.1 Introduction

The design of future linear colliders includes intense energetic electron and positron bunch collisions in order to maximise centre of mass energy and collider luminosity. Associated with these intense bunches are strong electromagnetic fields which affect the physics processes at and near the interaction point. Of particular concern is unwanted pair production which causes background radiation in detectors and other collider components. Background studies of this pair production take as a starting point beamsstrahlung from the fermion bunches undergoing the pinch effect. The processes studied hitherto include the two-vertex Breit-Wheeler [BW34], Bethe-Heitler [BH34] and Landau-Lifshitz [LL34] processes. What has not been studied (and no rationale has been given for so neglecting) is the Breit-Wheeler process in the presence of the electromagnetic fields of the bunches in which a pair is produced from two real photons and a contribution from the bunch field. This process - stimulated two photon pair production (STPPP) in a beam field - is studied in this chapter.

The electron and positron beams at linear colliders are ultra relativistic and the electromagnetic fields produced by ultra relativistic beams approximate well to a constant, crossed plane wave. The Volkov solution can therefore be used with an external field 4-potential of suitable form. This work is done in sections 8.2 and 8.3.

Much of the analytic work performed in Chapter 3 for the STPPP process is reapplied to a real case of beam parameters proposed in the R&D for the International Linear Collider (ILC). Since differential cross section resonances were found for the STPPP in a circularly polarised field, their potential appearance for the STPPP process in a beam field is of particular concern. The resonances potentially increase the differential cross section by orders of magnitude. In order to quantify the resonances the electron self energy in the constant crossed field (EFESE) is calculated. This electron self energy calculation has been performed before [Rit72]. The calculation here is consistent with that of Ritus, and a new analytic expression is found when the external field is non azimuthally symmetric (section 8.5).

In section 8.6 the expression for the STPPP process in the constant crossed field is developed, the EFESE is included as a radiative correction to the propagator and numerical results are obtained. The cross section of the STPPP process is compared to the ordinary (non external field) Breit-Wheeler cross section and an estimate is provided, assuming azimuthal symmetry, of the overall cross section.

8.2 Electromagnetic Field of a Relativistic Charged Beam

Generally speaking, the charges of a typical charged bunch at the ILC move uniformly and ultra relativistically along a x-axis (see figure 8.1). The field potential at a point, P, is a special case of the Lienard-Weichert potentials ([LL75] section 63) and the associated field vectors can be written in cylindrical coordinates as

$$\begin{aligned} \underset{\sim}{E}(z) &= \frac{e}{4\pi\varepsilon_0\gamma^2}\frac{[\sin\alpha, 0, \cos\alpha]}{r_b^2(1-\beta^2\sin^2\alpha)^{3/2}} \\ \underset{\sim}{B}(z) &= \frac{e\beta}{4\pi\varepsilon_0 c\gamma^2}\frac{[0, \sin\alpha, 0]}{r_b^2(1-\beta^2\sin^2\alpha)^{3/2}} \end{aligned} \tag{8.1}$$

In the relativistic limit, $\underset{\sim}{E}$ and $\underset{\sim}{B}$ are predominantly equal in magnitude, mutually orthogonal and transverse to the direction of motion of the beam charge. That is, they take on the characteristics of a constant crossed plane wave field described by 4-potential A_μ and with field vector magnitudes

$$\begin{aligned} c|\underset{\sim}{E}| = |\underset{\sim}{B}| &= \frac{e\beta}{4\pi\varepsilon_0 c\gamma^2 r_b^2}\frac{1}{(1-\beta^2)^{3/2}} \\ A_\mu &= a_{1\mu}(kx) \end{aligned} \tag{8.2}$$

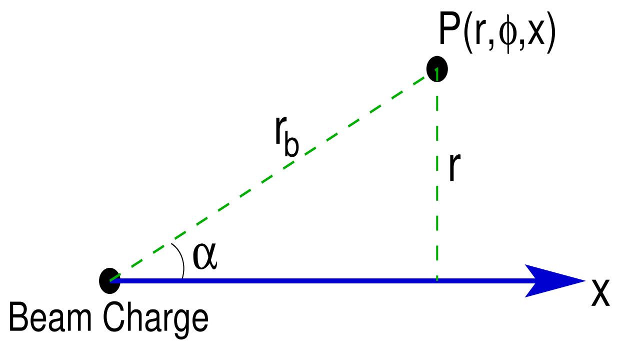

Figure 8.1: **Parameters associated with the beam charge field vectors**

Using Maxwell's field equations it becomes clear that the 3-potential $\underset{\sim}{a}_1$ lies in the direction of $\underset{\sim}{E}$ (i.e. radially to the z-axis) and the magnitude of the 3-potential can be related to $|\underset{\sim}{B}|$. An expression for the dimensionless parameter expressing field intensity ν^2 automatically follows

$$\begin{aligned} |\underset{\sim}{a}_1|\,\omega &= |\underset{\sim}{B}| \\ \nu^2 &= \frac{|\underset{\sim}{B}|^2 e^2}{\omega^2 m^2 c^2} \end{aligned} \tag{8.3}$$

The non linear first order processes considered in collider background studies are described by the dimensionless beamsstrahlung parameter Υ. This parameter is written alternatively as a ratio of beam magnetic field to Schwinger critical field, B_c or the magnitude of the 4-vector product of field tensor and particle 4-momentum. Υ is fixed for fixed bunch dimensions $(\sigma_x, \sigma_y, \sigma_z)$ and bunch charge N [YP91]

$$\begin{aligned} \Upsilon = \frac{|\underset{\sim}{B}|}{B_c} &= \frac{e\hbar}{m^3 c^5}\sqrt{|(F_{\mu\nu}p^\nu)^2|} \sim \frac{5}{6}\frac{N r_e^2 \gamma}{\alpha\sigma_z(\sigma_x+\sigma_y)} \\ \text{where} \qquad B_c &= \frac{\alpha\beta m}{e r_e}; r_e = \frac{e^2}{4\pi\varepsilon_0 m c^2} \\ \text{and} \qquad \beta &= \frac{v}{c} \quad ; \quad \alpha \sim \frac{1}{137} \end{aligned} \tag{8.4}$$

The energy spectrum of the beamsstrahlung process in the intense beam magnetic field, given by the Sokolov-Ternov equation [ST64] has a dependence on the external field completely described by a function of Υ. This is not possible for the second order STPPP process which is dependent on two dimensionless external field parameters ν^2 and $\frac{\omega}{m}$. Since ν^2 is a function of magnetic field strength and $\frac{\omega}{m}$, an independent expression for the frequency associated with the beam bunch magnetic field is required.

The bunch fields consist of intense electric as well as magnetic fields and a test charge will drift in the former and spiral in the latter. Crudely, however, the STPPP process occurs at the junction of colliding e^+ and e^- bunches. In such an environment the electric fields will tend to cancel and the magnetic field lines curl in the same direction. The angular frequency of a test charge starting from rest is given by

$$\omega = \frac{e|\underset{\sim}{B}|}{m} \tag{8.5}$$

With the aid of equations 8.3 and 8.4 the external field dimensionless parameters can be written in terms of bunch parameters. For a typical set of bunch parameters being considered at the ILC ($\sigma_x = 0.5\mu$m, $\sigma_y = 5$nm, $\sigma_z = 300\mu$m, $N = 2\times 10^{10}$, bunch particle energy= 250 GeV)

$$\begin{aligned}
\frac{\omega}{m}\left(\equiv\frac{\hbar\omega}{mc^2}\right) &= \frac{\hbar}{mc^2}\frac{e}{m}\frac{5}{6}B_c\frac{Nr_e^2\gamma}{\alpha\sigma_z(\sigma_x+\sigma_y)} = 0.0603 \\
\nu^2\left(\equiv\frac{e^2a^2}{m^2c^2}\right) &= \frac{e^2}{\omega^2m^2\beta}\frac{5}{6}B_c\frac{Nr_e^2\gamma}{\alpha\sigma_z(\sigma_x+\sigma_y)} = 1.000
\end{aligned} \tag{8.6}$$

A value of $\nu^2 \sim 1$ (as obtained here) is commonly recognised as the limit at which non linear effects become important [Bea99], though the results of Chapter 7 show that cross section resonances can occur at smaller values. The value of the parameter $\frac{\omega}{m}$ reflects the ratio of the beam field magnetic field strength to the Schwinger critical field strength at which point the field contains enough energy to produce a real e^+e^- pair.

8.3 Volkov functions in a constant crossed electromagnetic field

The Volkov solution for the Dirac equation in a general external plane wave field was provided in section 2.10. Its solution with a constant crossed electromagnetic field described by the 4-potential A_μ (equation 8.2) is

$$\begin{aligned}
\Psi_p^V(x) &= E_p(x)\, u_p \\
E_p(x) &= \left[1+\frac{e}{2(kp)}\not{k}\not{a}_1(kx)\right] \\
&\times\ \exp\left(-iqx + i\frac{e^2a^2}{2(kp)}(kx) - i\frac{e(a_1p)}{2(kp)}(kx)^2 - i\frac{e^2a^2}{6(kp)}(kx)^3\right) \\
&\text{where} \qquad q = p + \frac{e^2a^2}{2(kp)}k
\end{aligned} \tag{8.7}$$

As was done in Chapter 3 for the circularly polarised field, a Fourier transform of the exponential function in equation 8.7 is obtained. Since the argument of this exponential function is non periodic it will be a continuous Fourier transform

$$\begin{aligned}
&\exp\left(iQ\,(kx) - iQ_\varphi\,(kx)^2 - iQ\frac{(kx)^3}{3}\right) \to \frac{1}{2\pi}\int_{-\infty}^{\infty}F_0(r)\exp(-ir(kx))dr \\
&\text{where} \qquad F_0(r) = \int_{-\infty}^{\infty}\exp\left(i(r+Q)t - iQ_\varphi t^2 - iQ\frac{t^3}{3}\right)dt \\
&\qquad Q\equiv\frac{e^2a^2}{2(kp)} \quad ; \quad Q_\varphi\equiv\frac{e(a_1p)}{2(kp)}
\end{aligned} \tag{8.8}$$

The Fourier transform variable (kx) appears also as a cofactor of the slash vectors appearing in $E_p(x)$. After inserting the Volkov wave function into a trace calculation there are, potentially, several Fourier transforms involving powers of the integration variable which expressions need to be found for. These can be collectively labelled

$$F_{n,r} = \int_{-\infty}^{\infty} t^n \exp\left[i(r+Q)t - iQ_\varphi t^2 - iQ\frac{t^3}{3}\right] dt \tag{8.9}$$

Q_φ, as indicated in its subscript, is dependent on the azimuthal angle φ_f and its explicit form is to be considered. From equation 8.8 Q_φ is vectorially dependent on $\underset{\sim}{a}_1$, $\underset{\sim}{k}$, and $\underset{\sim}{p}$. Figure 8.2 represents these vectors and defines the azimuthal angle φ_f around the external field 3-momentum $\underset{\sim}{k}$, and the angle θ_f between the fermion 3-momenta $\underset{\sim}{p}$ and $\underset{\sim}{k}$.

Using the same gauge in which the 4th component of $a_{1\mu}$ is zero, the scalar products (a_1p) can be written

$$(a_1p) = -\underset{\sim}{a}_1.\underset{\sim}{p} = -a_1|\underset{\sim}{p}|\sin\theta_f\cos\varphi_f \tag{8.10}$$

There will be two sets of Fourier transforms - azimuthally symmetric and non azimuthally symmetric - depending on whether (a_1p) and therefore Q_φ can be neglected. It is clear from equation 8.10 that (a_1p) can be neglected if $\underset{\sim}{k}$ and $\underset{\sim}{p}$ are collinear. As will be seen, the resultant Fourier transforms are Airy functions which appear in both the Ritus expression for the electron self energy in the crossed field [Rit72] and the Sokolov-Ternov equation (as equivalent Bessel K functions of fractional order). It is pertinent to ask whether an assumption of azimuthal symmetry is justified.

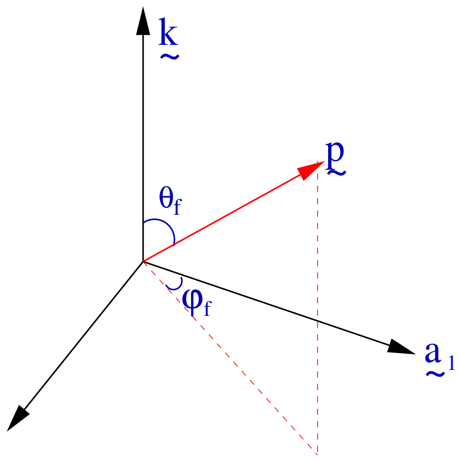

Figure 8.2: **Parameters associated with the beam charge field vectors**

These Fourier transforms will be inserted in both the STPPP calculation and the EFESE calculations. The STPPP process for ILC-like collisions will occur with initial photons which are highly energetic, nearly collinear with the external field, and directed oppositely to each other. It is likely from momentum considerations that the resultant fermions will also be collinear and azimuthal symmetry is obtained. However this consideration doesn't encompass all possible collisions. Even if the final state fermions have significant transverse momentum, azimuthal symmetry is still retained if the collision takes place on axis and if the beam profile is round. Neither of these is necessarily the case at the ILC.

In the EFESE calculation, the symmetry to be considered is between intermediate momentum states and the external field. Integrations have to be carried out over all these states and again azimuthal symmetry can only be assumed if the external field is azimuthally symmetric. If so, then the reference frame can be rotated around the field axis until $\underset{\sim}{a_1}$ and $\underset{\sim}{p}$ are perpendicular and Q_φ goes to zero.

Both sets of Fourier transforms are written below. In both cases the integration over φ_f is performed resulting in a factor of 2π for azimuthal symmetry and Bessel functions for non azimuthal symmetry. First the azimuthally symmetric transforms

$$\begin{aligned}
F_{0,r} &= \int_{-\infty}^{\infty} \exp\left[i(r+Q)t - iQ\frac{t^3}{3}\right] = 2\pi Q^{-\frac{1}{3}}\mathrm{Ai}(z) \\
F_{1,r} &= \int_{-\infty}^{\infty} t\ \exp\left[i(r+Q)t - iQ\frac{t^3}{3}\right] = 2\pi i Q^{-\frac{2}{3}}\mathrm{Ai}'(z) \\
F_{2,r} &= \int_{-\infty}^{\infty} t^2\ \exp\left[i(r+Q)t - iQ\frac{t^3}{3}\right] = -2\pi\frac{z}{Q}\mathrm{Ai}(z)
\end{aligned} \tag{8.11}$$

$$\text{where} \qquad Q = \frac{e^2a^2}{2(kp)} \quad ; \quad z = -(r+Q)Q^{-\frac{1}{3}}$$

and the non azimuthally symmetric

$$\begin{aligned}
F_{0,r}^{(\varphi)} &= 2\int_0^{\infty} J_0(Pt^2)\cos\left[(r+Q)t - Q\frac{t^3}{3}\right]dt \equiv \mathrm{Ai}_0\mathrm{J}_0(P,Q) \\
F_{1,r}^{(\varphi)} &= 2i\int_0^{\infty} t\ J_0(Pt^2)\sin\left[(r+Q)t - Q\frac{t^3}{3}\right]dt \equiv \mathrm{Ai}_1\mathrm{J}_0(P,Q) \\
F_{2,r}^{(\varphi)} &= 2\int_0^{\infty} t^2\ J_0(Pt^2)\cos\left[(r+Q)t - Q\frac{t^3}{3}\right]dt \equiv \mathrm{Ai}_2\mathrm{J}_0(P,Q)
\end{aligned} \tag{8.12}$$

$$\text{where} \qquad P = \frac{ea|\underset{\sim}{p}|}{2(kp)}\sin\theta_f$$

The numerical differences between the two sets of Fourier transforms will be considered in section 8.4. Finally, for both the EFESE and STPPP calculations, the Volkov wave functions appear in combinations like

$$\begin{aligned}
\overline{E}_p(x)\gamma_\mu E_{p'}(x) &= \frac{1}{2\pi}\int_{-\infty}^{\infty} H_r(p,p')\ \exp\left[i(q-q'-rk)x\right] \\
\text{where}\quad H_r(p,p') &= \gamma_\mu F_{0,r}^{(\varphi)}(p,p') + \left(\frac{e}{2(kp)}\not{a}_1\not{k}\gamma_\mu - \frac{e}{2(kp')}\gamma_\mu\not{a}_1\not{k}\right) F_{1,r}^{(\varphi)}(p,p') \\
&+ \frac{e^2a^2}{4(kp)(kp')}\not{k}\gamma_\mu\not{k}F_{2,r}^{(\varphi)}(p,p')
\end{aligned} \tag{8.13}$$

and the functions $F_{n,r}^{(\varphi)}(p,p')$ refer to either the azimuthally symmetric or non azimuthally symmetric Fourier transforms which contain

$$\begin{aligned}
Q(p,p') &= \frac{e^2a^2}{2}\left[\frac{1}{(kp')} - \frac{1}{(kp)}\right] \\
Q_\varphi(p,p') &= \frac{e}{2}\left[\frac{(a_1p')}{(kp')} - \frac{(a_1p)}{(kp)}\right]
\end{aligned} \tag{8.14}$$

8.4 Numerical comparison of Fourier transforms $F_{n,r}$ and $F_{n,r}^{(\varphi)}$

In this section the Airy functions associated with azimuthal symmetry and the AiJ functions that emerged for non azimuthal symmetry, are computed numerically. The AiJ transforms do not reduce to known functions and will have to be computed numerically

Figure 8.4 shows a numerical comparison between $F_{0,r}(p)$ and $F_{0,r}^{(\varphi)}(p)$. As r decreases below zero, the argument of both functions is positive and the two functions converge and fall to zero. As r increases above zero and the argument becomes negative, the Airy function remains large and oscillatory, but the AiJ function is damped. This will impact ultimately on process cross sections considered in this chapter.

The computer program Mathematica v5.0 was used to perform the numerical integration of the AiJ function and its accuracy is of concern. Figure 8.4 shows the ratio of Airy function to its equivalent numerical integration as calculated by Mathematica. The result should be 1 if the numerical integration performs well, which it does until the argument reaches $z \approx 100$. As will be seen, numerical analysis of the resonance cross section involves arguments of at least 10^4, so this method of calculation will not suffice

An alternative is to find an asymptotic expansion for the AiJ function. Such was done successfully for the generalised Bessel functions that appear for linearly polarised [LS81] and elliptically polarised [PE02] external fields. Time constraints did not permit this to be done in this thesis, so the use of AiJ functions in numerical calculations of the EFEES and STPPP processes is curtailed for the present.

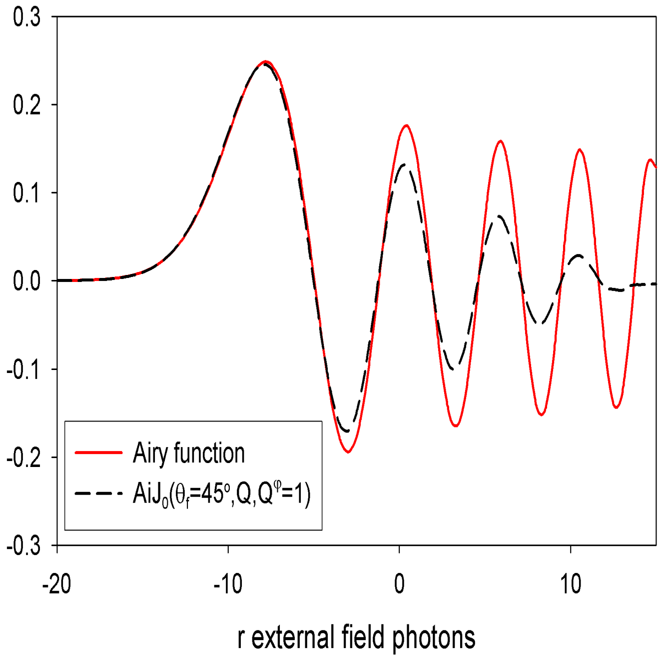

Figure 8.3: **Comparison of azimuthally symmetric and non azimuthally symmetric Fourier Transforms.**

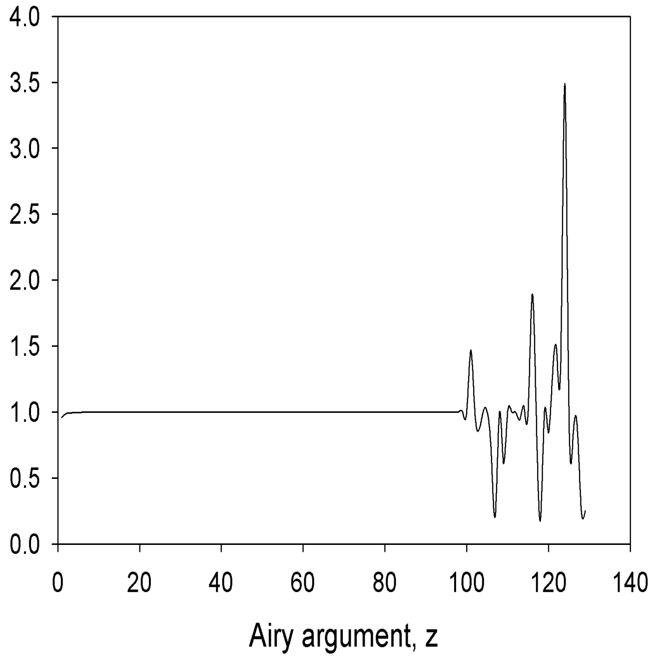

Figure 8.4: **Ratio of an Airy function to its numerically equivalent integration using Mathematica 5.0.**

8.5 Electron self energy in a constant crossed electromagnetic field

As was the case for the SCS and STPPP processes in the circularly polarised field, the STPPP process in the constant crossed field is expected to contain resonances. The electron self energy in the constant crossed field (EFESE) has been calculated before by [Rit72] and contains Airy functions and their derivatives. [Rit72] makes use of the optical theorem to show that the mass operator gives the previously calculated expression for the probability of emission of a photon by an electron in a crossed field [NR67].

The methods developed in Chapter 6 and Appendix E can be used to obtain an expression for the imaginary part of the EFESE using the transforms to Airy functions (equation 8.11). This result should be consistent with that obtained by [NR67]. The assumption of azimuthal symmetry will then be dropped and the transforms of equation 8.12 will be used to obtain a new result for the imaginary part of the EFESE in the constant crossed electromagnetic field.

The general form of the EFESE was written down in equation 6.3. Using the expression for products of Volkov functions in the presence of the constant crossed field (equation 8.14) the EFESE is

$$\begin{aligned}
\Sigma^e(p) &= \frac{i4e^2}{VT(2\pi)^4}\int d^4x_1 d^4x_2 d^4k' d^4q' \frac{1}{(2\pi)^4}\int_{-\infty}^{\infty} dr\ ds \\
&\times\ H_r(p,p')\left(\not{q}' + \frac{e^2a^2}{2(kp')}\ \not{k} + m\right) H_s(p,p')\frac{1}{q'^2 - m_*^2}\frac{1}{k'^2} \\
&\times\ exp\left[i(q-q'+k'-rk)x_2\right]\ exp\left[i(q'-q-k'-sk)x_1\right]
\end{aligned} \tag{8.15}$$

The integrations over x_1, x_2 and s produce a delta function whose argument expresses the conservation of 4-momenta and the condition $s = -r$. Noting the symmetry of the functions $F_{n,r}$ and H_r, the momentum space EFESE becomes

$$\begin{aligned}
\Sigma^e(p) &= \frac{i4e^2}{VT(2\pi)^4}\int d^4k' d^4q' \frac{1}{(2\pi)^2}\int_{-\infty}^{\infty} dr H_r(p,p')(\not{q}' + \tfrac{e^2a^2}{2(kp')}\not{k} + m) \\
&\times\ \overline{H}_r(p,p')\frac{1}{q'^2 - m_*^2}\frac{1}{k'^2}\delta(q-q'+k'-rk)
\end{aligned} \tag{8.16}$$

$$\text{since}\quad F^*_{0,-r} = F_{0,r} \quad ; \quad F^*_{1,-r} = -F_{1,r} \quad ; \quad F^*_{2,-r} = F_{2,r}$$

$$\overline{H}_r(p,p') = H^*_r(p',p)$$

The identities of Appendix E allow the expression for the EFESE to be written in the form of a dispersion relation, and the average over electron yields a trace of 4-vectors. The imaginary part of the external field electron energy shift (EFEES) in the constant crossed field becomes (cf. equation 6.8)

$$\begin{aligned}
\Im\Delta\varepsilon_p(D^2) &= -\frac{e^2m^2}{16\pi\varepsilon_p}\int_{-\infty}^{\infty}dr\int_{-1}^{1}d\cos\theta\left(1-\frac{m_*^2}{D^2}\right) \\
&\left\{\left(2-2\nu^2+2r[(kD)-(kK)]+\nu^2\left(\frac{(kD)}{(kK)}+\frac{(kK)}{(kD)}\right)\right)F_{0,r}^2\right. \\
&\left.+\nu^2\left(\frac{(kD)}{(kK)}+\frac{(kK)}{(kD)}\right)F_{1,r}^2+2\nu^2F_{0,r}F_{2,r}\right\}\Theta(D^2-(m_*+\epsilon)^2)
\end{aligned} \tag{8.17}$$

$$\text{where} \qquad K\equiv q'+\tfrac{1}{2}D \quad \text{and} \quad D\equiv q-rk$$

Making a transformation of variable to $u=\frac{(kD)-(kK)}{(kK)}$ and with θ defined as the angle between $\underset{\sim}{K}$ and $\underset{\sim}{k}$, we have

$$\left(1-\frac{m_*^2}{D^2}\right)d\cos\theta=\frac{2du}{(1+u)^2} \tag{8.18}$$

The regularisation procedure is the same as for the circularly polarised external field. The Heaviside Step function ensures that the field free unregularised mass shift goes to zero (see equation 6.12). The condition $D^2=-2r\rho>0;\rho=(kp)$ ensues, and its convenient to make the shift $r\to -r$. The imaginary part of the regularised EFEES is

$$\begin{aligned}
\Im\Delta\varepsilon_p^R(\rho) &= \frac{e^2m^2}{16\pi\varepsilon_p}\int_{0+\epsilon}^{\infty}dr\int_{0+\epsilon}^{u_r}\frac{du}{(1+u)^2}Q^{-\frac{2}{3}} \\
\times &\left[-4\mathrm{Ai}(z)^2-2\nu^2\left(1-\frac{r}{Q}\right)\left(2+\frac{u^2}{1+u}\right)\left(\mathrm{Ai}(z)^2+\frac{1}{z}\mathrm{Ai}'(z)^2\right)\right] \\
\text{where} &\qquad z=Q^{-\frac{1}{3}}(r-Q) \quad ; \quad Q=\frac{\nu^2u}{2\rho} \\
&\qquad u_r=\frac{2r\rho}{1+\nu^2} \quad ; \quad \rho=(kp)
\end{aligned} \tag{8.19}$$

Via the optical theorem, equation 8.19 should also be the transition probability for the emission of a photon by an electron in the crossed field. Indeed, comparison with equation 45 of [NR67], after a suitable change of integration variables, shows this to be the case.

Equation 8.19 contains a pole as either of the integration variables reach zero. Mathematically the pole can be traced back to the Fourier transform, $F_{n,r}$. In the limit of vanishing external field $F_{n,r}$ reduces to a Dirac delta function which expresses the constraint that $r=0$ external field photons should contribute to the process. The pole in equation 8.19 can be avoided with consideration of the Heaviside step function argument which requires the lower bound of the r integration be greater than zero by an infinitesimal amount ϵ. The integrations could proceed by taking the Cauchy principal value. Computationally however, it is convenient to shift integration variables in order to absorb the poles. These shifts (equation 8.20) are valid because the lower bounds of u and r are never quite zero.

$$u \to \frac{1}{r}\frac{\nu^2}{2\rho}u \qquad\qquad r \to Q^{-4/3}r^{2/3} \tag{8.20}$$

Finally, the imaginary part of the EFEES is

$$\begin{aligned}
\Im\Delta\varepsilon_p^R(\rho) &= \frac{e^2m^2}{16\pi\varepsilon_p}\int_{0+\epsilon}^{\infty}dr\int_{0+\epsilon}^{u_r}\frac{3\,du}{2(\sigma+u^3r^{3/2})^2} \\
\times &\left[-4\sigma ru^2\mathrm{Ai}(z)^2 + 2\nu^2(1-u)\left(2\sigma+\frac{r^3u^6}{\sigma+u^3r^{3/2}}\right)\left(ru\mathrm{Ai}(z)^2+\frac{1}{1-u}\mathrm{Ai}'(z)^2\right)\right] \\
&\text{where} \quad z = ru(1-u) \quad ; \quad u_r = \frac{\nu^2}{1+\nu^2} \quad ; \quad \sigma = \frac{\nu^2}{2\rho} \quad ; \quad \rho = (kp)
\end{aligned} \tag{8.21}$$

Some results which show the dependence of $\Im\Delta\varepsilon_p^R(\rho)$ on the variables r, ρ and ν^2 are shown in figures 8.5 and 8.6. These figures show similar trends as the equivalent ones studied in Chapter 6, for the imaginary part of the EFEES in the circularly polarised field. In particular figure 8.5 should be compared with figures 6.2 and 6.3, and figure 8.6 should be compared with figures 6.7 and 6.8. Much of the same analysis of Chapter 6 can be applied and only a few extra remarks are required.

The variation of $\Im\Delta\varepsilon_p^R(\rho)$ with the number of external field photons in figure 8.5 shows a peak at $r = 0$. For the circularly polarised case, the lower x ordinate was discrete and ended on $b = 1$ external field photons since the $b = 0$ point was subtracted out by the regularisation procedure. In the crossed field case considered here the x-ordinate is continuous and the $r = 0$ point was removed by the shift in integration variables.

The variation of $\Im\Delta\varepsilon_p^R(\rho)$ with ρ in figure 8.6 shows the same trend as the circularly polarised case, i.e. increasing probability of photon emission[1] when an electron travelling in the external field is more energetic or the external field is more intense. The overall values of $\Im\Delta\varepsilon_p^R(\rho)$ are greater than those of Chapter 6 because the values of ρ considered are greater. The numerical values for $\Im\Delta\varepsilon_p^R(\rho)$ for appropriate values of ρ will be inserted into the propagator denominators of the STPPP

[1] Equating the probability of photon emission with $\Im\Delta\varepsilon_p^R(\rho)$

process in the crossed field (section 8.6) to properly calculate the contribution of resonances to the STPPP cross section.

A non azimuthally symmetric version of $\Im\Delta\varepsilon_p^R(\rho)$ containing AiJ functions can be developed. The required expression is obtained by substituting the Fourier transforms of equation 8.12 into equation 8.17. The same shift of integration variable $\cos\theta \to u$ can be made and the argument of the Bessel function becomes

$$P = \sqrt{\frac{\nu^2 u(u_r - u)}{4\omega^2(1+u_r)}} \tag{8.22}$$

The non azimuthally symmetric version of $\Im\Delta\varepsilon_p^R(\rho)$ contains products of the functions $F_{n,r}^{(\varphi)}(p,p')$ which can be simplified. Writing the product explicitly

$$\begin{aligned} F_{n,r}^{(\varphi)}(p,p')F_{m,-r}^{(\varphi)}(p,p') &= \int dt\, dt'\; t^n\, t'^m \\ \times\;\; \exp&\left[i(r+Q)(t-t') - iP(t^2-t'^2)\cos\varphi_f - i\frac{Q}{3}(t^3-t'^3)\right] \end{aligned} \tag{8.23}$$

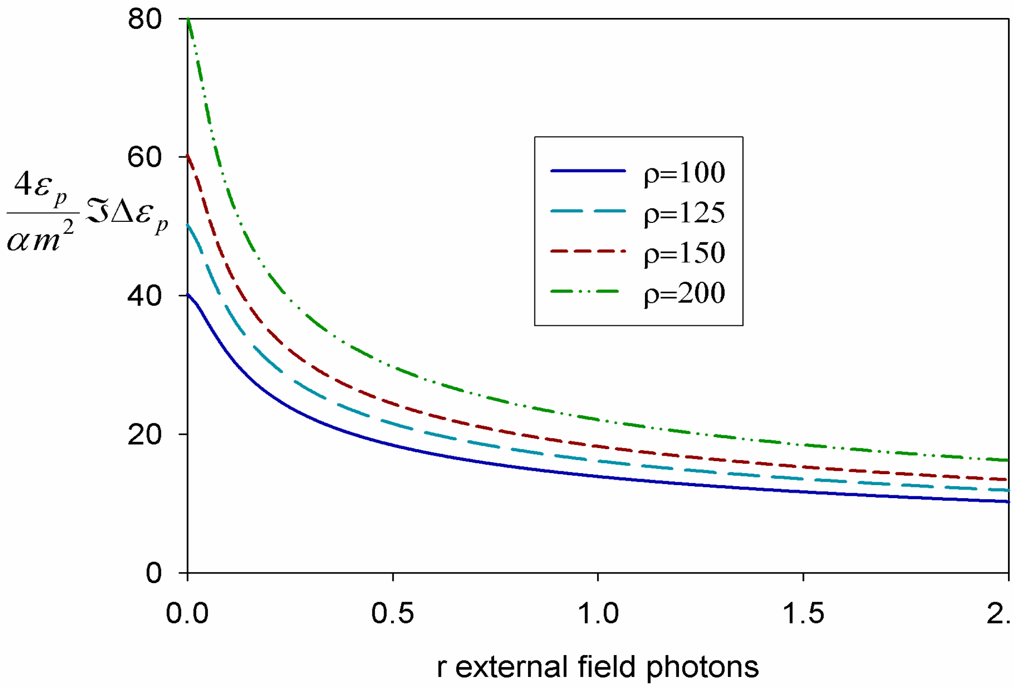

Figure 8.5: **Variation of the regularised, imaginary part of the EFEES in a crossed field with contribution of r external field photons and different ρ values**

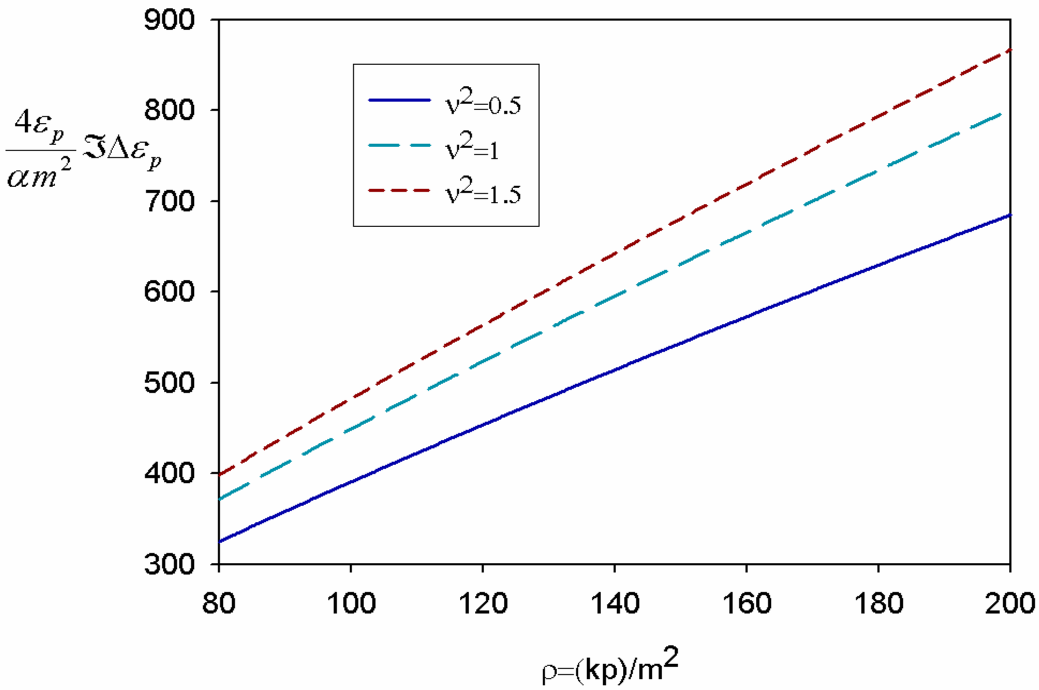

Figure 8.6: **Electron Energy shift in a crossed field.**

The integration over φ_f will result in a Bessel function of order zero and an argument which is a difference $Pt^2 - Pt'^2$. The following identity is of use ([Wat22] pg.30)

$$J_0(a-b) = \sum_{m=-\infty}^{\infty} J_m(a)J_m(b) \tag{8.24}$$

With AiJ functions defined in equation 8.12 , the product of $F^{(\varphi)}_{n,r}$ transforms can be written

$$\int d\varphi_f F^{(\varphi)}_{m,r}(p,p')F^{(\varphi)}_{n,-r}(p,p') \quad = \sum_{m=-\infty}^{\infty} \mathrm{Ai}_n\mathrm{J}_m(P,Q)^2 \tag{8.25}$$

The non azimuthally symmetric version of the regularised, imaginary part of the EFEES is obtained after substitution of equation 8.25 into equation 8.17 and use of the dispersion relations method outlined in Appendix E

$$\begin{aligned}\Im\Delta\varepsilon^R_p(\rho) \quad &= \frac{e^2m^2}{16\pi\varepsilon_p}\sum_{m=-\infty}^{\infty}\int_{0+\epsilon}^{\infty}dr\int_{0+\epsilon}^{u_r}\frac{du}{(1+u)^2} \\ &\times\left[\left(-4-4\nu^2\left(1-\frac{r}{Q}\right)\left(\frac{u^2}{1+u}\right)\right)\mathrm{Ai}_0\mathrm{J}_m(P,Q)^2-\right. \\ &\left.2\nu^2\left(2+\frac{u^2}{1+u}\right)\mathrm{Ai}_1\mathrm{J}_m(P,Q)^2-4\nu^2\mathrm{Ai}_2\mathrm{J}_m(P,Q)^2\right]\end{aligned} \tag{8.26}$$

Equations 8.19 and 8.26 can be identified with the probability of emission, W_p by an electron of 4-momentum p_μ in the constant crossed field. To obtain the energy spectrum of emitted photons, W_p needs to be integrated with respect to photon energy w'. There will be two such expressions for the energy spectrum of emitted photons; one for azimuthally symmetric emission with respect to the external field and one for the non azimuthal symmetry. Only expressions for the azimuthally symmetric spectra will be written down here, though there is nothing especially difficult in obtaining the non azimuthally symmetric expression

Considering the integration variable u as a function of K and recalling that K was used to represent the 4-momentum q'_μ, the conservation of 4-momenta $q_\mu - q'_\mu - k'_\mu - rk_\mu = 0$ can be used to shift the integration variable du to dA

$$\begin{gathered} u = \frac{(kk')}{(kq')} \equiv \frac{A}{\rho - A} \qquad \text{where} \qquad A = (kk') = \omega\omega'(1-\cos\theta) \\ \frac{du}{(1+u)^2} \rightarrow \frac{dA}{\rho} \end{gathered} \tag{8.27}$$

Substituting equation 8.27 into equation 8.19, taking the derivative with respect to A and integrating over variable r using known integrals of products of Airy functions [Alb77], the azimuthally symmetric emitted photon energy spectrum is

$$\begin{aligned} \frac{dW_p^{az}}{dA} &= -\frac{e^2m^2}{4\pi\rho\varepsilon_p}[Q^{\frac{1}{3}}\mathrm{Ai}(-Q^{\frac{2}{3}}) + Q^{-\frac{1}{3}}\mathrm{Ai}'(-Q^{\frac{2}{3}}) \\ &+ \ \frac{\nu^2}{2Q}(\frac{\rho - A}{A} + \frac{A}{\rho - A})\mathrm{Ai}(-Q^{\frac{2}{3}})\mathrm{Ai}'(-Q^{\frac{2}{3}})] \end{aligned} \tag{8.28}$$

$$\text{where} \qquad Q = \frac{\nu^2}{2\rho}\frac{A}{\rho - A}$$

8.6 STPPP in a constant crossed electromagnetic field

The calculation of the imaginary part of the EFEES provides both a correction to the bound electron propagator and the energy spectrum of beamsstrahlung photons. Both of these are to be inserted into the STPPP cross section. The Feynman diagrams and matrix element of the STPPP process in a general external field were provided in section 3.7. The matrix element is

$$\begin{aligned} S^e_{fi} &= -\frac{e^2}{2}\int_{-\infty}^{\infty} d^4x_1 d^4x_2 d^4q\; e^\mu(k_1)\bar{e}^\mu(k_1)e^\nu(k_2)\bar{e}^\nu(k_2)\frac{1}{p^2 - m^2}\bar{u}(p_-)(\mathcal{A}+\mathcal{B})v(p_+) \\ &\text{where} \quad \mathcal{A} = \overline{E}_{p_-}(x_2)\gamma_\mu E_p(x_2)(\not{p}+m)\overline{E}_p(x_1)\gamma_\nu E_{-p_+}(x_1)e^{-ik_1x_2 - ik_2x_1} \\ &\text{and} \qquad \mathcal{B} = \overline{E}_{p_-}(x_2)\gamma_\nu E_p(x_2)(\not{p}+m)\overline{E}_p(x_1)\gamma_\mu E_{-p_+}(x_1)e^{-ik_2x_2 - ik_1x_1} \end{aligned} \tag{8.29}$$

Using the expression for products of Volkov E_p functions (equation 8.13), making the transform to functions $F_{n,r}$ and performing integrations over x_1, x_2 and q, the matrix element becomes (omitting polarisation vectors $e(k)$ and bispinors $u(p)$) is

$$\begin{aligned} S^e_{fi} &= -\frac{e^2}{2}\frac{1}{(2\pi)^2}\int_{-\infty}^{\infty} drds\Big\{H^\mu_r(p_-,\bar{p})\frac{\bar{\not p}+m}{\bar{p}^2-m^2}H^\nu_s(\bar{p},-p_+) \\ &+ H^\nu_r(p_-,\bar{\bar{p}})\frac{\bar{\bar{\not p}}+m}{\bar{\bar{p}}^2-m^2}H^\mu_s(\bar{\bar{p}},-p_+)\Big\}\delta(q_-+q_+-k_1-k_2-(r+s)k) \end{aligned} \tag{8.30}$$

where $\quad \bar{q} = q_- - k_1 - rk \quad ; \quad \bar{\bar{q}} = q_- - k_2 - rk$

Since the ILC will collide ultra relativistic charge bunches that produce beamsstrahlung in the forward direction, $\underset{\sim}{k}_1, \underset{\sim}{k}_2$ and $\underset{\sim}{k}$ are considered collinear, and a centre of mass frame $\underset{\sim}{k}_1 + \underset{\sim}{k}_2 + r\underset{\sim}{k} = 0$ is used. These restrictions mean that one of the 4-vector products, (kk_1) or (kk_2), be zero. Choosing $(kk_2) = 0$, the functions Q and Q_φ reduce to

$$\begin{aligned} Q(p_-,\bar{\bar{p}}) &= Q(\bar{p},-p_+) = Q_\varphi(p_-,\bar{\bar{p}}) = Q_\varphi(\bar{p},-p_+) = 0 \\ Q(p_-,\bar{p}) &= Q(\bar{\bar{p}},-p_+) = \frac{e^2a^2(kk_1)}{2(kp_-)(kp_+)} \\ Q_\varphi(p_-,\bar{p}) &= Q_\varphi(\bar{\bar{p}},-p_+) = \frac{e(a_1p_-)}{2}\frac{(kk_1)}{(kp_-)(kp_+)} \end{aligned} \tag{8.31}$$

Further consequences of the special kinematics and the above relations are that the Fourier transforms $F^\varphi_{n,s}$ involving integration variable s, contain a Dirac delta function with reduced argument, $\delta(sk)$ requiring $s = 0$ for the second term of equation . For the second term of the equation the condition is $r = 0$.

The matrix element of equation 8.6 is squared and the product of Dirac delta functions ensures that there remains only one integration over variable r. The sum over polarisations and spins introduces a trace and the square of the matrix element becomes

$$\begin{aligned} \sum_{if}|S^e_{fi}|^2 &= \frac{e^2}{16m^2}\frac{1}{(2\pi)^4}\frac{1}{\bar{p}^2-m^2}\frac{1}{\bar{\bar{p}}^2-m^2}\int_{-\infty}^{\infty} dr \\ &\times \ \mathrm{Tr}\{G_{\mu\nu\nu\mu}(\bar{p},\bar{p}) + G_{\mu\nu\nu\mu}(\bar{\bar{p}},\bar{\bar{p}}) + G_{\mu\nu\mu\nu}(\bar{p},\bar{\bar{p}}) + G_{\mu\nu\mu\nu}(\bar{\bar{p}},\bar{p})\} \end{aligned} \tag{8.32}$$

where $\quad G_{\mu\nu\nu\mu}(\bar{p},\bar{p}) = (\not p_- + m)H^\mu_r(p_-,\bar{p})(\bar{\not p}+m)H^\nu_0(\bar{p},-p_+)$

$$\times \ (\not p_+ + m)H^\nu_0(-p_+,\bar{p})(\bar{\not p}+m)H^\mu_{-r}(\bar{p},p_-)$$

The trace calculation is performed once again with the Feyncalc Mathematica package. Its analytic form is similar to the one already written down in Appendix B with suitable substitutions of Fourier transform functions $F_{n,s}^{(\varphi)}$ for the Bessel functions associated with the circularly polarised field. The STPPP differential cross section can be obtained after transforming the phase space integral and defining scattering angles θ_f and φ_f by which the direction of 3-momentum $\vec{q}_-$ is specified.

To obtain numerical values, typical ILC values for the parameters ν^2 and $\frac{\omega}{m}$ are required. To establish the midpoint of the range of initial photon energies that need to be considered, the expression for average beamsstrahlung energy which describes the ratio between beamsstrahlung energy ω and the electron energy E which emits the beamsstrahlung, can be used [YP91]

$$\frac{\omega_1}{E} \sim \frac{4\sqrt{3}}{15}\Upsilon\frac{\sqrt{1+\Upsilon^{2/3}}}{(1+(1.5\Upsilon)^{2/3})^2} = 0.0145 \tag{8.33}$$

For the 250 GeV electrons planned for the default International Linear Collider parameter set, the average beamsstrahlung energy is $\dfrac{\langle\omega\rangle}{m} = 7094$. Numerical evaluation of the STPPP differential cross section requires careful consideration of the integration over the variable r. The Dirac delta function describing the conservation of 4-momenta indicates that r external field photons contribute to the process. Since r is continuous it is probably more correct to say that the external field contributes energy $r\omega$ to the STPPP process. The integration over r cannot be performed analytically since the integrand is a complicated function. It is convenient to perform the calculation in the centre of mass reference frame defined by

$$\begin{aligned} \underset{\sim}{k}_1 + \underset{\sim}{k}_2 + r\underset{\sim}{k} &= \underset{\sim}{q}_- + \underset{\sim}{q}_+ = 0 \\ \omega_1 + \omega_2 + r\omega &= \varepsilon_{q_-} + \varepsilon_{q_+} \end{aligned} \tag{8.34}$$

In this frame, with ω_1 and $r\omega$ a given, the other energies and momenta are found with the aid of the relations

$$\begin{aligned} \omega_2 &= |\omega_1 - r\omega| \\ \varepsilon_{q-} = \varepsilon_{q+} &= \tfrac{1}{2}(\omega_1 + \omega_2 + r\omega) \end{aligned} \tag{8.35}$$

Since the cross section contains an integration over r, there are infinite reference frames. However the frames travel at constant speed relative to each other and can be connected via Lorentz transformations. The initial particle energies in the frame given by equation 8.35 (the primed frame) are related to quantities in the centre of mass frame with $r = 0$ via the relativistic quantities γ, β and the relations

$$
\begin{aligned}
\omega' &= \gamma(1-\beta\,\mathrm{sign}(r))\omega \\
\omega_1' &= \gamma(1-\beta\,\mathrm{sign}(r))\omega_1 \\
\omega_2' &= |\omega_1' - r\omega'| \\
\varepsilon_{q-}' = \varepsilon_{q+}' &= \tfrac{1}{2}(\omega_1' + \omega_2' + r\omega')
\end{aligned}
\tag{8.36}
$$

The parameter r appears in the denominators of STPPP propagators. Resonances in the cross section appear if these denominators (uncorrected by radiative corrections) reach zero. The regularised imaginary part of the EFEES is inserted to render resonances finite. There are two propagator denominators, one for each of the STPPP Feynman diagrams

$$
\begin{aligned}
&4[(q_-k_1) + r(k\bar{p})]^2 + 4(\varepsilon_{\bar{p}}\Im\Delta\varepsilon_{\bar{p}}^R)^2 \\
&4[(q_-k_2) + r(k\bar{\bar{p}})]^2 + 4(\varepsilon_{\bar{\bar{p}}}\Im\Delta\varepsilon_{\bar{\bar{p}}}^R)^2
\end{aligned}
\tag{8.37}
$$

and resonance occurs when

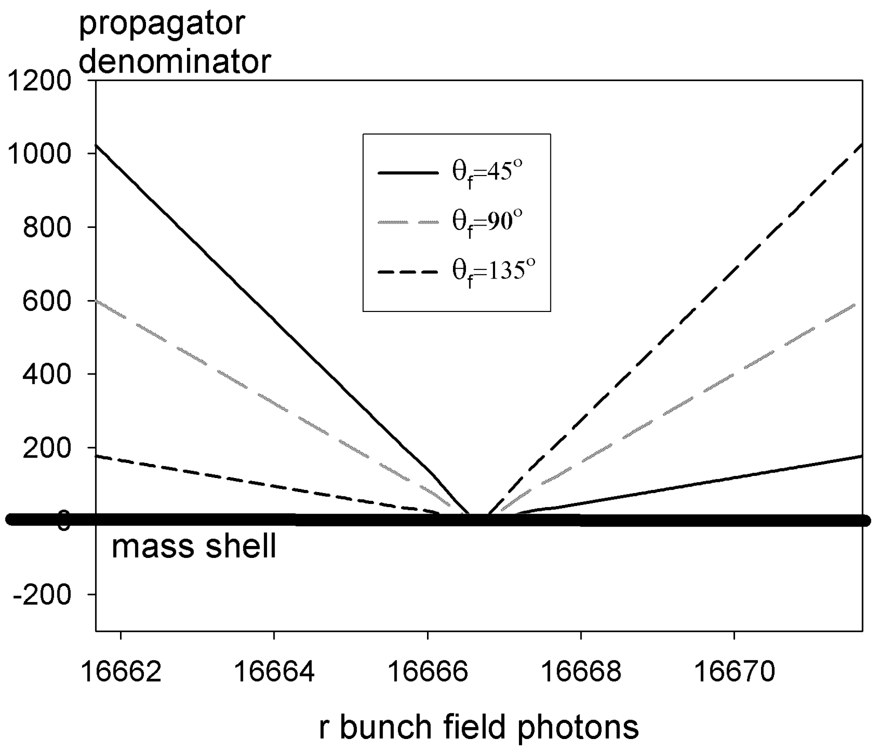

Figure 8.7: **The r value at which the peak 1 resonance occurs for $\frac{\omega_1}{m} = 1000$ and different values of scattering angle θ_f.**

$$
\begin{aligned}
r &= -\frac{(q_- k_1)}{(k\bar{p})} \qquad \text{peak 1 resonance} \\
r &= -\frac{(q_- k_2)}{(k\bar{\bar{p}})} \qquad \text{peak 2 resonance}
\end{aligned}
\tag{8.38}
$$

The reference frame, kinematics and numerical regime considered, set the peak 1 resonance occurring at large positive values of r and the peak 2 resonance at large negative values. At large absolute values of r the cross section numerators are dominated by terms like $r^2 Ai(r)^2$ which is very small for large negative values of r and large for large positive values of r. The peak 2 resonances are therefore suppressed and the peak 1 resonances need to be considered further.

The variation of the peak 1 resonance point (the r value) with the scattering angle θ_f is shown in figure 8.7. The cross section values at resonance are determined by a combination of the highly oscillatory nature of Airy functions at large negative values of their argument, and the value of the imaginary part of the EFEES. A typical resonance is shown in figure 8.8

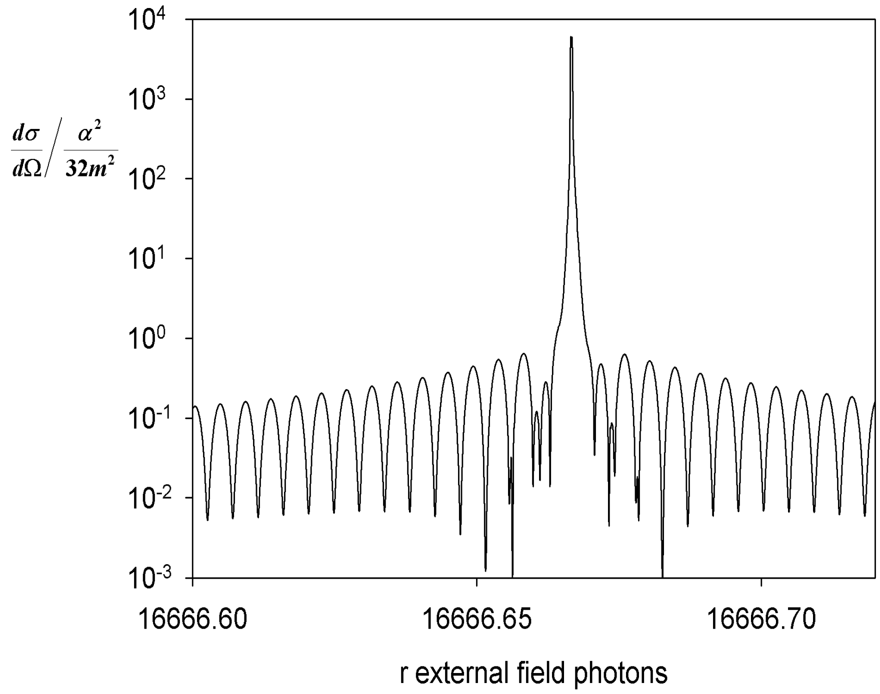

Figure 8.8: **A typical STPPP differential cross section resonance peak.**

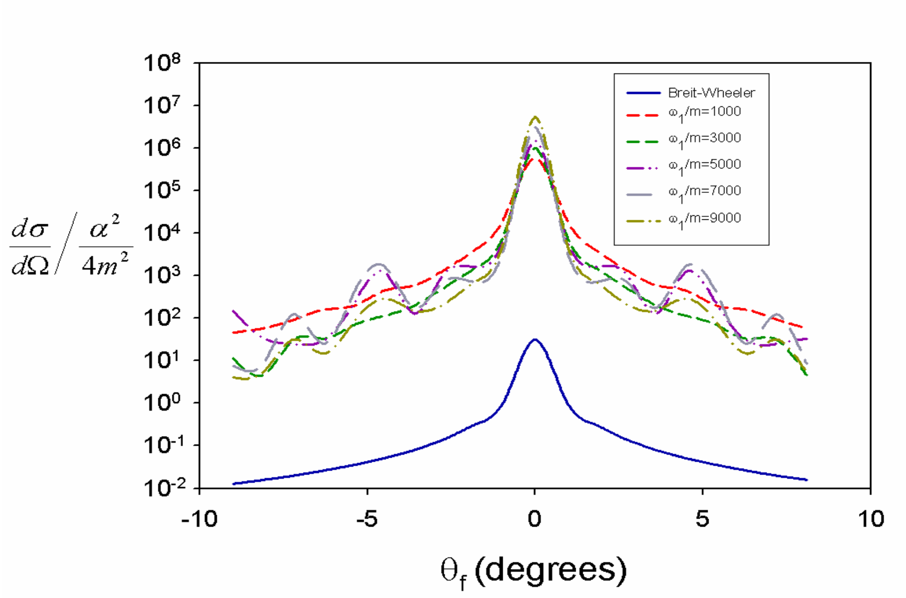

Figure 8.9: **The STPPP differential cross section for various values of the initial photon energy and electron scattering angle.**

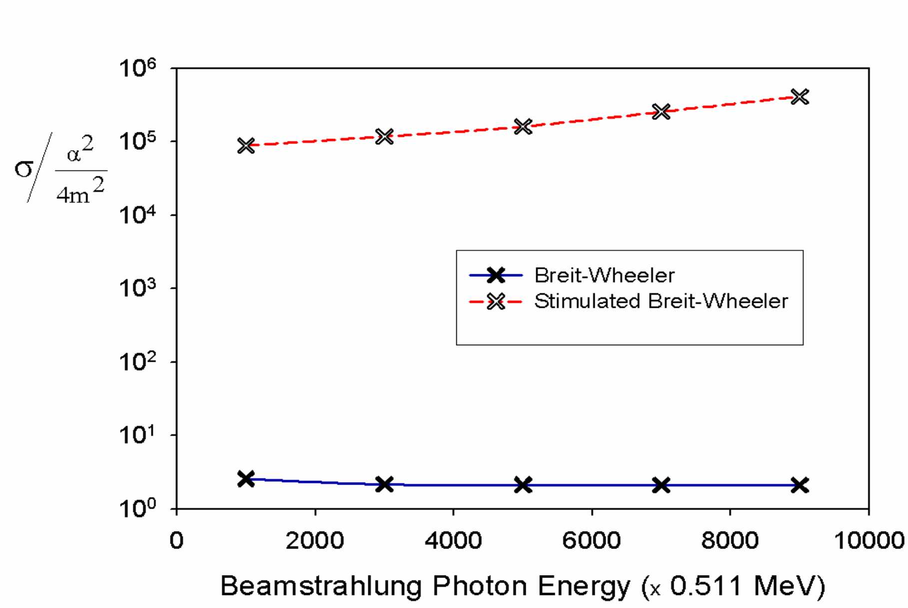

Figure 8.10: **The STPPP full cross section for various values of the initial photon energy.**

The STPPP differential cross section is to be integrated numerically over the resonance to calculate the contribution to the overall cross section. The contribution from the peak 1 resonance is plotted in figure 8.9 for different scattering angles θ_f and different initial photon energies.

The STPPP differential cross section is peaked at the same position as that of the Breit-Wheeler process. However, as expected, it exceeds the ordinary Breit-Wheeler differential cross section by several orders of magnitude. Integration over angles θ_f and φ_f is straightforward and the variation of the full cross section with beamsstrahlung energy ω_1 is plotted in figure 8.10. Whereas the Breit-Wheeler cross section declines with increasing ω_1, the STPPP cross section increases. For the range of beamsstrahlung photon energies expected at the ILC, the STPPP cross section exceeds the Breit-Wheeler process by 5 to 6 orders of magnitude.

Overall, the Breit-Wheeler process contributes minutely to the expected number of pairs at a typical ILC bunch collision (most come from Bethe-Heitler and Landau-Lifshitz processes). However inclusion of the STPPP process should lead to a significant increase in the expected number of pairs. The precise number is not quoted here because the numerical calculation was performed with the assumption of azimuthal symmetry and a separate study, taking into account real ILC bunch collisions, is required. It is believed that ILC processes that produce pairs from the STPPP process will not in fact be able to lay claim to azimuthal symmetry. It is known that the AiJ functions differ substantially from the Airy functions at large r. Therefore a method of numerically calculating the AiJ functions becomes important for future work on this process.

8.7 Conclusion

The differential cross sections for the external field electron energy shift (EFEES) and stimulated two photon pair production (STPPP) processes were analytically calculated for the case of a constant crossed external field. The EFEES calculation had been performed before [Rit72], but the analytic results obtained here would agree only if azimuthal symmetry around the field was assumed. The Airy functions appearing in the EFEES had to be replaced with new AiJ functions. The EFEES in the constant crossed electromagnetic field was investigated numerically and found to diminish as the external field intensity parameters ν^2 and scalar product parameter $\rho = (kp)$ diminished.

The STPPP in the constant crossed electromagnetic field was considered analytically and was found to depend on products of Airy functions (azimuthal symmetry) or products of AiJ functions (non azimuthal) symmetry. Two conditions for resonance were found corresponding to minimum values of the propagator denominator for each of the process Feynman diagrams.

Numerical calculations of the STPPP differential cross section, assuming azimuthal symmetry, were performed using parameter values expected at the ILC. A significant increase in the cross section of at 5 to 6 orders of magnitude was found compared to the equivalent, non external field, Breit-Wheeler process. As a result ILC bunch collisions are expected to produce more background pairs than were previously taken into account.

The calculations here can be improved on by further work. A satisfactory method of numerically calculating the AiJ functions at large values of their arguments should be developed and the numerical effect on the STPPP and EFEES cross sections calculated. The external field doesn't remain constant through a real bunch collision. The bunch is disrupted and the effect on the overall process cross sections should be gauged.

Chapter 9

Conclusion

The continued desire to test the theory of quantum electrodynamics by theoretical and experimental investigation of the consequences of the theory is the root motivation for the present work. With the presence of an external electromagnetic field the basic processes of quantum electrodynamics are altered and a new range of phenomena are introduced.

An investigation of the literature reveals that all the first order QED processes in an external electromagnetic field have been considered. Analytic expressions are well known and numerical consequences have been investigated. The transition probabilities of these processes are optimised when the external field intensity parameter is approximately unity, a condition that became available to experimental testing within the last decade.

In contrast, the second order processes remain only partially investigated for two main reasons. Firstly the presence of the external field renders the analytic expressions much more complex for the second order processes than for first order. Secondly it has been naively assumed that the transition probabilities of these processes will be an order of the fine structure constant smaller than those of the first order processes, thus rendering them less amenable to experimental detection.

However some studies show that the possibility of second order IFQED resonant processes, due to the electron gaining a level structure when it is embedded in an electromagnetic plane wave. Approximate calculations reveal that differential cross sections can increase by several orders of magnitude at resonance, suggesting experimental investigation. What is needed is a precise theoretical prediction of the parameters associated with the phenomena.

In this thesis, to that end, a detailed and unique examination of some of the second order IFQED processes, and the experimental conditions under which resonance can be achieved, was carried out. Both the stimulated Compton scattering (SCS) and stimulated two photon pair production (STPPP) processes were investigated without recourse to special kinematics or non relativistic restrictions. The external field that was considered was a plane wave electromagnetic field for which the Dirac equation can be solved exactly. Two particular plane waves were considered. A circularly polarised field was used in both SCS and STPPP processes. A constant crossed electromagnetic field, being a reasonable representation of the field of an ultra relativistic charge bunch was used in applying the STPPP calculation to the interaction region of a e^+e^- collider. The advantages of using a circularly polarised field was two-fold, in that high powered lasers which produce intense electromagnetic fields in experimental investigations, readily achieve this state of polarisation. Also, the solutions of the Dirac equation for a circularly polarised electromagnetic field contain the well known Bessel functions. Solutions of the Dirac equation for a constant crossed electromagnetic field contain Airy-type functions.

The external field was chosen to have a Lorentz gauge in which the three vectors defining the external field form a Cartesian coordinate system and in so doing provided a simplification of cross section expressions. In order to write down the expressions for the scattering cross section, Feynman's formulation of S-matrix theory was used in the Bound Interaction Picture which has proved to be the most convenient way of performing external field problems.

The scattering matrix element for the SCS process was written down with the aid of Feynman diagrams, and the Volkov electron wave function and the Ritus representation for the external field electron propagator were used. Integrations over space-time were achieved by writing the Volkov wave functions as infinite summations of Bessel and exponential functions. The infinite summations contain integer multiples of the external field 4-momentum which were interpreted, in the usual way, as the contribution to the process of quanta from the external field.

The square of the matrix element and a summation over electron spin and photon polarisation was performed to produce the usual trace expression of Dirac gamma matrices and the 4-vectors which describe the scattering. The scale of the trace sum required[1] was reduced, in the first instance by use of the reference frame in which the initial electron is at rest. A further simplification was achieved by expanding the trace sum into 22 independent trace sums which served as a base from which all other trace sums were calculated via a mapping of scattering parameters.

Calculation of the SCS cross section required an integration over final particle momenta which was transformed to an integration over the solid angle into which the SCS photon was scattered. This integration could not be performed analytically due to the complexity of the integrand. Further, the cross section contained infinite summations over products of Bessel functions, exponential functions and algebraic factors for which no analytic solution is known. However an original solution of a similar infinite summation was provided which may provide the basis for a solution of the infinite summations of interest. These infinite summations are associated with all calculations of second (and probably higher) order IFQED processes for the case of a circularly polarised electromagnetic field. In this work these infinite summations were performed numerically. The number of terms required for numerical convergence was roughly proportional to twice the ratio of initial photon energy to external field energy.

[1]An algebraic expansion of the trace sum results in over 100,000 terms.

As a test of the correctness of the obtained differential cross section expressions, limiting cases of the scattering parameters were investigated. For the cases of vanishing external field and vanishing initial photon, the expressions obtained in this thesis agreed with those of the literature. However for the special kinematic case of parallel initial photon and laser field the differential cross section obtained here differed slightly from that obtained by [AM85]. Numerical investigation showed that whereas the results of this thesis always return positive values for the differential cross section, the expressions obtained by [AM85] sometimes return incorrect negative values.

The stimulated two photon pair production (STPPP) process was also considered. The expression for the STPPP matrix element square was written down directly with the aid of the SCS expressions and a crossing symmetry which linked the two sets of Feynman diagrams. This crossing symmetry could be used even with the presence of the external field. In obtaining the STPPP differential cross section a suitable reference frame was chosen and the phase space integral integration variables were transformed into an integration over the element of solid angle into which the electron passes after its creation.

Numerical evaluation of the SCS and STPPP differential cross sections was carried out for a range of process parameters. For the SCS process this parameter range included incident photon energy ($0.001 \leq \omega_i \leq 25.6\ keV$), external field quanta energy ($0.001 \leq \omega \leq 51.2\ keV$), incident photon angle ($0^\circ \leq \theta_i \leq 360^\circ$), final photon scattering angles ($0^\circ \leq \theta_f, \phi_f \leq 360^\circ$) and intensity of the external field ($0 \leq \nu^2 \leq 2$). The STPPP parameters range included incident photon energy ($0.061 \leq \omega_1, \omega_2 \leq 5.12\ MeV$), external field quanta energy ($0.051 \leq \omega \leq 5.12\ MeV$), incident photon angle ($0^\circ \leq \theta_i \leq 180^\circ$), final electron scattering angles ($-180^\circ \leq \theta_f, \phi_f \leq 180^\circ$) and intensity of the external field ($0 \leq \nu^2 \leq 2$).

Analysis of the numerical results obtained for both processes was simplified by considering separate summation terms in the differential cross section expressions. These summation terms corresponded to the number, l of external field quanta which contributed to the process. Each summation term of the differential cross section itself contained an infinite summation of terms (denoted by r). The differential cross section was investigated with respect to the simplest of these summation terms for the case of collinear initial photons and external field propagation direction (i.e. the $r = -1, 0, 1$ terms of the $l = 0$ external field quanta contribution for $\theta_i = 0^\circ$).

Analysis of the numerical data presented for both the SCS and STPPP processes was made in terms of the effect of the external field. A general relationship was found between the external field intensity and the number of external field quanta terms which contribute significantly to the differential cross section. The joint increase in both is related to the tendency of external field quanta to participate in the interaction as the external field photon number density increases.

The differential cross section of the SCS process for the $l = 0, \theta_i = 0$ case was compared with the Klein-Nishina differential cross section. The greatest difference between the two occurred at $\theta_f = 180°$. A maximum enhancement of the SCS differential cross section took place when the external field energy was in excess of the initial photon energy, and a maximum diminishment at the same final scattering angle when the external field energy was smaller than initial photon energy. The variations from the Klein-Nishina differential cross section were explained in terms of the momentum transferred from the external field to the SCS electron.

The angular variation of the SCS l contributions was examined. The observed oscillatory behaviour of the differential cross section was explained by oscillatory momentum components gained by the electron due to its interaction with the external field. These momentum components were described as a Fourier series of discrete harmonic contributions from the external field. The oscillatory behaviour of the differential cross section was closely allied to the magnitude of the Bessel function arguments present in the differential cross section expressions. The larger the arguments, the more oscillatory the behaviour of the SCS differential cross section as the polar scattering angle varied from $0°$ to $360°$.

Further explanation of differential cross section variation lay in the comparison of the relative strengths of the l contributions. When the ratio $\frac{\omega_i}{\omega}$ was less than unity, the $l = 0$ contributions were exceeded by other contributions. The converse was true when $\frac{\omega_i}{\omega}$ was greater than unity. The analysis of the SCS differential cross section variation was confirmed by comparison with theory of radiation by an accelerated classical electron

The variation of the SCS differential cross section l contributions were also investigated for a scattering geometry in which the initial photon momentum makes an angle of $45°$ to the external field propagation direction. For this geometry the electron embedded in the external field receives a static momentum component along the direction of propagation of the external field, an oscillatory component along the direction of propagation of the electromagnetic field, as well as a momentum component from the initial photon. Analysis of the SCS differential cross section was given in terms of these competing influences and the behaviour predicted was close to that obtained.

The investigation of the variation of the SCS differential cross section summed over all l contributions enabled the overall effect of the external field on the process to be determined. In large part, analysis of the behaviour for this case was in terms of the relative strengths of the l contributions considered separately.

The main feature of the SCS differential cross section as the initial scattering angle varied from $0°$ to $90°$ was the development of peaks in the $\theta_f = 90°$ direction. These peaks have their origin in the transverse component of momentum received from the initial photon and the longitudinal component received from the external field. The greater the longitudinal component the greater the probability that the final states of the process with $\theta_f = 90°$ carry the transverse momentum. The argument was supported by an examination of trends in the relevant components.

The effect on the SCS process of increasing external field intensity was a generally enhanced cross section. External field photon number density increases, as does the probability that l external field photons will participate in the process. Increase in external field intensity also has the effect of slightly shifting differential cross section peaks.

The location of differential cross section peaks was also determined by the ratio of the initial photon energy with the product of external field intensity and energy. With this ratio comparable to or less than unity, differential cross section peaks indicate the preferred direction of radiation from the SCS electron was transverse to the external field propagation direction.

With variation in the initial scattering geometry, the relative peak heights of the $\theta_f = 90°$ and $\theta_f = 270°$ peaks vary. This variation was explained in terms of two competing processes in which momentum contributions preference scattering in one direction whereas the energy level structure of the electron in the external field preference scattering in another.

The predicted non azimuthal symmetry of the SCS process whenever $\theta_i \neq 0$ was confirmed by the numerical evaluations. Comparison of various scattering geometries indicated that the SCS differential cross section increased at the greatest rates with increase in the external field intensity when the initial photon propagation direction is not parallel with the external field propagation direction.

Numerical presentation and analysis of the STPPP differential cross section followed a similar order to that of the SCS process. The STPPP differential cross section for the $r = 0, l = 0, \theta_1 = 0°$ case was investigated as the external field intensity was increased. The zero external field case corresponded to Breit-Wheeler scattering with the dominant feature being the characteristic $\theta_f = -180°, 0°, 180°$ peaks. Increasing external field intensity led to a general decrease in the differential cross section. This was explained by the increased energy required to produce the fermion pair.

The complete STPPP differential cross section $l = 0$ contribution was either enhanced or diminished with respect to the Breit-Wheeler differential cross section. This was dependent on whether the ratio of initial photon energy to external field energy was greater than or less than unity. STPPP differential cross section peaks varied with increasing external field intensity. Peaks were broadened in relation to the ratio of initial photon energy to external field energy. An evident secondary peak structure was associated with the produced electron gaining oscillatory momentum components parallel to the external field propagation direction.

The STPPP differential cross section l contribution peaks varied depending on the value of l. The $\theta_f = 0°$ peaks increased as l increased and the $\theta_f = -180°, 180°$ peaks decreased. The explanation was given in terms of the momentum contribution from the external field which increased the probability that the fermion pair momentum was parallel rather than anti-parallel to the external field propagation direction.

The STPPP differential cross section was investigated for initial scattering geometries other than $\theta_1 = 0°$. With increasing external field intensity differential cross section peaks appeared both in directions parallel to initial photon momenta and parallel to the external field propagation direction.

The relative strengths of the peaks was in part determined by the ratio of initial photon energy to external field energy, with the largest peaks occurring in directions collinear to the most energetic particles.

STPPP differential cross section peaks displayed a tendency to resolve into double peaks whenever the external field intensity increased. The explanation was in terms of two competing trends, the increased probability that the fermion pair would be created with momentum parallel to the external field propagation direction, and the decreased probability that the external field quanta would participate in the process. Variation of the STPPP differential cross section with the final azimuthal angle revealed no change when $\theta_1 = 0°$, a result consistent with the azimuthal symmetry of the process for that scattering geometry.

Further investigation of the variation of the STPPP differential cross section with external field intensity revealed a general increase of both, with the largest rates of differential cross section increase recorded for scattering geometry in which $\theta_1 = 0°$. In some cases however the differential cross section diminished initially before increasing with increasing external field intensity. The explanation was in terms of two competing tendencies, one which increased the energy required to produce the fermion pair and the other which increased the likelihood that external field quanta will participate in the process. In some circumstances a "stepped" increase in the STPPP differential cross section with increasing external field intensity was observed. This phenomenon was related to the existence of a energy threshold for the pair production process to occur. As ν^2 increased so did the rest mass of the bound fermion requiring more external field quanta to participate as a necessary condition for the fermion creation. Close examination revealed that the "steps" in the differential cross section were not discontinuous.

Both the SCS and STPPP differential cross sections contained resonant infinities which corresponded to points at which the energy of the intermediate electron was exactly equivalent to an energy level of the fermion-external field system. The presence of resonant infinities indicated that the interaction between the intermediate electron and the virtual electron-positron field had not been taken into account. Such an interaction results in a shift of electron energies and the shift is affected by the presence of the external field. This external field electron energy shift (EFEES) calculation was carried out using the Volkov function representation for the electron propagator and an average over electron spin. Dispersion relations were used to separate out real and imaginary parts. The final result consisting of a rapidly convergent infinite summation and a single integration of a function of products of Bessel functions was confirmed via the optical theorem and the known results for first order IFQED processes. The real part of the EFEES reduced to zero at resonance points. However, only the imaginary part of the EFEES was necessary for the removal of the resonant infinities. The imaginary part of the EFEES was investigated numerically with respect to variation with the external field intensity and variation of a parameter ρ consisting of a scalar product of the external field and electron 4-momenta.

Investigation of the summation terms of the imaginary part of the EFEES revealed that convergence was achieved within the first ten terms for the range of parameter values of interest. Analysis of the numerical variation was facilitated by considering the expression for the recoil momentum of the electron scattered by its own field and the external field. A comparison was drawn with the theory of radiation by an electron in the field of a nucleus in which the probability of radiation bears an inverse relationship to the recoil momentum. The EFEES imaginary part increased linearly with respect to ρ and ν^2 except when ρ and ν^2 were large. This behaviour was explainable in terms of the analytic form of the recoil momentum.

A comparison was made between the numerical results achieved here and the approximation formulae obtained by [BM76]. Good agreement was found within the validity of the approximation, but as much as a $13.4\,\%$ error for other required parameter values. The full expressions for the EFEES imaginary part obtained here were necessary for further calculation of the SCS and STPPP resonant differential cross sections.

SCS and STPPP resonant cross sections were rendered finite by the insertion of EFEES imaginary part into the external field electron propagator denominator. However the presence of divergences in the EFEES expressions required an appropriate regularisation and renormalisation procedure which also took into account the external field. Regularisation and renormalisation was applied to the self energy (EFESE) and was shown to be the same as for the non external field case. The EFESE was inserted into the denominator of the bound electron propagator and was shown to be equivalent to the insertion of the energy shift (EFEES) to order α.

Analytic expressions for the location, spacing and widths of the SCS and STPPP resonant differential cross sections were developed. Resonance heights were obtained by recalculating the SCS and STPPP differential cross sections at the parameter values at which the resonance occurred. The resonant differential cross sections were investigated for various sets of parameters. These were $\nu^2 = 0.1, 1$, $\omega = 25.6, 61.4$ keV and $\omega_i = 51.2$ keV for the SCS process, and $\nu^2 = 0.1, 0.5$, $\omega = 0.768, 1.024$ MeV and $\omega_1, \omega_2 = 0.409, 0.768, 1.28$ MeV for the STPPP process. Some differential cross sections exceeded the non resonance differential cross sections, the differential cross sections of the equivalent first order processes and the differential cross sections of the equivalent non external field processes by several orders of magnitude.

After integration over scattering angles, with particular care paid to the points of resonance, full SCS and STPPP cross sections were obtained. A general increase of the cross section with external field intensity was established. However, the SCS full cross-section sharply peaked at particular values of ν^2 (0.2 for the particular parameter set considered) and the STPPP cross section enhancement was generally smaller. Nevertheless the SCS cross section exceeded the Klein Nishina cross section by 5 to 6 orders of magnitude at peak, and the STPPP cross section exceeded the Breit-Wheeler cross section by one order of magnitude by $\nu^2 = 0.5$.

This result was recognised as being of importance. IFQED experimental efforts to date have been directed towards the first order IFQED processes. It can be naively assumed that the first order processes have larger cross sections and are hence more detectable because of the lower order of the fine structure constant contained in their expressions. However the extent of the SCS and STPPP resonant cross sections indicated that this is not the case. The appearance of large resonant cross sections at relatively low external field intensities is experimentally beneficial as moderately intense lasers should be sufficient to test theoretical predictions of the second order IFQED calculations.

In agreement with [AM85] no resonances were found at $\theta_i = 0°$ for the SCS process. This result vindicated the original decision to calculate the SCS and STPPP differential cross sections without the benefit of special kinematics.

Generally, more resonances occur for the STPPP process than for the SCS process. This was due to the greater range of fermion energies traversed (and hence fermion quasi-energy levels traversed) for the investigated STPPP parameter range. Resonance widths were $\sim 4°$ for the SCS differential cross section and $\sim 0.1°$ for the STPPP differential cross section as ν^2 approached its upper limit.

Analytic work for the STPPP process was applied to collisions between e^+e^- bunches at the proposed International Linear Collider. These relativistic bunches produce an electromagnetic field that is essentially constant and transverse to the bunch motion. The Volkov solution could be used once its form was found for the case of constant crossed external field. Fourier transforms were introduced and the Volkov solution contained Airy functions only if azimuthal asymmetry was assumed. More generally, the transforms were integrations over products of Bessel functions and cos functions of Airy-type arguments. These transforms were labelled AiJ.

Investigation of cross section resonances for the STPPP process in charge bunch collisions required calculation of the EFEES in a constant crossed electromagnetic field. This calculation contained poles at the lower limit of certain integrations. These were avoided by introducing an infinitesimal photon mass and transforming integration variables. As for the STPPP process in a constant crossed electromagnetic field, the EFEES in the same field contained products of Airy (or AiJ) functions. The Airy functions diverged for large negative values of its argument and provided difficulty in carrying out numerical calculations. The AiJ functions, however, are damped for both large negative and large positive values of their argument. In future work - once numerical methods are developed for computing the AiJ functions - calculation of the constant crossed EFEES and STPPP processes over all parameter ranges should be possible.

The constant crossed EFEES was inserted into bound propagator denominators and the STPPP differential and full cross sections were calculated. Using numerical values of parameters suggested by the expected operation of the International Linear Collider, the contribution to the STPPP differential cross section was at 5 to 6 orders of magnitude greater than the Breit-Wheeler process (i.e. the STPPP process in the absence of the field). The expected end result is that there will be significantly more background pairs per bunch crossing at the ILC. More detailed investigation of the parameter range awaits future work.

Experimental conditions required for the detection of these resonances were considered. Operating parameters of the present generation of high-powered lasers should be sufficient to detect the theoretically predicted SCS and STPPP resonant cross sections. The potential cross sections measured by a stationary particle detector which subtends the top half of the largest SCS and STPPP resonance peaks, were calculated. The predicted event rates should be easily observable.

Appendix A

The Jacobian of the Transformation $d^4p \rightarrow d^4q$

The cross section calculations in this thesis involve transformation of integration variable between the free electron 4-momentum p_μ and the electron 4-momentum shifted by the presence of the external field q_μ $\left(= p_\mu - \frac{\nu^2}{2\omega(q_0-q_3)}\, k_\mu\right)$. The Jacobian of this transformation is written in equation A.1, where the subscripts $1, 2, 3$ refer to the time, x, y and z axes respectively

$$d^4p = J\, d^4q \quad ; \quad J = \begin{vmatrix} \frac{\partial p_0}{\partial q_0} & \frac{\partial p_0}{\partial q_1} & \frac{\partial p_0}{\partial q_2} & \frac{\partial p_0}{\partial q_3} \\ \frac{\partial p_1}{\partial q_0} & \frac{\partial p_1}{\partial q_1} & \frac{\partial p_1}{\partial q_2} & \frac{\partial p_1}{\partial q_3} \\ \frac{\partial p_2}{\partial q_0} & \frac{\partial p_2}{\partial q_1} & \frac{\partial p_2}{\partial q_2} & \frac{\partial p_2}{\partial q_3} \\ \frac{\partial p_3}{\partial q_0} & \frac{\partial p_3}{\partial q_1} & \frac{\partial p_3}{\partial q_2} & \frac{\partial p_3}{\partial q_3} \end{vmatrix} \tag{A.1}$$

In finding the Jacobian of this transformation we must make use of a coordinate system in which the external field photons propagate along the z-axes, $k_\mu = (\omega, 0, 0, \omega)$, with the result that the free electron momentum can be written

$$p_\mu = q_\mu + \frac{e^2a^2}{2\omega(q_0 - q_3)}\, k_\mu \tag{A.2}$$

The Jacobian J then reduces to

$$J = \begin{vmatrix} \frac{\partial p_0}{\partial q_0} & 0 & 0 & \frac{\partial p_0}{\partial q_3} \\ \frac{\partial p_1}{\partial q_0} & 1 & 0 & \frac{\partial p_1}{\partial q_3} \\ \frac{\partial p_2}{\partial q_0} & 0 & 1 & \frac{\partial p_2}{\partial q_3} \\ \frac{\partial p_3}{\partial q_0} & 0 & 0 & \frac{\partial p_3}{\partial q_3} \end{vmatrix} = \frac{\partial p_0}{\partial q_0}\frac{\partial p_3}{\partial q_3} - \frac{\partial p_0}{\partial q_3}\frac{\partial p_3}{\partial q_0} = 1 \tag{A.3}$$

Appendix B

The Full Expressions and Trace results for $\mathrm{Tr}\, Q_1$ and $\mathrm{Tr}\, Q_2$

In this appendix the complete trace expressions for $\mathrm{Tr}\, Q_1$ and $\mathrm{Tr}\, Q_2$ are presented. The trace expressions can be algebraically expanded and subdivided into 17 independent trace coefficients for $\mathrm{Tr}\, Q_1$ and 15 independent trace coefficients for $\mathrm{Tr}\, Q_2$. These independent trace coefficients can be designated in terms of their co-products, the functions $X_{ij}^{r,r'}$.

$$\begin{aligned}
\overline{X}_{ij}^{r} &\equiv \frac{\overline{M}_{ir}\overline{N}_{jr}}{(\bar{p}_r^2 - m^2)} \\
C1(\bar{p}, p_f, \gamma_\mu) &\equiv \gamma_\mu - \frac{e^2 a^2}{4(k\bar{p})(kp_f)} \not{k}\gamma_\mu \not{k} \\
C2(\bar{p}, p_f, \gamma_\mu) &\equiv -\frac{e}{2(k\bar{p})}\gamma_\mu \not{a}_1 \not{k} + \tfrac{e}{2(kp_f)} \not{a}_1 \not{k}\gamma_\mu \\
C3(\bar{p}, p_f, \gamma_\mu) &\equiv -\frac{e}{2(k\bar{p})}\gamma_\mu \not{a}_2 \not{k} + \tfrac{e}{2(kp_f)} \not{a}_2 \not{k}\gamma_\mu
\end{aligned} \tag{B.1}$$

B.1 The results for $\mathrm{Tr}\, Q_1$

$$\begin{aligned}
\mathrm{Tr}\, Q_1(\bar{p}_r, \bar{p}_{r\prime}) &= \mathrm{Tr}(\not{p}_f + m)\left[C1(\bar{p}, p_f, \gamma_\mu)\overline{N}_{1r} + C2(\bar{p}, p_f, \gamma_\mu)\overline{N}_{2r} + C3(\bar{p}, p_f, \gamma_\mu)\overline{N}_{3r}\right] \\
&\times \left[\frac{\bar{\not{p}}_r + m}{\bar{p}_r^2 - m^2}\right]\left[C1(\bar{p}, p_i, \gamma_\nu)\overline{M}_{1r} + C2(p_i, \bar{p}, \gamma_\nu)\overline{M}_{2r} + C3(p_i, \bar{p}, \gamma_\nu)\overline{M}_{3r}\right] \\
&\times (\not{p}_i + m)\left[C1(\bar{p}, p_i, \gamma_\nu)\overline{M}^*_{1r'} + C2(\bar{p}, p_i, \gamma_\nu)\overline{M}^*_{2r'} + C3(\bar{p}, p_i, \gamma_\nu)\overline{M}^*_{3r'}\right] \\
&\times \left[\frac{\bar{\not{p}}_{r\prime} + m}{\bar{p}_{r'}^2 - m^2}\right]^*\left[C1(\bar{p}, p_f, \gamma_\mu)\overline{N}^*_{1r'} + C2(p_f, \bar{p}, \gamma_\mu)\overline{N}^*_{2r'} + C3(p_f, \bar{p}, \gamma_\mu)\overline{N}^*_{3r'}\right]
\end{aligned}$$

The coefficient of $\overline{X}^r_{11}[\overline{X}^{r'}_{11}]^*$

$$16\left\{4m^2\left[(\bar{p}_r\bar{p}_{r'})+m^2\right]+(p_f\bar{p}_{r'})(p_i\bar{p}_r)+(p_f\bar{p}_r)(p_i\bar{p}_{r'})+2e^4a^4-8e^2a^2m^2\right\}$$
$$-16(2m^2-e^2a^2)\left[(p_f\bar{p}_r)+(p_i\bar{p}_r)+(p_f\bar{p}_{r'})+(p_i\bar{p}_{r'})\right]$$
$$-16\left[(\bar{p}_r\bar{p}_{r'})-m^2\right]\left\{(p_ip_f)+e^2a^2\left[\frac{(kp_i)}{(k\bar{p})}+\frac{(kp_f)}{(k\bar{p})}\right]\right\}$$

The coefficient of $\overline{X}^r_{11}[\overline{X}^{r'}_{12}]^*$

$$8\left[\frac{1}{(kp_f)}-\frac{1}{(k\bar{p})}\right]\left[(\bar{p}_r\bar{p}_{r'})-m^2\right](\bar{\alpha}_{1i}-\bar{\alpha}_{1f})(kp_i)(kp_f)$$
$$-8\left[4m^2-2e^2a^2-(p_i\bar{p}_r)-(p_i\bar{p}_{r'})\right]\bar{\alpha}_{1f}$$
$$+16(r-r')(kp_i)\left[(k\bar{p})+(kp_f)\right]\bar{\alpha}_{1i}$$

The coefficient of $\overline{X}^r_{11}[\overline{X}^{r'}_{22}]^*$

$$-16(k\bar{p})\left[(kp_i)+(kp_f)\right]\bar{\alpha}_{1i}\bar{\alpha}_{1f}$$
$$+8e^2a^2\left\{[\bar{p}^2+m^2]\left[\frac{(kp_i)}{(k\bar{p})}+\frac{(kp_f)}{(k\bar{p})}\right]+(p_ip_f)\left[1+\frac{(kp_i)}{(k\bar{p})}\right]-(p_i\bar{p}_r)\left[\frac{(kp_f)}{(k\bar{p})}+\frac{(kp_f)}{(kp_i)}\right]\right.$$
$$\left.(p_i\bar{p}_{r'})\left[1+\tfrac{(k\bar{p})}{(kp_i)}\right]-(p_f\bar{p}_r)\left[\tfrac{(kp_i)}{(k\bar{p})}+\tfrac{(kp_i)}{(kp_f)}\right]-(p_f\bar{p}_{r'})\left[1+\tfrac{(k\bar{p})}{(kp_f)}\right]\right\}$$

The coefficient of $\overline{X}^r_{12}[\overline{X}^{r'}_{12}]^*$

$$8e^2a^2(kp_f)\left[\frac{1}{(kp_f)^2}+\frac{1}{(k\bar{p})^2}\right]\left\{\left[4m^2-(p_i\bar{p}_r)-(p_i\bar{p}_{r'})-2e^2a^2\right](k\bar{p})+\left[(\bar{p}_r\bar{p}_{r'})-m^2\right](kp_i)\right\}$$

The coefficient of $\overline{X}^r_{12}[\overline{X}^{r'}_{21}]^*$

$$16\left[(kp_i)(kp_f)+(k\bar{p})^2\right]\bar{\alpha}_{1i}\bar{\alpha}_{1f}$$
$$-8e^2a\left\{{}^2[\bar{p}^2-m^2]\left[1+\frac{(kp_i)(kp_f)}{(k\bar{p})^2}\right]-2m^2\left[\frac{(kp_i)}{(k\bar{p})}+\frac{(kp_f)}{(k\bar{p})}\right]-(p_ip_f)\left[1+\frac{(k\bar{p})}{(kp_i)}\right]\left[1+\frac{(k\bar{p})}{(kp_f)}\right]\right.$$
$$\left.+(p_i\bar{p}_{r'})\left[\frac{(kp_f)}{(kp_i)}+\frac{(kp_f)}{(k\bar{p})}\right]+(p_i\bar{p}_r)\left[1+\frac{(k\bar{p})}{(kp_i)}\right]+(p_f\bar{p}_r)\left[\frac{(kp_i)}{(k\bar{p})}+\frac{(kp_i)}{(kp_f)}\right]+(p_f\bar{p}_{r'})\left[1+\frac{(k\bar{p})}{(kp_f)}\right]\right\}$$

The coefficient of $\overline{X}^r_{11}[\overline{X}^{r'}_{23}]^*$

$$8\left[(k\bar{p})+(kp_f)\right]\left[(k\bar{p})+(kp_i)\right]\left(\bar{\alpha}_{1i}\bar{\alpha}_{2f}-\bar{\alpha}_{2i}\bar{\alpha}_{1f}\right)$$

The coefficient of $\overline{X}^r_{12}[\overline{X}^{r'}_{22}]^*$

$$8e^2a^2(kp_f)(k\bar{p})\left[\frac{1}{(kp_f)^2}+\frac{1}{(k\bar{p})^2}\right]\left[(kp_i)-(k\bar{p})\right]\bar{\alpha}_{1i}$$

The coefficient of $\overline{X}^r_{12}[\overline{X}^{r'}_{23}]^*$

$$8e^2a^2(kp_f)(k\bar{p})\left[\frac{1}{(kp_f)^2}-\frac{1}{(k\bar{p})^2}\right]\left[(kp_i)+(k\bar{p})\right]\bar{\alpha}_{1i}$$

B.2 The results for Tr Q_2

$$\begin{aligned}
\operatorname{Tr} Q_2(\bar{p}_r,\bar{\bar{p}}_{r\prime}) &= \operatorname{Tr}(\not{p}_f+m)\left[C1(\bar{p},p_f,\gamma_\mu)\overline{N}_{1r}+C2(\bar{p},p_f,\gamma_\mu)\overline{N}_{2r}+C3(\bar{p},p_f,\gamma_\mu)\overline{N}_{3r}\right]\\
&\times\ \left[\frac{\bar{\not{p}}_r+m}{\bar{p}_r^2-m^2}\right]\left[C1(\bar{p},p_i,\gamma_\nu)\overline{M}_{1r}+C2(p_i,\bar{p},\gamma_\nu)\overline{M}_{2r}+C3(p_i,\bar{p},\gamma_\nu)\overline{M}_{3r}\right]\\
&\times\ (\not{p}_i+m)\left[C1(\bar{\bar{p}},p_i,\gamma_\mu)\overline{\overline{M}}^*_{1r'}+C2(\bar{\bar{p}},p_i,\gamma_\mu)\overline{\overline{M}}^*_{2r'}+C3(\bar{\bar{p}},p_i,\gamma_\mu)\overline{\overline{M}}^*_{3r'}\right]\\
&\times\ \left[\frac{\bar{\bar{\not{p}}}_{r\prime}+m}{\bar{\bar{p}}_{r'}^2-m^2}\right]^*\left[C1(\bar{\bar{p}},p_f,\gamma_\nu)\overline{\overline{N}}^*_{1r'}+C2(p_f,\bar{\bar{p}},\gamma_\nu)\overline{\overline{N}}^*_{2r'}+C3(p_f,\bar{\bar{p}},\gamma_\nu)\overline{\overline{N}}^*_{3r'}\right]
\end{aligned}$$

The coefficient of $\overline{X}^r_{11}[\overline{\overline{X}}^{r'}_{11}]^*$

$$\begin{aligned}
&16m^2\left[(p_i\bar{p}_r)+(p_i\bar{\bar{p}}_{r\prime})+(p_f\bar{p}_r)+(p_f\bar{\bar{p}}_{r\prime})+(p_ip_f)+(\bar{p}_r\bar{\bar{p}}_{r\prime})-2(\bar{p}_r\bar{\bar{p}}_{r\prime})(p_ip_f)-2m^2\right]\\
&-8e^2a^2\left\{(k_ip_i)\left[1-\frac{(kp_f)}{(kp_i)}\right]\left[1-\frac{(k\bar{\bar{p}})}{(k\bar{p})}\right]-(k_fp_i)\left[1-\frac{(kp_f)}{(kp_i)}\right]\left[1-\frac{(k\bar{p})}{(k\bar{\bar{p}})}\right]\right.\\
&\left.+(k_fp_f)\left[1-\frac{(kp_i)}{(kp_f)}\right]\left[1-\frac{(k\bar{\bar{p}})}{(k\bar{p})}\right]-(k_ip_f)\left[1-\frac{(kp_i)}{(kp_f)}\right]\left[1-\frac{(k\bar{p})}{(k\bar{\bar{p}})}\right]\right\}\\
&-8m^2e^2a^2\left[(kp_i)+(kp_f)\right]^2\left[\frac{1}{(k\bar{p})(k\bar{\bar{p}})}+\frac{1}{(kp_i)(kp_f)}\right]\\
&+32e^4a^4\left[\frac{(kp_i)}{(kp_f)}+\frac{(kp_f)}{(kp_i)}+\frac{(k\bar{p})}{(k\bar{\bar{p}})}+\frac{(k\bar{\bar{p}})}{(k\bar{p})}\right]
\end{aligned}$$

The coefficient of $\overline{X}^{r}_{11}[\overline{\overline{X}}^{r'}_{12}]^*$

$$
\begin{aligned}
&8m^2\left[\frac{1}{(k\bar{\bar{p}})}+\frac{1}{(kp_f)}\right][(kp_f)(k\bar{p})\alpha_{\overline{1f}}-(kp_i)(k\bar{\bar{p}})\alpha_{\overline{\overline{1i}}}]\\
&-8m^2\left[\frac{1}{(k\bar{\bar{p}})}-\frac{1}{(kp_f)}\right][(kp_f)(k\bar{\bar{p}})\alpha_{\overline{\overline{1f}}}+(kp_i)(k\bar{p})\alpha_{\overline{1i}}]\\
&-8(\alpha_{1i}-\alpha_{1f})\left\{\frac{e^2a^2}{(k\bar{\bar{p}})}\Big[(kp_i)(k\bar{\bar{p}})+(kp_f)(k\bar{p})\Big]-m^2\left[\frac{1}{(k\bar{\bar{p}})}+\frac{1}{(kp_f)}\right](kp_i)(kp_f)+2(\bar{p}_r\bar{\bar{p}}_{r\prime})(kp_i)\right\}\\
&-8(\alpha_{\bar{1}}-\alpha_{\bar{\bar{1}}})\left\{\frac{e^2a^2}{(kp_f)}\Big[(kp_i)(k\bar{\bar{p}})+(kp_f)(k\bar{p})\Big]-m^2\left[\frac{1}{(k\bar{\bar{p}})}+\frac{1}{(kp_f)}\right](k\bar{p})(k\bar{\bar{p}})+2(p_ip_f)(k\bar{p})\right\}
\end{aligned}
$$

The coefficient of $\overline{X}^{r}_{11}[\overline{\overline{X}}^{r'}_{22}]^*$

$$
\begin{aligned}
&16(k\bar{p})\,[(kp_f)-(kp_i)]\,[(\alpha_{1f}-\alpha_{1i})(\alpha_{\bar{1}}-\alpha_{\bar{\bar{1}}})]+16e^2a^2\left[(p_ip_f)\frac{(k\bar{p})}{(k\bar{\bar{p}})}-(\bar{p}_r\bar{\bar{p}}_{r\prime})\right]\\
&8e^2a^2m^2\left\{\frac{(k\bar{p})}{(k\bar{\bar{p}})}\left[1-\frac{(kp_f)}{(kp_i)}\right]-\frac{(k\bar{p})}{(kp_f)}\left[\frac{(k\bar{\bar{p}})}{(kp_i)}+\frac{(kp_i)}{(k\bar{\bar{p}})}\right]+\frac{(k\bar{p})}{(kp_i)}+\frac{(k\bar{\bar{p}})}{(kp_f)}\right\}\\
&+8e^2a^2\left\{\frac{(p_f\bar{p}_r)}{(kp_f)}-\frac{(p_i\bar{p}_r)}{(kp_i)}-\frac{(k\bar{p})}{(k\bar{\bar{p}})}\left[\frac{(\bar{\bar{p}}_{r\prime}p_f)}{(kp_f)}-\frac{(\bar{\bar{p}}_{r\prime}p_i)}{(kp_i)}\right]\right\}[(kp_f)-(kp_i)]
\end{aligned}
$$

The coefficient of $\overline{X}^{r}_{12}[\overline{\overline{X}}^{r'}_{21}]^*$

$$
\begin{aligned}
&8e^2a^2m^2\left\{4+\left[\frac{(k\bar{\bar{p}})}{(kp_i)}+\frac{(kp_i)}{(k\bar{\bar{p}})}\right]\left[\frac{(k\bar{p})}{(kp_f)}+\frac{(kp_f)}{(k\bar{p})}\right]-\frac{(k\bar{p})}{(kp_i)}-\frac{(kp_i)}{(k\bar{p})}-\frac{(k\bar{\bar{p}})}{(kp_f)}-\frac{(kp_f)}{(k\bar{\bar{p}})}\right\}\\
&-8e^2a^2\left[(p_f\bar{\bar{p}}_{r\prime})\frac{(kp_i)}{(kp_f)}-(p_i\bar{\bar{p}}_{r\prime})\right]\left[\frac{(kp_f)}{(kp_i)}+\frac{(k\bar{p})}{(k\bar{\bar{p}})}\right]\\
&-8e^2a^2\left[(p_i\bar{p}_r)\frac{(kp_f)}{(kp_i)}-(p_f\bar{p}_r)\right]\left[\frac{(kp_i)}{(kp_f)}+\frac{(k\bar{\bar{p}})}{(k\bar{p})}\right]-8e^4a^4\left[\frac{(k\bar{\bar{p}})(kp_f)}{(k\bar{p})(kp_i)}+\frac{(k\bar{p})(kp_i)}{(k\bar{\bar{p}})(kp_f)}+2\right]
\end{aligned}
$$

The coefficient of $\overline{X}^{r}_{11}[\overline{\overline{X}}^{r\prime}_{23}]^*$

$$
8(k\bar{p})\,[(kp_f)-(kp_i)]\,[(\alpha_{2f}-\alpha_{2i})(\alpha_{\bar{1}}-\alpha_{\bar{\bar{1}}})+(\alpha_{1f}-\alpha_{1i})(\alpha_{\bar{2}}-\alpha_{\bar{\bar{2}}})]
$$

The coefficient of $\overline{X}^{r}_{12}[\overline{\overline{X}}^{r'}_{31}]^*$

$$
-8\,[(kp_f)(k\bar{\bar{p}})-(kp_i)(k\bar{p})]\,[(\alpha_{2f}-\alpha_{2i})(\alpha_{\bar{1}}-\alpha_{\bar{\bar{1}}})-(\alpha_{1f}-\alpha_{1i})(\alpha_{\bar{2}}-\alpha_{\bar{\bar{2}}})]
$$

The coefficient of $\overline{X}^r_{12}[\overline{\overline{X}}^{r\prime}_{22}]^*$

$$8e^2a^2\left[(kp_f)(k\bar{\bar{p}})+(kp_i)(k\bar{p})\right]\left[\frac{1}{(kp_f)}(\alpha_{\bar{1}}-\alpha_{\bar{\bar{1}}})+\frac{1}{(k\bar{\bar{p}})}(\alpha_{1f}-\alpha_{1i})\right]$$

The coefficient of $\overline{X}^r_{12}[\overline{\overline{X}}^{r\prime}_{32}]^*$

$$8e^2a^2\left[(kp_i)(k\bar{p})-(kp_f)(k\bar{\bar{p}})\right]\left[\frac{1}{(kp_f)}(\alpha_{\bar{2}}-\alpha_{\bar{\bar{2}}})-\frac{1}{(k\bar{\bar{p}})}(\alpha_{2f}-\alpha_{2i})\right]$$

The coefficient of $\overline{X}^r_{22}[\overline{\overline{X}}^{r\prime}_{22}]^*$

$$8e^4a^4\left[\frac{(kp_i)}{(kp_f)}+\frac{(kp_f)}{(kp_i)}+\frac{(k\bar{p})}{(k\bar{\bar{p}})}+\frac{(k\bar{\bar{p}})}{(k\bar{p})}\right]$$

The coefficient of $\overline{X}^r_{23}[\overline{\overline{X}}^{r'}_{23}]^*$

$$8e^4a^4\left[\frac{(kp_i)}{(kp_f)}+\frac{(kp_f)}{(kp_i)}-\frac{(k\bar{p})}{(k\bar{\bar{p}})}-\frac{(k\bar{\bar{p}})}{(k\bar{p})}\right]$$

Appendix C

The explicit form of certain functions of M_j and M_k

$\alpha_{1x}M_2 + \alpha_{2x}M_3$	$\alpha_{1x}N_2 + \alpha_{2x}N_3$	$M_2N_2 + M_3N_3$	$\overline{M}_2\overline{\overline{M}}_2^* + \overline{M}_3\overline{\overline{M}}_3^*$
$\alpha_{1x}M_2 - \alpha_{2x}M_3$	$\alpha_{1x}N_2 - \alpha_{2x}N_3$	$M_2N_2 - M_3N_3$	$\overline{N}_2\overline{\overline{N}}_2^* + \overline{N}_3\overline{\overline{N}}_3^*$
$\alpha_{1x}M_3 + \alpha_{2x}M_2$	$\alpha_{1x}N_3 + \alpha_{2x}N_3$	$M_2N_3 - M_3N_2$	$\overline{N}_2\overline{\overline{M}}_2^* + \overline{N}_3\overline{\overline{M}}_3^*$
$\alpha_{1x}M_3 - \alpha_{2x}M_2$	$\alpha_{1x}N_3 - \alpha_{2x}N_2$	$M_2N_3 + M_3N_2$	$\overline{N}_2\overline{\overline{M}}_3^* + \overline{N}_3\overline{\overline{M}}_2^*$

Table C.1: **General algebraic functions involving M_i and N_j**

The trace calculation associated with the SCS and STPPP cross sections can be divided into a series of terms involving trace coefficients (see Appendix B) and as co-products, simple algebraic functions of M_j and N_k defined in equation 3.4. In this appendix the most general of these algebraic functions, tabulated in table C, are written down explicitly. The subscripts x refer to either i for initial state quantities or f for final state quantities.

Evaluation of these algebraic functions of M_j and N_k , are based on the basic properties of Bessel functions and involve exponential functions of six angles defined by

$$\begin{array}{ccccc} \overline{\phi} = \overline{\phi}_{0i} - \overline{\phi}_{0f} & ; & \overline{\overline{\phi}} = \overline{\overline{\phi}}_{0i} - \overline{\overline{\phi}}_{0f} & ; & \psi_i = \overline{\phi}_{0i} - \overline{\overline{\phi}}_{0i} \\ \psi_f = \overline{\phi}_{0f} - \overline{\overline{\phi}}_{0f} & ; & \overline{\chi} = \overline{\phi}_{0i} - \overline{\overline{\phi}}_{0f} & ; & \overline{\overline{\chi}} = \overline{\overline{\phi}}_{0i} - \overline{\phi}_{0f} \end{array} \tag{C.1}$$

$\alpha_{1x}, \alpha_{2x}, \phi_{0x}$ and z_x are functions of scalar products of external field 4-vectors and obey the relations of equation 2.27 and 2.28. Using the addition formulae for the Bessel functions [Wat22], M_j and N_k obey the relations of equation 3.14 and

$$
\begin{aligned}
\alpha_{1x}M_2 + \alpha_{2x}M_3 &= \frac{z_x}{2}\left[J_{r-1}(z_i)e^{i\phi_{0x}-i\phi_{0i}} + J_{r+1}(z_i)e^{-i\phi_{0x}+i\phi_{0i}}\right]e^{ir\phi_{0i}} \\
\alpha_{1x}N_2 + \alpha_{2x}N_3 &= \frac{z_x}{2}\left[J_{s-1}(z_f)e^{-i\phi_{0x}+i\phi_{0f}} + J_{s+1}(z_f)e^{i\phi_{0x}-i\phi_{0f}}\right]e^{-is\phi_{0f}} \\
\alpha_{1x}M_2 - \alpha_{2x}M_3 &= \frac{z_x}{2}\left[J_{r-1}(z_i)e^{-i\phi_{0x}-i\phi_{0i}} + J_{r+1}(z_i)e^{i\phi_{0x}+i\phi_{0i}}\right]e^{ir\phi_{0i}} \\
\alpha_{1x}N_2 - \alpha_{2x}N_3 &= \frac{z_x}{2}\left[J_{s-1}(z_f)e^{i\phi_{0x}+i\phi_{0f}} + J_{s+1}(z_f)e^{-i\phi_{0x}-i\phi_{0f}}\right]e^{-is\phi_{0f}} \\
\alpha_{1x}M_3 + \alpha_{2x}M_2 &= i\frac{z_x}{2}\left[J_{r-1}(z_i)e^{-i\phi_{0x}-i\phi_{0i}} - J_{r+1}(z_i)e^{i\phi_{0x}+i\phi_{0i}}\right]e^{ir\phi_{0i}} \\
\alpha_{1x}N_3 + \alpha_{2x}N_2 &= -i\frac{z_x}{2}\left[J_{s-1}(z_f)e^{i\phi_{0x}+i\phi_{0f}} - J_{s+1}(z_f)e^{-i\phi_{0x}-i\phi_{0f}}\right]e^{-is\phi_{0f}} \\
\alpha_{1x}M_3 - \alpha_{2x}M_2 &= i\frac{z_x}{2}\left[J_{r-1}(z_i)e^{i\phi_{0x}-i\phi_{0i}} - J_{r+1}(z_i)e^{-i\phi_{0x}+i\phi_{0i}}\right]e^{ir\phi_{0i}} \\
\alpha_{1x}N_3 - \alpha_{2x}N_2 &= -i\frac{z_x}{2}\left[J_{s-1}(z_f)e^{-i\phi_{0x}+i\phi_{0f}} - J_{s+1}(z_f)e^{i\phi_{0x}-i\phi_{0f}}\right]e^{-is\phi_{0f}} \\
M_2N_2 + M_3N_3 &= \tfrac{1}{2}\left[J_{r-1}(z_i)J_{s-1}(z_f)e^{-i\phi} + J_{r+1}(z_i)J_{s+1}(z_f)e^{i\phi}\right]e^{ir\phi_{0i}-is\phi_{0f}} \\
M_2N_2 - M_3N_3 &= \tfrac{1}{2}\left[J_{r-1}(z_i)J_{s+1}(z_f)e^{-i\phi_{0i}-i\phi_{0f}} + J_{r+1}(z_i)J_{s-1}(z_f)e^{i\phi_{0i}+i\phi_{0f}}\right]e^{ir\phi_{0i}-is\phi_{0f}} \\
M_2N_3 + M_3N_2 &= i\tfrac{1}{2}\left[J_{r-1}(z_i)J_{s+1}(z_f)e^{-i\phi_{0i}-i\phi_{0f}} - J_{r+1}(z_i)J_{s-1}(z_f)e^{i\phi_{0i}+i\phi_{0f}}\right]e^{ir\phi_{0i}-is\phi_{0f}} \\
M_2N_3 - M_3N_2 &= -i\tfrac{1}{2}\left[J_{r-1}(z_i)J_{s-1}(z_f)e^{-i\phi} - J_{r+1}(z_i)J_{s+1}(z_f)e^{i\phi}\right]e^{ir\phi_{0i}-is\phi_{0f}} \\
M_2M^*_{3'} - M_3M^*_{2'} &= -i\tfrac{1}{2}\left[J_{r-1}(z_i)J_{r'-1}(z_i) - J_{r+1}(z_i)J_{r'+1}(z_i)\right]e^{ir\phi_{0i}-is\phi_{0f}} \\
N_2N^*_{3'} - N_3N^*_{2'} &= i\tfrac{1}{2}\left[J_{s-1}(z_f)J_{s'-1}(z_f) - J_{s+1}(z_f)J_{s'+1}(z_f)\right]e^{ir\phi_{0i}-is\phi_{0f}} \\
M^*_{2'}N_2 - M^*_{3'}N_3 &= \tfrac{1}{2}\left[J_{r'-1}(z_i)J_{s+1}(z_f)e^{i\phi} - J_{r'+1}(z_i)J_{s-1}(z_f)e^{-i\phi}\right]e^{ir\phi_{0i}-is\phi_{0f}} \\
\overline{M}_2\overline{\overline{M}}{}^*_2 + \overline{M}_3\overline{\overline{M}}{}^*_3 &= \tfrac{1}{2}\left[J_{r-1}(z_{\bar{i}})J_{r'-1}(z_{\bar{\bar{i}}})e^{-i\psi_i} + J_{r+1}(z_{\bar{i}})J_{r'+1}(z_{\bar{\bar{i}}})e^{i\psi_i}\right]e^{ir\overline{\phi}_{0i}-ir\overline{\overline{\phi}}_{0i}} \\
\overline{N}_2\overline{\overline{N}}{}^*_2 + \overline{N}_3\overline{\overline{N}}{}^*_3 &= \tfrac{1}{2}\left[J_{s-1}(z_{\bar{f}})J_{s'-1}(z_{\bar{\bar{f}}})e^{i\psi_f} + J_{s+1}(z_{\bar{f}})J_{r'+1}(z_{\bar{\bar{f}}})e^{-i\psi_f}\right]e^{ir\overline{\phi}_{0i}-ir\overline{\overline{\phi}}_{0i}} \\
\overline{N}_2\overline{\overline{M}}{}^*_{2'} - \overline{N}_3\overline{\overline{M}}{}^*_{3'} &= \tfrac{1}{2}\left[J_{r'-1}(\bar{\bar{z}}_i)J_{s+1}(\bar{z}_f)e^{i\overline{\overline{\chi}}} - J_{r'+1}(\bar{\bar{z}}_i)J_{s-1}(\bar{z}_f)e^{-i\overline{\overline{\chi}}}\right]e^{ir'\overline{\overline{\phi}}_{0i}-is\overline{\phi}_{0f}} \\
\overline{N}_2\overline{\overline{M}}{}^*_3 - \overline{N}_3\overline{\overline{M}}{}^*_2 &= -i\tfrac{1}{2}\left[J_{r\prime-1}(z_{\bar{\bar{i}}})J_{s+1}(z_{\bar{f}})e^{i\overline{\overline{\chi}}} - J_{r'+1}(z_{\bar{\bar{i}}})J_{s-1}(z_{\bar{f}})e^{-i\overline{\overline{\chi}}}\right]e^{-ir\prime\phi_{\overline{\overline{0f}}}-is_{\overline{0f}}}
\end{aligned}
$$

Appendix D

Solution to $\sum_{n=-\infty}^{\infty} \frac{1}{n+a} \left(\frac{z_1}{z_2}\right)^n J_n(z_1) J_{n-l}(z_2)$

Second order IFQED processes in a circularly polarised electromagnetic field involve infinite summations of products of Bessel functions, exponential functions and algebraic functions of the form

$$\sum_{n=-\infty}^{\infty} \frac{1}{n+a} \left(\frac{z_1}{z_2}\right)^n J_n(z_1) J_{n-l}(z_2) \tag{D.1}$$

Numerical evaluation of the second order IFQED cross sections would be substantially simplified if an analytic solution of equation D.1 could be obtained. No such solution exists in the literature. Presented here is the analytic solution of a related summation which is, as far as can be established, an original result.

The starting point is Ramanujan's Integral ([Wat22], pg.449). This integral is in the form of a Fourier transform. So taking in the inverse Fourier transform

$$\frac{1}{2\pi} \int_{-\pi}^{\pi} \left[2 \cos \frac{\phi}{2}\right]^{-l} \mathrm{e}^{il\phi/2}\, w^l\, J_{-l}(w)\, \mathrm{e}^{-in\phi}\, \mathrm{d}\phi \quad = \frac{J_{-n}(z_1)}{z_1^{-n}} \frac{J_{n-l}(z_2)}{z_2^{n-l}} \tag{D.2}$$

where $\quad w = [(z_1^2 \mathrm{e}^{i\phi/2} + z_2^2 \mathrm{e}^{-i\phi/2}) 2 \cos \phi/2]^{1/2}$

Next, a summation involving an exponential divided by a polynomial is required ([Bro26], pg.370)

$$\sum_{n=-\infty}^{\infty} \frac{(-1)^n \mathrm{e}^{-in\phi}}{n+a} = \pi \csc \pi a\, \mathrm{e}^{ia\phi} \quad ; \quad -\pi < \phi < \pi \tag{D.3}$$

Both sides of equation D.3 are multiplied by the integrand of the left hand side of equation D.2 and the integration over ϕ is performed on the right hand side

$$\int_{-\pi}^{\pi} \sum_{n=-\infty}^{\infty} \left[2\cos\frac{\phi}{2}\right]^{-l} \mathrm{e}^{il\phi/2}\, w^l\, J_{-l}(w)\, \mathrm{e}^{-in\phi}\, \mathrm{d}\phi = \pi \csc \pi a \frac{J_a(z_1)}{z_1^a}\, \frac{J_{-a-l}(z_2)}{z_2^{-a-l}} \tag{D.4}$$

The integrand on the left hand side of equation D.4 is uniformly convergent on the interval $-\pi < \phi < \pi$ as long as $n + a \neq 0$. The summation and the summation terms not dependent on ϕ can be taken outside the integral. The integration can then be performed using equation D.2 and a common factor $(z_2)^l$ can be removed from both sides

$$\boxed{\sum_{n=-\infty}^{\infty} \frac{1}{n+a} \left(\frac{z_1}{z_2}\right)^n J_n(z_1) J_{n-l}(z_2) = (-1)^l \pi \csc \pi a \left(\frac{z_2}{z_1}\right)^a J_{-a}(z_1) J_{a+l}(z_2)} \tag{D.5}$$

Appendix E

Dispersion Relation Method used in self energy Calculations

The radiative corrections made to the QED processes considered in this thesis, involve calculation of the electron energy shift. The initial analytic expression contains an integration over 4 momenta of a product of electron and photon propagators

$$\Delta\epsilon_p = \frac{ie^2}{(2\pi)^4}\sum_b \int d^4k'\, d^4q'\, \delta^4(q'-q-k'-bk)\mathrm{Tr}\left\{\mathcal{F}(q',k')\right\}\, \frac{1}{q'^2-m_*^2}\,\frac{1}{k'^2} \tag{E.1}$$

We require expressions for both the real and imaginary parts of the electron energy Shift. The method will be to transform equation E.1 into the form of a dispersion relation ([Käl64] pg.112; [Mui65] pg.410).

The integration over k' can be carried out immediately. The presence of the Dirac delta function results in k' being replaced by other 4-momenta. A shift in integration variable q' is made so that

$$\begin{aligned} q' &\to q' + \tfrac{1}{2}D \\ k' &\to q' - \tfrac{1}{2}D \\ \text{where} \qquad D &= q + bk \end{aligned} \tag{E.2}$$

Two new integrations over symbols $K(\equiv q' + \frac{1}{2}D)$ and $L(\equiv q' - \frac{1}{2}D)$ are introduced by use of identities

$$\begin{aligned} \frac{1}{(q'+\frac{1}{2}D)^2-m_*^2+i0} &= \int d^4K\delta(K^2-m^2)\delta^3(\underset{\sim}{q}' + \tfrac{1}{2}\underset{\sim}{D} - \underset{\sim}{K})\left[\frac{\Theta(K_0)}{q_0'+\frac{1}{2}D_0-K_0+i0} - \frac{\Theta(-K_0)}{q_0'+\frac{1}{2}D_0-K_0-i0}\right] \\ \frac{1}{(q'-\frac{1}{2}D)^2+i0} &= \int d^4L\delta(L^2)\delta^3(\underset{\sim}{q}' - \tfrac{1}{2}\underset{\sim}{D} - \underset{\sim}{L})\left[\frac{\Theta(L_0)}{q_0'-\frac{1}{2}D_0-L_0+i0} - \frac{\Theta(-L_0)}{q_0'-\frac{1}{2}D_0-L_0-i0}\right] \end{aligned} \tag{E.3}$$

Making the shifts in equation E.2 and using the identities in equation E.3, the electron energy shift becomes

$$\begin{aligned}
\Delta\epsilon_p(D^2) \quad &= \frac{e^2}{(2\pi)^4}\sum_b \int d^4q'\ d^4K\ d^4L\ \mathrm{Tr}\left\{\mathcal{F}(K,L)\right\}\delta(K^2-m^2)\delta(L^2) \\
&\times\ \delta^3(\underset{\sim}{q}' + \tfrac{1}{2}\underset{\sim}{D} - \underset{\sim}{K})\delta^3(\underset{\sim}{q}' - \tfrac{1}{2}\underset{\sim}{D} - \underset{\sim}{L})\left[\tfrac{\Theta(K_0)}{q_0'+\frac{1}{2}D_0-K_0+i0} - \tfrac{\Theta(-K_0)}{q_0'+\frac{1}{2}D_0-K_0-i0}\right] \\
&\times\ \left[\tfrac{\Theta(L_0)}{q_0'-\frac{1}{2}D_0-L_0+i0} - \tfrac{\Theta(-L_0)}{q_0'-\frac{1}{2}D_0-L_0-i0}\right]
\end{aligned} \tag{E.4}$$

A contour integration over q_0' $(d^4q' = d\underset{\sim}{q}' dq_0')$ gives zero for terms containing $\Theta(K_0)\Theta(L_0)$ and $\Theta(-K_0)\Theta(-L_0)$, and a $2\pi\sum$residues form for the other terms. The integration over $\underset{\sim}{q}'$ proceeds easily with the aid of 3-delta functions and the result is

$$\begin{aligned}
\Delta\epsilon_p(D^2) \quad &= \frac{2\pi i e^2}{(2\pi)^4}\sum_b \int d^4K\ d^4L\ \mathrm{Tr}\left\{\mathcal{F}(K,L)\right\}\delta(K^2-m^2)\delta(L^2) \\
&.\delta^3(\underset{\sim}{D} - \underset{\sim}{K} + \underset{\sim}{L})\left[\tfrac{\Theta(K_0)(\Theta(-L_0)}{D_0-K_0+L_0+i0} - \tfrac{\Theta(-K_0)(\Theta(L_0)}{D_0-K_0+L_0-i0}\right]
\end{aligned} \tag{E.5}$$

The electron energy shift can be written in the form of a dispersion relation by introducing

$$\begin{aligned}
\rho(\sigma^2) \quad &= \frac{2\pi i e^2}{(2\pi)^4}\sum_b \int d^4q' d^4K d^4L \mathrm{Tr}\left\{\mathcal{F}(K,L)\right\}\delta(K^2-m^2)\delta(L^2) \\
&\times\ \delta^4(\sigma - K + L)[\Theta(K_0)\Theta(-L_0) + \Theta(-K_0)\Theta(L_0)] \\
&\text{and} \qquad \Delta\epsilon_p(D^2) = \textstyle\int d^4\sigma\rho(\sigma)\delta^3(\underset{\sim}{D} - \underset{\sim}{\sigma})\left[\tfrac{\Theta(\sigma_0)}{D_0-\sigma_0+i0} - \tfrac{\Theta(-\sigma_0)}{D_0-\sigma_0-i0}\right] \\
&\Delta\epsilon_p(D^2) \equiv \textstyle\int_0^\infty d\sigma^2\ \dfrac{\rho(\sigma^2)}{D^2-\sigma^2+i0}
\end{aligned} \tag{E.6}$$

Comparing this last expression with the basic form of a dispersion relation ([Mui65] pg.410) the real and imaginary parts of the electron energy shift can be written

$$\begin{aligned}
\Im\Delta\epsilon_p(D^2) \quad &= -2\pi\rho(D^2) \\
\Re\Delta\epsilon_p(D^2) \quad &= \frac{1}{\pi}P\int_{-\infty}^{\infty}\frac{\Im\Delta\epsilon_p(\sigma^2)}{\sigma^2-D^2}d\sigma^2
\end{aligned} \tag{E.7}$$

and performing the integration over L

$$\begin{aligned}
\rho(D^2) \quad &= \frac{2\pi i e^2}{(2\pi)^4}\int d^4K\ \mathrm{Tr}\left\{\mathcal{F}(K,K-D)\right\}\delta(K^2-m^2)\delta(D^2-2(KD)+m_*^2) \\
&.[\Theta(K_0)\Theta(-K_0+D_0) + \Theta(-K_0)\Theta(K_0-D_0)]
\end{aligned} \tag{E.8}$$

The electron energy shift is an algebraic function of scalar products of 4-vectors and is therefore invariant with respect to proper 4-rotations of the coordinate frame. The delta functions and step functions in the expression for $\rho(D^2)$ require that the integral goes to zero for space-like D_μ, and since proper 4-rotations leave time-vectors as time-vectors, $\rho(D^2)$ can be calculated in the reference frame in which $\underset{\sim}{k} = 0$ ([Käl64], pg.112). The evaluation of $\rho(D^2)$ proceeds by performing the integration over K in 4-dimensional spherical polar coordinates

$$\begin{aligned} \mathrm{d}^4K &= -|K|^3\,\mathrm{d}|K|\ \sinh\zeta\,\mathrm{d}\cosh\zeta\,\mathrm{d}\cos\theta\,\mathrm{d}\phi \\ |\underset{\sim}{K}| &= |K|\sinh\zeta \\ K_0 &= |K|\cosh\zeta \end{aligned} \tag{E.9}$$

and rotating the coordinate system until $D^2 = D_0^2$. The integrations over $|K|$ and $\cosh$ are straightforward and the trace calculation will result in a function $\mathcal{G}$ of scalar products and scattering angles. In any reference frame, the imaginary part of the electron energy shift turns out to be

$$\Im\Delta\epsilon_p(D^2) = -\frac{e^2}{16\pi}\sum_b\int \mathrm{d}\cos\theta\,\mathrm{d}\varphi\ \left(1-\frac{m_*^2}{D^2}\right)\ \mathcal{G}(D^2,(kq),\theta,\varphi)\ \Theta(D^2-m_*^2) \tag{E.10}$$

The argument of the Heaviside step function proves crucial in the consideration of divergences. The inclusion of an infinitesimally small photon mass ϵ into the photon propagator denominator at the outset results in

$$\Theta(D^2-m_*^2) \rightarrow \Theta(D^2-(m_*+\epsilon)^2) \tag{E.11}$$

Bibliography

[AB65] A.I. Akheizer and V.B. Berestetskii. *Quantum Electrodynamics*. Interscience, New York, 1965.

[AK87] I. Affleck and L. Kruglyak. *Phys Rev Lett*, 59(10):1065–1068, 1987.

[Alb77] J.R. Albright. *J Phys A*, 10(4):485–490, 1977.

[Ald02] J. Alda. *Encyclopedia of Optical Engineering*. Marcel Dekker, New York, 2002.

[AM85] A.I Akhiezer and N.P. Merenkov. *Sov. Phys. JETP*, 61(1):41–47, 1985.

[AS65] M. Abramovich and I.A. Stegun. *Handbook of Mathematical Functions*. Dover, New York, 1965.

[BBB70] Z. Bialynicka and I. Bialynicki-Birula. *Phys Rev D*, 2(10):2341–2345, 1970.

[Bea65] C. Bemporad et al. *Phys Rev*, 138:B1546, 1965.

[Bea74] V.G. Bagrov et al. *Russian Physics Journal*, 17(12):1709–1712, 1974.

[Bea75] V.G. Bagrov et al. *Russian Physics Journal*, 18(7):909–912, 1975.

[Bea79a] J. Bos et al. *J Phys A*, 12(5):715–730, 1979.

[Bea79b] J. Bos et al. *J Phys A*, 12(12):2573–2581, 1979.

[Bea99] C. Bamber et al. *Phys Rev D*, 60(9):092004, 1999.

[Bec81] W. Becker. *Phys Rev A*, 23(5):2381–93, 1981.

[Bec88] W. Becker. *Z Phys*, D7:353, 1988.

[Bec89] W. Becker. *J Opt Soc Am*, B6:1083, 1989.

[Bec91] W. Becker. *Laser Part Beams*, 9(2):603–618, 1991.

[Bel77] I.V. Belousov. *Opt Comm*, 20(2):205–208, 1977.

[Bes84] V.S. Beskin. *Sov Phys Lebedev Institute Reports*, 4:33, 1984.

[BH34] H. Bethe and W. Heitler. *Proc Roy Soc*, 146:83–112, 1934.

[Bha35] H.J. Bhabha. *Proc Roy Soc*, 152:559–586, 1935.

[BK64] L.S. Brown and T.W.B. Kibble. *Phys Rev*, 133(3A):A705, 1964.

[BM75] W. Becker and H. Mitter. *J. Phys. A: Math. Gen.*, 8(10):1638–1657, 1975.

[BM76] W. Becker and H. Mitter. *J. Phys. A: Math. Gen.*, 9(12):2171–2184, 1976.

[BN37] F. Bloch and A. Nordiseck. *Phys Rev*, 52:54, 1937.

[BO67] V.M. Buimstrov and V.P. Oleinik. *Sov Phys - Semiconductors*, 1(1):65–73, 1967.

[Boa83] M.L. Boas. *Mathematical Methods in the Physical Sciences*. John Wiley & Sons, New York, 2nd edition, 1983.

[BP82] E.M. Berestetskii, V.B. Lifshitz and L.P. Pitaevskii. *Quantum Electrodynamics*. Pergamon Press, second edition, 1982.

[Bro26] J. Bromwich. *An introduction to the theory of infinite series*. MacMillian, London, 2nd edition, 1926.

[BS68] V.M. Baier, V.N. Katkov and V.M. Strakhovenko. *Sov Phys JETP*, 26:854, 1968.

[BS69] V.M. Baier, V.N. Katkov and V.M. Strakhovenko. *Sov Phys JETP*, 28:807, 1969.

[BS71a] I.A. Batalin and A.E. Shabad. *Sov Phys JETP*, 33:483, 1971.

[BS71b] J.B. Bjorken, J.D. Kogut and D.E Soper. *Phys Rev D*, 3(6):1382–1399, 1971.

[BS72] V.M. Baier, V.N. Katkov and V.M. Strakhovenko. *Sov J Nucl Phys*, 14:572, 1972.

[BS75a] V.M. Baier, V.N. Katkov and V.M. Strakhovenko. *Sov Phys JETP*, 41:198, 1975.

[BS75b] V.M. Baier, V.N. Katkov and V.M. Strakhovenko. *Sov Phys JETP*, 40:225–232, 1975.

[BS76] V.M. Baier, V.N. Katkov and V.M. Strakhovenko. *Sov Phys JETP*, 42:400–407, 1976.

[BT70] F.V. Bunkin and I.I. Tugov. *Sov Phys Doklady*, 14(7):678, 1970.

[BV81a] J. Bergou and S. Varro. *J Phys A*, 14:1469, 1981.

[BV81b] J. Bergou and S. Varro. *J Phys A*, 14:2281, 1981.

[BW34] G. Breit and J.A. Wheeler. *Phys Rev*, 46(12):1087–1091, 1934.

[BW65] A. Boivin and E. Wolf. *Phys Rev*, 138(6B):B1561–B1565, 1965.

[BZ77] O.G. Borisov, A.V. Goryaga and V.Ch. Zhukovskii. *Russian Physics Journal*, 20(2):176–181, 1977.

[Com23] A.H. Compton. *Phys Rev*, 22(5):409–413, 1923.

[CW73] S. Coleman and E. Weinberg. *Phys Rev D*, 7(6):1888–1910, 1973.

[Dav79] L.W. Davis. *Phys Rev A*, 19(3):1171–1179, 1979.

[DG27] C. Davisson and L.H. Germer. *Phys Rev*, 30(6):705–740, 1927.

[DH83] J.K. Daugherty and A.K. Harding. *Astrophysical Journal*, 273:761, 1983.

[Dir28a] P.A.M. Dirac. *Proc Roy Soc*, 117:610, 1928.

[Dir28b] P.A.M Dirac. *Proc Roy Soc*, 118:351, 1928.

[DT95] H.S Derlet, P.M. Perlman and G.J. Troup. *Phys Lett A*, 209(3):165–172, 1995.

[Dys49] F.J. Dyson. *Phys Rev*, 75:486, 1949.

[Ebe69] J.H. Eberly. *Progress Opt*, 7:359, 1969.

[Ehl87] F. Ehlotzky. *J Phys B*, 20:2619–2626, 1987.

[Ein05] A. Einstein. *Ann Physik*, 17:132–148, 1905.

[ER83] T.J. Englert and E.A. Rinehart. *Phys Rev A*, 28(3):1539, 1983.

[ES91] E. Esarey and P. Sprangle. *Phys Rev A*, 45(8):5872, 1991.

[ES92] E. Esarey and P. Sprangle. *Phys Fluids B*, 4(7):2241, 1992.

[FE64] Z. Fried and J.H. Eberly. *Phys Rev*, 136(3B):B871–B887, 1964.

[Fea80] L. Federici et al. *Nuovo Cimento*, 59B:247–256, 1980.

[Fed75] M.V. Fedorov. *Sov Phys JETP*, 41:601, 1975.

[Fer32] E. Fermi. *Rev Mod Phys*, 4:87, 1932.

[Fer73] R.A. Ferrel. *Amer. J Phys*, 41(1):111–113, 1973.

[Fey48a] R.P. Feynman. *Rev Mod Phys*, 20:367–387, 1948.

[Fey48b] R.P. Feynman. *Phys Rev*, 74(8):939–946, 1948.

[Fey49a] R. Feynman. *Phys Rev*, 79(6):749, 1949.

[Fey49b] R. Feynman. *Phys Rev*, 76(6):769, 1949.

[FR84] M.V. Federov and S.P. Roshchupkin. *J Phys Math*, 17:3143–3149, 1984.

[Fra65] L.M. Frantz. *Phys Rev*, 139(5B):B1326–B1336, 1965.

[Fri61] Z. Fried. *Nuovo Cimento*, 22(6):1303, 1961.

[Fri63] Z. Fried. *Phys Lett*, 3:349, 7 1963.

[Fur51] W.H. Furry. *Phys Rev*, 81:115, 1951.

[Gea83a] I. Ginzburg et al. *Nucl Inst Meth*, 205:47, 1983.

[Gea83b] I.F. Ginzburg et al. *Sov J Nucl Phys*, 38(4), 1983.

[GGG75] R. Guccione-Gush and H.P. Gush. *Phys Rev D*, 12(2):404–12, 1975.

[Gla63] R.J. Glauber. *Phys Rev*, 131(6):2766–2788, 1963.

[Gol64] I.I Goldman. *Sov Phys JETP*, 19(4):954, 1964.

[GR83] Ya.T. Grinchishin and M.P. Rekalo. *Sov Phys JETP*, 57(5):935–40, 1983.

[GR85] W. Muller B. Greiner and J. Rafelski. *Quantum Electrodynamics of Strong Fields*. Springer, Heidelberg, 1985.

[GR03] W. Greiner and J. Reinhardt. *Quantum Electrodynamics*. Springer-Verlag, Berlin, 3rd edition, 2003.

[Gri82] Ya.T. Grinchishin. *Sov J Nucl Phys*, 36(6):844–47, 1982.

[GS89] A.D. Gazazyan and B.G. Sherman. *Sov Phys JETP*, 69(1):38–45, 1989.

[Hah05] T. Hahn. *Comp Phys Comm*, 168(2):78–95, 2005.

[Hei54] W. Heitler. *Quantum Theory of Radiation*. Oxford University Press, London, 3rd edition, 1954.

[Hor88] H. Hora. *Nature*, 333:337, 1988.

[HP29] W. Heisenberg and W. Pauli. *Z Phys*, 56:1, 1929.

[HP30] W. Heisenberg and W. Pauli. *Z Phys*, 59:166, 1930.

[IS03] G.L. Ivanov, D.Yu. Kotkin and V.G. Serbo. *eprint arXiv*, hep-ph:0310325, 2003.

[IZ80] C. Itzykson and J.B. Zuber. *Quantum Field Theory*. McGraw-Hill, 1980.

[Jac75] J.D. Jackson. *Classical Electrodynamics*. John Wiley and Sons, New York, 1975.

[JR76] J.M. Jauch and F. Rohrlich. *The Theory of Photons and Electrons*. Springer-Verlag, Berlin, 1976.

[Kah68] J. Kahane. *J Math Phys*, 9:1732, 1968.

[Käl64] G. Källen. *Elementary Particle Physics*. Addison-Wesley, Reading, 1964.

[Kea90a] Y.I Klimenko et al. *Russian Physics Journal*, 33(10):835–840, 1990.

[Kea90b] Y.I Klimenko et al. *Russian Physics Journal*, 33(10):880–885, 1990.

[KF47] P. Kusch and H.M. Foley. *Phys Rev*, 72(12):1256–1257, 1947.

[KF48] P. Kusch and H.M. Foley. *Phys Rev*, 73(4):412, 1948.

[Kib65] T.W.B. Kibble. *Phys Rev*, 138(3B):B740–B753, 1965.

[KM87] A.A. Kozlenkov and I.G Mitrafanov. *Sov Phys JETP*, 64:1173, 1987.

[KN28] O. Klein and T. Nishina. *Z Phys*, 52:853, 1928.

[KN64] J.J. Klein and B.P. Nigam. *Phys Rev*, 135(5B):B1279–B1280, 1964.

[Kor84] F.F. Kormendi. *Optica Acta*, 31(3):301–11, 1984.

[KR63] F.C Khanna and F. Rohrlich. *Phys Rev*, 131(6):2721–2723, 1963.

[Kry80] G.Y. Kryuchkov. *Sov Phys JETP*, 51:225, 1980.

[KS70] J.B. Kogut and D.E. Soper. *Phys Rev D*, 1(10):2901–2914, 1970.

[KW73] N. Kroll and K.M. Watson. *Phys Rev A*, 8(2):804–809, 1973.

[Lea89] T.S. Luk et al. *Opt Lett*, 14:1113, 1989.

[Leb70] I.V. Lebedev. *Opt Spectr*, 29:503, 1970.

[LL34] L. Landau and E. Lifshitz. *Physik Z*, 6:244, 1934.

[LL75] L.D. Landau and E.M. Lifshitz. *The classical theory of Fields*. Pergamon, New York, 4th edition, 1975.

[LM75] W.H. Lax, M. Louisell and W.B. McKnight. *Phys Rev A*, 11:1365–1370, 1975.

[LR47] W.E Lamb and R.C. Rutherford. *Phys Rev*, 72:241, 1947.

[LS81] C. Leubner and E.M. Strohmaier. *J Phys A*, 14:509–520, 1981.

[Lyu75] V.A. Lyul'ka. *Sov Phys JETP*, 40(5):815, 1975.

[Max92] J.C. Maxwell. *A Treatise of Electricity and Magnetism*. Clarendon Press, Oxford, 3rd edition, 1892.

[McD91] K. McDonald. Proposal for a study of qed at critical field strength in intense laser high energy electron collisions at slac. Technical report, SLAC, 1991.

[McM61] W.H. McMaster. *Rev Mod Phys*, 33:8, 1961.

[ME88] P.W. Miloni and J.M. Eberly. *Lasers*. John Wiley and Sons, New York, 1988.

[Mea91] M.M. Murnane et al. *Science*, 251:531, 1991.

[Mea95] D.D. Meyerhofer et al. *Phys Rev Lett*, 74:2439–2442, 1995.

[Mea96] D.D. Meyerhofer et al. *J Opt Soc Am B*, 13:113, 1996.

[Mer91] R. Mertig. *Comp Phys Comm*, 60:165, 1991.

[Mik82] K.O. Mikaelian. *Phys Lett*, 115B:267, 1982.

[Mil63] R.H. Milburn. *Phys Rev Lett*, 10(3):75–77, 1963.

[Mit75] H. Mitter. *Acta Physica Austriaca.*, XIV:397–468, 1975.

[Mit79] H. Mitter. Intense fields and quantum electroynamics. In *Multiphoton Processes - Proceedings of the International Conference at the University of Rochester*, 1979.

[MN77] D.A. Morozov and N.B. Narozhnyi. *Sov Phys JETP*, 45(1):23, 1977.

[Mol32] C. Moller. *Ann Physik*, 14:568, 1932.

[MR75] D.A Morozov and V.I. Ritus. *Nucl Phys B*, 86(2):309–332, 1975.

[MS84] F. Mandl and G. Shaw. *Quantum Field Theory*. John Wiley and Sons, 1984.

[Mui65] H. Muirhead. *The Physics of Elementary Particles*. Pergamon Press, Oxford, 1965.

[Nac90] O. Nachtmann. *Elementary Particle Physics: Concepts and Phenomena*. Springer, 1990.

[Nar69] N.B. Narozhnyi. *Sov Phys JETP*, 28(2):371, 1969.

[Nar79] N.B. Narozhnyi. *Phys Rev D*, 20(6):1313–1319, 1979.

[NR64a] A.I. Nikishov and V.I. Ritus. *Sov. Phys. JETP*, 19(2):529–541, 1964.

[NR64b] A.I. Nikishov and V.I. Ritus. *Sov. Phys. JETP*, 19(5):1191–1199, 1964.

[NR65a] A.I. Narozhnyi, N.B. Nikishov and V.I. Ritus. *Sov. Phys. JETP*, 20(3):622–629, 1965.

[NR65b] A.I Nikishov and V.I. Ritus. *Sov Phys JETP*, 20:757, 1965.

[NR67] A.I Nikishov and V.I. Ritus. *Sov Phys JETP*, 52:1707–1719, 1967.

[NR71] R.A. Neville and F. Rohrlich. *Phys Rev D*, 3:1692–1707, 1971.

[Ole67] V.P. Oleinik. *Sov. Phys. JETP*, 25(4):697–708, 1967.

[Ole68] V.P. Oleinik. *Sov. Phys. JETP*, 26(6):1132–1138, 1968.

[Ole72] V.P. Oleinik. *Sov Phys JETP*, 34(1):14, 1972.

[OS75] V.P. Oleinik and V.A. Sinyak. *Opt Comm*, 14(2):179–183, 1975.

[Pai86] A. Pais. *Inward Bound:Of matter and forces in the Physical World*. Clarendon Press, Oxford, England, 1986.

[PE02] J.Z. Panek, P. Kaminski and F. Ehlotzky. *Opt Comm*, 213:121–128, 2002.

[PE03] J.Z. Panek, P. Kaminski and F. Ehlotzky. *Euro Phys J D*, 26:3–6, 2003.

[PE04] J.Z. Panek, P. Kaminski and F. Ehlotzky. *Phys Rev A*, 69:1–7, 013404.

[PL89] A.K. Puntajer and C. Leubner. *Phys Rev A*, 40:279, 1989.

[Pla01] M. Planck. *Ann Physik*, 4(3):564–566, 1901.

[PV49] W. Pauli and F. Villars. *Rev Mod Phys*, 21:434, 1949.

[PV68] H. Prakash and Vachaspati. *Nuovo Cimento*, 53B(1):34, 1968.

[RA00] V.A. Roschupkin, S.P. Tsybulnik and Chmirev A.N. *Laser Physics*, 10(6):1256–1272, 2000.

[RE66] H.R Reiss and J.L. Eberly. *Phys Rev*, 151:1058–1066, 1966.

[Rei62] H.R. Reiss. *J Math Phys*, 3(1):59, 1962.

[Rit70] V.I. Ritus. *Sov Phys JETP*, 30(6):1183–1187, 1970.

[Rit72] V.I. Ritus. *Ann Phys*, 69:555–582, 1972.

[Ros84] S.P. Roschchupkin. *Opt Spektrosc*, 56:22, 1984.

[Ros96] S.P. Roschupkin. *Laser Phys*, 6:837, 1996.

[San67] S.S. Sannikov. *Sov Phys JETP*, 25(2):306, 1967.

[San95] S.S. Sannikov. *Russian Physics Journal*, 38:796–803, 8 1995.

[Sch48a] J. Schwinger. *Phys Rev*, 73:416, 1948.

[Sch48b] J. Schwinger. *Phys Rev*, 74:1439, 1948.

[Sch51] J. Schwinger. *Phys Rev*, 82:664, 1951.

[Sch54] J. Schwinger. *Proc Nat Acad Sci*, 40:132, 1954.

[Sch62] S. Schweber. *An introduction to Relativistic Quantum Field Theory*. Harper and Row, 1962.

[Sch01] C. Schubert. *Nucl Phys B*, 609:313–324, 2001.

[Sea83] A.M. Sandorfi et al. *IEEE Trans Nucl Sci*, NS-30:3083, 1983.

[Sea91] C. Sauteret et al. *Opt Letters*, 16(4):238, 1991.

[Sea92] P. Sprangle et al. *J Appl Phys*, 72(11):5032, 1992.

[SG67] N.D. Sen Gupta. *Z Phys*, 200:13, 1967.

[Sha75] A.E. Shabad. *Ann Phys*, 90:166–195, 1975.

[ST64] A.A. Sokolov and I.M. Ternov. *Sov Phys Doklady*, 8(12):1203–1205, 1964.

[Ste63] P. Stehle. *J Opt Soc Am*, 53(8):1003, 1963.

[Stu43] E.C.G. Stuckleberg. *Helv Phys Acta*, 17:13, 1943.

[Tea47] S. Tomonaga et al. *Prog Theoret Phys*, 2:101, 1947.

[Tho97] J.J. Thomson. *Philosophical Magazine*, 44:293, 1897.

[Tho27] J.J. Thomson. *Proc Phys Soc*, 40:79–89, 1927.

[Tho33] J.J. Thomson. *Conduction of Electricity through Gases*, volume II. Cambridge University Press, Cambridge, England, 1933.

[TK68] V.G. Tegnov, I.M. Bagrov and A.M. Khapaev. *Ann Phys*, 22:25, 1968.

[Tol52] J. Toll. *Thesis*. Princeton University, 1952.

[Tom46] S. Tomonaga. *Prog Theoret Phys*, 1:27, 1946.

[Tom48] S. Tomonaga. *Phys Rev*, 74:224, 1948.

[Tsa93] Y.S. Tsai. *Phys Rev D*, 48(1):96–115, 1993.

[Ueh35] E.A. Uehling. *Phys Rev*, 48:55, 1935.

[Vac62] Vachaspati. *Phys Rev*, 128(2):664, 1962.

[Vac63] Vachaspati. *Phys Rev*, 130(6):2598, 1963.

[Val51] J. Valatin. *J Phys Radium*, 12:607, 1951.

[VE84] S. Varro and F. Ehlotzky. *J Phys B*, 17:L759–L764, 1984.

[Vol35] D.M. Volkov. *Zeitschrift für Physik*, 94:250–260, 1935.

[VR66] O. Von Roos. *Phys Rev*, 150(4):1112–1118, 1966.

[Wat22] G.N. Watson. *A treatise on the Theory of Bessel Functions*. Cambridge University Press, London, 1922.

[Wat89] S. Watanabe. *J Opt Soc Am B*, 6:1870, 1989.

[Wea83] A. Weingartshofer et al. *J Phys B*, 16:1805, 1983.

[Wea02] I. Watts et al. *Phys Rev Lett*, 88(15):155001–1, 2002.

[Wei95] S. Weinberg. *The Quantum Theory of Fields. Vol1:Foundations*. Cambridge University Press, New York, 1995.

[Yak67] V.P. Yakovlev. *Sov Phys JETP*, 24:411, 1967.

[YP91] K. Yokoya and Chen P. Beam-beam phenomena in linear colliders kek preprint 91-2. Technical report, KEK, 1991.

[Zei91] V. Zeimann. Beamstrahlung simulation and diagnostics slac-pub-5595. Technical report, SLAC, 1991.

[Zel67] Ya.B. Zeldovich. *Sov Phys JETP*, 24:1006–1008, 1967.

[ZG90] D.H. Zhang, W. Feng and R. Gilmore. *Rev Mod Phys*, 62(4):867–927, 1990.

[ZH72] V.C. Zhukovskii and J. Herrmann. *Sov J Nucl Phys*, 14(2):569, 1972.